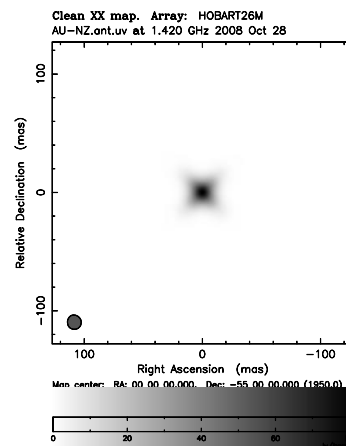
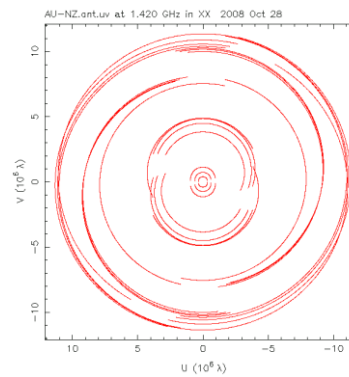
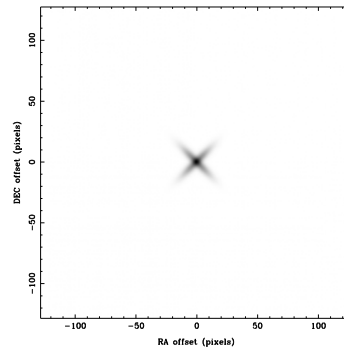


# Development of Very Long Baseline Interferometry (VLBI) Techniques in New Zealand: Array Simulation, Image Synthesis and Analysis



Stuart Weston

**Development of Very Long Baseline Interferometry (VLBI)  
Techniques in New Zealand: Array Simulation, Image Synthesis  
and Analysis**

**Stuart Duncan Weston B.Sc (Honours)**

A thesis submitted to

Auckland University of Technology

in fulfilment of the requirements for the degree of

Master of Philosophy (MPhil)

2008

School of Computing & Mathematical Sciences

Supervisors: Prof. Sergei Gulyaev and Tim Natusch

## **Abstract**

This thesis presents the design and development of a process to model Very Long Base Line Interferometry (VLBI) aperture synthesis antenna arrays. In line with the Auckland University of Technology (AUT) Institute for Radiophysics and Space Research (IRSR) aims to develop the knowledge, skills and experience within New Zealand, extensive use of existing radio astronomical software has been incorporated into the process namely AIPS (Astronomical Imaging Processing System), MIRIAD (a radio interferometry data reduction package) and DIFMAP (a program for synthesis imaging of visibility data from interferometer arrays of radio telescopes).

This process has been used to model various antenna array configurations for two proposed New Zealand sites for antenna in a VLBI array configuration with existing Australian facilities and a possible antenna at Scott Base in Antarctica; and the results are presented in an attempt to demonstrate the improvement to be gained by joint trans-Tasman VLBI observation. It is hoped these results and process will assist the planning and placement of proposed New Zealand radio telescopes for cooperation with groups such as the Australian Long Baseline Array (LBA), others in the Pacific Rim and possibly globally; also potential future involvement of New Zealand with the SKA.

The developed process has also been used to model a phased building schedule for the SKA in Australia and the addition of two antenna in New Zealand. This has been presented to the wider astronomical community via the Royal Astronomical Society of New Zealand Journal, and is summarized in this thesis with some additional material.

A new measure of quality (“figure of merit”) for comparing the original model image and final CLEAN images by utilizing normalized 2-D cross correlation is evaluated as an alternative to the existing subjective visual operator image comparison undertaken to date by other groups. This new unit of measure is then used in the presentation of the results to provide a quantitative comparison of the different array configurations modelled.

Included in the process is the development of a new antenna array visibility program which was based on a Perl code script written by Prof Steven Tingay to plot antenna visibilities

for the Australian Square Kilometre Array (SKA) proposal. This has been expanded and improved removing the hard coded fixed assumptions for the SKA configuration, providing a new useful and flexible program for the wider astronomical community.

A prototype user interface using *html/cgi/perl* was developed for the process so that the underlying software packages can be served over the web to a user via an internet browser. This was used to demonstrate how easy it is to provide a friendlier interface compared to the existing cumbersome and difficult command line driven interfaces (although the command line can be retained for more experienced users).



## Acknowledgements

I wish to thank several people who have supported me through this research.

To my supervisors Prof. Sergei Gulyaev and Tim Natusch for their wisdom and guidance. I am especially grateful to Prof Sergei Gulyaev for his confidence in me as a mature student returning after many years in the wilderness of commercial IT.

Prof Steven Tingay who provided much invaluable assistance, guidance and mentoring while visiting the IRSR Group at AUT here in New Zealand and long distance through emails. In addition for providing a copy of the Perl scripts used for the SKA proposal by his group.

To my late father Dr N.T Weston who just before he passed away encouraged me with the sentiments “that although it is interesting to study for one’s own self interest, it is far more noble to be helping others through your endeavours however small your contribution”.

Leonid Kogan of the National Radio Astronomy Observatory, USA (NRAO). When I got stuck and frustrated with AIPS and the task UVCON he provided the two emails that got me going again.

Dr. Peter Thomasson for his assistance in arranging a visit to Jodrell Bank Observatory, UK in June 2007, and providing supervision during my stay. Also the many hours spent during this visit de-mystifying AIPS.

For my wife for her forbearance and the encouragement of my son who had lots of hard questions that needed answering about space, the universe and all those other mind bending cosmological ideas that seem so simple to an 8 year old boy interested in dinosaurs and Astronomy.

**Front Cover:** A collage of three plots. The top plot is a model image used in this thesis that was generated by MIRIAD to represent an Active Galactic Nuclei. The middle plot is the  $u, v$  Coverage for 12hrs with antennae in Australia and New Zealand. The bottom plot is the final CLEAN image generated from the process via DIFMAP from the data represented by the preceding plots.

"I hereby declare that this submission is my own work and that, to the best of my knowledge and belief, it contains no material previously published or written by another person (except where explicitly defined in the acknowledgements), nor material which to a substantial extent has been submitted for the award of any other degree or diploma of a university or other institution of higher learning."

**STUART DUNCAN WESTON**

## Table of Contents

<b>ABSTRACT.....</b>	<b>III</b>
<b>ACKNOWLEDGEMENTS.....</b>	<b>V</b>
<b>TABLE OF CONTENTS.....</b>	<b>VII</b>
<b>LIST OF FIGURES .....</b>	<b>X</b>
<b>LIST OF TABLES .....</b>	<b>XVI</b>
<b>LIST OF SYMBOLS AND FUNCTIONS .....</b>	<b>XVIII</b>
<b>1. INTRODUCTION.....</b>	<b>1</b>
1.1. OVERVIEW OF THESIS STRUCTURE .....	12
<b>2. DISCUSSION OF VLBI AND APERTURE SYNTHESIS THEORY .....</b>	<b>14</b>
2.1. INTERFEROMETRY .....	15
2.2. ANTENNA COORDINATES AND $(U, V, W)$ .....	18
2.3. VISIBILITY FUNCTION.....	23
2.4. DECONVOLUTION AND CLEAN .....	26
2.5. THE SQUARE KILOMETRE ARRAY .....	30
<b>3. SIMULATION MODEL METHOD .....</b>	<b>33</b>
3.1. VLBI MODELLING PROCESS OVERVIEW .....	36
3.2. ARRAY CONFIGURATION .....	39
3.2.1. <i>Geographic location of antennae in Australia, New Zealand and Antarctica</i>	41
3.2.2. <i>SKA Antenna Data</i> .....	46
3.3. SKY VISIBILITY .....	51

3.4.	MODEL SOURCE .....	56
3.4.1.	<i>Model Source: AGN</i> .....	57
3.4.2.	<i>Model Source: Galaxy Triplet</i> .....	62
3.4.3.	<i>Model Source: Bright Source with a Jet</i> .....	66
3.5.	GENERATION OF $U, V$ DATA .....	69
3.5.1.	<i>MIRIAD observatories.dat</i> .....	72
3.6.	$U, V$ DATA PROCESSING .....	73
3.6.1.	<i><math>u, v</math> Data Weighting</i> .....	76
3.6.2.	<i><math>u, v</math> Taper</i> .....	80
3.7.	FIGURE OF MERIT .....	87
3.7.1.	<i>Full Width at Half Maximum Intensity</i> .....	90
3.7.2.	<i>Mean Square Error</i> .....	94
3.7.3.	<i>2-D Cross-Correlation</i> .....	99
3.7.4.	<i>Normalized 2-D Cross-Correlation</i> .....	105
3.7.5.	<i>Figure of Merit Summary</i> .....	111
3.8.	NOISE AND ERRORS MODELLED .....	112
<b>4.</b>	<b>SIMULATION MODEL RESULTS AND DISCUSSION .....</b>	<b>113</b>
4.1.	AUSTRALIAN SUB-ARRAY ONLY ARRAY .....	114
4.1.1.	<i>Simulation Results</i> .....	116
4.1.2.	<i>Analysis of Results</i> .....	124
4.2.	AUSTRALIAN SUB-ARRAY – NEW ZEALAND ARRAY .....	127
4.2.1.	<i>Simulation Results</i> .....	128

4.2.2.	<i>Analysis of Results</i> .....	136
4.3.	AUSTRALIAN SUB-ARRAY – NEW ZEALAND – SCOTT BASE.....	139
4.3.1.	<i>Simulation Results</i> .....	140
4.3.2.	<i>Analysis of Results</i> .....	148
4.4.	ARRAY COMPARISON .....	151
4.5.	SKA PHASED BUILDING SIMULATION .....	156
4.5.1.	<i>SKA Building Scenario Results</i> .....	163
4.5.2.	<i>Analysis of Results</i> .....	167
4.5.3.	<i>Summary of the simulated SKA phased building</i> .....	169
5.	<b>CONCLUSION</b> .....	173
6.	<b>REFERENCES:</b> .....	175
	<b>APPENDIX A. ELECTRONIC SUPPLEMENT</b> .....	179
	<b>APPENDIX B. DIFMAP CLEAN MAP EXPLANATION</b> .....	180
	<b>APPENDIX C. USER INTERFACE</b> .....	182
	<b>APPENDIX D. VISIBILITY PERL PROGRAM</b> .....	189
	<b>APPENDIX E. MIRIAD OBSERVATORIES.DAT</b> .....	199
	<b>APPENDIX F. MATLAB SCRIPTS FOR FITS IMAGE CORRELATION</b> .....	205

## List of Figures

Figure 1: Atmospheric Window ( <a href="http://www.answers.com/topic/atmospheric-electromagnetic-transmittance-or-opacity-jpg-1">http://www.answers.com/topic/atmospheric-electromagnetic-transmittance-or-opacity-jpg-1</a> ) .....	2
Figure 2: Basic two-element interferometer .....	5
Figure 3: East-West antenna array rotational synthesis .....	7
Figure 4: $u, v$ Plots for AU-NZ Array. For declinations $\delta = -90^\circ$ (left), $\delta = -50^\circ$ (middle) and $\delta = 0^\circ$ (the right panel).....	8
Figure 5 : (Left) Australian VLBI array (Long Baseline Array – LBA), (Right) Very Long Baseline Array – VLBA (NRAO / AUI / NSF) .....	9
Figure 6: The Earth with NZ at Top .....	11
Figure 7: Two-element interferometer. The path delay $\tau_g$ is compensated by the delay circuit in the receiver.....	15
Figure 8: The (X,Y,Z) Coordinate system for specification of relative positions of antennae. ....	18
Figure 9: Mapping of the celestial sphere onto a plane in one dimension.....	19
Figure 10: The geometrical relationship between an interferometer, a celestial source and the $u, v$ -plane, seen in relationship to the celestial sphere. SCP is the south celestial pole; $b_\lambda$ is the baseline between antennae.....	20
Figure 11: Two elliptical loci representing the projection of the baseline vectors onto the $(u, v)$ plane as a source is tracked across the sky (Thompson 1999). The lower curve corresponds to a reversal of the direction of the baseline vector. ....	22
Figure 12: Geometric relationship between a source under observation $I(l, m)$ and an interferometer or one antenna pair. The antenna baseline vector, measured in wavelengths, has length $D_\lambda$ and components $(u, v, w)$ (Diamond, Garrington et al. 2003). ....	23
Figure 13: The top image is the Dirty Beam map of an observation for source 3C258. Bottom image is the final CLEAN map of the same source using DIFMAP. This example is taken from actual data from MERLIN for an observation of this source taken in March 2006.....	28
Figure 14: SKA Specifications by Key Science Project goals (Carilli and Rawlings 2004)32	
Figure 15: Aperture Synthesis Model HTML User Interface .....	35

Figure 16: Process flow diagram for VLBI Modelling .....	37
Figure 17: Cartesian Coordinates XYZ ( <a href="http://www.ngs.noaa.gov/">http://www.ngs.noaa.gov/</a> ) .....	39
Figure 18: Map of relative antenna locations for Australian sub-array, New Zealand and Scott Base used in this analysis. (Mercator projection), ( <a href="http://maps.google.com">http://maps.google.com</a> ).....	43
Figure 19: Comparison of CLEAN images between SKA simulations. Top using all 125 antennas from the Australian SKA proposal. Bottom using the chosen sub-sets CORE, INT and MAX to simulate the full SKA array as used in this thesis.....	47
Figure 20: SKA Antenna stations sub-sets CORE, INT, MAX from Table 6 to 8 and NZ as taken from Table 4. ....	49
Figure 21: Example of output from uptime (Tingay 2005).....	53
Figure 22: Example of output from vis.pl. Straight lines show the beginning (start) and the end of the period of common visibility for a given radio source (Declination = $-30^\circ$ and RA = $0^h$ ). ....	54
Figure 23: Sky Visibility vs. Declination. (The plot is generated automatically when a non-existing value for declination Dec = $100^\circ$ is used as the input parameter.) .....	55
Figure 24: Image of X-Shaped Radio Galaxy J1327+0203 (Cheung 2007).....	58
Figure 25: Model Images, Top AGN1 middle AGN2 and bottom AGN3 .....	61
Figure 26: Leo Triplet (From <a href="http://astro.ihermans.com/galaxies/LeoTriplet/">astro.ihermans.com/galaxies/LeoTriplet/</a> ) .....	62
Figure 27: Radio contours of the massive protostellar object G34.26 + 0.15 showing a cometary ultra compact HII region and two hyper compact sources to the NE and SE. (Johnson 2004). ....	63
Figure 28: SKA Model Source Image – Galaxy Triplet .....	65
Figure 29: A contour map of VLA image of the radio emission from 3C84 – a bright radio galaxy with weak component(s). (Pedlar, Ghataure et al. 1990). ....	66
Figure 30: Model Source: Bright Source with a Jet.....	68
Figure 31: MIRIAD UVGEN parameters .....	69
Figure 32: DIFMAP script written for Australian sub-array - New Zealand simulation.....	74
Figure 33: SKA uvweight DIFMAP script .....	75
Figure 34: Top Model Source and bottom $u, v$ Plot for SKA sub-set array CORE+INT+MAX.....	78

Figure 35: Examples of different UVWEIGHT settings and the resultant CLEAN Images	79
Figure 36: DIFMAP CLEAN image showing the beam shape and size.....	80
Figure 37: A Gaussian $u,v$ Taper Function .....	83
Figure 38: Top Model Source used for the $u,v$ Taper examples and bottom $u,v$ Plot for SKA sub-set array CORE+INT+MAX .....	85
Figure 39: Examples of applying different UVTAPER parameters and the resultant CLEAN Images .....	86
Figure 40: Comparing examples of CLEAN images to demonstrate the various distortions. From left to right first is the Model Image for AGN3, CLEAN image for a 12hr observation with the Australian sub-array only array at declination $-30^\circ$ , CLEAN image for a 12hr observation with the Australian sub-array only array at declination $-80^\circ$ , CLEAN image for a 12hr observation with the Australian sub-array – New Zealand array at declination $-30^\circ$ .	89
Figure 41: FWHM method for Australian sub-array Antennae Only. Top left is the input model image to the process and top right is the final CLEAN image for source AGN2 at a declination of $-80^\circ$ . Bottom is a plot of the FWHM for both images using line of pixels through the images of $Y=256$ , $X=1,512$ (the images are $512 \times 512$ pixels) .....	92
Figure 42: FWHM for Australian sub-array & New Zealand Antennae. Top left is the input model image to the process and top right is the final CLEAN image for source AGN2 at a declination of $-80^\circ$ . Bottom is a plot of the FWHM for both images using line of pixels through the images of $Y=256$ , $X=1,512$ (the images are $512 \times 512$ pixels) .....	93
Figure 43: Comparison of the Mean Square Error for the source AGN1 against Declination for the different arrays.....	97
Figure 44: Comparison of the Mean Square Error for the source AGN2 against Declination for the different arrays.....	97
Figure 45: Comparison of the Mean Square Error for the source AGN3 against Declination for the different arrays.....	98
Figure 46: Comparison of the 2-D cross-correlation value with the modelled 12hr observations for source AGN1 against declination for the different arrays.....	103
Figure 47: Comparison of the 2-D cross-correlation value with the modelled 12hr observations for source AGN2 against declination for the different arrays.....	103
Figure 48: Comparison of the 2-D cross-correlation value with the modelled 12hr observations for source AGN3 against declination for the different arrays.....	104
Figure 49: For AGN1 a plot of the normalized cross-correlation value vs. declination for each array with the 12hr observation .....	109



Figure 50: For AGN2 a plot of the normalized cross-correlation value vs. declination for each array with the 12hr observation .....	109
Figure 51: For AGN3 a plot of the normalized cross-correlation value vs. declination for each array with the 12hr observation .....	110
Figure 52: Sky Visibility vs. Declination for Australian sub-array antennas. The array is defined in 3.2.1. Note that it does not include Ceduna. ....	114
Figure 53: Australian sub-array -12 hr Integration, -30° Declination.....	117
Figure 54: Australian sub-array - 12hr Integration, -55° Declination.....	118
Figure 55: Australian sub-array -12hr Integration, -80° Declination.....	119
Figure 56: Australian sub-array - 4hr Integration, 10° Declination .....	120
Figure 57: Australian sub-array - 4hr Integration, -20° Declination.....	121
Figure 58: Australian sub-array - 4hr Integration, -50° Declination.....	122
Figure 59: Australian sub-array - 4 hr Integration, -80° Declination.....	123
Figure 60: Sky Visibility vs. Declination for Australian sub-array & New Zealand Antennae .....	127
Figure 61: Australian sub-array & New Zealand – 12 hr Integration, -30° Declination....	129
Figure 62: Australian sub-array & New Zealand – 12 hr Integration, -55° Declination....	130
Figure 63: Australian sub-array & New Zealand – 12 hr Integration, -80° Declination....	131
Figure 64: Australian sub-array & New Zealand – 4 hr Integration, 10° Declination .....	132
Figure 65: Australian sub-array & New Zealand – 4 hr Integration, -20° Declination.....	133
Figure 66: Australian sub-array & New Zealand – 4 hr Integration, -50° Declination.....	134
Figure 67: Australian sub-array & New Zealand – 4 hr Integration, -80° Declination.....	135
Figure 68: Sky Visibility vs. Declination for Australian sub-array, New Zealand & Scott Base Antennae.....	139
Figure 69: Australia, New Zealand & Scott Base – 12 hr Integration, -30° Declination...	141
Figure 70: Australia, New Zealand & Scott Base – 12 hr Integration, -55° Declination...	142
Figure 71: Australia, New Zealand & Scott Base – 12 hr Integration, -80° Declination...	143
Figure 72: Australia, New Zealand & Scott Base – 4 hr Integration, 10° Declination .....	144

Figure 73: Australia, New Zealand & Scott Base – 4 hr Integration, -20° Declination.....	145
Figure 74: Australia, New Zealand & Scott Base – 4 hr Integration, -50° Declination.....	146
Figure 75: Australia, New Zealand & Scott Base – 4 hr Integration, -80° Declination.....	147
Figure 76: For AGN1 a plot of the Normalized 2-D Cross Correlation value vs. declination for each array with the 4hr observation.....	153
Figure 77: For AGN1 a plot of the Normalized 2-D Cross Correlation value vs. declination for each array with the 12hr observation.....	153
Figure 78: For AGN2 a plot of the Normalized 2-D Cross Correlation value vs. declination for each array with the 4hr observation.....	154
Figure 79: For AGN2 a plot of the Normalized 2-D Cross Correlation value vs. declination for each array with the 12hr observation.....	154
Figure 80: For AGN3 a plot of the Normalized 2-D Cross Correlation value vs. declination for each array with the 4hr observation.....	155
Figure 81: For AGN3 a plot of the Normalized 2-D Cross Correlation value vs. declination for each array with the 12hr observation.....	155
Figure 82: Collecting Area and Baseline during construction (Gulyaev and Weston 2007) .....	157
Figure 83: SKA Model Source.....	158
Figure 84: SKA Scenario 1 Visibility, Top CORE, CORE+INT, CORE+INT+MAX and Bottom CORE+INT+MAX+NZ.....	160
Figure 85: SKA Scenario 2 Visibility, Top CORE+MAX, Middle CORE+MAX+NZ and Bottom CORE+INT+MAX+NZ.....	161
Figure 86: Example DIFMAP commands in applying $u,v$ Weighting.....	162
Figure 87: SKA Phased Building Simulation, Scenario 1 .....	164
Figure 88: SKA Phased Building Simulation, Scenario 2 .....	165
Figure 89: Plot of Normalized 2-D Cross Correlation value vs. year for each SKA construction scenario.....	169
Figure 90: Dynamic range as a function of time (SKA construction phases) for the two scenarios.....	171
Figure 91: DIFMAP CLEAN Map .....	180

Figure 92: Aperture Synthesis Model Web Page ..... 183

Figure 93: Web Page for the top level Visibility Program..... 184

Figure 94: Web Page for the Visibility Submission Form ..... 185

Figure 95: Web Page showing the feedback from the Visibility Program ..... 186

Figure 96: Web Page with Final Visibility Plot ..... 187

## List of Tables

Table 1: Antenna size for a given angular resolution $\theta$ at wavelength $\lambda$ .....	3
Table 2: Resolution for Baselines (Australia baselines <a href="http://www.atnf.csiro.au/vlbi/documentation/">http://www.atnf.csiro.au/vlbi/documentation/</a> ). .....	6
Table 3: Australian sub-array antennae.....	45
Table 4: New Zealand proposed antennae .....	45
Table 5: Antarctica possible antenna .....	45
Table 6: SKA Stations for the CORE subset .....	50
Table 7: SKA Stations for subset INT .....	50
Table 8: SKA Stations for subset MAX.....	50
Table 9: Gaussian Taper Factors.....	82
Table 10: FWHM Ratio for VLBI Arrays Australian sub-array and Australian sub-array - New Zealand .....	91
Table 11: MSE values for the Australian sub-array array for a 12hrs observation for the different model sources at different declinations. ....	96
Table 12: MSE values for the Australian sub-array - New Zealand array for a 12hrs observation for the different model sources at different declinations. ....	96
Table 13: MSE values for the Australian sub-array - New Zealand - Antarctica array for a 12hrs observation for the different model sources at different declinations. ....	96
Table 14: Cross Correlation values for the Australian sub-array array for a 12hr observation .....	102
Table 15: Cross Correlation values for the Australian sub-array - New Zealand array for a 12 hr observation.....	102
Table 16: Cross Correlation values for the Australian sub-array - New Zealand - Antarctica array for a 12hr observation .....	102
Table 17: Normalized 2-D Cross-Correlation for Australian sub-array with 12hr observation .....	107
Table 18: Normalized 2-D Cross-Correlation values for the Australian sub-array - New Zealand array with a 12hr observation.....	107

Table 19: Normalized 2-D Cross-Correlation values for the Australian sub-array - New Zealand - Scott Base array with a 12hr observation .....	108
Table 20: Normalized Cross-Correlation for Australian sub-array array with 12hr observation .....	126
Table 21: Normalized Cross-Correlation for Australian sub-array array with 4hr observation .....	126
Table 22: Normalized Cross-Correlation values for the Australian sub-array - New Zealand array with a 12hr observation.....	138
Table 23: Normalized Cross-Correlation values for the Australian sub-array - New Zealand array with a 4hr observation.....	138
Table 24: Normalized Cross-Correlation values for the Australian sub-array - New Zealand - Scott Base array with a 12hr observation .....	150
Table 25: Normalized Cross-Correlation values for the Australian sub-array - New Zealand - Scott Base array with a 4hr observation .....	150
Table 26: MIRIAD IMGEN definition for the SKA source .....	158
Table 27: Normalized Cross-Correlation values per year for the SKA Scenario 1 .....	166
Table 28: Normalized Cross-Correlation values per year for the SKA Scenario 2 .....	166
Table 29: Dynamic range values by date for SKA Scenario 1 .....	170
Table 30: Dynamic range values by date for SKA Scenario 2 .....	170

## List of Symbols and Functions

$\lambda$	wavelength
$\nu$	frequency
$c$	the speed of light
$l, m, n$	direction cosines on the sky conjugate to $u, v$ and $w$
$u, v, w$	antenna spacing coordinates in units of wavelength
$V$	visibility function
$I$	radio brightness (intensity)
mas	milli-arc seconds
$\alpha$	Right Ascension
$\delta$	Declination
$H$	hour-angle
$\phi$	geographic latitude
$h$	altitude
$X, Y, Z$	geocentric coordinates
$T$	Taper Function
$z$	Red Shift

# 1. INTRODUCTION

For much of man's history as he has gazed upon the heavens, great deductions and advances in knowledge have been made using a very small part of the electro-magnetic spectrum which is visible to the human eye. For many years this was the only instrument available for observation which was later enhanced with optical aids in the form of optical telescopes using lenses and mirrors. But what of the rest of the electro-magnetic spectrum?

In 1933 Karl Jansky working for Bell Labs was tasked with investigating static that interfered with the development of long range radio communication. He identified one source of static that increased and decreased in amplitude, this cyclic nature coinciding with the period of 23 hours and 56 minutes characteristic of the motion of fixed stars and the Milky Way (a sidereal day) and he thus concluded that the source was beyond the Earth. The maximum coincided with the constellation Sagittarius (what we now know to be the centre of the Milky Way galaxy) being at the zenith. This "hiss" Jansky concluded was radio electromagnetic radiation coming from the Milky Way. Although he played no further significant role, his discoveries led to a realization that other regions of the electro-magnetic spectrum were available to astronomers. It is not unreasonable to claim that he was responsible for the birth of the field of study we now know as radio astronomy.

For various physical reasons the Earth's atmosphere is transparent to other bands of the electro-magnetic spectrum apart from visible light. The windows of transparency for the electro-magnetic spectrum are shown in Figure 1.

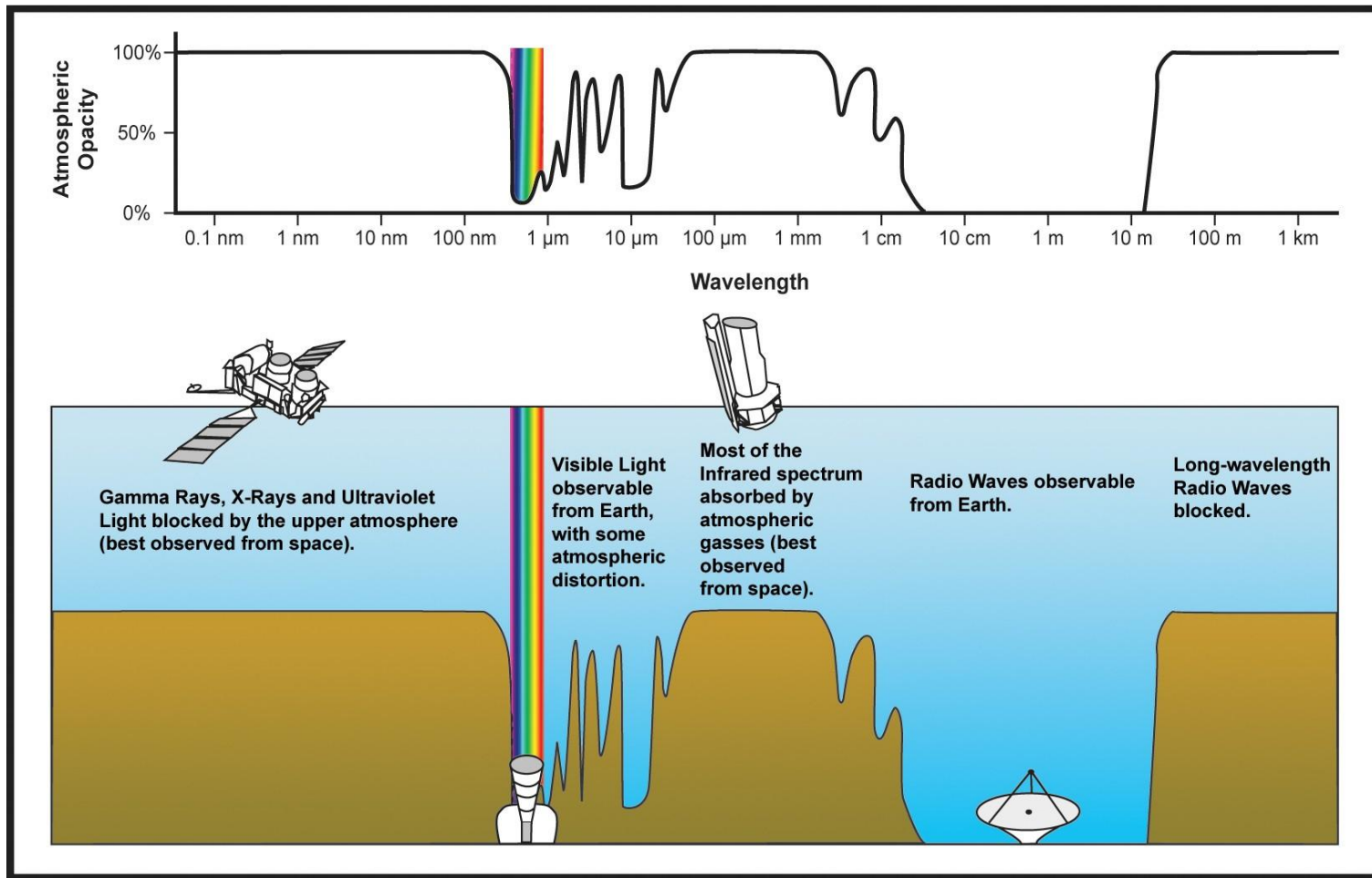


Figure 1: Atmospheric Window (<http://www.answers.com/topic/atmospheric-electromagnetic-transmittance-or-opacity-jpg-1>)



This new field of astronomical research soon became aware of one limitation, due to the large wavelength of radio waves there are practical and physical limitations to the angular resolution of a radio telescope antenna.

To determine angular resolution,  $\theta$ , in radians for a given wavelength  $\lambda$  and telescope objective diameter,  $D$ , equation (1.1) is used (Burke and Graham-Smith 2002).

$$\theta \approx \frac{\lambda}{D} \text{ radians} \quad (1.1)$$

To demonstrate the issue of angular resolution, equation (1.1) has been used to generate Table 1 for several wavelengths commonly used in radio astronomy. The first column is the frequency, the second is the wavelength  $\lambda$  for the frequency, the next three columns show the diameter of a single dish or the baseline distance between antennae required to achieve the angular resolution at the top of the column. The resolutions shown are 1 minute, 1 second and 0.001 second (1 milli arc second - mas). Included is 21cm (1.42 GHz) a frequency used later in this thesis for the simulations.

Freq Band $\nu$ , GHz	$\lambda$ , cm	$\theta = 1'$	$\theta = 1''$	$\theta = 0.001''$
1.4	21	738 m	44 km	44,350 km
1.6	18	646 m	38 km	38,800 km
2.3	13	449 m	26 km	27,000 km
5	6	206 m	12 km	12,400 km
6.7	4.5	154 m	9 km	9,250 km
8.4	3.5	123 m	7 km	7,400 km
12.2	2.5	86 m	5 km	5,200 km
22	1.3	47 m	3 km	2,800 km
		Large antenna or compact array	Short Base- line Interf.	VLBI/Space VLBI

Table 1: Antenna size for a given angular resolution  $\theta$  at wavelength  $\lambda$

Some commonly used frequencies which are used in Table 1: the frequency of 1.420 GHz is the emission line of neutral hydrogen (JPL spectral line catalog: <http://spec.jpl.nasa.gov/>), which corresponds to the transition between the hyperfine levels in the ground state of hydrogen atom; 1.665 GHz is a spectral line of the hydroxyl (OH) maser, 6.694 and 12.16 GHz are frequencies of methanol maser; 22.23 GHz is frequency of water (H<sub>2</sub>O) maser spectral line, and so on.

One can see from Table 1 that in order to obtain a high angular resolution in radio wavelengths very large antennae, often beyond practical physical boundaries are required. The largest diameter radio telescope is the RATAN-600 (<http://w0.sao.ru/ratan/>) of the Special Astrophysical Observatory (SAO) of the Russian Academy of Sciences with a 600 m diameter circular antenna. The radio telescope with the largest collecting area is at the Arecibo observatory (<http://www.naic.edu/index.htm>) and is 305 m in diameter. The largest fully steerable dish in the world is the Green Bank Telescope (GBT) described as a 100 m (<http://www.gb.nrao.edu/>) but the actual dimensions are 100 by 110 m, this is slightly bigger than the Effelsberg telescope ([http://www.mpifr-bonn.mpg.de/div/effelsberg/index\\_e.html](http://www.mpifr-bonn.mpg.de/div/effelsberg/index_e.html))

A solution to the resolution dilemma was sought and found through Interferometry; Figure 2 gives a simplified two antenna interferometer (Burke and Graham-Smith 2002; Thompson, Moran et al. 2004), where S is an astronomical radio source and the time delay between the two antennas for receiving a signal from the source S is denoted by  $\tau_g$ . The two instrument data streams may be combined through interferometric means to achieve a resolution greater than that of either separate telescope. In fact the parameter D from equation (1.1) now becomes the separation between the two antennas, this being commonly referred to as the “baseline” as marked with  $b_\lambda$  in Figure 2.

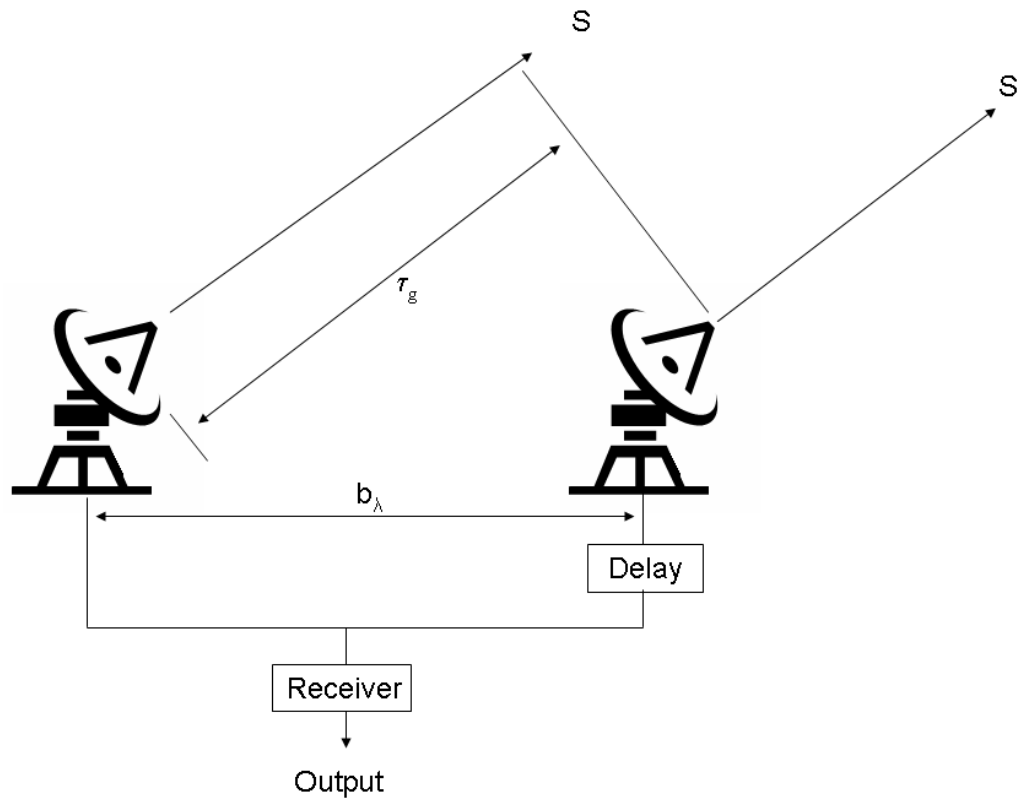


Figure 2: Basic two-element interferometer

Table 2, which is the reverse of Table 1, shows possible resolutions for baselines between New Zealand, Australia and Scott Base and gives the theoretical angular resolution of an array. Not all frequency bands are matched as the subset chosen shows the trend and possible resolution achievable.

Freq Band $\nu$ , GHz	Description	Baseline D, km	Resolution $\theta$ , arcsec
1.4	Australia	1396	0.031
	Australia – New Zealand	2416	0.018
	Australia – Scott Base	5348	0.008
1.6	Australia	1396	0.027
	Australia – New Zealand	2416	0.016
	Australia – Scott Base	5348	0.007
2.3	Australia	1396	0.019
	Australia – New Zealand	2416	0.011
	Australia – Scott Base	5348	0.005
8.4	Australia	1396	0.005
	Australia – New Zealand	2416	0.003
	Australia – Scott Base	5348	0.001
12	Australia	1396	0.0036
	Australia – New Zealand	2416	0.002
	Australia – Scott Base	5348	0.00096

Table 2: Resolution for Baselines (Australia baselines <http://www.atnf.csiro.au/vlbi/documentation/>).<sup>1</sup>

From Table 2 we see the possible resolutions with baselines available using existing Australian antennas and some proposed antenna locations in New Zealand and Scott Base in Antarctica. One can compare this with the finest optical telescopes such as the Hubble Space Telescope (HST) which has a resolution of 0.1 arc-seconds, or Keck (0.04 to 0.4 arc-seconds depending on atmospheric conditions). Thus using radio interferometry spatial resolution can exceed that obtained in optical wavelengths.

As has been shown in Table 2 creating long baselines across continents such as Australia and North America or even between continents or land masses, provides the means to obtain a very high angular resolution. For Australia to Scott Base in Antarctica at 8.4 GHz

---

<sup>1</sup> Note that the longest possible baseline currently within Australia is between Ceduna and Hobart. For Australia to New Zealand the longest possible baseline is between Ceduna and a proposed antenna at Awarua in South Island. The longest baseline between Australia and Scott Base is Ceduna to Scott Base.

and 12 GHz a 0.001'' (1 milli-arc second – 1 mas) resolution is theoretically possible. However often much higher resolution is required for modern astrometry and too study astrophysical objects like Galactic Nuclei (AGN) which have a very small angular size due to their extreme distance from the Earth.

To image a source the technique of aperture synthesis was first demonstrated by Prof. Ryle (Ryle and Hewish 1960) using the then “New Cambridge Radio Telescope” (Ryle 1962). Antennae able to track a source for an extended period as the Earth rotates will trace paths in a plane perpendicular to the direction of the astronomical source from the Earth. In Figure 3 (a) are two antennae placed along a E-W line as seen from the south celestial pole, (b) as the Earth rotates over a 12 hr period the antennae will trace out a semi circular path in this plane.

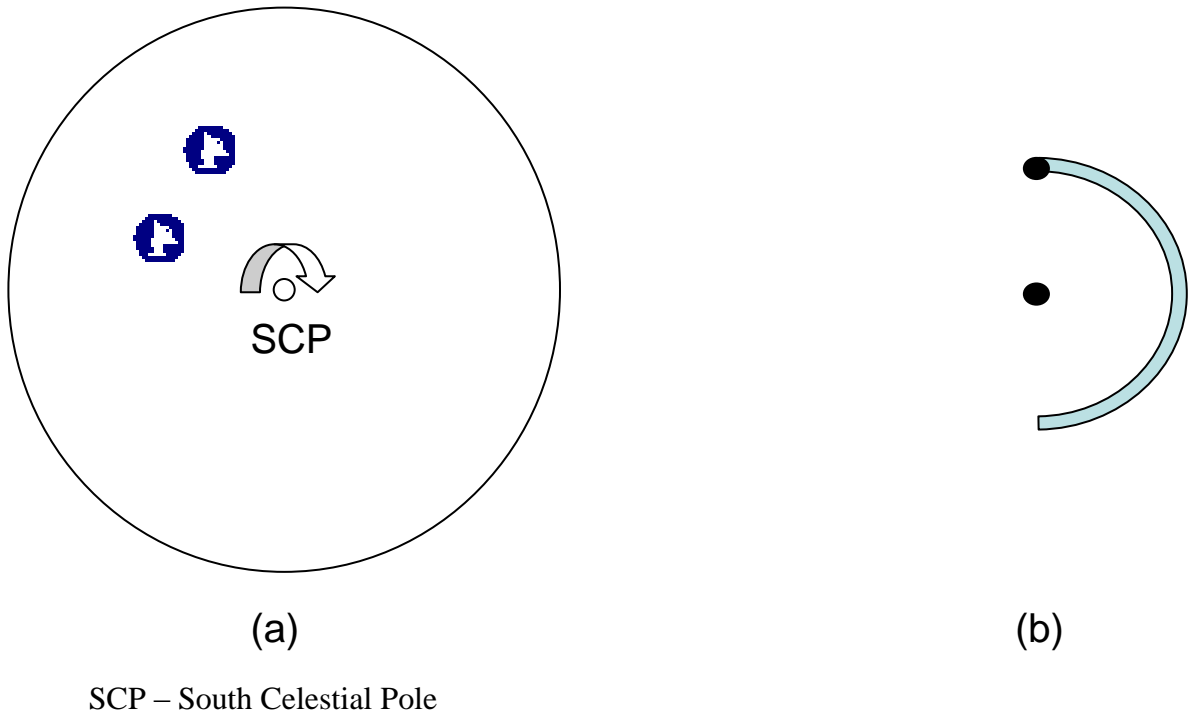


Figure 3: East-West antenna array rotational synthesis

The astronomical source is a two dimensional image on the celestial sphere, and it is described by the coordinate system  $l$  and  $m$ . The projection of  $l$  and  $m$  to the plane which is perpendicular to the direction of the astronomical source from the Earth are defined by a

corresponding coordinate system  $u$  and  $v$ , this plane is commonly referred to as the  $u,v$  plane.

To compare the paths drawn in the  $u,v$  plane and the coverage at different declinations for a source see Figure 4, where an array of six antennae (4 in Australia and 2 in New Zealand, see Section 3.2.1) rather than the simple 2 antenna array have been used to generate the  $u,v$  plots. As the antennas follow a source at the South Celestial Pole ( $\delta = -90^\circ$ ) the baselines trace out circular paths (the left panel in Figure 4). It is important to note that for an array of  $N$  antennae there will be  $N(N-1)/2$  pairs of loci, as seen in the example  $u,v$  plots in Figure 4. But as the declination of a source changes, we note the circular paths are transformed to partial ellipses where the minor axis diminishes by the sine of the declination (the middle panel in Figure 4) and finally straight lines as a source declination  $\delta = 0^\circ$  is reached (the right panel in Figure 4)

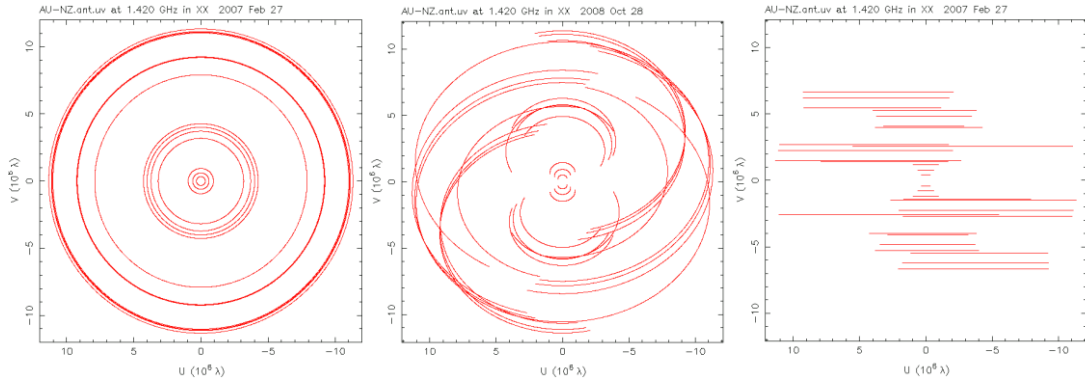


Figure 4:  $u,v$  Plots for AU-NZ Array. For declinations  $\delta = -90^\circ$  (left),  $\delta = -50^\circ$  (middle) and  $\delta = 0^\circ$  (the right panel).

With this coverage of the  $u,v$  plane (as clearly shown in Figure 4 for a declination of  $-90^\circ$ ) it can be seen as a partially filled circular aperture. Using Fast Fourier Transforms (FFT) and deconvolution techniques such as CLEAN (Högbom 1974) or the Maximum Entropy Method (MEM) (Ables 1974; Ponsonby 1974) it is possible to produce the distribution of radio brightness in the selected area on the sky – an “image” of the celestial radio source.

This method was used for antenna arrays on a small scale as the techniques to process the data are quite complex. The “New Cambridge Array” was three antennas on railway tracks

that could be used to simulate a circular aperture of 5,000 ft in diameter. As communications and data processing techniques improved this was extended to larger arrays of fixed antennae spread over greater distances such as MERLIN ( Multi-Element Radio Linked Interferometer Network ) in the United Kingdom. Also the idea of the Cambridge Array was extended to include more antennae in a localized area which can be moved changing the geometry and hence  $u, v$  coverage such as the VLA ( Very Large Array ) in the United States and ATCA ( Australia Telescope Compact Array ) in Australia.

To obtain even higher resolutions this concept was next extended to span continents as Very Long Baseline Interferometry (VLBI). In Figure 5 are shown the VLBI array across Australia the Long Baseline Array (LBA) (<http://www.atnf.csiro.au/vlbi/index.html>) and the United States Very Long Baseline Array (VLBA) (<http://www.vlba.nrao.edu/>). There is also the European VLBI Network (EVN) (<http://www.evlbi.org/evn.html>), which requires cooperation between many research groups, institutes and countries. Australia being a large continent has combined its antennae into a VLBI; this has been linked with Japan and New Zealand on occasion. US antennae have linked with antennae in Europe for observations.

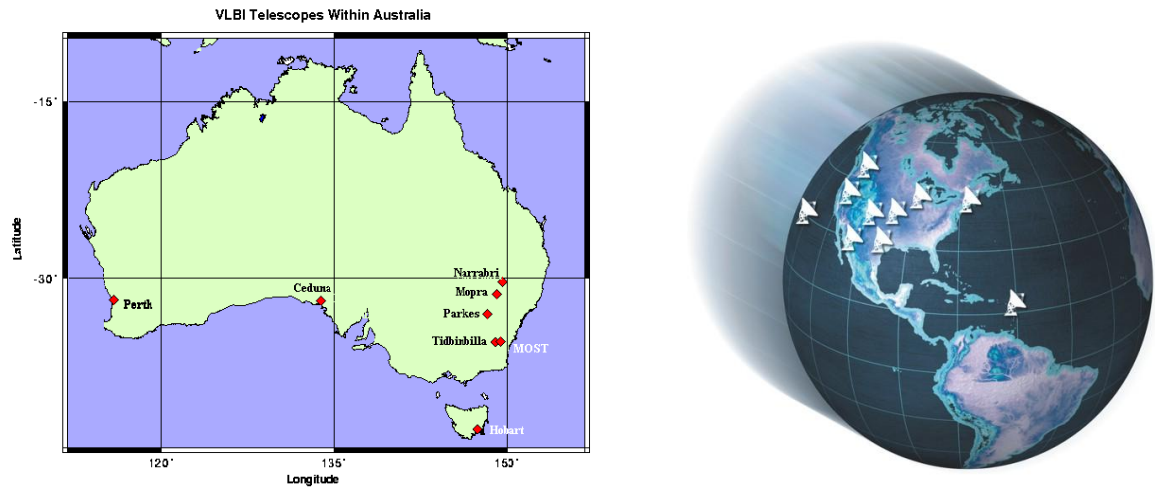


Figure 5 : (Left) Australian VLBI array (Long Baseline Array – LBA), (Right) Very Long Baseline Array – VLBA (NRAO / AUI / NSF)

To conclude Figure 6 demonstrates how important New Zealand could be as a base or partner in Southern Hemisphere VLBI observations. Note the many very long baselines possible for observations of radio sources to existing and proposed future antennae.





Figure 6: The Earth with NZ at Top

## **1.1. Overview of Thesis Structure**

This thesis explains a process built for modelling different proposed VLBI array configurations involving antennas being built or proposed in New Zealand and Scott Base, Antarctica and partnering with existing antennas in Australia for VLBI and aperture synthesis observations. This process can be used elsewhere and is not exclusive to the Southern Hemisphere or New Zealand and Australian antennae. The results of modelling several possible collaborations and array configurations, including the Square Kilometre Array (SKA), are presented. It reviews and compares these arrays using comparison of an initial model image with a final CLEAN image synthesized for each array.

Chapter 2 is a presentation of the theory behind interferometry and aperture synthesis. It concludes with a discussion of the Square Kilometre Array and its importance to the future of radio astronomy.

In Chapter 3 the process developed for this research is presented and dissected in some detail. The process to model VLBI image synthesis is broken down into its constituents. Each part has its own section, some of these are detailed and expand on concepts that are important to the understanding of what is being simulated and modelled.

Chapter 4 describes a web based interface that was developed for use with the underlying astronomical software which the process was built on. This interface follows closely the procedural steps of the developed process.

In Chapter 5 the results of the various antenna arrays simulated (Australia, Australia – New Zealand and Australia – New Zealand – Scott Base) using the developed process are presented along with a discussion of the results obtained. There is also a section investigating two possible options for a phased building scenario for the SKA.

Finally Chapter 6 presents the conclusions.

An electronic Appendix is provided that contains the input data, results, images and source for the programs and scripts developed. The file structure is intended to map the sections within this dissertation and ease the task of finding appropriate data for further work or

review by the reader. Some images have been reduced in size and resolution for the purposes of printing; the originals are within this appendix if required for more detailed study and comparison.

Appendix B contains a listing of the Visibility Perl program developed with the assistance of Prof Steven Tingay of Curtin University of Technology.

Appendix C contains a listing of the new observatories.dat file that was developed for use in MIRIAD.

Appendix D contains listings of the MATLAB scripts written for determining the image figures of merit.

## 2. Discussion of VLBI and Aperture Synthesis Theory

This chapter gives an introduction to the theory of interferometry and aperture synthesis. It begins with an introduction to interferometry by examining a simple two element interferometer. This is followed by an explanation of the XYZ coordinate system and the transposition of the antennae in this reference frame to the  $u,v$  plane. It then explains how Aperture Synthesis is achieved by exploitation of the Earth's rotation and the movement in the  $u,v$  plane this imposes on antennas involved. The deconvolution process used to obtain an image via the CLEAN algorithm from  $u,v$  data is also reviewed.

The section concludes with an overview of the SKA and some of the important specifications of its design with respect to the science that it will be able to explore.

## 2.1. Interferometry

An example of a basic two-element interferometer is shown in Figure 7, and illustrates the principal features of interferometry in its simplest form. The signals from a source  $S$  (assumed to be effectively at infinity) are received by the two antennae shown. The received signals are amplified by a radio receiver in each separate antenna, and then combined to give total power as a function of time (Thompson 1999).

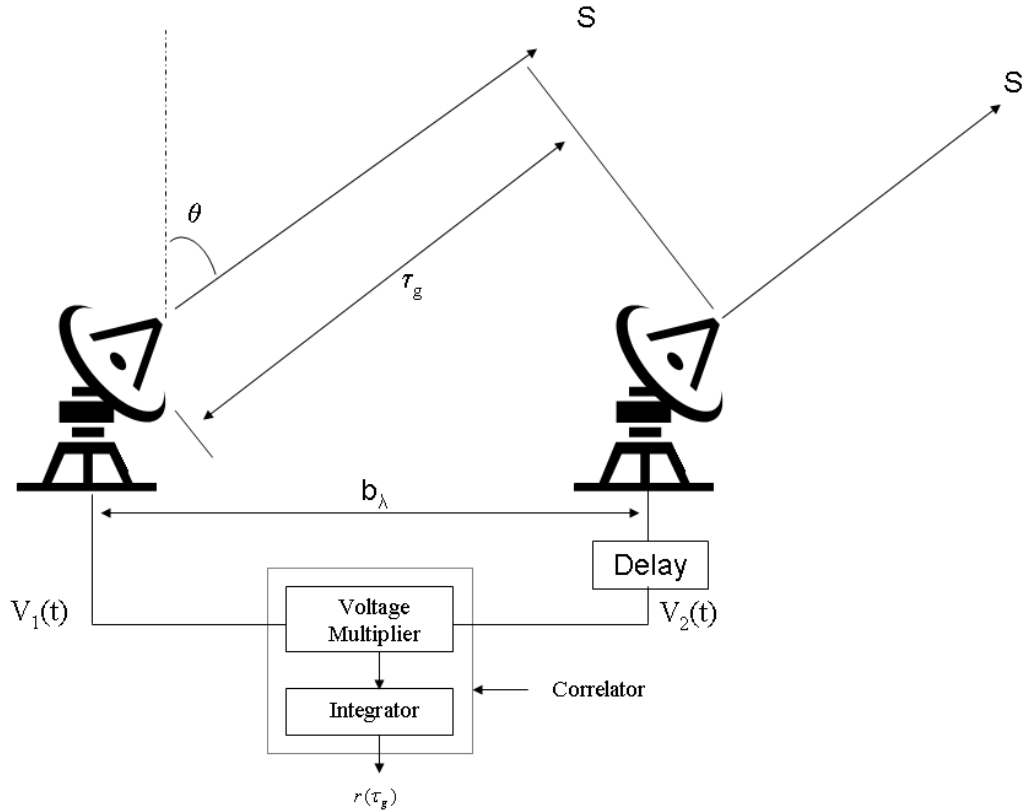


Figure 7: Two-element interferometer. The path delay  $\tau_g$  is compensated by the delay circuit in the receiver.

It is important to note that the signal from the source  $S$  arriving at the antenna 1 is delayed by a factor called the geometric time delay  $\tau_g$  relative to the same signal arriving at the antenna 2. A delay is built into the circuit to allow the signals to be resynchronized in time

and combined to find total signal power as a function of time. This “instrumental delay” may be thought of as compensating for the physical path delay  $\tau_g$ .

The geometric time delay is defined in equation (2.1), where  $b_\lambda$  is the antenna spacing,  $\theta$  is the angular position of the source S, and  $c$  is the speed of light.

$$\tau_g = b_\lambda / c \sin \theta \quad (2.1)$$

The antennae are assumed to be looking at a radio source located effectively at infinity, with a fixed single frequency  $\nu$  (monochromatic). Due to the large distance of the source from the antenna any curvature of the wave front is infinitesimal, thus the incoming wave front can be treated as a plane wave with negligible loss of accuracy. Accordingly the received signals can be represented by the quasi-monochromatic Fourier components (Thompson 1999) of frequency  $\nu$ , which have the form:

$$V_1(t) = \nu_1 e^{i2\pi\nu t} \quad (2.2)$$

$$V_2(t) = \nu_2 e^{i2\pi\nu t} \quad (2.3)$$

The signals  $V_1(t)$  and  $V_2(t)$  pass through amplifiers that incorporate filters to select the required frequency band  $\Delta\nu$  centred on frequency  $\nu$ . The component where the signals are combined is called a correlator (marked in Figure 7). In its simplest form a correlator consists of a voltage multiplier followed by a time averaging (integrating) circuit. The output of the correlator is proportional to:

$$\langle V_1(t - \tau_g) V_2(t) \rangle \quad (2.4)$$

The angular brackets denote a time average, also there is the physical path delay for  $V_1$  given by  $\tau_g$ . Thus taking the integral over a period of observation from  $-T$  to  $+T$  the output of the correlator (2.4) becomes:

$$r(\tau_g) = \frac{1}{2T} \int_{-T}^{+T} V_1(t - \tau_g) V_2(t) dt \quad (2.5)$$

We can expand equation (2.5) using equations (2.2) and (2.3) and appropriate trigonometric identities. The resulting equation contains terms in  $\cos(t)$  and  $\sin(t)$  which average to 0 over any long period such as the several hours of a VLBI observation, thus those components can be eliminated leaving the output of the correlator as equation (2.8). An alternative method is to take the complex function where \* denotes the complex conjugate in equation (2.6).

$$r(\tau_g) = \frac{1}{2T} \int_{-T}^{+T} V_1^*(t - \tau_g) V_2(t) dt \quad (2.6)$$

Equation (2.6) becomes:

$$r(\tau_g) = \frac{1}{2T} \int_{-T}^{+T} v_1 v_2 e^{i2\pi v \tau_g} dt \quad (2.7)$$

Taking the real part of the complex function we get:

$$r(\tau_g) = v_1 v_2 \cos 2\pi v \tau_g \quad (\text{Thompson 1999}) \quad (2.8)$$

$\tau_g$  varies slowly with time as the Earth rotates, and the resulting oscillations of the cosine term in equation (2.8) represent the motion of the source S through the interferometer fringe pattern.

## 2.2. Antenna Coordinates and $(u,v,w)$

An interferometer consists of an array of antennas; each must be assigned a location in a common reference frame. It is convenient to use a Cartesian coordinate system with axes pointing towards hour-angle  $h = 0$  and declination  $\delta=0$  for X-axis, towards  $h=-6^h$  and  $\delta=0$  for Y, and towards  $\delta=90^\circ$  for Z as shown in Figure 8.

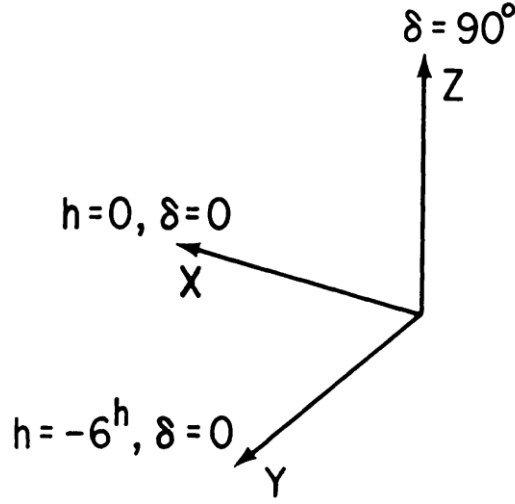


Figure 8: The (X,Y,Z) Coordinate system for specification of relative positions of antennae.

The frame of reference for astronomical sources is the celestial sphere which is a geocentric reference frame.

The celestial sphere is projected onto the  $u,v$  plane as shown in Figure 9 for one dimension  $v$ . The position of the point P is measured in terms of the directional cosine  $m$  with respect to the  $v$  axis. When projected onto a plane surface with a scale linear in  $m$ , P appears at the point marked P' at a distance from the field centre C proportional to  $\sin \psi$ .





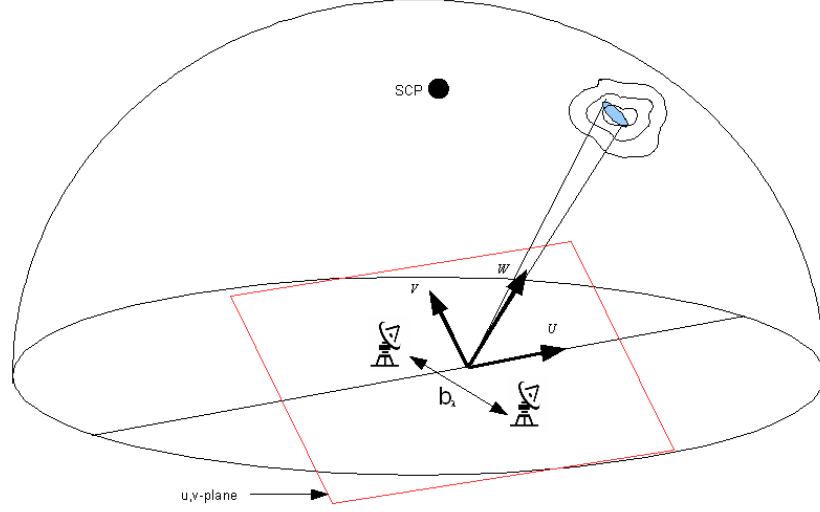


Figure 10: The geometrical relationship between an interferometer, a celestial source and the  $u,v$ -plane, seen in relationship to the celestial sphere. SCP is the south celestial pole;  $b_\lambda$  is the baseline between antennae.

The interferometer is not stationary in space and as the Earth rotates the orientation of the projected baseline changes, sweeping out an ellipse in the  $u,v$  plane. The components  $u, v, w$  are given by expression (2.9) (Thompson, Moran et al. 2004).

$$\begin{pmatrix} u \\ v \\ w \end{pmatrix} = \frac{1}{\lambda} \begin{pmatrix} \sin H_0 & \cos H_0 & 0 \\ -\sin \delta_0 \cos H_0 & \sin \delta_0 \sin H_0 & \cos \delta_0 \\ \cos \delta_0 \cos H_0 & -\cos \delta_0 \sin H_0 & \sin \delta_0 \end{pmatrix} \begin{pmatrix} L_X \\ L_Y \\ L_Z \end{pmatrix} \quad (2.9)$$

Here  $L_X, L_Y, L_Z$  are the coordinate differences for two antennas (projections of the baseline on axes  $X, Y$  and  $Z$ ) and  $H_0$  and  $\delta_0$  are the equatorial coordinates (hour-angle and declination) of a chosen position in the radio source. By eliminating  $H_0$  from the

expressions for  $u$  and  $v$  (As  $H_0$  is the hour angle and it is customary for VLBI observations to set the  $X$  axis in the Greenwich meridian,  $H=0$ ), we can obtain the equation

$$u^2 + \left( \frac{v - (L_Z / \lambda) \cos \delta_0}{\sin \delta_0} \right)^2 = \frac{L_X^2 + L_Y^2}{\lambda^2} \quad (2.10)$$

As  $L_X$ ,  $L_Y$  and  $L_Z$  are constants for a given pair of antennas, this is the equation of an ellipse in the  $u, v$  plane. (It becomes the equation of a circle  $u^2 + v^2 = \text{const}$  when  $\delta_0 = \pm 90^\circ$ ).

The resultant equation (2.10) defines an ellipse in the  $u, v$  plane, and the resultant ellipse is presented in Figure 11.

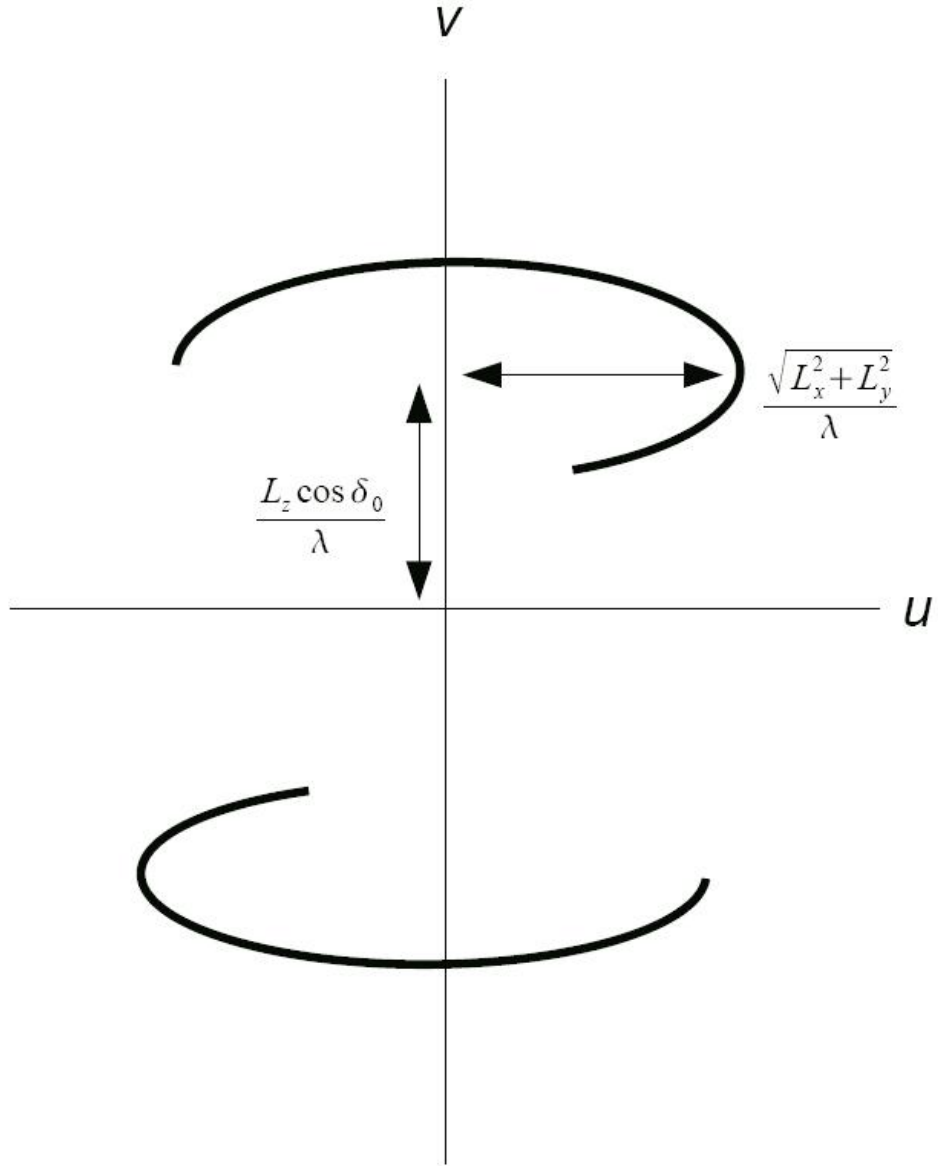


Figure 11: Two elliptical loci representing the projection of the baseline vectors onto the  $(u, v)$  plane as a source is tracked across the sky (Thompson 1999). The lower curve corresponds to a reversal of the direction of the baseline vector.

For an array of  $N$  antennae we will have  $N(N-1)/2$  pairs of elliptical loci. This collection of loci are known as the transfer function or sampling function,  $S(u, v)$  and is a function of the declination of the celestial radio source, time duration or the observation and antenna spacing.

### 2.3. Visibility Function

With appropriate treatment (Rohlfs and Wilson 2004) the output of the correlator (2.7) may be shown to be proportional to a function  $V(u,v)$  that is commonly referred to as the *visibility function* or source visibility. Further, it may be shown that the visibility function is related to the Fourier transform of the source intensity (brightness) distribution  $I(l,m)$  (Thompson, Moran et al. 2004).

To bring some rigour to the situation and derive equations that are of real practical use we introduce appropriate coordinate systems as follows Figure 12:

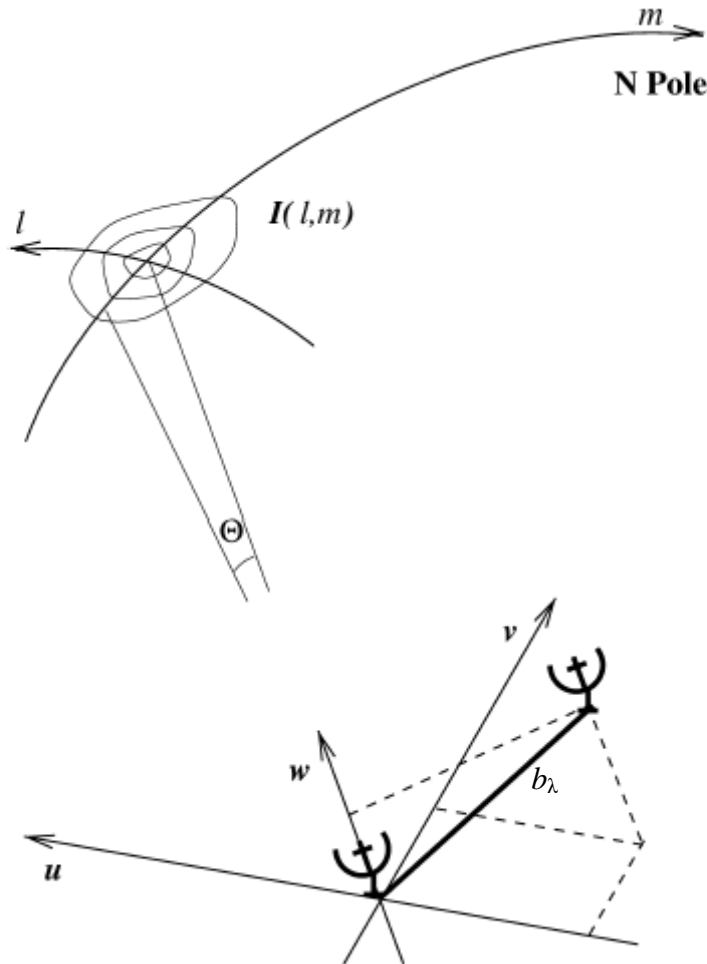


Figure 12: Geometric relationship between a source under observation  $I(l,m)$  and an interferometer or one antenna pair. The antenna baseline vector, measured in wavelengths, has length  $D_\lambda$  and components  $(u,v,w)$  (Diamond, Garrington et al. 2003).

The baselines of the antennae are specified by coordinates  $u, v$  and the corresponding coordinates in the sky are directional cosines  $l, m$  (see Figure 9,  $l$  is the same only in the other dimension  $u$ ) relative to the  $u, v$  axes as shown in Figure 12.

With these definitions we find that the visibility measured by an interferometer is a sample of the visibility function  $V(u, v)$ , and may be expressed as the Fourier transform of the modified sky intensity  $I$  as (Thompson, Moran et al. 2004):

$$V(u, v) = \iint I(l, m) e^{-2\pi i(ul+vm)} dl dm \quad (2.11)$$

This visibility function is in theory sufficiently well behaved that we may recover what astronomers are really after,  $I(l, m)$  the source intensity on the sky, by taking its inverse Fourier transform. Before doing this however we note that in all practical cases we do not have complete sampling of the  $u, v$  plane as discussed in Section 2.2, and since  $V(u, v)$  is not known everywhere the sampling function  $S(u, v)$  is introduced. In the previous section it was shown that over time the Earth's rotation continually changes the orientation of the baselines so that the Fourier component measured changes with time. What we actually know as a result of performing an experiment is the sampled visibility function  $V(u, v) S(u, v)$ . Rewritten in terms of this sampling function the inverse transform of (2.11) becomes (Clark 1995):

$$\tilde{I}(l, m) = \iint V(u, v) S(u, v) e^{2\pi i(ul+vm)} dl dm \quad (2.12)$$

The function  $\tilde{I}(l, m)$  from equation (2.12) is what radio astronomers often refer to as the “dirty image”. We may regard this dirty image as the true image of the source modified by the effects of incomplete sampling of the  $u, v$  plane.

With aperture synthesis the aim is to obtain an image of the source from the measurements of the visibility made by all the interferometers in the array. Thus as the visibility is sampled out to a maximum radius  $b_{max}$  in the  $u, v$  plane, the array produces the same information as a single circular aperture of diameter  $D = \lambda b_{max}$ . Hence an image with resolution  $1/b_{max}$  (this is only approximate, and depends on the sampling function  $S(u, v)$ ) can be produced by Fourier inversion through digital processing using a Fast Fourier

Transform (FFT). So we have the derivation of the term “aperture synthesis” and as this is made possible due to the Earth’s rotation we have the full term “Earth rotational aperture synthesis”.

## 2.4. Deconvolution and CLEAN

As shown in the previous section the intensity distribution  $\tilde{I}(l, m)$  (dirty image) obtained in synthesis mapping can be regarded as the true intensity distribution  $I(l, m)$  convolved with the synthesized beam  $b_0(l, m)$  as shown in equation (2.13) (Thompson, Moran et al. 2004) where  $*$  denotes convolution:

$$\tilde{I}(l, m) = I(l, m) * b_0(l, m) \quad (2.13)$$

Knowing  $\tilde{I}(l, m)$  and  $b_0(l, m)$  it is possible to solve for  $I(l, m)$  by an analytic procedure for deconvolving two functions. Take the Fourier transform of the convolution which is equal to the product of Fourier transforms of the components, divide out the Fourier transform of the known function and transform back.

It was shown in Section 2.3 that the  $u, v$  plane is not completely sampled, thus this analytic approach cannot be used. Several algorithms have been found to affect a solution, of which the most widely used is the CLEAN algorithm. Devised by (Högbom 1974), this is a numerical deconvolution process applied in the  $(l, m)$  domain. This follows the steps as described below with reference to the program DIFMAP (Shepherd 1997; Lovell 2001) used to produce CLEAN images:

1. Find the strength and position of the highest intensity peak within the dirty image, or via CLEAN windows search only within specified areas of the image. This is done via the DIFMAP command “mappl” to display the dirty map of which an example is provided in Figure 13, and define CLEAN windows. From the Dirty Beam map in Figure 13 it can be seen that there are two stronger components and these would be candidates for CLEAN windows. Also note the diffraction rings in this map.
2. Subtract a scaled copy of the synthesized beam from the dirty map at the position of the peak or peaks defined by CLEAN windows, by the use of the DIFMAP commands “clean” and “selfcal”.



3. The scaled copy of the synthesized beam is deemed due to a point source at the location of the peak(s). The position and magnitude of any such point source subtracted is recorded and becomes an element in a “model” of the image.
4. Review the residual. Go to (1) unless any remaining peak is below some user specified level. The remainder of the dirty image is now termed the residual.
5. Convolve the accumulated point source model with an idealized CLEAN beam. The beam is usually an elliptical Gaussian fitted to the central lobe of the dirty beam.
6. Add the residuals of the dirty image to the CLEAN image formed in (5).

The output from step 6 will produce the final CLEAN image, the deconvolution of the dirty image with the synthesized beam. Compare the initial Dirty Map in Figure 13 and the final CLEAN image in the same figure (the CLEAN image has been centred and expanded on the objects of interest, the double source). This example is taken from actual MERLIN data that was used by Dr. Peter Thomasson during my visit to Jodrell Bank in June 2007 to assist in teaching me the MERLIN data processing pipeline.

The CLEAN maps shown in Figure 13 are used extensively through out this thesis, so that the reader can read and understand these plot an explanation of the components has been provided in Appendix B.

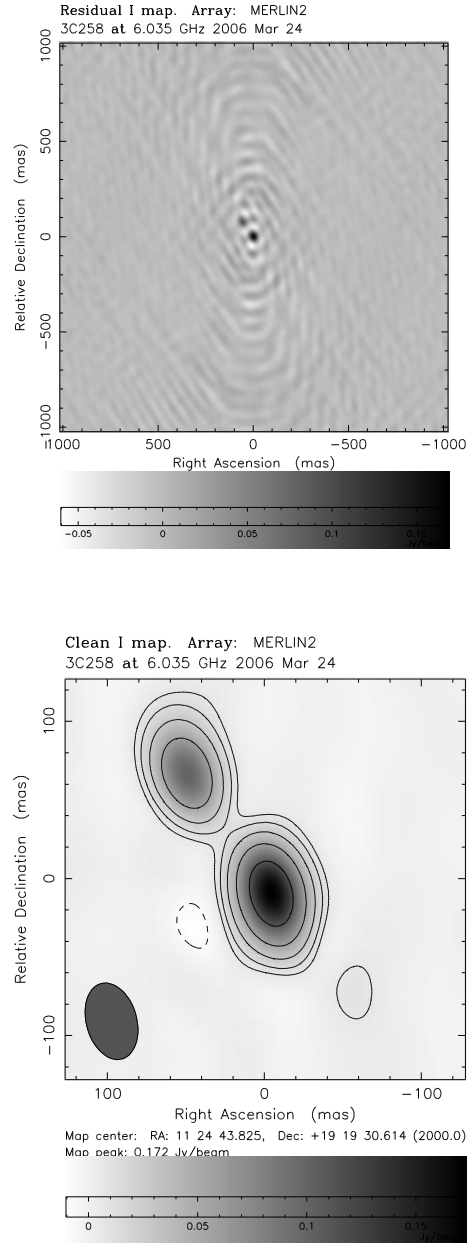


Figure 13: The top image is the Dirty Beam map of an observation for source 3C258. Bottom image is the final CLEAN map of the same source using DIFMAP.<sup>2</sup> This example is taken from actual data from MERLIN<sup>2</sup> for an observation of this source taken in March 2006.

---

<sup>2</sup> Based on observations made with MERLIN, a National Facility operated by the University of Manchester at Jodrell Bank Observatory on behalf of STFC

Of interest is that the CLEAN algorithm has never been rigorously shown to be mathematically complete by rigorous theory (Burke and Graham-Smith 2002), but there have been many tests of reliability using artificial data as in this thesis. Further it has a well-known problem, the generation of spurious structure in the form of spots or ridges as modulation on broad features. It should also be noted that there are alternatives to the Högbom CLEAN algorithm, for example Clark (Clark 1980) and Cotton-Schwab (Schwab 1984). Other methods of deconvolution such as Maximum Entropy (MEM) and Non-Negative Least Squares matrix inversion (NNLS) exist. A good explanation and comparison of CLEAN and MEM is provided in (Cornwell, Braun et al. 1999), NNLS is discussed in some detail by (Briggs 1995). The commonly adopted algorithm for obtaining CLEAN images is the Högbom algorithm described above – it is widely used by standard VLBI data processing software packages such as MIRIAD, DIFMAP and AIPS.

The NNLS solution requires greater computer resources than CLEAN or MEM but was demonstrated to be capable of superior performance (Briggs 1995). Now with the ready availability of greater computer capacity and relatively inexpensive multi-CPU, multi-core servers NNLS should be investigated for future imaging work in this field.

## 2.5. The Square Kilometre Array

Since the 1970's and 80's radio telescopes have allowed the study of HI (21cm) to the redshift  $z^3 \approx 0.2$  but have since effectively remained stagnant (Carilli and Rawlings 2004). In the same period optical telescopes have seen an order-of-magnitude increase in collecting area.

In the early 1990s an initiative emerged to develop a radio telescope to provide two orders of magnitude increase in collecting area and hence sensitivity over existing facilities at metre to decimetre wavelengths. To achieve this goal a telescope with one Square Kilometre ( $1,000,000 \text{ m}^2$ ) of collecting area was proposed, providing 50 times the sensitivity compared to current state of the art arrays such as the Very Large Array ([VLA](#)). It is currently impractical to build a single dish of such size, but advances in the use of antenna arrays now make it practical to combine many dishes to provide the collecting area, and hence was devised the Square Kilometre Array (SKA).

The increase in collecting area and sensitivity would make it possible to extend the study of HI in galaxies up to cosmological distances  $z \approx 4$  rather than  $z \approx 0.2$  and attempt study of the Dark Ages and the epoch of reionization at redshifts  $z > 6$ .

Referring to (Carilli and Rawlings 2004) and Figure 14 some of the desired specifications for the SKA are:

- Frequency range: 100 MHz - 25 GHz Goal: 60 MHz - 35 GHz
- Sensitivity at 45° elevation ( $A_{\text{eff}}/T_{\text{sys}}$  in units of  $\text{m}^2 \text{ K}^{-1}$ ): (Goal: 2500 at 60 MHz) 5000 at 200 Hz, 20000 between 0.5 and 5 GHz, 15000 at 15 GHz, and 10000 at 25 GHz (Goal: 5000 at 35 GHz).

---

<sup>3</sup>  $z$  is a unit less measure of the relative difference between the observed and know emitted wavelengths of electro-magnetic radiation from a object moving towards or away from the observer at relatively high speed. An object moving away will cause the observed wavelengths to be lengthened due to the Doppler affect and a corresponding shift to the “red” end of the spectrum and a +ve number for  $z$ .

- Configuration: Minimum baselines 20m, 20% of total collecting area within 1 km diameter, 50% of total collecting area within 5 km diameter, 75% of total collecting area within 150 km diameter, maximum baselines at least 3000 km from array core (angular resolution  $< 0.02 / f$  GHz arcsec)
- Image quality: Dynamic Range<sup>4</sup>  $> 10^6$  and image fidelity  $> 10^4$  between 0.5 and 25 GHz, over a range of 90° in declination and 100 in angular resolution

In Figure 14 the Specifications are compared with the Key Science Project goals for the SKA. The inclusion of New Zealand with the Australian proposal to host the SKA will provide baselines significantly longer than the 3000 km required, taking the theoretical resolution to a far higher specification than envisaged in the initial SKA requirements.

---

<sup>4</sup> Dynamic range is usually defined as the ratio between the peak brightness in an image and the r.m.s noise in a region of the image free of emission or components.

Topic	$A_{\text{eff}}/T_{\text{sys}}$ ( $\text{m}^2 \text{ K}^{-1}$ )	Frequencies (GHz)	Max Baseline (km)	Special
Gravity	20 000 at 1.4 GHz timing array	0.5–15 Galactic Center	3000 astrometry	multifielding desirable? (TBD); significant central core
Dark Ages	10 000 at 0.1 MHz & 20 GHz CO emission at $z > 6$ (M 82) HI structure at $6 < z < 13$	0.1–20	3000 HI absorption SMBH studies	35 GHz for CO studies; central core for HI; full FOV imaging at 1.4 GHz
Magnetism	20 000 at 1.4 GHz RM grid	0.3–10 large RMs	300 confusion-limited imaging at 1.4 GHz	–40 dB polarization purity; central core; full FOV imaging at 1.4 GHz
Cradle of Life	10 000 at 20 GHz 10 K rms at 1 mas in 100 hrs	$\geq 20$ terrestrial planet formation	3000 0.15 AU at 150 pc at 20 GHz	100 pencil beams within FOV for targeted searches; central core
Evolution & LSS	20 000 at 1.4 GHz $M_*$ galaxy at $z = 2$	0.3–1.4 <sup>3</sup> galaxies to $z = 4$	300	dedicated beam with FOV of 200 deg <sup>2</sup> at 0.7 GHz is highly desirable to increase survey speed

Figure 14: SKA Specifications by Key Science Project goals (Carilli and Rawlings 2004)

### 3. Simulation Model Method

This chapter describes in some detail the process that was developed and the various components to model and simulate artificial VLBI array observations.

The method which the process has been built upon was developed after an extensive review of astronomical computer software commonly used in Radio Observatories such as AIPS (NRAO 2008), DIFMAP (Shepherd, Pearson et al. 1995), MIRIAD (ATNF 2007) and SCHED (Walker 2006). A lot of time was spent trying to understand how they worked and how to get  $u, v$  plots out with no knowledge or skills to call upon within New Zealand for these software packages. Much invaluable remote assistance was provided by Prof Steven Tingay of Swinburne with respect to MIRIAD and DIFMAP, Leonid Kogan NRAO for AIPS and Peter Thomasson during a visit to Jodrell Bank Observatory in June 2007 for the AIPS MERLIN Data Pipeline.

In April 2006 Prof Steven Tingay visited AUT and provided some tutoring to IRSR members in the use of DIFMAP. Following this tutoring, the processing of VLBI images became a lot easier and clearer. The knowledge gained from this and subsequent experience has been collated within an AUT “DIFMAP Users Guide” (Weston 2006), a copy of which is provided in the electronic appendix.

The Virtual Radio Interferometer VRI (McKay, McKay et al. 1997) was found to be a useful tool to demonstrate the concepts behind an interferometer, but did not have the functionality required for this research. It also appears to have been used to demonstrate the use of Java and Applets. As stated by the authors “While the authors hope that this applet will be useful, it is not a definitive scientific tool. For more detailed analysis of  $u, v$  coverage, etc. use MIRIAD, in particular, the UVGEN task.”.

The period of this research did not provide the time to produce a simulation package from scratch, thus the following aims became the focus for how to proceed:

- Primary aim: For a VLBI aperture synthesis modelling process to use existing software tools where possible and replicate real life radio astronomy data processing.
- Secondary aim: To gain the experience needed with the software for the future.

Willis (Willis 2000) discusses Imaging simulations for a SKA using artificial observations and a model sky. Willis attempted to use three different packages containing simulators, AIPS programme UVCON, MIRIAD programme UVGEN and AIPS++. Willis concluded that MIRIAD was a better package for ease of use and speed. Heddle and Webster (Heddle and Webster 2000) had used AIPS to create an automated process for simulating the then proposed ALMA 60 antenna array (Atacama Large Millimeter Array). Cohen (Cohen 2004) explored the imaging capability of a proposed phase II for the LWA (Long Wavelength Array) using AIPS but with a known source Cygnus A.

Thus the first direction of this research was to try AIPS for generating simulated  $u,v$  data for an artificial observation. Corroboration was found with Willis in that AIPS is a very cumbersome package to use and difficult to automate.

Following this experience with AIPS attention was turned to MIRIAD and the task UVGEN as a way to generate the  $u,v$  data for an artificial observation, followed by the use of DIFMAP to process the artificial  $u,v$  data and generate the final de-convolved CLEAN image. It was found that MIRIAD had other easy to use modules such as IMGEN that readily allowed the generation of an image for the model source; visual comparison of input and output images provided a means of assessing the quality of the simulation process.

Each module in MIRIAD can be used within a simple command line interface or on its own from an operating system command call. This later capability allowed easy scripting through PERL of a set of commands to reproduce the process in a repetitive and repeatable manner. It was also found that DIFMAP could be with an input command file allowing the automation of CLEAN and image generation and printing. Combining these two capabilities allowed complete automation of the process through a PERL script.



Although some PERL scripts were generated to automate parts of the process for repetitive runs, time was also spent prototyping a basic web interface to the process using HTML/CGI and PERL. It has been our experience that User Interfaces to astronomical software for the first time user are very cumbersome and non intuitive. A case in point is AIPS; the learning curve for the interface alone is difficult without the additional task of understanding what the various modules do and how to use them. Using the built in widgets from HTML/CGI supported with PERL scripts behind to provide the UI logic what was felt to be a much friendlier user interface was readily constructed, the initial HTML page is shown in Figure 15 and the interface developed is discussed in more detail within Appendix C. This approach also has the benefit of easily allowing sharing with others through the web. Indeed it was used by Prof. Steven Tingay in Australia to review the final sky visibility program.

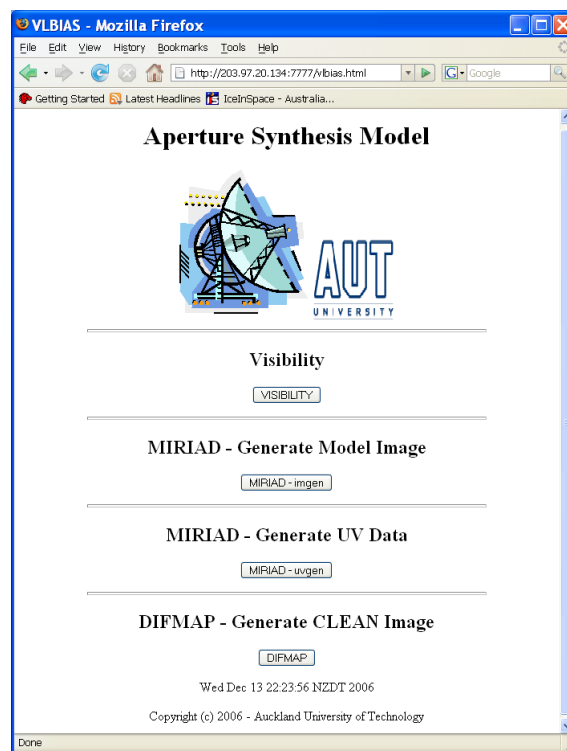


Figure 15: Aperture Synthesis Model HTML User Interface

### 3.1.VLBI Modelling Process Overview

Figure 16 is a flow diagram showing in outline the process developed for this research, and referred to in this section to explain the components of the process.

The first process item “Define Antenna Array” of Figure 16 is discussed in some detail within Section 3.2 of this thesis. Specification of the antennae to be used in a VLBI array for modelling occurs at this stage. The output from this process item is an “Antenna Array File”.

This “Antenna Array File” is in turn passed to the task “Determine Sky Visibility for source” where the sky visibility of a source for the defined array at a specified Date, Hour Angle and Declination (this should not be confused with the Visibility Function discussed in Section 2.3) is determined. This process item is discussed in detail within Section 3.3. The result obtained is the maximum duration a source is visible to the whole array. If the period that the source is visible for the array is greater than 4 hours (a minimum specified for the SKA) then the process can continue to the latter tasks. Otherwise the array or source will have to be reviewed and this part of the process will be repeated until a source visibility of greater than 4 hrs is obtained.

In the flow diagram a parallel branch to the above, are the process items “Source Model Component file” and “Produce Source Image”. The aim is to create an appropriate model source and generate a “Source Image” definition file; these tasks are explained in Section 3.4. The output from this part of the process is an image of the model source. This is stored as a FITS<sup>1</sup> (Flexible Image Transport System) (NASA/GSFC 2006) file and GIF for future reference.

---

<sup>1</sup> FITS - The standard data format used in astronomy 'Flexible Image Transport System' Endorsed by NASA and the International Astronomical Union.

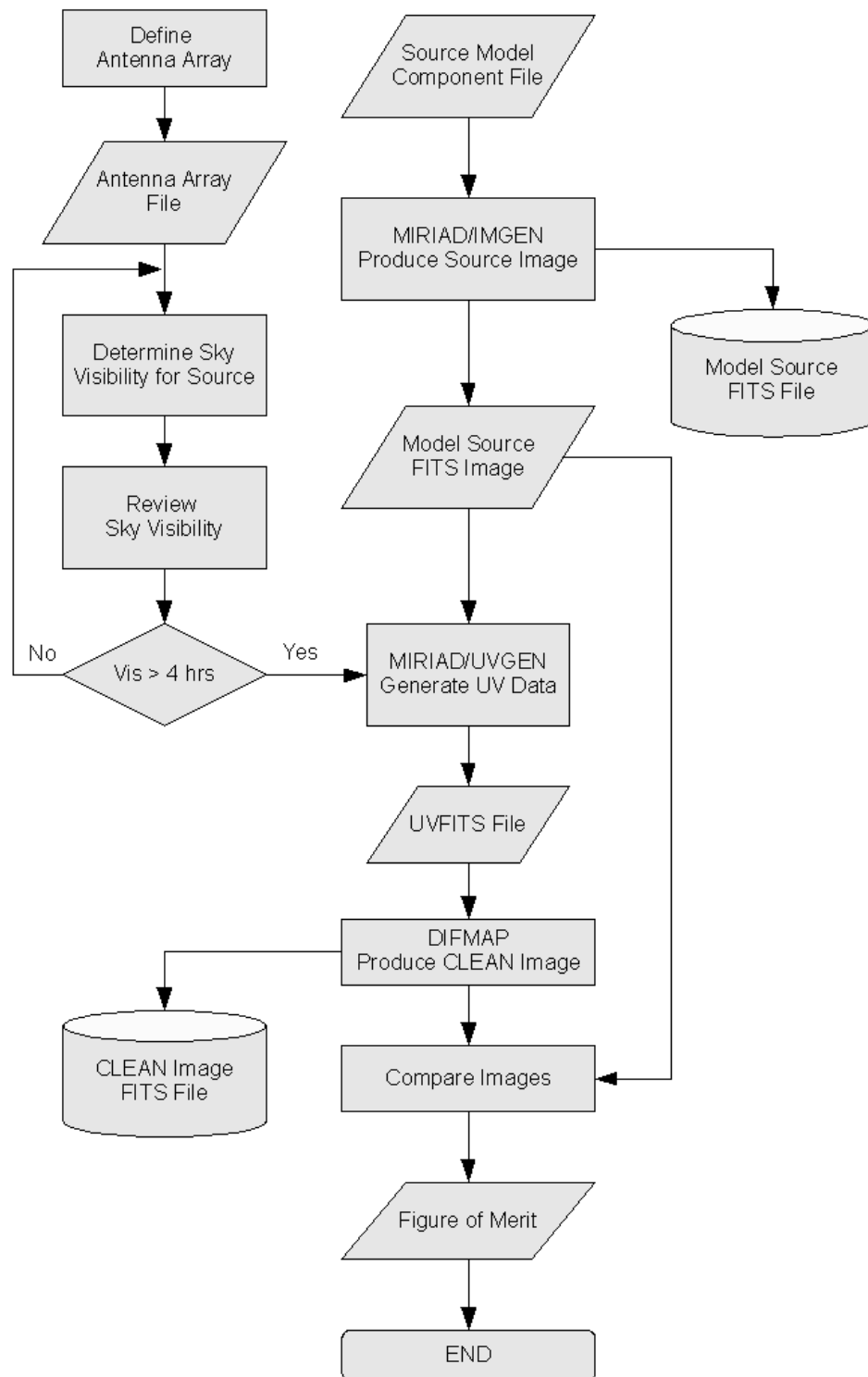


Figure 16: Process flow diagram for VLBI Modelling

With the defined VLBI array and model source from the steps above the process progresses to the item “MIRIAD/UVGEN Generate  $u,v$  Data”. With the antenna array file, model source and other parameters such as date, frequency, hour angle and declination now defined the  $u,v$  data for the artificial observation is generated, and this is discussed and explained in Section 3.5. The output from this part of the process is a FITS format file containing the  $u,v$  data of the artificial observation.

Taking the generated  $u,v$  data for an artificial observation the process proceeds to the step “DIFMAP Produce CLEAN Image”. This is where the artificial observation  $u,v$  data from the FITS  $u,v$  data file is processed to generate a final CLEAN image, the details of this are discussed and explained in Section 3.6.

The process then proceeds to the step “Compare Images”, where some visual comparison of the final image against the input model image can be done as an initial inspection of end quality.

The final step in the process from Figure 16 called “Figure of Merit” is discussed in Section 3.7 of this thesis, and is where a method to provide a quantitative measure and comparison between the CLEAN images is introduced and explained.

### 3.2.Array Configuration

This section deals with the step that defines geographically where each antenna in the modelled interferometer array is located in a common frame of reference. The common frame of reference for objects upon the Earth's surface is the geographic latitude, longitude and altitude. We select existing antennae and define possible new antennae for a VLBI array to be modelled with this reference frame.

Typically astronomical software packages use a combination of two frames of reference, the first being geographic Latitude ( $\phi$ ), Longitude ( $\lambda$ ) and Ellipsoid Height ( $h$ ) and the second being Geocentric XYZ-coordinates on the GRS80 (Geodetic Reference System 1980) ellipsoid (DGF 1999) ellipsoid. How a location is defined on the Earth's surface for the geocentric reference frame is shown in Figure 17.

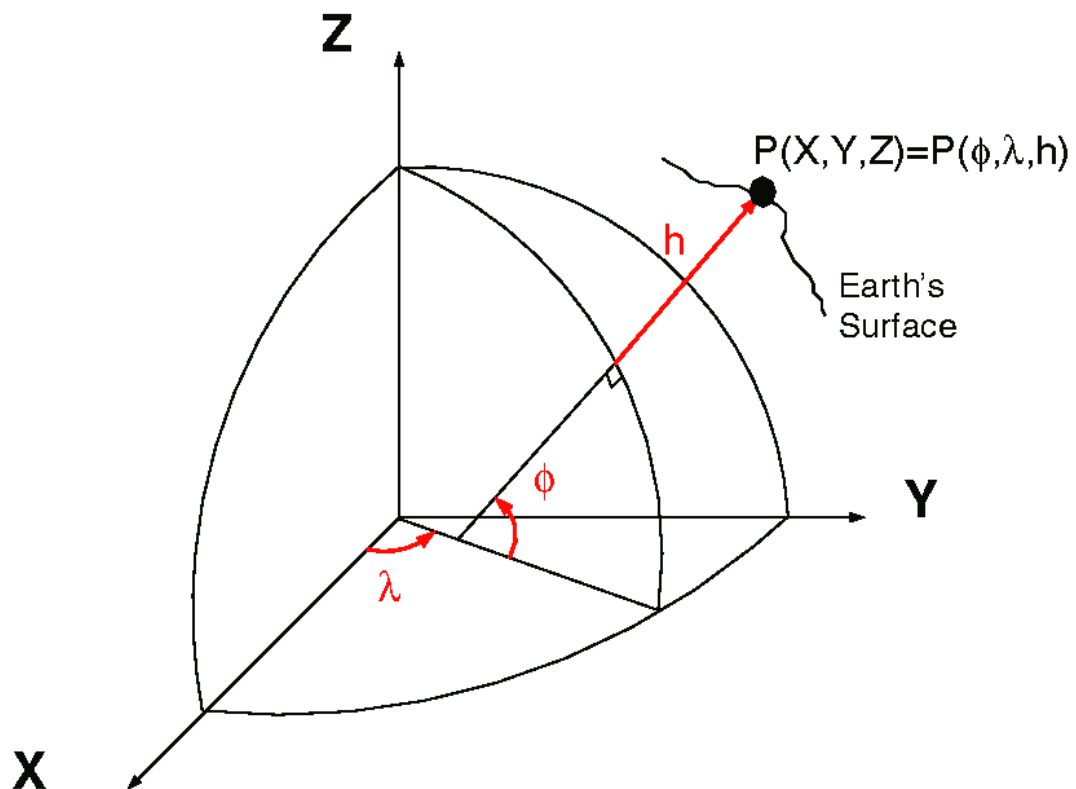


Figure 17: Cartesian Coordinates XYZ (<http://www.ngs.noaa.gov/>)

The antenna locations in latitude, longitude and altitude have to be converted to the geocentric coordinates of X,Y and Z upon the Earth's ellipsoid as defined by GRS80. This was achieved by use of a small software package as described in Professional Surveyor Magazine (Frakes 2003) and available from (NGS 2005). This program XYZWIN was used for generating the X,Y,Z coordinates in the antenna files detailed in the following sub-sections.

### **3.2.1. Geographic location of antennae in Australia, New Zealand and Antarctica**

The first step in the process of modelling and comparing various VLBI configurations between Australia, NZ and Scott Base Antarctica, is to select the antennae that will make up the arrays to be modelled. The output from this part of the process is an antenna file in the correct format for input to the computer software used later in the process.

Geographic locations for Australian (AU) antenna that were used for VLBI observations with New Zealand in May 2005 (LBA Schedules <http://www.atnf.csiro.au/vlbi/wiki/index.php?n=Main.LBAMay2005Summary>, Vt03a1, Vt03a2, Vt03b1, Vt03b2 and Vt03d), where ATCA (At), Mopra (Mp), Parkes (Pa) and Hobart (Ho) are given in Table 3. Two proposed locations for antennas given in New Zealand's proposal for hosting part of the SKA in collaboration with Australia have been used (Gulyaev 2005), these are shown in Table 4 as Warkworth (Wa) and Awarua (Aw). A recent idea floated has been the possible placing of an antenna at or near the New Zealand Antarctic Base – Scott Base (Sb), which is given in Table 5. The geographic locations of these antennae have been placed approximately on a map in Figure 18 for comparison. Due to the scale and the close geographic location for ATCA and Mopra these have been represented by just one antenna symbol.

Because the main purpose of this thesis is the development of a methodology (image synthesis algorithms, image quality analysis - figures of merits, and so on) it was decided to limit ourselves by the most commonly used sub-array of Australian antennas PAMHELA (Johnston, Bailes et al. 2007; Phillips 2007) located along the East Coast (except Tidbinbilla) and in Tasmania. (In Section 4.5, however, we extended our analysis to the full SKA array, consisting of 60 stations distributed across the whole Australian continent). Everywhere in the thesis, when we discuss "Australian sub-array" we mean this limited (four East Coast antennas) array of radio telescopes most widely used for most of applications. Due to connectivity issues (limited connectivity to Ceduna), availability (eg Tidbinbilla antenna is operated by NASA and not always available for astrophysical

observations) and specification (for example when this thesis was in preparation, Ceduna antenna became operational in L-band 2007), thus these two antennas were excluded.

There is a geodetic antenna already at Syowa Station, Antarctica which has been used for geodetic Very Long Baseline Interferometry (VLBI) observations (FUKUZAKI, SHIBUYA et al. 2005). Also there is the German Antarctic Receiving Station (GARS) antenna at O'Higgins, Antarctica (NASA 2008).

At the start of this research Warkworth in New Zealand consisted of several Satellite Earth Stations used by Telecom New Zealand, as of October 2008 AUT now have a 12m antenna available at Warkworth. Also in the intervening time of this thesis the European Space Agency (ESA) have installed an Earth station at Awarua in South Island, this also could be available in a similar fashion to Tidbinbilla in Australia. There are a number of other radio telescopes in Australia - both used and planned. There are planned antennas in Katherine and Yarragadee (operational in 2009-2010) and the ASKAP array (operational in 2011). At some locations there are several antennas: ATCA is an array of 6 antennas, a new 12-m antenna was built in 2008 in Parkes in addition to the 64m radio telescope, there are two antennas in Hobart - 14m and 26 m and a new 12m antenna which will be built there in 2009.





Figure 18: Map of relative antenna locations for Australian sub-array, New Zealand and Scott Base used in this analysis. (Mercator projection), ([http:// maps.google.com](http://maps.google.com)).

These antennae locations were then used to generate antenna files for each simulation to be modelled, in a format acceptable to MIRIAD. An example of an Antenna Array file provided to MIRIAD for generating the  $u,v$  data via task UVGEN is of the form:

```
#   Station      Code   Latitude Longitude Elevation      X      Y      Z
#
#   ATCA          At   -30.31000  -149.57000   217.   -4752008.07  2791332.20 -3200197.64
#   MOPRA         Mp   -31.26782  -149.09964   867.   -4682768.63  2802619.06 -3291759.90
#   PARKES        Pa   -32.99840  -148.26351   415.   -4554232.01  2816758.96 -3454035.85
#   HOBART        Ho   -42.80359  -147.44052    65.   -3950236.74  2522347.55 -4311562.54
-4752008.07  2791332.20 -3200197.64
-4682768.63  2802619.06 -3291759.90
-4554232.01  2816758.96 -3454035.85
-3950236.74  2522347.55 -4311562.54
```

Station	Code	Latitude ( $^{\circ}$ )	Longitude ( $^{\circ}$ )	Elevation (m)	X	Y	Z
ATCA	At	-30.31000	-149.57000	217.0	-4752008.07	2791332.20	-3200197.64
MOPRA	Mp	-31.26782	-149.09964	867.0	-4682768.63	2802619.06	-3291759.90
PARKES	Pa	-32.99840	-148.26351	415.0	-4554232.01	2816758.96	-3454035.85
HOBART	Ho	-42.80359	-147.44052	65.0	-3950236.74	2522347.55	-4311562.54

Table 3: Australian sub-array antennae

Station	Code	Latitude ( $^{\circ}$ )	Longitude ( $^{\circ}$ )	Elevation (m)	X	Y	Z
Warkworth	Wa	-36.4350 <sup>5</sup>	-174.6633 <sup>4</sup>	90.0	-5115281.85	477835.26	-3767187.42
Awarua	Aw	-46.5166	-168.3083	10.0	-4305611.17	890996.14	-4604962.76

Table 4: New Zealand proposed antennae

Station	Code	Latitude ( $^{\circ}$ )	Longitude ( $^{\circ}$ )	Elevation (m)	X	Y	Z
Scott Base	Sb	-77.8	-166.8	100.	-1316483.59	308778.44	-6212353.69

Table 5: Antarctica possible antenna

---

<sup>5</sup> These are the very recently acquired professionally surveyed positions, which are different to the actual values used later in this thesis. These values arrived too late to be used but are provided here for accuracy.

### 3.2.2. SKA Antenna Data

This process has also been used to investigate and model a phased approach to building the SKA in Australia and New Zealand.

The Australian proposal (Boyle 2005) for siting the SKA has two configurations consisting of 125 and 62 antenna stations. We have concentrated on the former in selecting sub sets of antennae to best represent the short and long baselines available.

A run was tried for all 125 stations in the proposed SKA array, this took many hours to run on the computer available, in addition software changes were required to MIRIAD for the very large number of antennae and  $u, v$  data generated. It was found that several arrays within the code had to be increased.

Through our experimentation it was found that not all proposed stations for the SKA were required in the antenna file. In particular it was found that a large number of the small baselines within the core made little difference to the final CLEAN image produced. It was found that subsets of the total stations could be used that reduced computational overheads but still gave results similar to a simulation using all antennas. In choosing the sub-sets to be used when moving out from the core, whilst N-S separation was found to be of benefit in image improvement, the greatest factor in increasing resolution is seen from the E-W separation of antennas. Thus a different approach to the antenna file was used; instead of defining all antennas/stations for a phase in the building program a subset was used through the modelling process. In Figure 19 are shown two CLEAN images as a comparison to demonstrate the validity of this method, the top image used all 125 antennas in the Australian proposal for the SKA, the bottom image uses the sub-sets core, int and max as used latter in this thesis to simulate the full Australian component of the SKA.

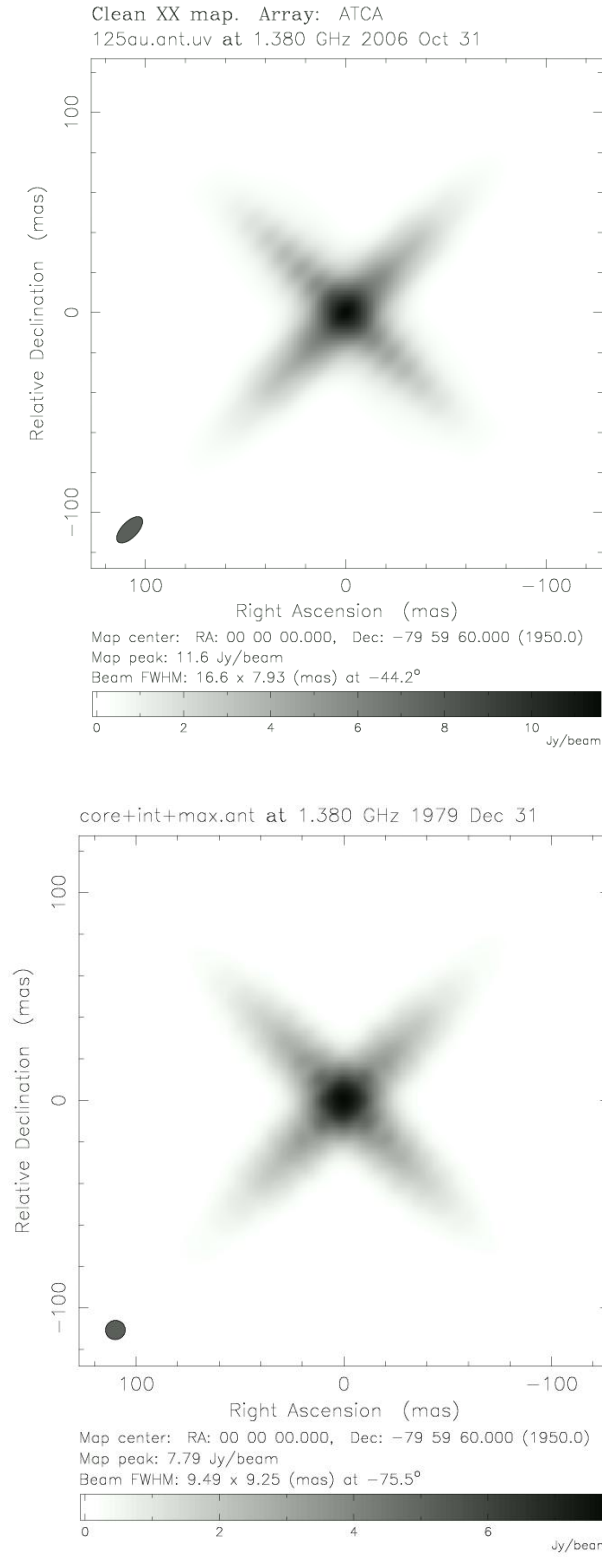


Figure 19: Comparison of CLEAN images between SKA simulations. Top using all 125 antennas from the Australian SKA proposal. Bottom using the chosen sub-sets CORE, INT and MAX to simulate the full SKA array as used in this thesis.

This initial experimentation led us to consider the following groups of antenna stations in the modelling process. First we define the sub-set of antennas that form a core of the SKA for the model; these are listed in Table 6. The next group of stations out from the core is a subset called “INT” for intermediate; these are defined as those that lie between the core in Western Australia and those on the eastern side of Australia. This sub-set of stations is shown in Table 7 and they are the stations approximately half way across Australia from the core. The final group of SKA stations is called “MAX” as these are the furthest east stations from the central core within Australia, this subset of stations are listed in Table 8. For New Zealand two proposed antennae Warkworth, North Island and Awarua, South Island have already been defined in an earlier section and are presented in Table 4, these make up the group of stations called “NZ”. The subsets are shown on a very rough map in Figure 20 for geographic reference, note that the point designated by CORE-0 on the map consists of three points CORE-0, OUT-1 and OUT-2 which due to the scale of the map are unable to be separated. These subsets names for the antennae are self evident in the headers for the CLEAN images presented later in this thesis.



Figure 20: SKA Antenna stations sub-sets CORE, INT, MAX from Table 6 to 8 and NZ as taken from Table 4.

Station	Latitude (°)	Longitude (°)	Elevation (m)	X	Y	Z
CORE-0	117.5111	-26.6204	466.0	-2635844.3639	5061015.784	-2840885.7682
OUT-1	117.4794	-26.6169	452.0	-2633122.0334	5062612.9896	-2840535.3374
OUT-2	117.4976	-26.6462	458.0	-2634058.0337	5060490.8903	-2843441.3018
REM-8	117.5970	-23.4721	313.0	-2711754.9000	5187769.3516	-2524895.2655
REM-10	115.8148	-30.4068	225.0	-2397559.0765	4956318.4560	-3209470.4495
REM-15	117.9080	-34.0793	255.0	-2475322.5549	4673482.1220	-3553886.6675

Table 6: SKA Stations for the CORE subset

Station	Latitude (°)	Longitude (°)	Elevation (m)	X	Y	Z
REM-21	-25.12	133.15	461.0	-3952183.9061	4216015.2413	-2691311.6895
REM-22	-31.87	133.81	160.0	-3753358.0029	3912598.3533	-3348282.5277
REM-23	-20.0	134.25	359.0	-4184072.8268	4295070.8985	-2167819.5730

Table 7: SKA Stations for subset INT

Station	Latitude (°)	Longitude (°)	Elevation (m)	X	Y	Z
MAX-0	-35.40	148.98	670	-4460955.9476	2682532.5537	-3674517.9619
MAX-1	-30.3129	149.5501	237.0	-4750913.3026	2792909.0223	-3200485.2865
MAX-2	-42.8050	147.4392	43.0	-3950075.0960	2522372.2446	-4311662.7623
REM-26	-26.3006	146.1967	320.0	-4754652.9575	3183359.3177	-2809098.3428

Table 8: SKA Stations for subset MAX



### 3.3. Sky Visibility

This section explains the step in the process that determines the sky visibility of a source for a given array of antennas produced in Section 3.2. Sky Visibility is defined as the period for which the source is visible to all antennas simultaneously. The term visibility in this context should not be confused with the term used in Section 2.3 for the output of the interferometer. We have attempted to differentiate in this context by the prefix “sky”: sky visibility.

I thank Prof Steven Tingay for providing a copy of the Perl script written by his group for the Australian SKA proposal. This program had limitations, such as a hardcoded date 2000-01-01:00:00 and the Right Ascension,  $RA = 0^h$ . This was rewritten with input from Prof Tingay, and it will now take any date and time after 2000-01-01 using the algorithms produced by Jean Meeus (Meeus 1998) . It will also allow the input of a RA and Dec for any arbitrary source to be observed.

The algorithms from Jean Meeus are now discussed with respect to the sky visibility program. Taking the desired date for the sky visibility calculation of Year ( $Y$ ), Month ( $M$ ) and Date ( $D$ ) the Julian Date (JD) is calculated with (3.1)-(3.3). There are adjustments to the Month and Year such that January and February are considered to be part of the preceding year.

$$A = INT\left(\frac{Y}{100}\right) \quad (3.1)$$

$$B = 2 - A + INT\left(\frac{A}{4}\right) \quad (3.2)$$

$$JD = INT(365.25(Y + 4716)) + INT(30.6001(M + 1)) + D + B - 1524.5 \quad (3.3)$$

Using the Julian Date the sidereal time at Greenwich ( $\theta_0$ ) is calculated:

$$T = \frac{JD - 24515450}{36525} \quad (3.4)$$

$$\theta_0 = 100.46061837 + 36000.770053608 * T + 0.000387933 * T^2 - T^3/38710000 \quad (3.5)$$

The local hour angle,  $H$ , is calculated from (3.6), where  $\theta_0$  is the sidereal time at Greenwich,  $\lambda$  is the antenna longitude (+ve West, -ve East from Greenwich), and  $\alpha$  is the Right Ascension of the source.

$$H = \theta_0 - L - \alpha \quad (3.6)$$

There is no correction made for nutation on  $\alpha$  as it is too small for the accuracy required in this program.

We are now ready to transform the coordinates and find the altitude  $h$  from 3.7, where  $\varphi$  is the antennae latitude,  $\delta$  is the source Declination (+ve if North of the celestial equator, -ve if South), and  $H$  was calculated by Equation 3.6.

$$h = a \sin(\sin \varphi \sin \delta + \cos \varphi \cos \delta \cos H) \quad (3.7)$$

The aim of the programs is to calculate the visibility of a source for each antenna. This is achieved by looping through the Universal Time (UT) for the date of the observation and calculating the hour angle for the source at  $UT + \Delta UT$ , checking to make sure it is above the horizon and antenna elevation limit. Using the generated rise and setting times of the source for each antenna then allows a comparison of these sky visibilities and the determination of a common period of time that the source is visible by all antennae.

The program written by Prof Steven Tingay for the SKA proposal is for a large number of antennas ( $> 100$ ). It computes periods of visibility of a given celestial source for each antenna (horizontal lines in Figure 21). The output is presented in a traditional two dimensional x,y plot as shown in Figure 21.

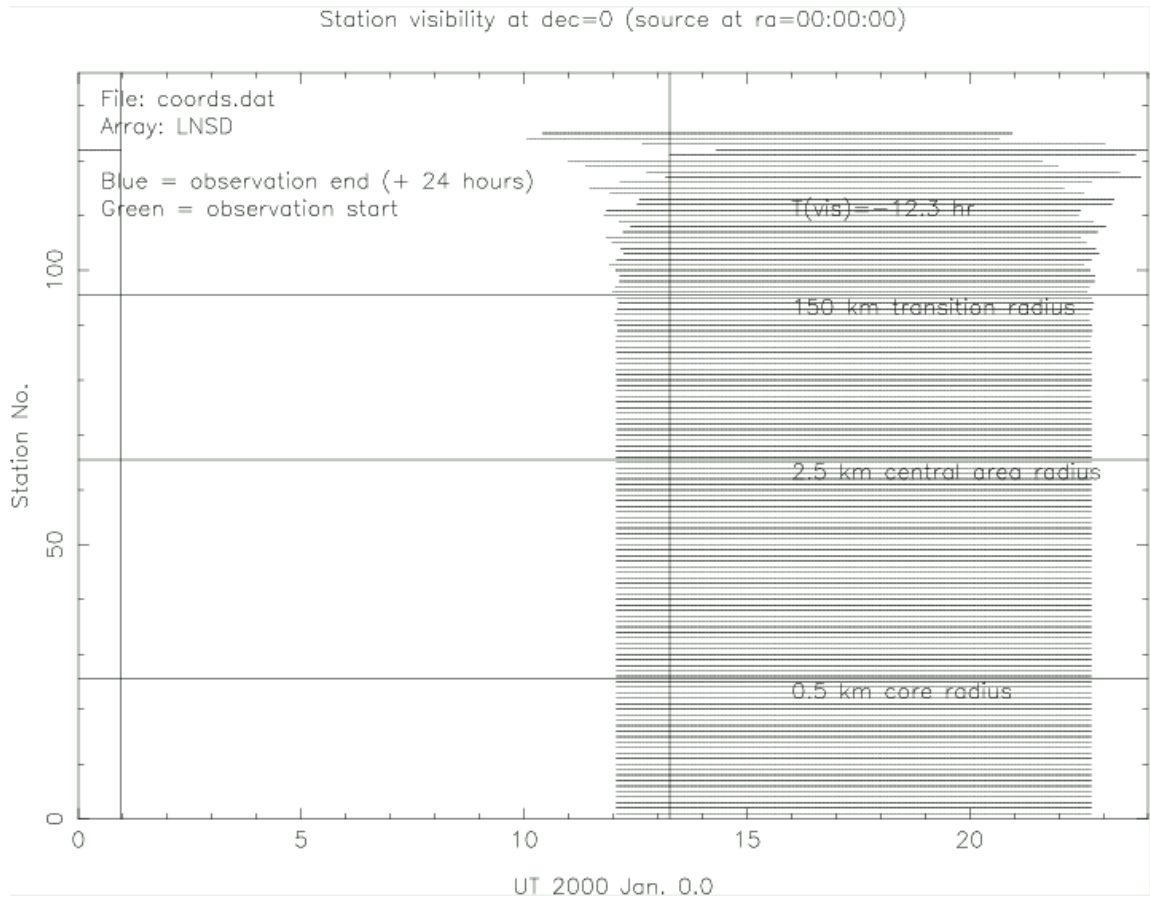


Figure 21: Example of output from uptime (Tingay 2005)

However, sometimes this presentation is not convenient. For example, for the Station #122 in Figure 21, the source visibility extends over 24:00 through to after 00:00 the next day with a break in the plot. It was felt that this was hard to read and interpret so a 24hr clock face approach to showing the visibilities was adopted.

For a small array, plotting sky visibility arcs in a 24hr clock face will give a more readable and easier to interpret presentation of the data. Also when visibilities crossed over 24:00 – 00:00 the arcs are continuous with no breaks thus improving the presentation and readability of the plot as shown in Figure 22.

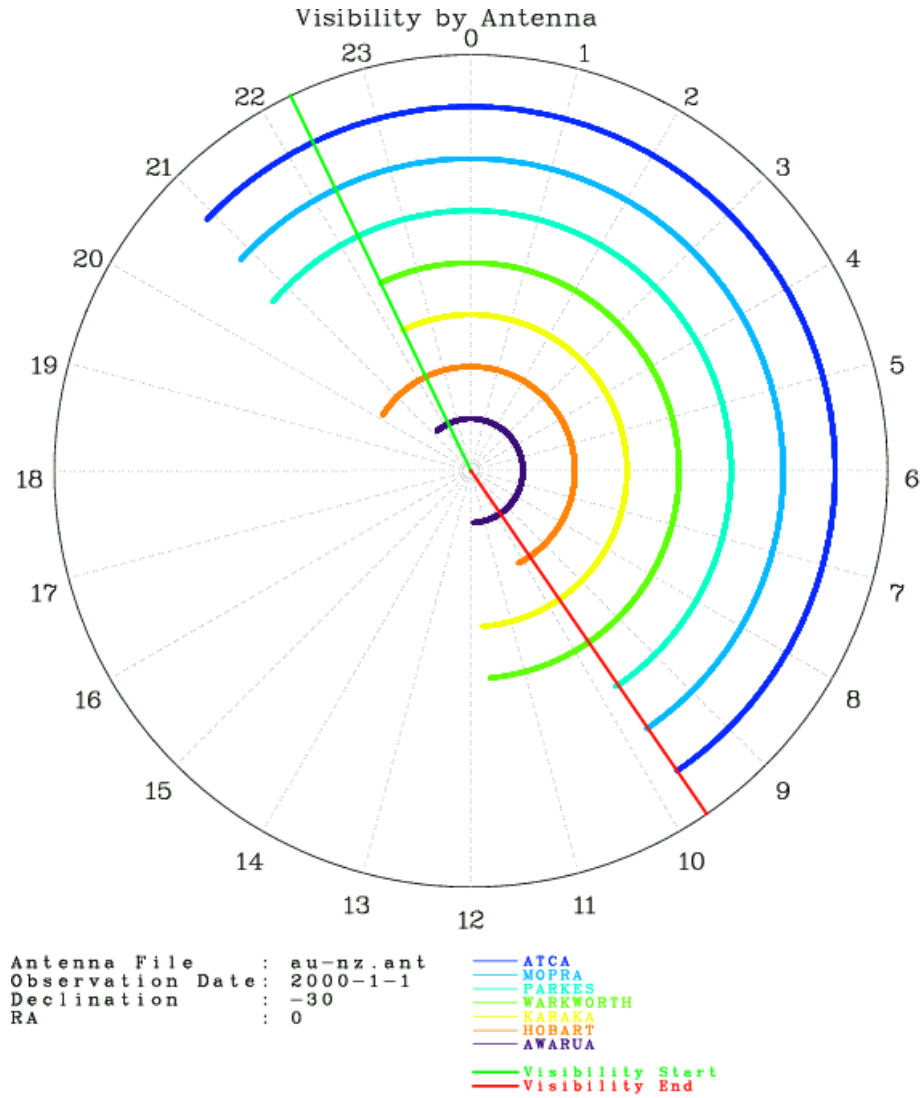


Figure 22: Example of output from vis.pl. Straight lines show the beginning (start) and the end of the period of common visibility for a given radio source (Declination =  $-30^\circ$  and RA =  $0^h$ ).

Figure 22 is a plot for the Australian sub-array antennae normally used for VLBI observations and two proposed New Zealand sites for antennae, Warkworth and Awarua. Admittedly this would become very cluttered for the large number of antennas in the full SKA, but for a small VLBI array this provides a clear and easy to read plot, with clear Start and End points for the sky visibility of the source for the antennas in an array.

In the input parameters to the sky visibility program a declination of  $100^\circ$  can be provided. This initiates a different plot as shown in Figure 23; this shows sky visibility for the whole array of antennae as hours vs. declination. This gives an overview of the period of common sky visibility of the array for objects at various declinations. This is then used to determine input time parameters for a theoretical observation in the later parts of the process.

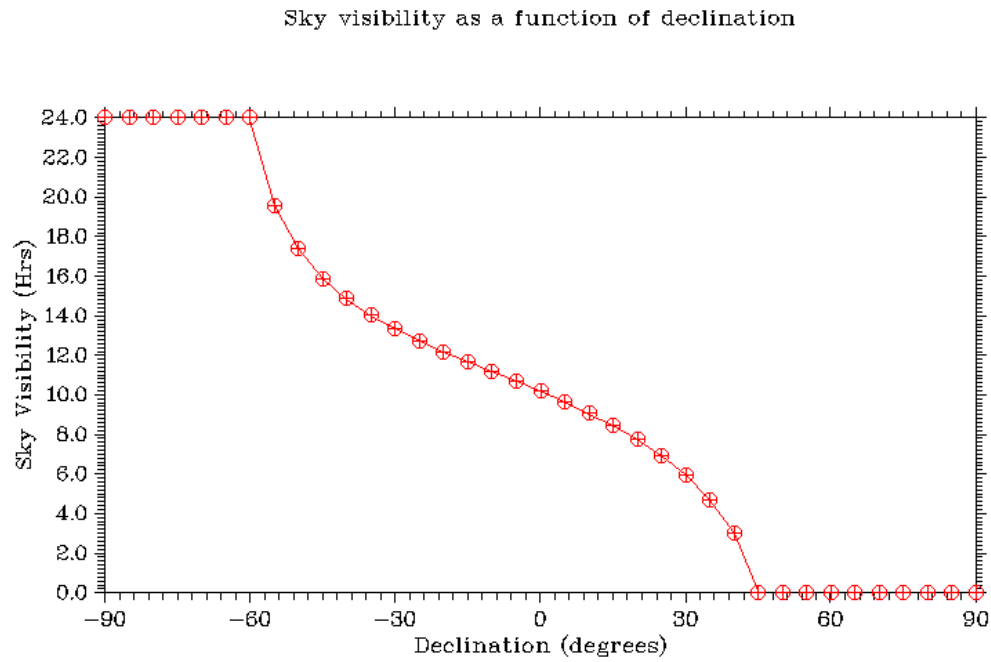


Figure 23: Sky Visibility vs. Declination. (The plot is generated automatically when a non-existing value for declination  $\text{Dec} = 100^\circ$  is used as the input parameter.)

This tool could be useful in the future for quick preliminary planning of observations, as existing methods using tools such as SCHED (Walker 2006) are very cumbersome and time consuming, requiring a very complex and detailed input file for processing.

### 3.4. Model Source

In this Section we will define model sources, which will be used below in this thesis when generating the  $u, v$  data. The aim is to have a known input image that can be used later for comparison with the final CLEAN image after modelling of a VLBI observation. The source definitions selected were based on several criteria as explained in the following two sections.

Although the structure of celestial radio sources can be quite complex, here we will use a simple gaussian distribution in brightness amplitude for each component of a source. A two dimensional elliptical gaussian function is expressed in Equation 3.8, where  $A$  is the peak amplitude,  $\sigma_x$  and  $\sigma_y$  are the rms lengths of the major and minor axes, and  $x_0$  and  $y_0$  are the position offset of the centre. If  $\sigma_x = \sigma_y$  then the function produces a circular gaussian distribution.

$$G(x,y)=A \exp [-(x-x_0)^2/2\sigma_x^2 - (y-y_0)^2/2\sigma_y^2] \quad (3.8)$$

Allowing for the ellipse major axis to be at an angle  $\phi$  to the horizontal

$$x' = (x-x_0) \cos\phi + (y-y_0) \sin\phi \quad (3.9)$$

$$y' = (y-y_0) \cos\phi - (x-x_0) \sin\phi \quad (3.10)$$

Thus Equation 3.8 expands to Equation 3.11 to express a 2 dimensional elliptical gaussian function at an angle to the horizontal.

$$G(x,y) = A \exp [-( (x-x_0) \cos\phi + (y-y_0) \sin\phi )^2/2\sigma_x^2 - ((y-y_0) \cos\phi - (x-x_0) \sin\phi )^2/2\sigma_y^2] \quad (3.11)$$

For the source description file provided to MIRIAD,  $Flux \equiv A$ ,  $DRA \equiv x_0$ ,  $DDEC \equiv y_0$ ,  $BMAJ \equiv \sigma_x$ ,  $BMIN \equiv \sigma_y$ , and  $BPA \equiv \phi$ .

### **3.4.1. Model Source: AGN**

The requirement was for a known model source that can be used as a reference in quantifying final image quality and for comparing the different arrays modelled. An area of interest to AUT's IRSR research is Active Galactic Nuclei (AGN) and the Interstellar Matter, thus several different but typical model sources were identified and modelled.

A source model in the form of an elliptical gaussian cross was selected as shown in Figure 25. This model represents, in a very idealised form, an AGN as seen edge on with two equal jets being emitted perpendicular to the plane of the galaxy.

The validity of the model source structure can be compared with a group of objects classed as "X-Shaped" Radio Galaxies (Cheung 2007). It can be seen that NGC 326 (J1327+0203) as shown in Figure 24 strikes a very close resemblance and visually compares well with some of the produced CLEAN images from the model sources produced later in this thesis.

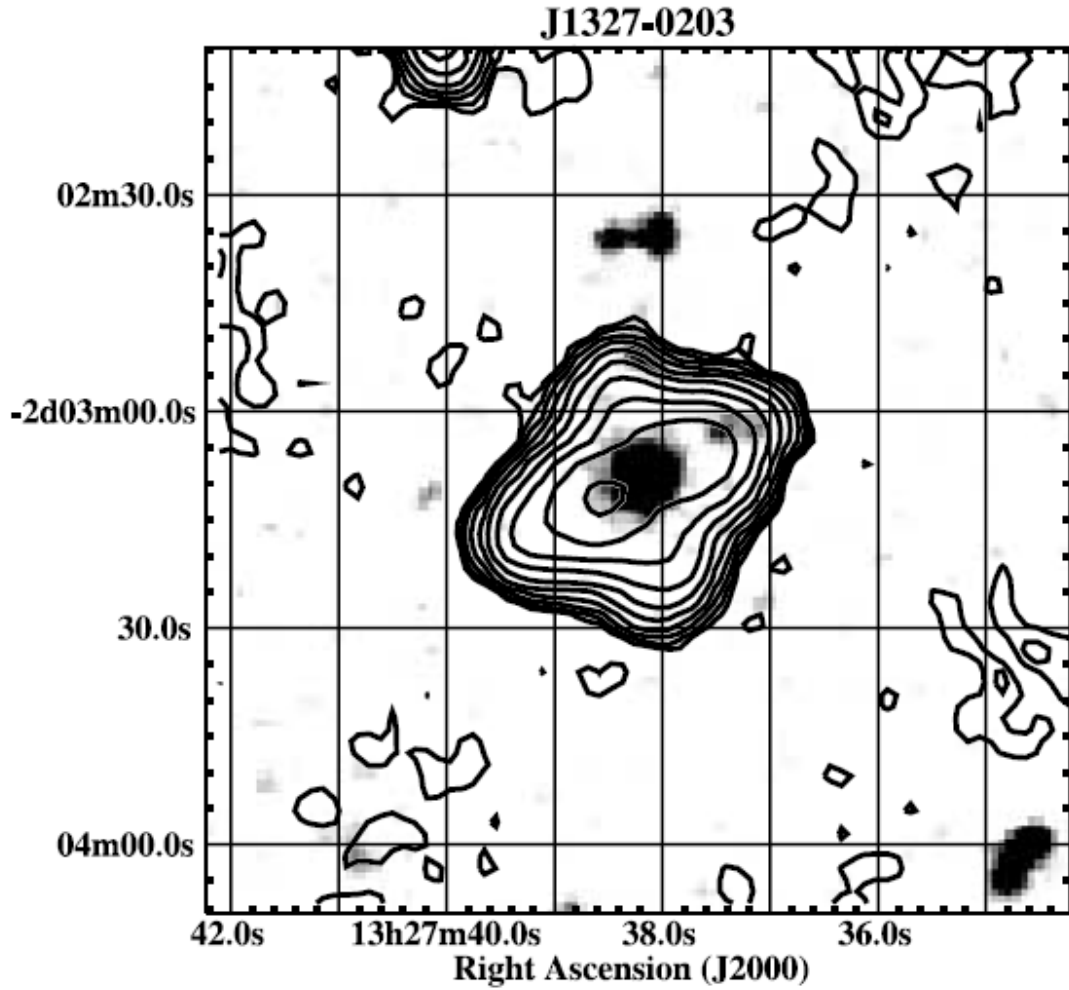


Figure 24: Image of X-Shaped Radio Galaxy J1327+0203 (Cheung 2007)

Comparing the theoretical resolution for AU, AU-NZ and AU-NZ-SB VLBI Arrays, using equation 1.1 it can be shown that for the AU (Australian sub-array antennae only) array where the baseline  $D$  is approximately  $4 \times 10^6$  m the angular resolution will be approximately 50 mas. For the AU-NZ (Australian sub-array and New Zealand Antennae) array where the baselines are approximately  $11 \times 10^6$  m it will have an angular resolution of approximately 18 mas. Three elliptical gaussian cross model sources were therefore selected that span this range of resolutions.



The model Source AGN1 is 25 mas on the major axis and 5 mas for the minor axis of an elliptical function. The definition of this source was supplied to the MIRIAD task IMGEN for generating the output image in a text file was of the form:

```
# MIRIAD Source File Format
# Flux    - total flux in Jy
# DRA,DDEC - Position offset from the phase centre in arcsec
# BMAJ     - Major Axis for ellipse in arcsec
# BMIN     - Minor Axis for ellipse in arcsec
# BPA      - Position angle of major axis measured N-E
# IFLUX    - % Polarization
# IPA      - Position Angle (default 0.0)
# VFLUX    - % Circular Polarization (default 0.0)
#
# Flux(Jy)  DRA   DDEC   BMAJ  BMIN  BPA   IFLUX  IPA   VFLUX
      100.0    0     0     0.025 0.005 45.0   0.0   0.0   0.0
      100.0    0     0     0.025 0.005 135.0  0.0   0.0   0.0
```

Model Source AGN2 is 50 mas on the major axis and 10 mas on the minor. The following input source description to MIRIAD defines model source AGN2.

```
# Flux(Jy)  DRA   DDEC   BMAJ  BMIN  BPA   IFLUX  IPA   VFLUX
      100.0    0     0     0.05  0.01 45.0   0.0   0.0   0.0
      100.0    0     0     0.05  0.01 135.0  0.0   0.0   0.0
```

Model source AGN3 is 100 mas on the major axis and 20 mas on the minor, with the following input source description to MIRIAD.

```
# Flux(Jy)  DRA   DDEC   BMAJ  BMIN  BPA   IFLUX  IPA   VFLUX
      100.0    0     0     0.1  0.02 45.0   0.0   0.0   0.0
      100.0    0     0     0.1  0.02 135.0  0.0   0.0   0.0
```

Note how we decrease the major and minor axis for the Elliptical Gaussian by a factor of 2 between model sources AGN3 to AGN2 and finally AGN1. We thus model a smaller and smaller source allowing us to compare arrays for finer and finer resolution and final image quality.

The model source images are shown in Figure 25. Running top to bottom are AGN1, AGN2 and AGN3, all produced to the same scale for comparison. The images of these model sources are 512 x 512 pixels, where each pixel is 0.25 mas.

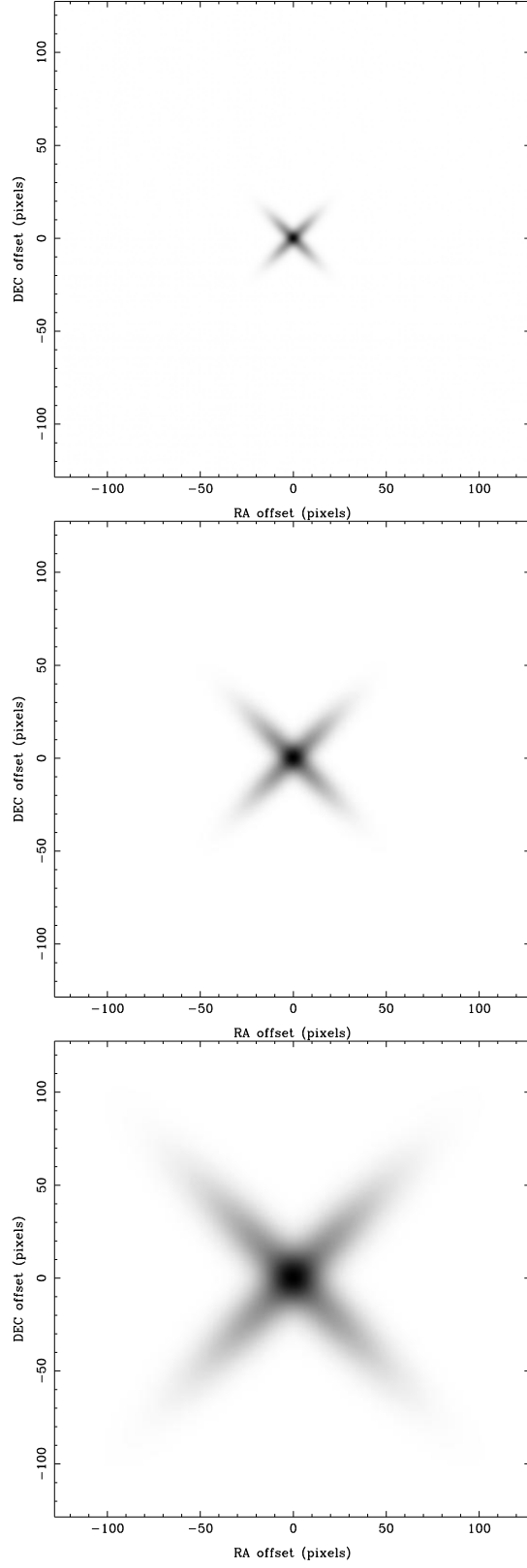


Figure 25: Model Images, Top AGN1 middle AGN2 and bottom AGN3

### 3.4.2. Model Source: Galaxy Triplet

Another model source, which we will use mainly for the SKA simulations is based on a small galaxy cluster type of astronomical object. The Leo Triplet (M66 Group) was considered as a prototype for this model (Figure 26).



Figure 26: Leo Triplet (From [astro.ihermans.com/galaxies/LeoTriplet/](http://astro.ihermans.com/galaxies/LeoTriplet/))

Small groups of galaxies and interacting galaxies are very common objects in astronomy (Fouque, Gourgoulhon et al. 1992). Some of the groups are very well studied, such as the Local Group, the Stephan Quintet (NGC7317 – NGC7320), the Leo Triplet, etc. Some of the groups consist of physically different components/objects, some reveal manifestation of the effect of gravitational lensing. Discovery of the first physically triple quasar was announced recently (Djorgovski, Courbin et al. 2007).

Groups of compact / ultracompact / hypercompact objects are common in physics of the interstellar matter. They can be groups of HII regions (areas in space which are luminous

with the emission spectrum of ionized hydrogen are called H II regions), protostellar objects, groups of sources of maser emission, etc. They can be observed in radio wavelengths as sources of thermal continuum radiation (both in continuum and radio recombination lines) or as sources of non-thermal maser emission (e.g. H<sub>2</sub>O masers). Figure 27 shows radio contours of G34.26+0.15 (a protostellar object) consisting of one ultra compact and two hyper compact objects (Johnson 2004).

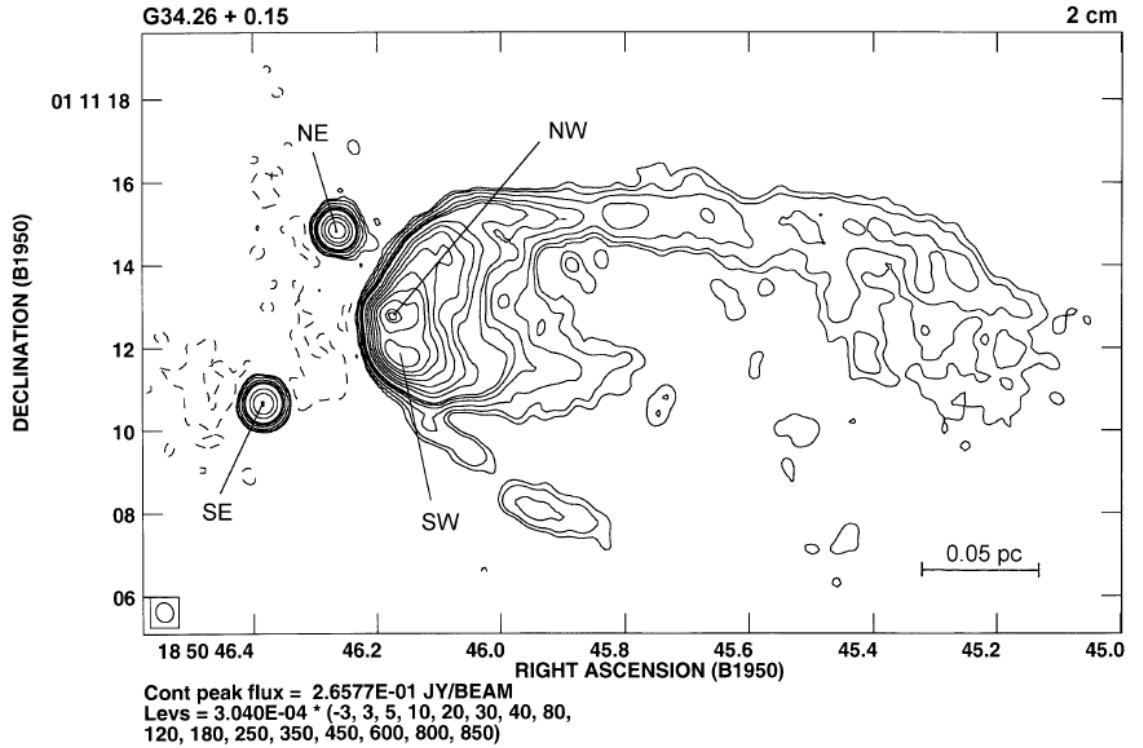


Figure 27: Radio contours of the massive protostellar object G34.26 + 0.15 showing a cometary ultra compact HII region and two hyper compact sources to the NE and SE. (Johnson 2004).

A model source was produced with three sources based on the theoretical resolution of the SKA's long baselines (SKA Memo 69, 2006). The definition of this source was supplied to the MIRIAD task IMGEN for generating the output image in a text file of the form:

```

# MIRIAD Source File Format
# Flux    - total flux in Jy
# DRA,DDEC - Position offset from the phase centre in arcsec
# BMAJ     - Major Axis for ellipse in arcsec
# BMIN     - Minor Axis for ellipse in arcsec
# BPA      - Position angle of major axis measured N-E
# IFLUX    - % Polarization
# IPA      - Position Angle (default 0.0)
# VFLUX    - % Circular Polarization (default 0.0)
#
# Flux(Jy)  DRA   DDEC   BMAJ  BMIN   BPA   IFLUX  IPA   VFLUX
      25.0   0.01  0.005   0.006 0.003  45.0  0.0   0.0   0.0
      25.0  -0.01  0.005   0.006 0.003 135.0  0.0   0.0   0.0
      25.0   0.0  -0.01   0.006 0.003  90.0  0.0   0.0   0.0

```

Figure 28 The created image produced by this definition is shown in Figure 28. The image of this model source is 512 x 512 pixels, where each pixel is 0.25 mas, the axis are scaled in arc second (arcsec). It is composed of three elliptical gaussian sources of major axis 5 mas and minor 3 mas. The top two components are separated by approximately 10mas and these are in turn separated from the bottom source by approximately 20 mas. The top left component has been inclined at 45° from the vertical, the top right component is inclined at 135° from the vertical and the final component is horizontal (inclined at 90° to the vertical).

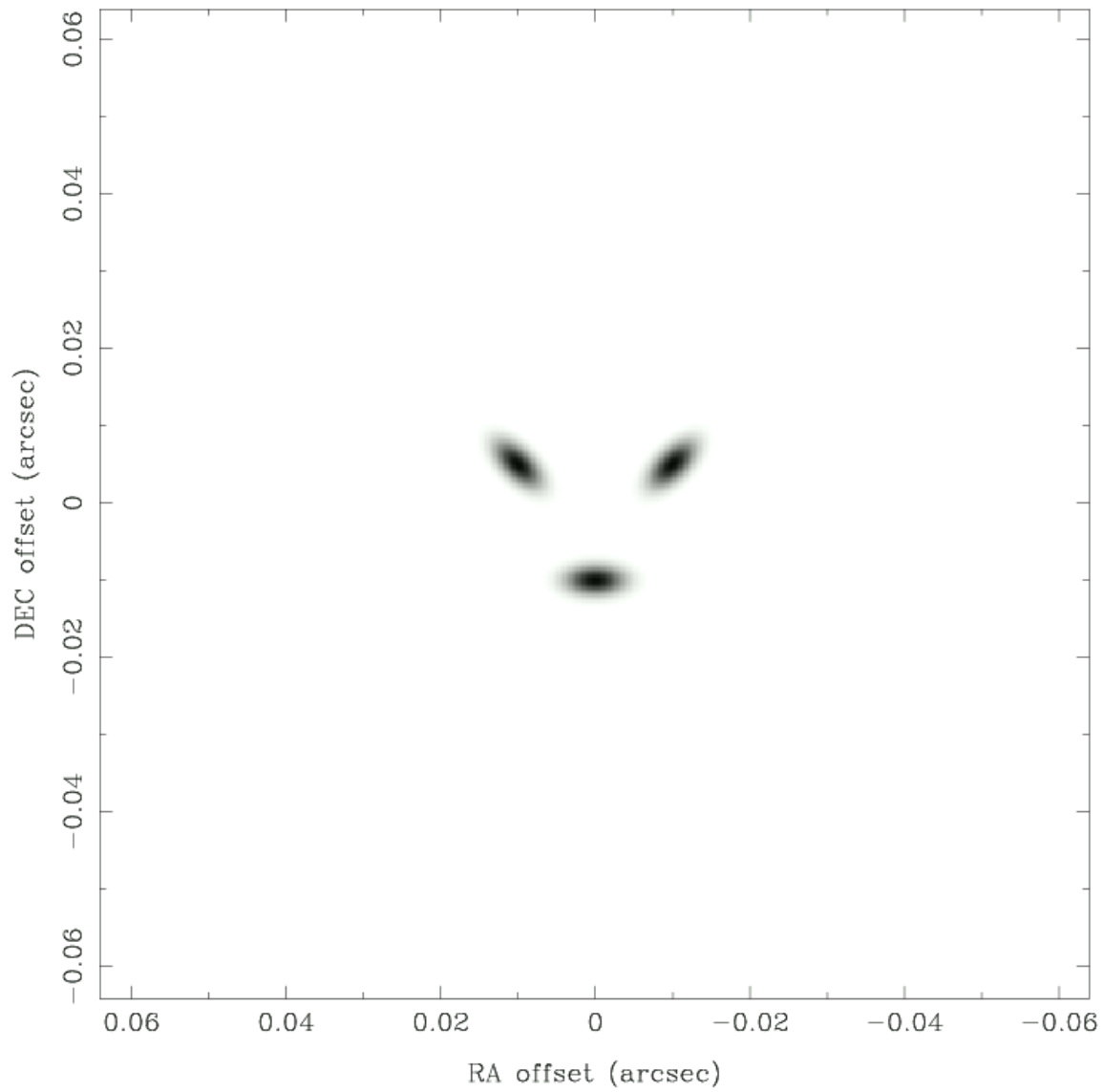


Figure 28: SKA Model Source Image – Galaxy Triplet

### 3.4.3. Model Source: Bright Source with a Jet

One more type of model source we use in this thesis for array modelling and image quality assessment is an asymmetric model source consisting of a bright core and a weaker component. This model imitates either a pair of radio galaxies or an AGN with a jet. Figure 29 shows a contour map of VLA image of the radio emission from 3C84 – a famous radio galaxy Perseus A (Pedlar, Ghataure et al. 1990).

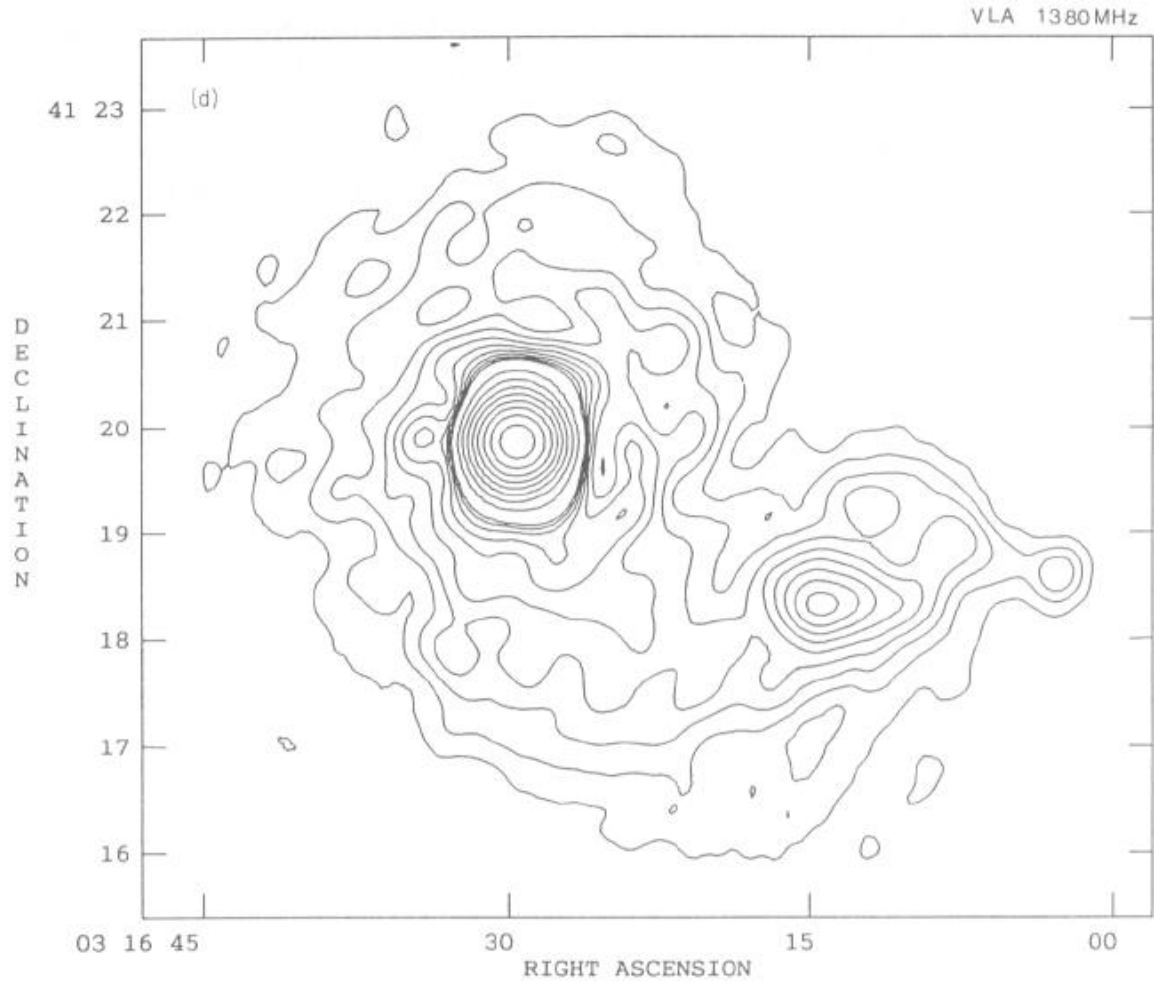


Figure 29: A contour map of VLA image of the radio emission from 3C84 – a bright radio galaxy with weak component(s). (Pedlar, Ghataure et al. 1990).



The definition of this source was supplied to the MIRIAD task IMGEN for generating the output image in a text file of the form.

```
# MIRIAD Source File Format
# Flux      - total flux in Jy
# DRA,DDEC  - Position offset from the phase centre in arcsec
# BMAJ      - Major Axis for ellipse in arcsec
# BMIN      - Minor Axis for ellipse in arcsec
# BPA       - Position angle of major axis measured N-E
# IFLUX     - % Polarization
# IPA       - Position Angle (default 0.0)
# VFLUX     - % Circular Polarization (default 0.0)
#
# Flux(Jy)  DRA   DDEC   BMAJ  BMIN   BPA   IFLUX  IPA   VFLUX
      100.0   0     0     0.05  0.05   0.0   0.0   0.0   0.0
      25.0   0.04  0.04   0.015 0.005  45.0  0.0   0.0   0.0
```

The created image produced by this definition is shown in Figure 30. This model source proved to be useful for our experiments with the Gaussian tapering function used in DIFMAP and  $u, v$  weighing.

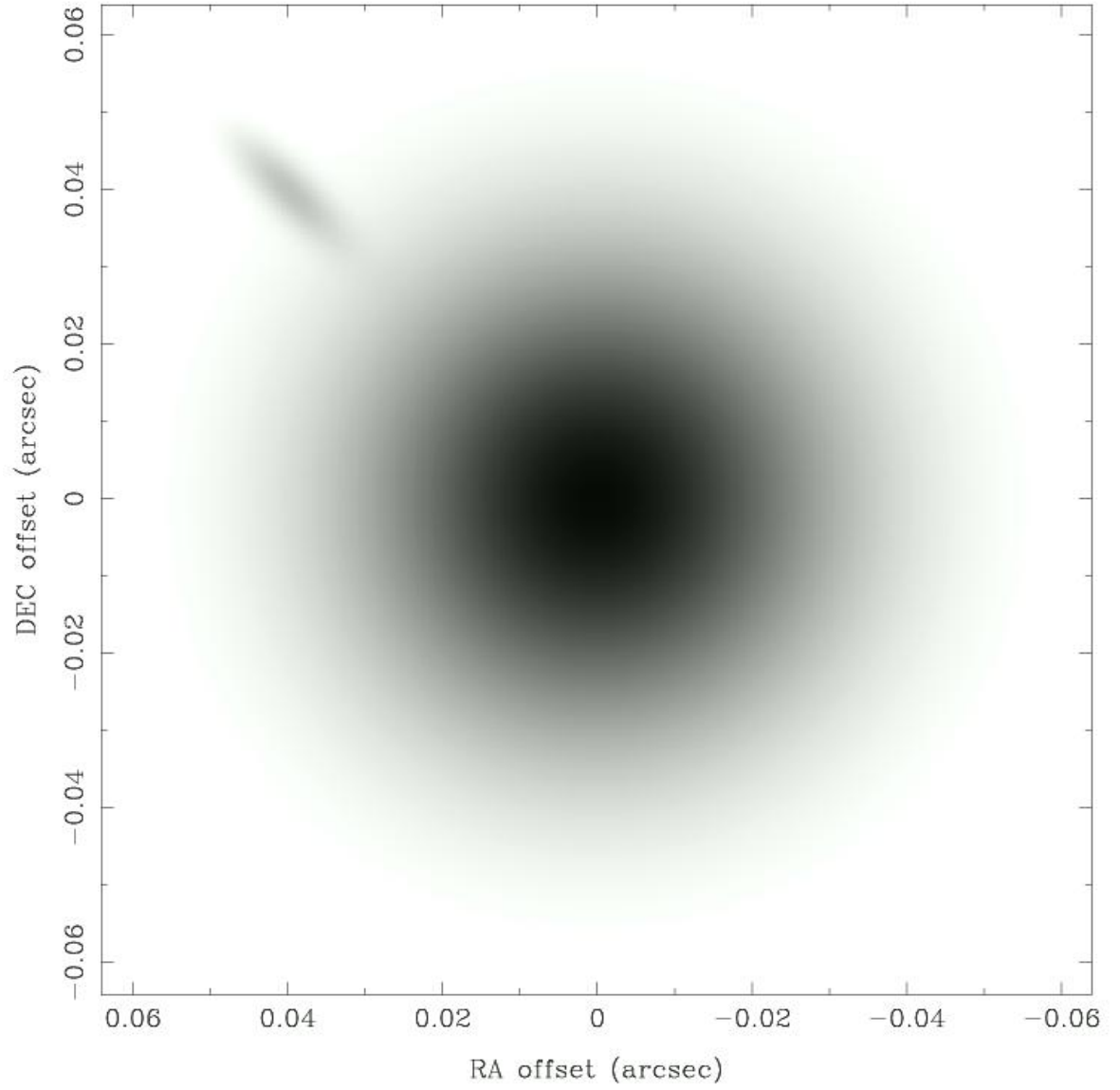


Figure 30: Model Source: Bright Source with a Jet

### 3.5. Generation of $u,v$ Data

This section explains the step where a chosen model image from 3.4 and the array definition from 3.2 are submitted to the MIRIAD module UVGEN. Together with other parameters which are explained in more detail later in this section the source model and array definitions are used to generate the simulated observation  $u,v$  data. The output of this stage is a FITS format  $u,v$  data file.

The parameters used in the MIRIAD UVGEN task are presented in Figure 31.

```
source= ( see Section 3.4 )
ant= (see Section 3.2 )
baseunit=3.33564
telescop=hobart26m
corr=0,1,0,104
freq=1.42
radec=0,$dec
stokes=xx,yy,xy,yx
lat=-40
harange=-6,6,0.01
systemp=300
jyperk=150
out=$name.fits.u,v
time=$date
```

Figure 31: MIRIAD UVGEN parameters

The parameters used in Figure 31 and their significance are explained as follows:

Source	This is the file containing the definition of the model source as discussed in 3.4.
Ant	This is the array definition file as discussed in 3.2.
Baseunit	specifies the coordinate system used in the antenna file, as we are using geocentric coordinates in meters. This parameter is set to 3.33564, this informs the program that the coordinate system being used is geocentric.
Telescop	specifies the antenna and associated parameter values to be used.
Corr	Defines the correlator setup. For all observations modelled the values shown in Figure 31 are Number of Channels 0 for wideband, Number of Spectral Windows 1, offset for centre frequency 0 MHz and width of spectral window 104 MHz.
freq	It was set at 1.42 GHz for the continuum objects being modelled.
radec	was defined in an earlier step of the process as it was used to determine the visibility of the source in Section 3.3.
stokes	This selects the polarization parameters. From Figure 31 the values used will form a file with the 4 polarizations parameters corresponding to an array with linear feeds.
Lat	Latitude of observatory: this was taken at $-40^{\circ}$ south.
harange	This was determined from using the visibility program described in Section 3.3.
systemp	System temperature used to generate additive random noise and total power. This value was selected based on data for antennae in Australia.
Jyperk	The system sensitivity: the default of 150 Jy/K was taken being a typical value for 6.1m antennas.
out	Gives the name of the output MIRIAD $u, v$ data file.

time            Date and time for theoretical observation that  $u,v$  data is being generated for.

It should be noted that for the harange consideration has to be given to the declination of the source. For a source with a +ve declination then a harange of -6,6 (for a 12 hr observation) and -2,2 (for a 4hr observation) must be used. If the source has a -ve declination then a harange of 6,18 (for a 12 hr observation) and 2, 4 (for a 4hr observation) must be used. If this is not followed then a mirror image of the actual  $u,v$  lines is obtained.

### **3.5.1. MIRIAD observatories.dat**

While using the package MIRIAD it was found that a pre-defined set of antennae and their characteristics had been hard-coded into the application. A proposal was submitted to the custodians of MIRIAD the Australia Telescope National Facility (ATNF) that the use of an antenna configuration file which could be read upon request by appropriate modules would allow a more flexible approach. This would allow a user of the software package to add or delete an antenna definition or modify existing values without having to modify source code and the subsequent recompilation and re-linking of what is a very large FORTRAN program. The proposal was accepted by ATNF and the change was undertaken by me to allow MIRIAD to read an antenna parameter file when required rather than have antenna characteristics hard coded into the program. This change was submitted and accepted by ATNF for release in the next version of MIRIAD. Appendix E includes an example copy of the new MIRIAD observatories.dat file. The modified FORTRAN source code files for MIRIAD as submitted to ATNF can be found in the electronic appendix.

For the SKA simulations software changes had to be made to the MIRIAD package due to a hard coded limit of 20 antennae allowed in an antenna array. This limit was increased to 150 thus allowing full simulation of the entire Australian proposed 125 station SKA array. Subsequently the compute time for such models on the computing equipment available<sup>6</sup> was found to be impractical for reasonable turn around with the resources available.

---

<sup>6</sup> An old Intel Server from my employer that was being thrown away. It had dual cpu's PIII (797 MHz, 256Kb Cache), RAM 771Mb running Red Hat Linux 7.2.

### **3.6. $u,v$ Data Processing**

This section deals with the processing of the FITS  $u,v$  file generated from MIRIAD task UVGEN as described in Section 3.5. It describes how to use the application DIFMAP (Taylor 1997) to process the FITS  $u,v$  file (the dirty map) and apply the CLEAN (Högbom 1974) deconvolution algorithm to produce a final CLEAN image.

We thank Steven Tingay for his time while visiting AUT in 2006 for providing instruction in the use of DIFMAP. Based on this visit and subsequent experience, an attempt has been made to catch some of this acquired knowledge in addition to the “Difmap Cookbook” document provided with the software. An AUT “User Guide for DIFMAP” was produced, a copy of which is attached in the electronic Appendix A of this Thesis.

To retain consistency between different DIFMAP simulations each dirty image (FITS  $u,v$  file) is set to perform a fixed number of CLEAN iterations. It was found for the Australian sub-array - New Zealand array simulations that a straightforward loop of CLEAN and SELFCAL was sufficient to produce an acceptable image. So a simple UNIX script was written to reproduce the steps required and to provide a reproducible process that remains consistent between simulations. A copy of the script is reproduced in Figure 32.

```

#!/bin/bash
rm difmap*.log*
difmap << EOF
obs $1
select
mapsize 512,1.0
uvweight
startmod
selfcal
do i=1,20
clean;selfcal
end do
docont=false
device clean_$2.ps/ps
mappl cln
save clean_$2
quit
EOF

```

Figure 32: DIFMAP script written for Australian sub-array - New Zealand simulation

For the more complex and larger SKA array simulation we are dealing with an array made up of short ( $< 10$  km) and very long ( $> 1000$  km) baselines. It was found that just using a set number of CLEAN iterations did not provide a satisfactory image. Considering the superior coverage of the  $u, v$  plane with such an instrument and the many very long baselines very high image quality and resolution was expected. To try and obtain the best possible image a combination of valid techniques including  $u, v$  weighting and a taper function were employed. These effects are demonstrated later in this section.

The  $u, v$  weight technique is explained and demonstrated in Section 3.6.1, and the application of  $u, v$  taper is explained and demonstrated in Section 3.6.2. For this also a UNIX shell script was written to easily reproduce a consistent processing of the  $u, v$  data. A copy of the script is reproduced in Figure 33.



```

#!/bin/bash
rm difmap*.log*
difmap << EOF
obs $1
select
mapsize 512,0.5
uvweight 2,-1
do i=1,40
clean;selfcal
end do
uvweight 0,-1
do i=1,40
clean;selfcal
end do
docont=false
device clean_$2.ps/ps
mappl cln
save clean_$2
quit
EOF

```

Figure 33: SKA uvweight DIFMAP script

### 3.6.1. $u,v$ Data Weighting

$u,v$  weighting (Briggs 1995) is used to compensate for the fact we do not have uniform coverage of the  $u,v$  plane and that data is concentrated within certain areas. This can be seen from the plots in Figure 4 where the antenna tracks have been plotted across the  $u,v$  plane.

Thus  $u,v$  weighting is achieved by applying a density weighting function that compensates for the areas in the  $u,v$  plane with a concentration of data. There are a number of different weighting functions in common use;

Natural weighting is where all points within the  $u,v$  plane are treated alike by applying a weight  $D_k$  to each point:

$$D_k = 1 \quad (3.12)$$

Uniform weighting is where  $N_s(k)$  the number of data points within a symmetric region of the  $u,v$  plane of width  $s$  centred on the  $k^{\text{th}}$  data point have a weight  $D_k$  applied to them:

$$D_k = \frac{1}{N_s} \quad (3.13)$$

This is discussed in some detail in (Briggs 1995) and (Briggs, Schwab et al. 1999).

Also discussed in (Briggs 1995) is robust weighting where the visibility weighting varies smoothly from natural to uniform weighting as a function of a real time parameter, the robustness. In areas where the weight density is low, the effective weighting applied is uniform. In areas where the weight density is high, the weighting applied is uniform. This can reduce the RMS thermal noise by 25%, while only marginally increasing the width of the fitted beam by 3%. It was originally derived to overcome a stripping problem generated by uniform weighting.

By default DIFMAP uses natural weighting where all points are treated alike but as can be seen from Figure 4 the  $u,v$  tracks tend to spend more time per unit area near the  $u,v$  origin

which corresponds to shorter baselines. Thus natural weighting will emphasize the short baselines. For uniform weighting in DIFMAP a commonly used definition is “uvweight 2,-1”, which corresponds to width  $s=2$  to the power of -1.

To demonstrate the effect of different weighting the SKA Antenna Array sub-sets CORE, INT and MAX (as defined and discussed in Section 3.2.2) have been used with the model source discussed in Section 3.4.2. This antenna array was selected for study as it has a mixture of short and long baselines as can be seen from the  $u,v$  plot in Figure 34. The effects of applying natural and uniform weighting are shown in Figure 35.

In Figure 35 the first line from left to right shows the CLEAN images after applying Natural weighting (0,-1) and Uniform weighting; (2,-1), (3,-1) and (5,-1). As we move to Uniform weighting of (3,-1) and (5,-1) the differences are more subtle. Due to these more subtle differences included on the second line are the corresponding CLEAN images on the second line are shown with contours that help to reveal the differences. For those images with contour lines they are at equal values of % (1, 2, 4, 8, 16, 32, and 64) of the maximum image pixel value.

The biggest improvement for a visual comparison of the CLEAN image compared to the model source image is seen with the switch from natural to uniform weighting. As we move out to larger grids, much smaller differences are apparent from the contour plots. Most noticeable is that the separation between the top two gaussian components becomes slightly more apparent.

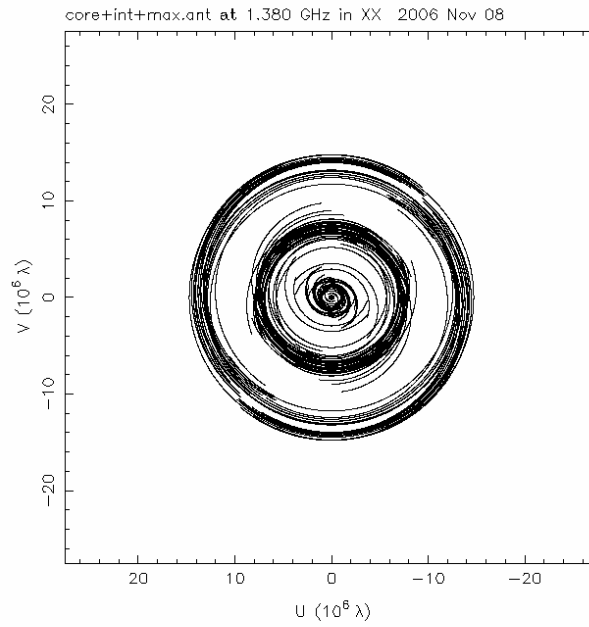
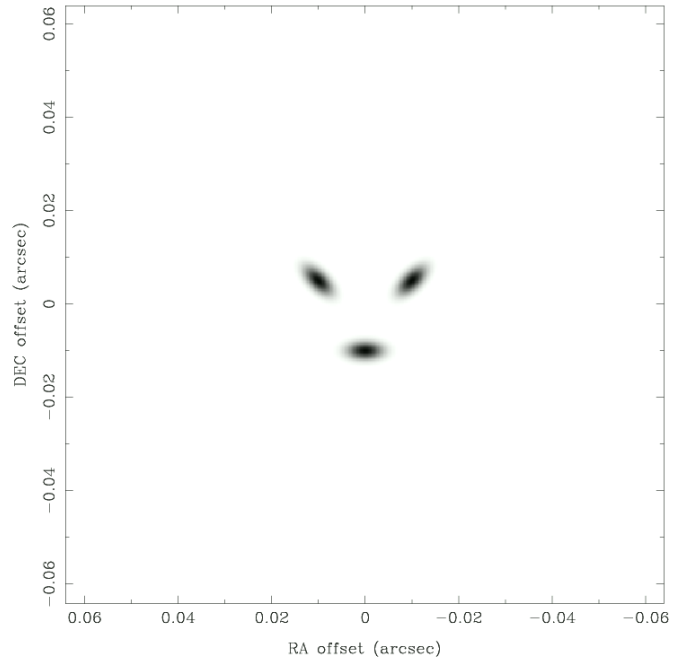
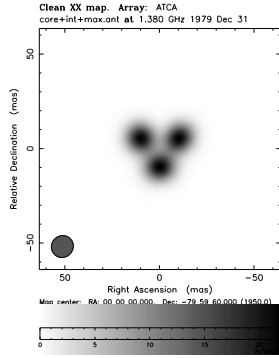
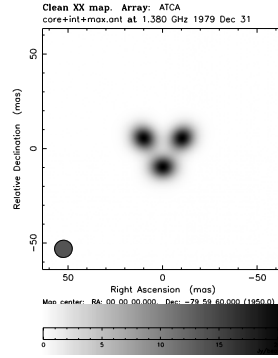


Figure 34: Top Model Source and bottom  $u, v$  Plot for SKA sub-set array CORE+INT+MAX

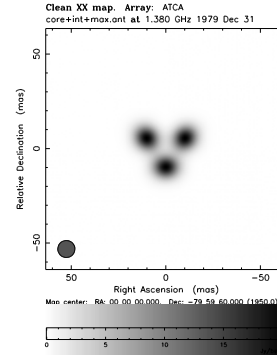
Natural (0,-1)



Uniform (2,-1)



Uniform (3,-1)



Uniform (5,-1)

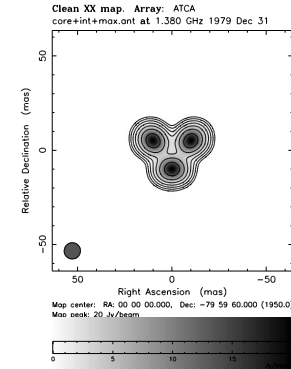
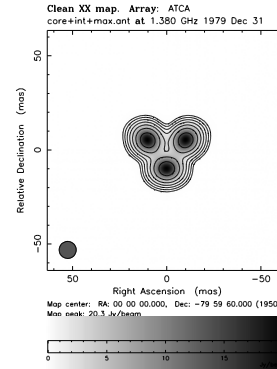
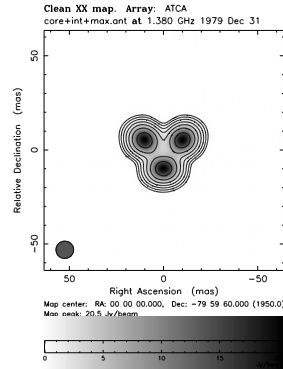
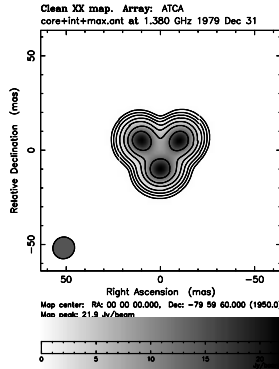
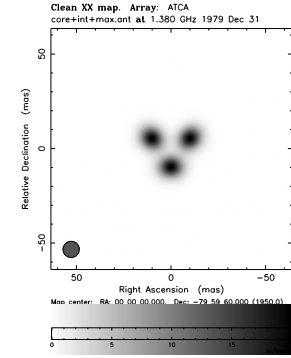


Figure 35: Examples of different UVWEIGHT settings and the resultant CLEAN Images

### 3.6.2. $u,v$ Taper

A Gaussian tapering function,

$$T(x) = \exp(-ax^2) \quad (3.14)$$

where  $x = \sqrt{u^2 + v^2}$  and  $a$  is a constant, can be used to downweight the data at the outer edge of the  $u,v$  coverage (long baselines) and reduce sidelobes. As demonstrated in Figure 36 this will in effect increase the beam size and thus will emphasize short baselines. This is different to  $u,v$  weighting where the emphasis is to resolve fine structure, here we are likely to be trying to exhibit a large component.

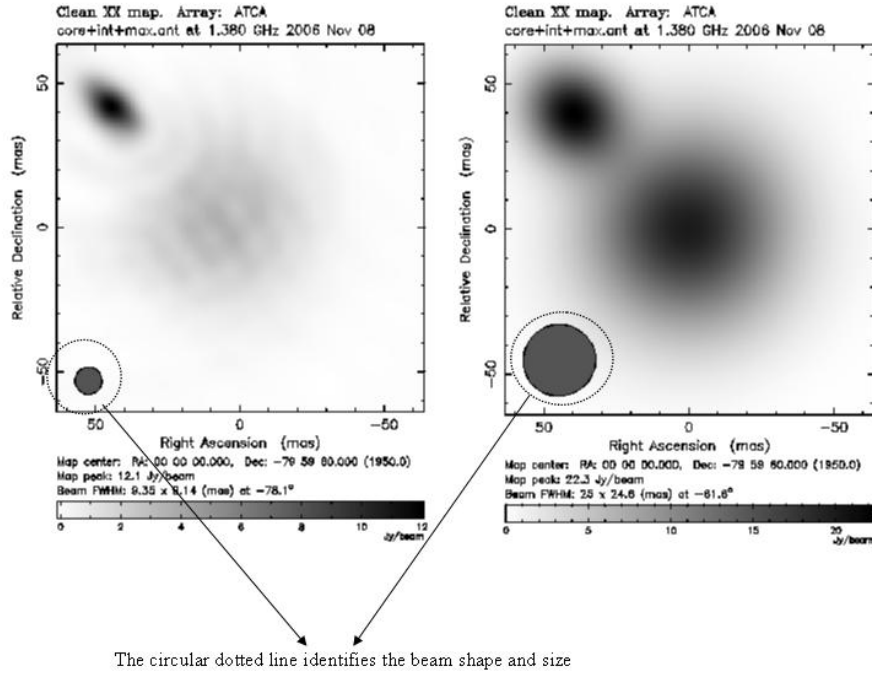


Figure 36: DIFMAP CLEAN image showing the beam shape and size

This is discussed in some detail in (Briggs 1995) and (Briggs, Schwab et al. 1999). As we are using DIFMAP to produce the CLEAN image, the *uvtaper* command in DIFMAP is used. The *uvtaper* command has two input parameters, *gaussian\_value* ( $g_v$ ) and *gaussian\_radius* ( $g_r$ ). From the DIFMAP Help these values are explained as follows:

*gaussian\_value*: The value of the gaussian taper function,  $T$ , at '*gaussian\_radius*'. Valid values lie between 0 and 1 exclusive. Other values cause the cancellation of any existing gaussian taper.

*gaussian\_radius*: The  $u, v$  radius at which gaussian taper function,  $T$ , should have fallen to '*gaussian\_value*'. (values  $\leq 0$  de-select gaussian tapering). Unless changed with the *mapunits* command, the units are million-wavelengths.

The gaussian factor,  $a$ , in the weight function  $T$  is:

$$a = -\frac{\log_e g_v}{g_r^2} \quad (3.15)$$

From the  $u, v$  Plot in Figure 34 it can be seen that the groups of antennae making the CORE lie within a radius of approximately 4 mega  $\lambda$  (for  $\lambda=21\text{cm}$ ), INT is approximately 8 mega  $\lambda$  and MAX are at approximately 16 mega  $\lambda$ . An additional taper function of 2 mega  $\lambda$  was also selected as this would represent the inner core antenna baselines as an experiment to see if the larger source would be enhanced and the smaller source minimized. Thus four taper functions within DIFMAP have been used, based on these radii. Equation (3.15) is used to generate Table 9 showing the gaussian function *difmap* ( $g_f$ ) which will be applied to the  $u, v$  data as a weighting function.

Difmap	gaussian_value ( $g_v$ )	gaussian_radius ( $g_r$ )	gaussian factor, $a$
uvtaper 0.8,2	0.8	2	0.055786
uvtaper 0.8,4	0.8	4	0.013946
uvtaper 0.8,8	0.8	8	0.003487
uvtaper 0.8,16	0.8	16	0.000872

Table 9: Gaussian Taper Factors

Reviewing the code for DIFMAP it was seen that the gaussian factor ( $g_f$ ) is used to weight the  $u,v$  data by the function shown in equation (3.16).

$$Weight = e^{(g_f * x^2)} \quad (3.16)$$

The weight is then applied to the  $u,v$  data, to see how the weight changes by  $u,v$  radius (x) we have used equation (3.17) where the  $u,v$  data is an arbitrary unit of 1.

$$WeightedDaa = 1.0 - e^{(g_f * x^2)} \quad (3.17)$$

The function for a Gaussian Taper from equation (3.17) is plotted and shown in Figure 37 for the four values selected in Table 9 for  $g_f$ .



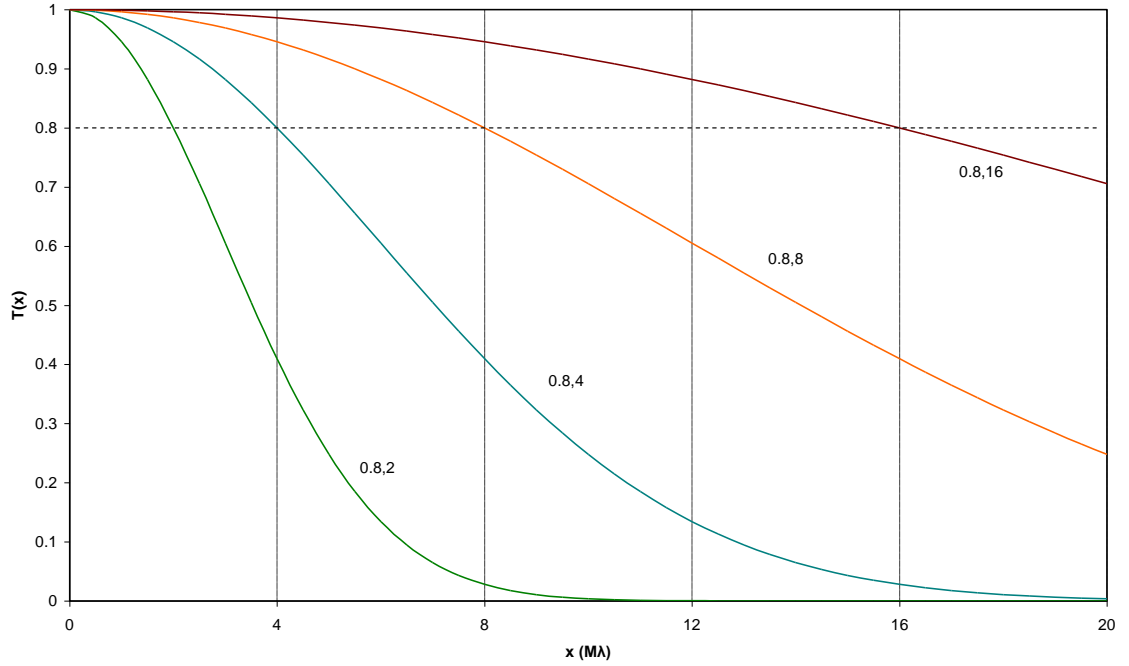


Figure 37: A Gaussian  $u,v$  Taper Function

A model source was chosen that consists of a large component which would be resolved by the short baselines and a small component that would be resolved only by the long baselines. The model source is shown in Figure 38 and is intended to represent a large source with a small jet (component in the top left hand corner). The same SKA array (CORE+INT+MAX), which we used to demonstrate weighting in 3.6.1, is also used here to demonstrate the tapering function. The results of applying taper functions to the  $u,v$  data and the resultant DIFMAP CLEAN image processing are shown in Figure 39. There are two rows of images presented in Figure 39. The top row from left to right shows the final CLEAN image; with no taper function, a taper function of 0.8 2, a taper function 0.8,4, a taper function 0.8,8 and finally a taper function of 0.8,16. The second row shows the corresponding CLEAN images to the first row but with contours.

As can be seen from Figure 39 using a sharp cutoff of 0.8,2 allows us to resolve the larger element of the model source. As the taper function is extended it is observed that the larger stronger source is reduced but the smaller weaker source becomes more prominent as the longer baselines come into play.

With no taper function applied for this source (Figure 39 – left hand column of images) it is interesting to note that DIFMAP and the CLEAN algorithm (for the full SKA antenna array model) pick up the weaker component in the CLEAN image and enhance it to the point where it becomes the dominant feature. The true larger and stronger component is almost lost if no taper function is used. Problems of this sort lead to the common practice (S. Tingay, private communication) of using a combination of *uvweight* and *uvtaper* to try and “stack” CLEAN images, each having the functions “tuned” for appropriate emphasis of long or short baselines.

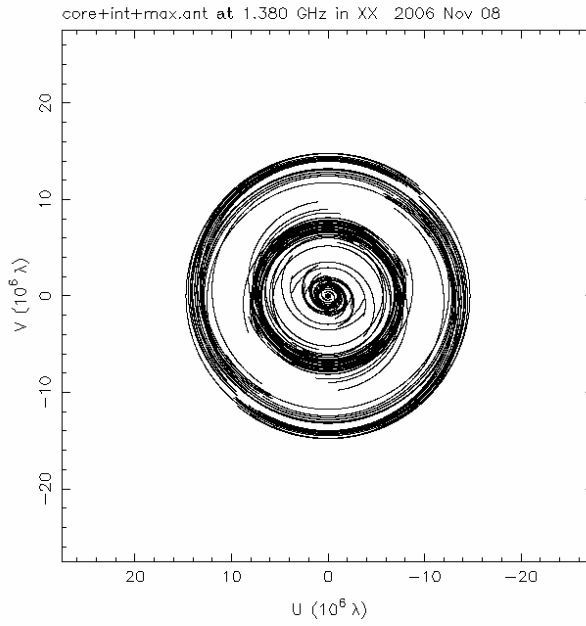
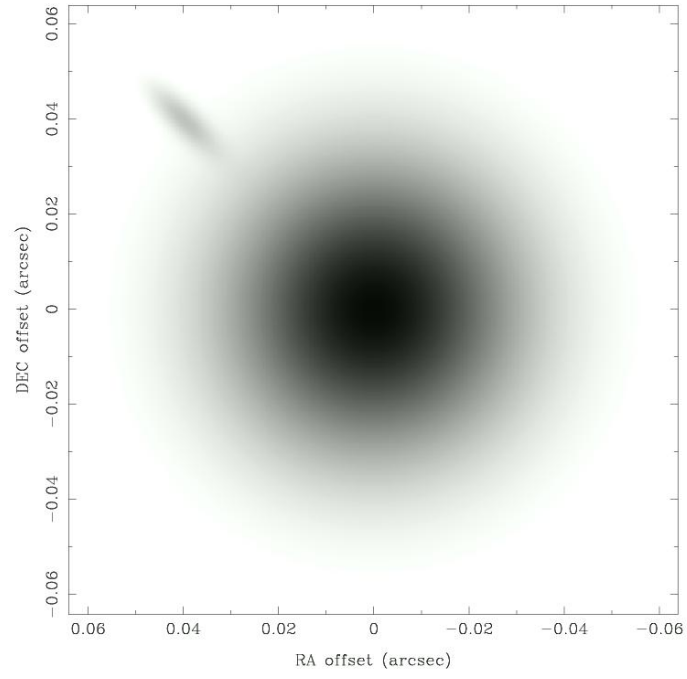


Figure 38: Top Model Source used for the  $u,v$  Taper examples and bottom  $u,v$  Plot for SKA sub-set array CORE+INT+MAX

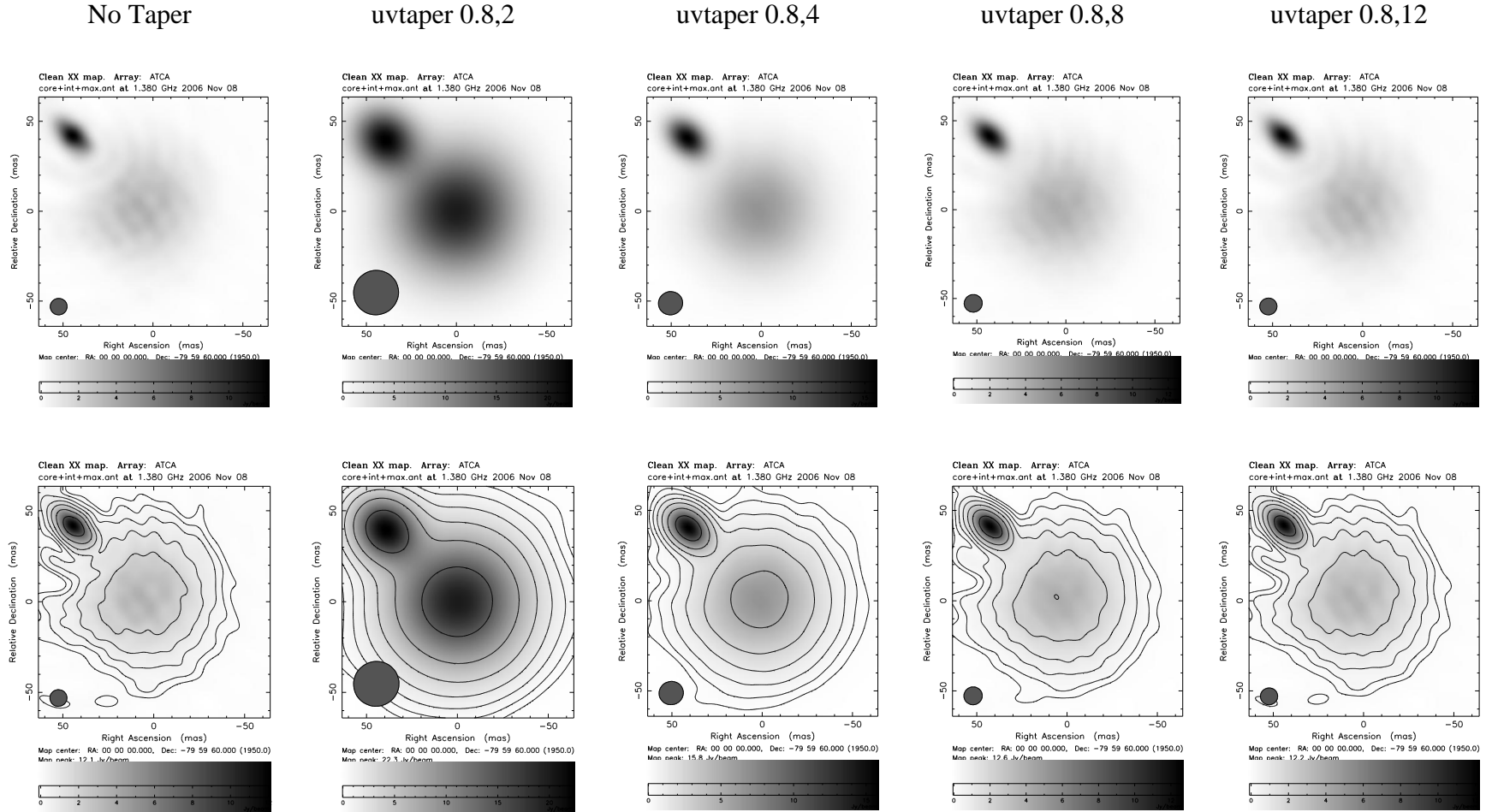


Figure 39: Examples of applying different UVTAPER parameters and the resultant CLEAN Images

### 3.7. Figure of Merit

In this section a number of different quantitative measures of image quality are investigated. Currently assessments of image quality are typically made by a human operator, the consistency and “intersubjectivity” of this process can be questioned. Some more robust means that provides consistent, reliable outputs is highly desirable. Further motivation for this study comes from recognizing the implications of the enormous data rates and volumes that proposed instruments such as the SKA will generate. Data accumulated would quickly overwhelm the capacity of Human operators to keep up and outstrip the budgetary resources available to buy the long term storage required to retain the raw data for later analysis. The bulk of the raw data will almost certainly need to be reduced in “real time”. Consistent, robust methods of image production from raw data amenable to automated computer operation will be an imperative for these instruments to succeed.

A number of studies have looked at this and related issues. For example (Heddle and Webster 2000) and (Cohen 2004) studied automated image simulations. They present their results as CLEAN images of known and well studied sources such as M51 and Cygnus A. The use of artificial observations was discussed by (Willis 2000) , where the image of the simulated sky for the modelled observation was presented along with the final CLEAN images for comparison.

The measures of image quality used in these works are subjective; the ultimate assessment of image quality is made by the observer applying their perception of image quality. No quantitative measure is given for the final image in these works. Figure 40 below contains the results of a simulation carried out for this thesis that illustrates the process; an input model image was generated and then processed assuming a number of different array configurations to produce the CLEAN images presented. Visually all the CLEAN images are X-like in shape, although all have some distortion and addition of background “noise” components (artefacts in the images which will limit the dynamic range). We are left with the question: which is closest to the input model image? We have looked to find a solution to this issue that provides a robust, intersubjective figure of merit.

The remainder of this section reviews a number of different quantitative measures of image quality. The aim is to find a robust, quantitative measure that can replace a subjective comparison. Effects such as the smearing of the image due to the effects on resolution of a given array configuration, the quality of  $u, v$  coverage, as well as defects introduced by the processing algorithms themselves (deconvolution in particular) have been considered.

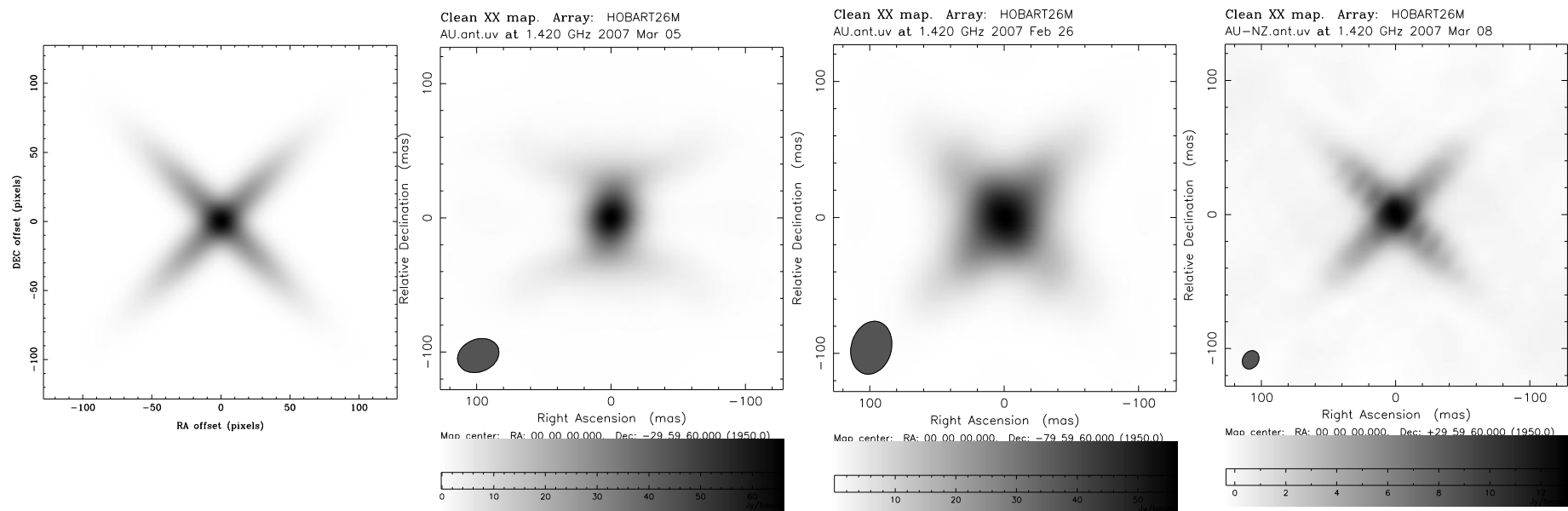


Figure 40: Comparing examples of CLEAN images to demonstrate the various distortions. From left to right first is the Model Image for AGN3, CLEAN image for a 12hr observation with the Australian sub-array only array at declination  $-30^\circ$ , CLEAN image for a 12hr observation with the Australian sub-array only array at declination  $-80^\circ$ , CLEAN image for a 12ht observation with the Australian sub-array – New Zealand array at declination  $-30^\circ$ .

### 3.7.1. Full Width at Half Maximum Intensity

Figure 41 shows a model input image (top left) and the output CLEAN image (top right). Distribution of image density through a horizontal slice at  $y=256$ ,  $x=1,512$  (the centre of the image) is given at the bottom for the figure. These graphs (for both model image and the output CLEAN image) are plots of the pixel value at each point  $p(x,y)$  along the dotted horizontal line which cuts the centres of the images.

The Full Width at Half Maximum (FWHM) for pixel values along the image slice can be taken as a measure for each image. So a ratio of (FWHM for Model) / (FWHM for CLEAN) is then used as a measure to compare the images.

$$FWHMRatio = \frac{J1 - I1}{J2 - I2} \quad (3.18)$$

$J1$  = Right Pixel position for FWHM of model image

$I1$  = Left Pixel position for FWHM of model image

$J2$  = Right Pixel position for FWHM of CLEAN image

$I2$  = Left Pixel position for FWHM of CLEAN image

Ideally, when the output image is identical to the model image, the ratio (3.18) approaches 1. Realistically, this ratio is between 1 and 0. This value gives us a quantitative measure of how close the final CLEAN image is to the original model image. The closer is its value to 1, the closer the output image is to the input (model) image, therefore the higher is the quality of the procedure applied for image synthesis, or the more optimal is the configuration of the array, providing better  $u, v$  coverage.



Figure 42 shows results of modelling for a VLBI array with baselines between Australian sub-array and New Zealand. This array gives a final CLEAN image that appears of higher quality than the CLEAN image in Figure 41 (for LBA antennas only); the values of the ratio for each array are presented in Table 10.

Array	FWHM Ratio
Australian sub-array	0.4375
Australia – New Zealand Antennae	0.8750

---

Table 10: FWHM Ratio for VLBI Arrays Australian sub-array and Australian sub-array - New Zealand

This simple approach can be used to compare different mathematical procedures applied for image processing/synthesis, or for comparison of different antenna configurations, provided that the model source is symmetrical and simple. For a simple single gaussian source, this would appear to be a good measure of quality. But astronomical sources being imaged by VLBI arrays typically have more complex structures with multiple merged and separate elements of nebulous structure. The model images chosen in this research are intended to represent valid sources in a simplified form. With such structural complexity we find ourselves confronted with deciding which image slice to use? Alternatively do we take the average of multiple slices? It is not obvious which is the best strategy and as a consequence it was felt that a more robust measure of image quality should be sought.

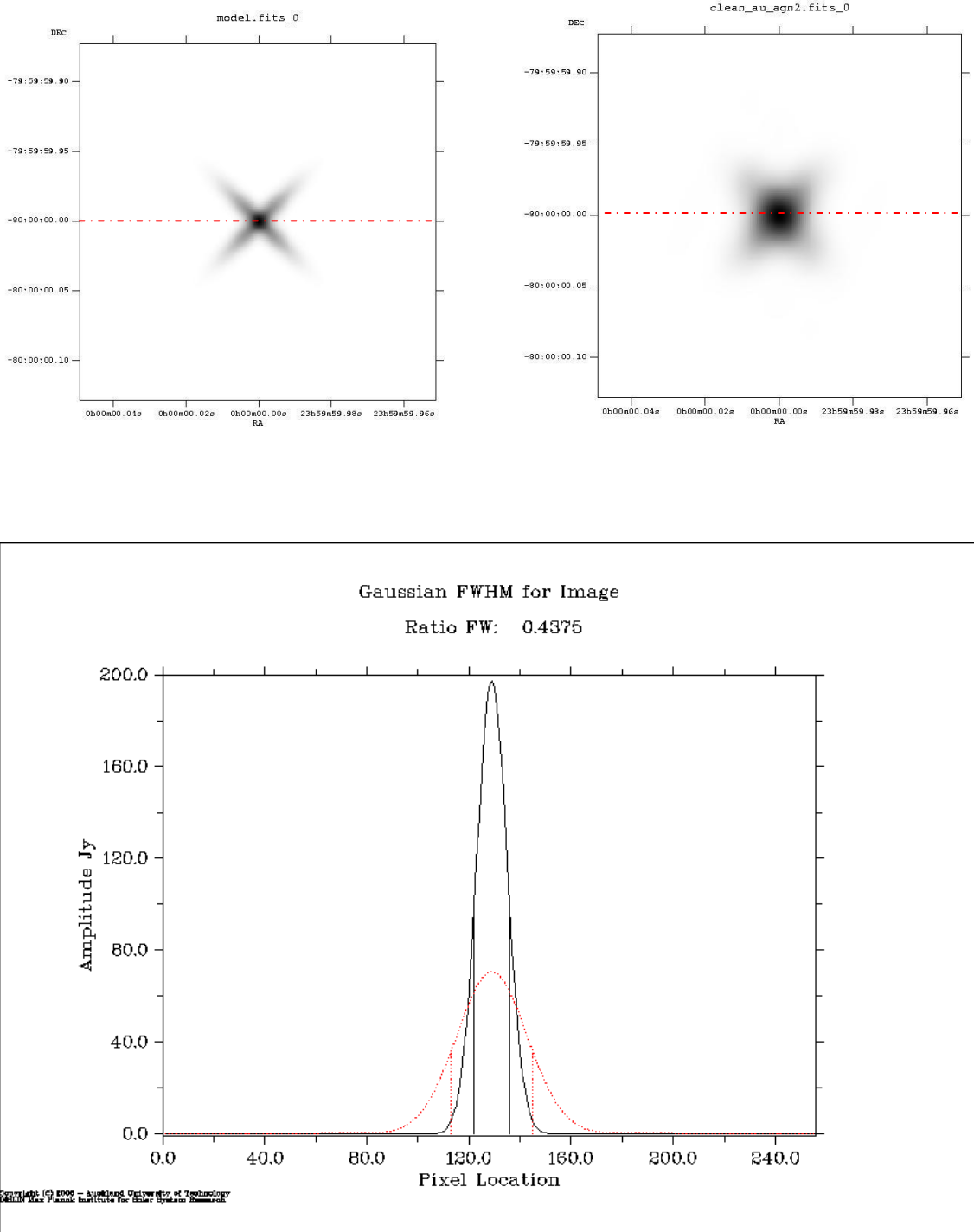


Figure 41: FWHM method for Australian sub-array Antennae Only. Top left is the input model image to the process and top right is the final CLEAN image for source AGN2 at a declination of  $-80^\circ$ . Bottom is a plot of the FWHM for both images using line of pixels through the images of  $Y=256$ ,  $X=1,512$  (the images are  $512 \times 512$  pixels)

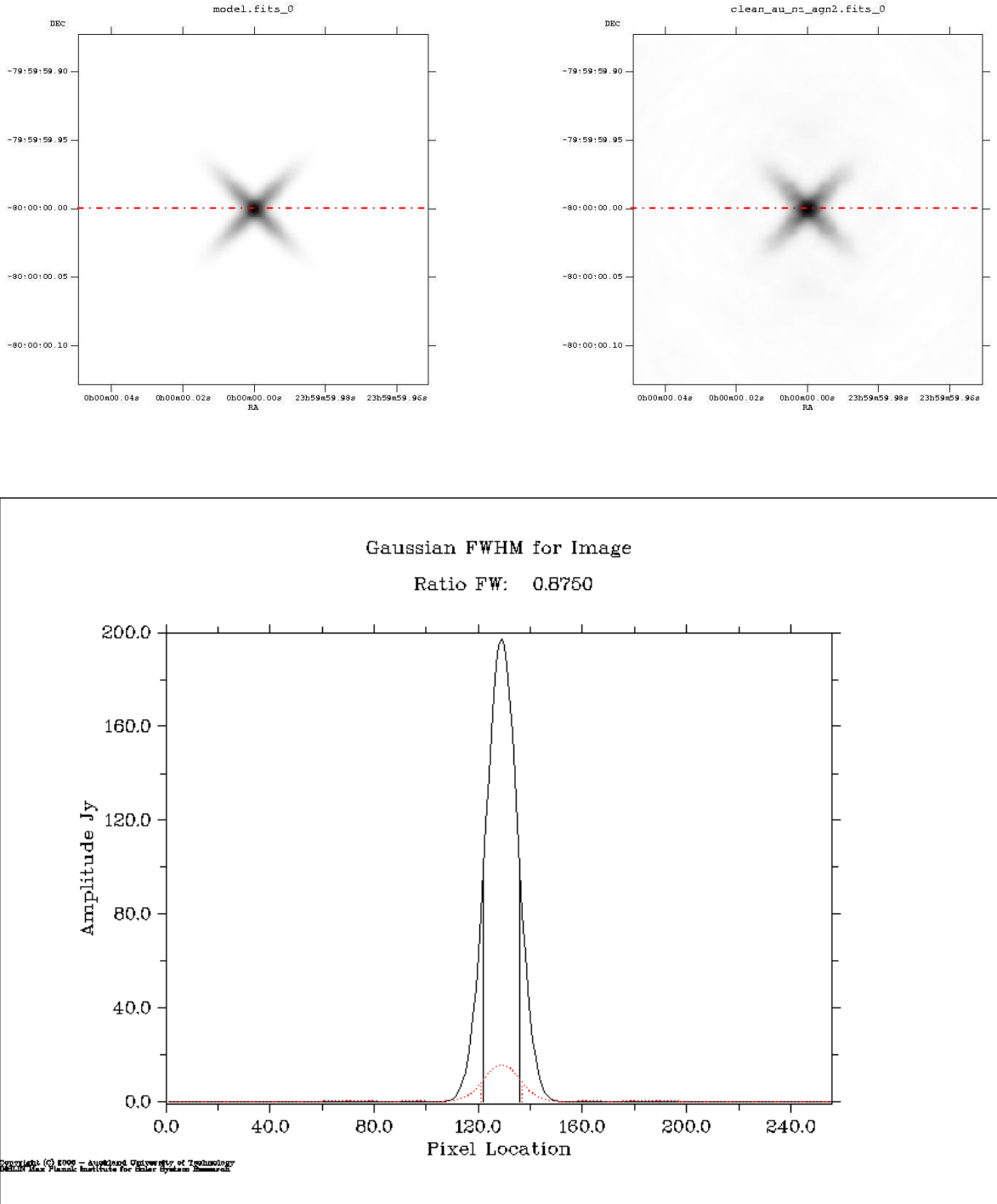


Figure 42: FWHM for Australian sub-array & New Zealand Antennae. Top left is the input model image to the process and top right is the final CLEAN image for source AGN2 at a declination of  $-80^\circ$ . Bottom is a plot of the FWHM for both images using line of pixels through the images of  $Y=256$ ,  $X=1,512$  (the images are  $512 \times 512$  pixels)

### 3.7.2. Mean Square Error

A well established technique to assess the quality of restored images is comparison of the mean squared error (MSE) for restored image and original image. We may apply this technique to our work by treating the “restored image” as the CLEAN image and the original image as the input model image (Sugiyama, Imaizumi et al. 2001) (Dolinar, Cheung et al. 1991).

To compute the Mean Square Error we use equation (3.19). For an image of N by M pixels where  $X_{jk}$  is the model image (N,M) pixel value and  $\hat{X}_{jk}$  is the CLEAN image (N,M) pixel value.

$$MSE = \frac{\sum_{j=0}^{N-1} \sum_{k=0}^{M-1} \left( X_{jk} - \hat{X}_{jk} \right)^2}{N * M} \quad (3.19)$$

MSE is sensitive to the deviation of an image from the original. As the sum of the differences in pixel values between the two images reduces then the MSE value will tend to 0.

The MSE value from the model images in Figure 25 and the resultant CLEAN images in Sections 4.1.1, 4.2.1 and 4.3.1 for the model 12hr observations of various arrays are presented below in tables: Table 11 is for the Australian sub-array, Table 12 for the Australian sub-array – New Zealand array, and finally, Table 13 is for the Australian sub-array – New Zealand – Antarctica array.

It has previously been reported that the Mean Squared Error (MSE), or its variants do not correlate well with subjective evaluation (Gonzalez and Woods 2002). We see this reflected in our results; Table 11 to Table 13 whose values have been plotted in Figures Figure 43 to Figure 45, for comparison purposes. It is clear that we have poor correlation between what we would expect from a visual comparison of the simulated images as presented in Section 4 and the MSE values. Also we are interested in the main component of the image, but by its nature the CLEAN process introduces spurious components as explained in Section 2.4.

These components lie outside the main source component that is being imaged and will produce a higher MSE value even though the source component of interest is resolved and visually compares well with the model source.

We can conclude that the proposed MSE measure does not always provide a consistent trend in values that agrees with the visual inspection of the images. In addition the un-normalized nature of the values makes comparison of MSE between different arrays, sources and declinations rather difficult.

Declination	-30°	-55°	-80°
Source			
agn1	122	205	190
agn2	37	70	80
agn3	228	190	179

Table 11: MSE values for the Australian sub-array array for a 12hrs observation for the different model sources at different declinations.

Declination	-30°	-55°	-80°
Source			
agn1	8.5	7.8	8
agn2	66.	72	75
agn3	412	420	420

Table 12: MSE values for the Australian sub-array - New Zealand array for a 12hrs observation for the different model sources at different declinations.

Declination	-30°	-55°	-80°
Source			
agn1	17	12	15
agn2	102	91	99
agn3	460	447	455

Table 13: MSE values for the Australian sub-array - New Zealand - Antarctica array for a 12hrs observation for the different model sources at different declinations.

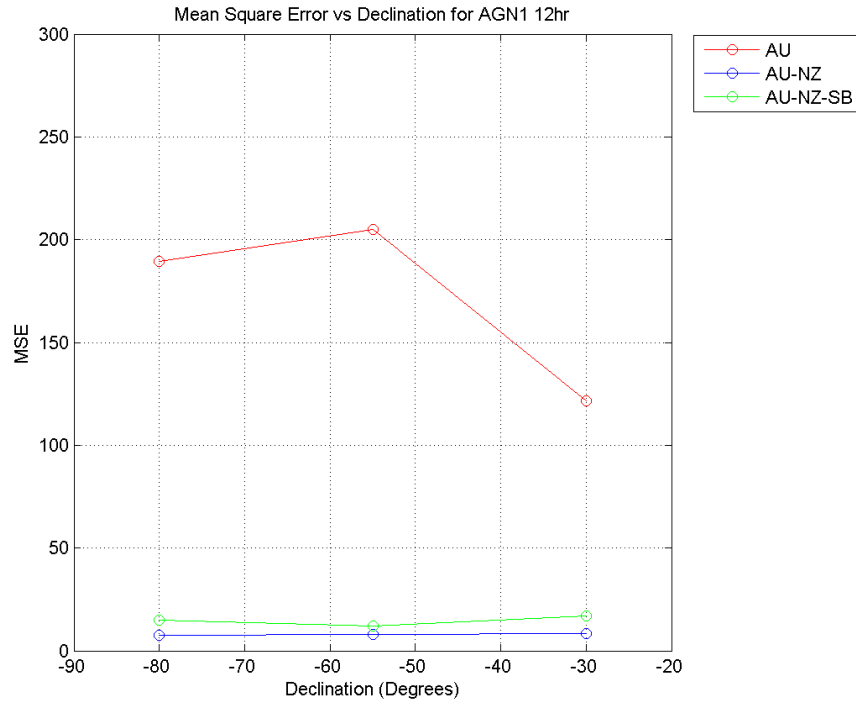


Figure 43: Comparison of the Mean Square Error for the source AGN1 against Declination for the different arrays.

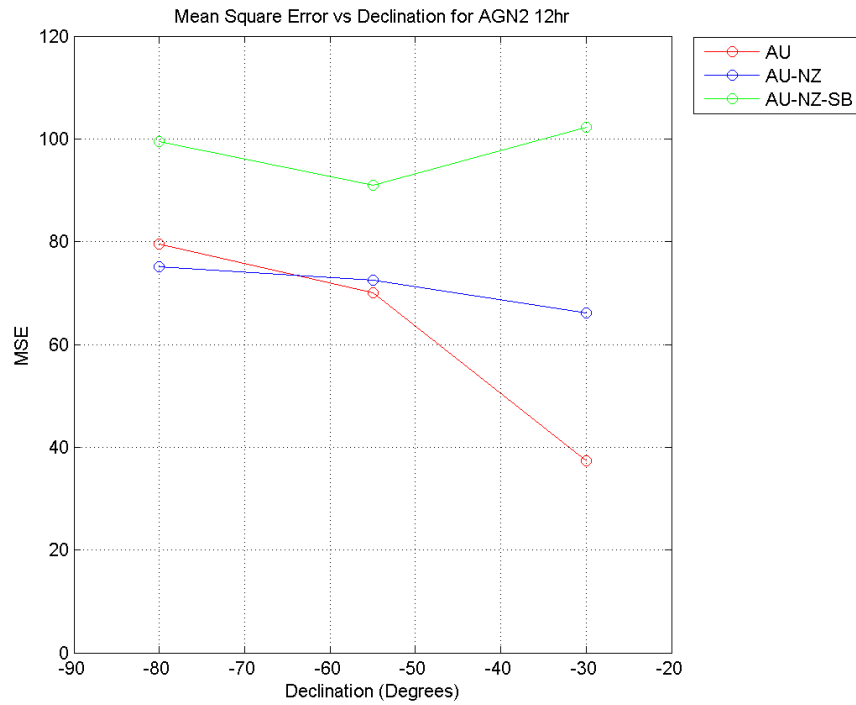


Figure 44: Comparison of the Mean Square Error for the source AGN2 against Declination for the different arrays.

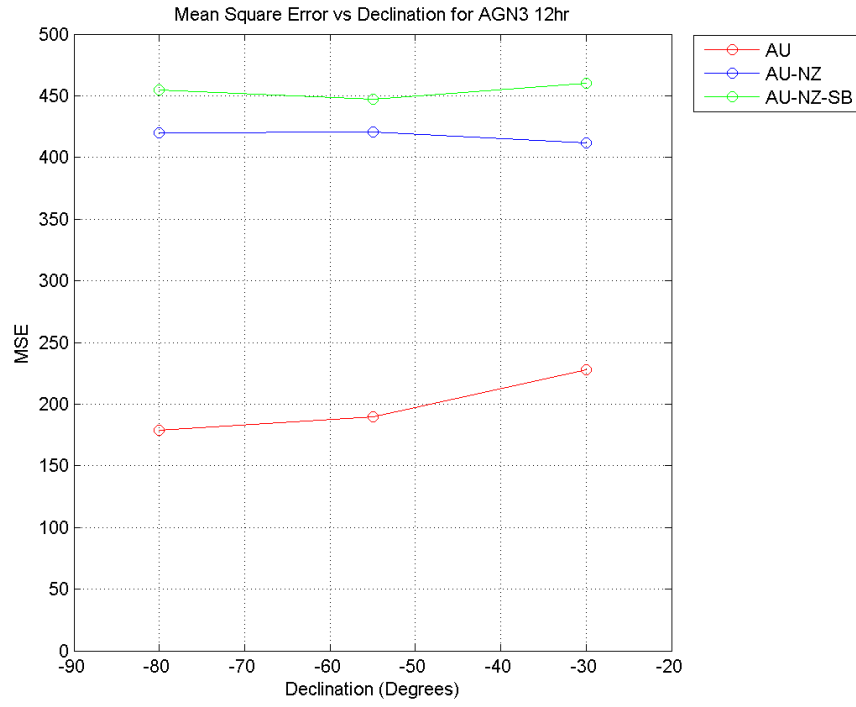


Figure 45: Comparison of the Mean Square Error for the source AGN3 against Declination for the different arrays.



### 3.7.3. 2-D Cross-Correlation

The principal use of 2-D cross correlation is for pattern-matching between matrices. In this scenario images are regarded as matrices of pixel values. We have the model image which is a matrix  $A$  of pixel values of dimensions  $(M_a, N_a)$  and a CLEAN image which is a matrix  $B$  of pixel values of dimensions  $(M_b, N_b)$  referred to as the template. The 2-D Cross Correlation is given by equation (3.20) (Gonzalez and Woods 2002).

$$C(i, j) = \sum_{m=0}^{(M_A-1)} \sum_{n=0}^{(N_a-1)} A(m, n) \cdot \text{conj}(B(m+i, n+j)) \quad (3.20)$$

Where  $0 \leq i < M_a + M_b - 1$  and  $0 \leq j < N_a + N_b - 1$

conj - Complex conjugate

The MATLAB function **xcorr2** was investigated as it closely follows equation (3.20). The function is explained as a template matrix  $B$  which is in effect moved about in  $M$  and  $N$  over the image matrix  $A$ , and the summation is taken over the image region where  $A$  and  $B$  overlap. The maximum value of  $C(i, j)$  determines where the best match is obtained. Thus the cross-correlation  $C(i, j)$  has its maximum value when the two matrices are aligned so that their forms achieve the best possible match. This is demonstrated by the following example:

$$A = \begin{bmatrix} 0 & 0 & 0 & 0 & 0 \\ 0 & 0 & 1 & 0 & 0 \\ 0 & 1 & 1 & 1 & 0 \\ 0 & 0 & 1 & 0 & 0 \\ 0 & 0 & 0 & 0 & 0 \end{bmatrix} \quad B1 = \begin{bmatrix} 0 & 1 & 0 \\ 1 & 1 & 1 \\ 0 & 1 & 0 \end{bmatrix}$$

The resultant cross correlation matrix for  $A$  and  $B1$  is:

$$C1 = \begin{bmatrix} 0 & 0 & 0 & 0 & 0 & 0 & 0 \\ 0 & 0 & 0 & 1 & 0 & 0 & 0 \\ 0 & 0 & 2 & 2 & 2 & 0 & 0 \\ 0 & 1 & 2 & 5 & 2 & 1 & 0 \\ 0 & 0 & 2 & 2 & 2 & 0 & 0 \\ 0 & 0 & 0 & 1 & 0 & 0 & 0 \\ 0 & 0 & 0 & 0 & 0 & 0 & 0 \end{bmatrix}$$

The central element of the result matrix  $C1$  is the correlation when the two matrices are perfectly aligned. If we now change matrix  $B$  thus:

$$B2 = \begin{bmatrix} 0 & 0 & 0 \\ 0 & 1 & 0 \\ 0 & 0 & 0 \end{bmatrix}$$

Then the resultant cross correlation of  $A$  and  $B2$  in this situation is:

$$C2 = \begin{bmatrix} 0 & 0 & 0 & 0 & 0 & 0 & 0 \\ 0 & 0 & 0 & 0 & 0 & 0 & 0 \\ 0 & 0 & 0 & 1 & 0 & 0 & 0 \\ 0 & 0 & 1 & 1 & 1 & 0 & 0 \\ 0 & 0 & 0 & 1 & 0 & 0 & 0 \\ 0 & 0 & 0 & 0 & 0 & 0 & 0 \\ 0 & 0 & 0 & 0 & 0 & 0 & 0 \end{bmatrix}$$

In the result matrix  $C2$  we can clearly see where  $B$  will overlap  $A$  and thus it can be fitted in 5 locations, giving us a spread and no clear fit point. In  $C1$  the highest value element is 5 and in  $C2$  the highest value element is 1, thus  $C1$  has highest cross-correlation and this maximum element value is taken as the 2-D Cross-Correlation value.

The cross correlation values for each CLEAN image to model source, observed with a particular array are presented in Table 14 to Table 16 for a 12hr observation.

In Figure 46 the Cross-Correlation values for model source AGN1 are plotted against declination for each array. It can be seen that the Australian sub-array only array and the modelled 12 hr observation for source AGN1, would indicate that the closest CLEAN image to the model occurs at a source declination of  $-50^\circ$ . Examining the CLEAN images in Section 4.1.1, we can clearly see that there is very little to differentiate the CLEAN images for AGN1 at the different declinations. The Cross-Correlation values would indicate that the AU array is superior to the other two arrays AU-NZ and AU-NZ-SB. Visual inspection of the CLEAN images in Sections 4.1.1, 4.2.1 and 4.3.1 does not corroborate these results.

Comparing the arrays for model source AGN2 in Figure 47 we see a trend that the observations at a declination of  $-80^\circ$  are slightly superior to those at  $-30^\circ$ , and that the CLEAN images for the AU only array are superior to the other two arrays. Visual inspection of the CLEAN images in Sections 4.1.1, 4.2.1 and 4.3.1 does not corroborate the values for the AU only array.

Finally looking at Figure 48 for model source AGN3 we have a similar scenario to the above, where the trend of the Cross-correlation values corroborates with a visual inspection of the CLEAN images. Again the Cross-Correlation values would indicate that the AU only array is superior to the other two until a cross over at approximately  $-42^\circ$  to  $-38^\circ$  declination. Again this is not corroborated by a visual inspection of the CLEAN images in Sections 4.1.1, 4.2.1 and 4.3.1.

As has been shown the Cross-Correlation values do not agree well with a visual comparison of the CLEAN images. Further these values are un-normalized which makes a comparison of values between arrays, sources and declinations impossible. This method was not adopted as a unit of measure.

The MATLAB script used to run these evaluations is provided in Appendix F.

Dec	-30°	-55°	-80°
Source			
agn1	$4.29 \times 10^6$	$4.50 \times 10^7$	$4.75 \times 10^6$
agn2	$1.24 \times 10^7$	$1.41 \times 10^7$	$1.47 \times 10^7$
agn3	$3.12 \times 10^7$	$4.36 \times 10^7$	$4.64 \times 10^7$

Table 14: Cross Correlation values for the Australian sub-array array for a 12hr observation

Dec	-30°	-55°	-80°
Source			
agn1	$3.29 \times 10^6$	$3.13 \times 10^6$	$3.04 \times 10^6$
agn2	$1.03 \times 10^7$	$1.00 \times 10^7$	$9.69 \times 10^6$
agn3	$3.66 \times 10^7$	$3.76 \times 10^7$	$3.66 \times 10^7$

Table 15: Cross Correlation values for the Australian sub-array - New Zealand array for a 12 hr observation

Dec	-30°	-55°	-80°
Source			
agn1	$2.61 \times 10^6$	$2.94 \times 10^6$	$2.61 \times 10^6$
agn2	$9.43 \times 10^6$	$9.81 \times 10^6$	$8.61 \times 10^6$
agn3	$3.43 \times 10^7$	$3.55 \times 10^7$	$3.31 \times 10^7$

Table 16: Cross Correlation values for the Australian sub-array - New Zealand - Antarctica array for a 12hr observation

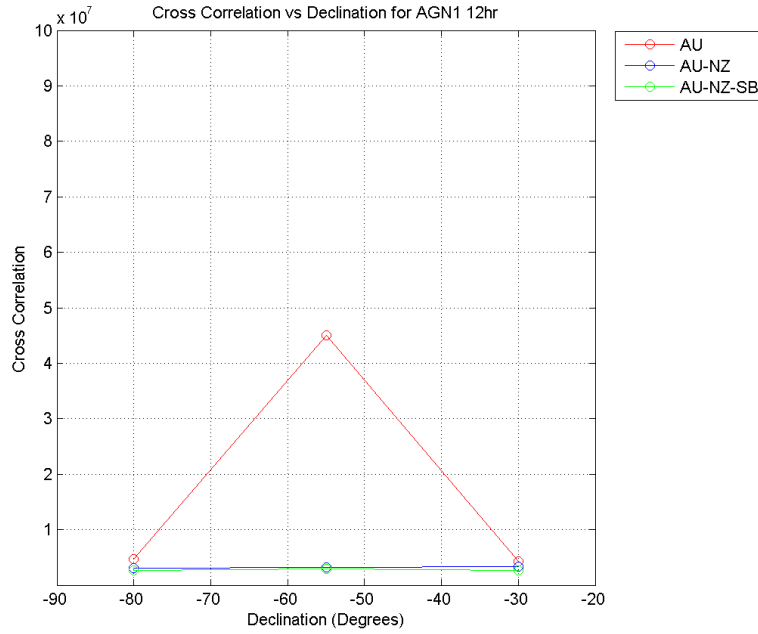


Figure 46: Comparison of the 2-D cross-correlation value with the modelled 12hr observations for source AGN1 against declination for the different arrays

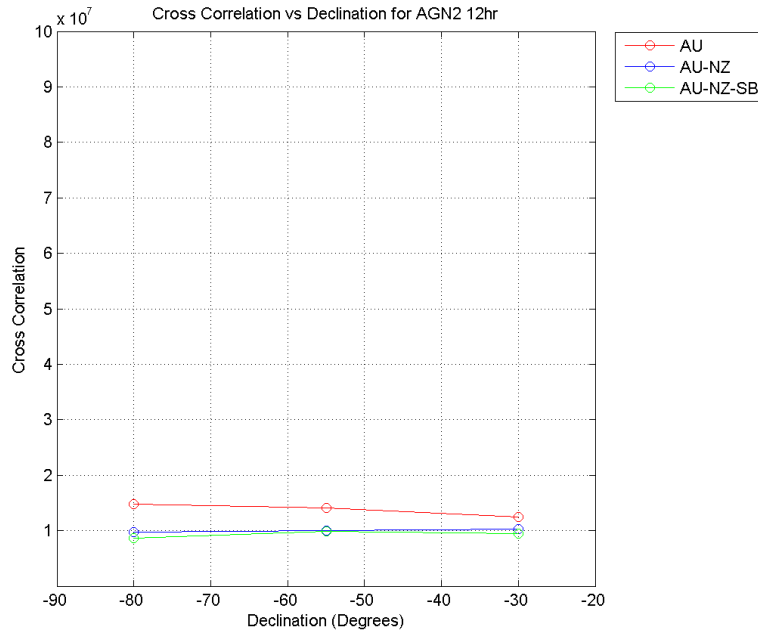


Figure 47: Comparison of the 2-D cross-correlation value with the modelled 12hr observations for source AGN2 against declination for the different arrays

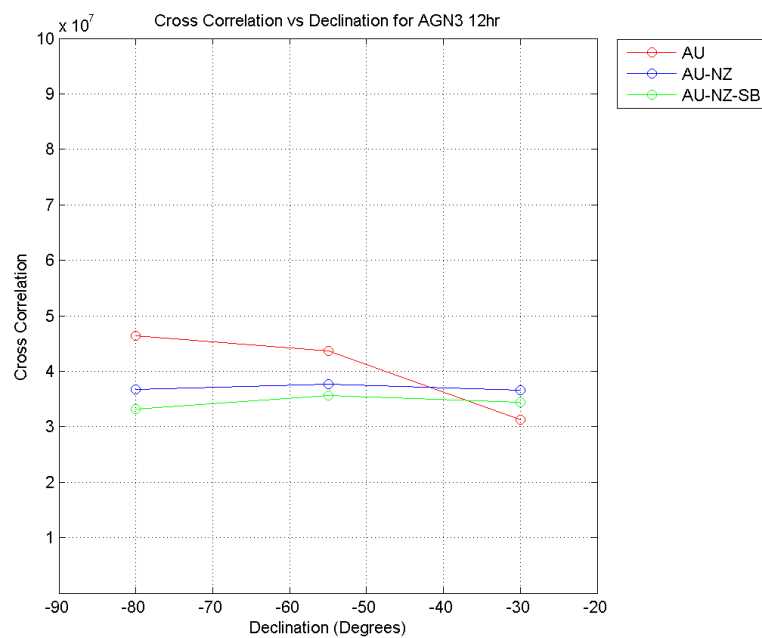


Figure 48: Comparison of the 2-D cross-correlation value with the modelled 12hr observations for source AGN3 against declination for the different arrays

### 3.7.4. Normalized 2-D Cross-Correlation

Comparison of the input model images and output CLEAN images reveals that the observational and image processing functions result in a notable maximum peak amplitude decrease. It is further observed that the degree of decrease varies between the different modelled artificial observations. The **xcorr2** MATLAB function examined above is not normalized and accordingly may not be coping well with these level shifts. Some method of normalization is required to be able to correctly match the images, this is achieved by the Normalized 2-D Cross Correlation as given by equation (3.21) (Gonzalez and Woods 2002).

$$\gamma(u, v) = \frac{\sum_{x,y} [f(x, y) - \bar{f}_{u,v}][t(x-u, y-v) - \bar{t}]}{\sqrt{\sum_{x,y} [f(x, y) - \bar{f}_{u,v}]^2 \sum_{x,y} [t(x-u, y-v) - \bar{t}]^2}} \quad (3.21)$$

Where  $f$  is the model image,

$\bar{t}$  is the average value of the pixels in CLEAN image  $t$ ,

$\bar{f}_{u,v}$  is the mean of  $f(x, y)$  in the region coincident with the current location of  $t$ ,

The summations are taken over the coordinates common to both  $f$  and  $t$ .

The MATLAB function **normxcorr2** has been investigated as it closely follows equation (3.21), how this is implemented in MATLAB to provide a “fast” algorithm is discussed in (Lewis 1995) where it was applied by the film industry for special effects image processing. In what follows  $f$  is the model image and  $t$  is the CLEAN image. The matrix  $f$  must be larger than the matrix template  $t$  for the normalization to be meaningful so  $f$  has been expanded, the extended area filled with zero pixel values. The resulting matrix  $C$  contains the correlation coefficients, which can range in value from -1.0 to 1.0, independent of scale changes in amplitude (pixel value) of  $f$  and  $t$ .

The Normalized 2-D Cross-Correlation values in Table 17 to Table 19 have been plotted for each array and each model source (AGN1, AGN2 and AGN3) in Figure 49 to Figure 51 by declination. For each model source the Normalized 2-D Cross-Correlation values improve from AU, AU-NZ to finally AU-NZ-SB, in agreement with a visual comparison of the CLEAN images in Sections 4.1.1, 4.2.1 and 4.3.1.

There is a discrepancy between the Normalized 2-D Cross-Correlation values with a visual comparison of the CLEAN images for the AU array with model sources AGN1 and AGN2 where the CLEAN image at declination  $-30^\circ$  would appear to be superior to the image at declination  $-80^\circ$ . It should be noted that these model sources would not be resolved with this array.

It also should be noted that the values improve between the model sources from AGN1 (smaller source) to AGN3 (larger source) for each individual array. For example with model source AGN1 the AU array has values in the approximate range 0.55 - 0.66, then with AGN2 the range is between 0.77 - 0.84 and finally for AGN3 the range is 0.90 - 0.91.

The MATLAB script used is provided in Appendix F.



Declination	-30°	-55°	-80°
Source			
agn1	0.69	0.69	0.67
agn2	0.86	0.85	0.84
agn3	0.88	0.94	0.94

Table 17: Normalized 2-D Cross-Correlation for Australian sub-array with 12hr observation

Declination	-30°	-55°	-80°
Source			
agn1	0.85	0.87	0.878
agn2	0.95	0.96	0.96
agn3	0.98	0.97	0.98

Table 18: Normalized 2-D Cross-Correlation values for the Australian sub-array - New Zealand array with a 12hr observation

Declination	-30°	-55°	-80°
Source			
agn1	0.95	0.96	0.95
agn2	0.98	0.98	0.98
agn3	0.96	0.93	0.97

Table 19: Normalized 2-D Cross-Correlation values for the Australian sub-array - New Zealand - Scott Base array with a 12hr observation

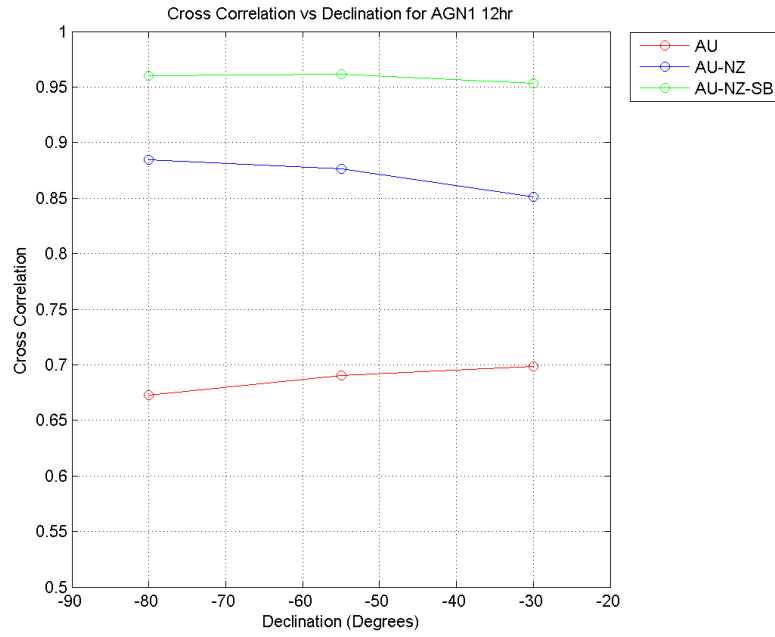


Figure 49: For AGN1 a plot of the normalized cross-correlation value vs. declination for each array with the 12hr observation

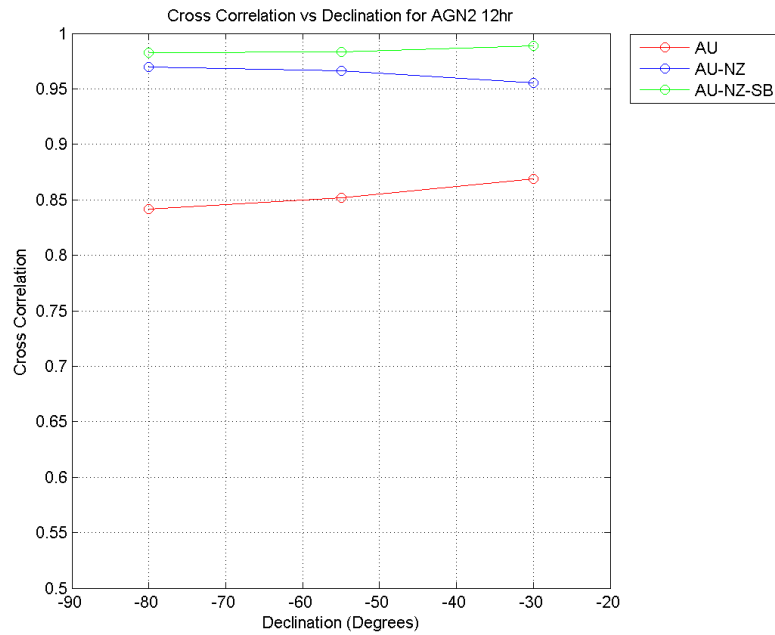


Figure 50: For AGN2 a plot of the normalized cross-correlation value vs. declination for each array with the 12hr observation

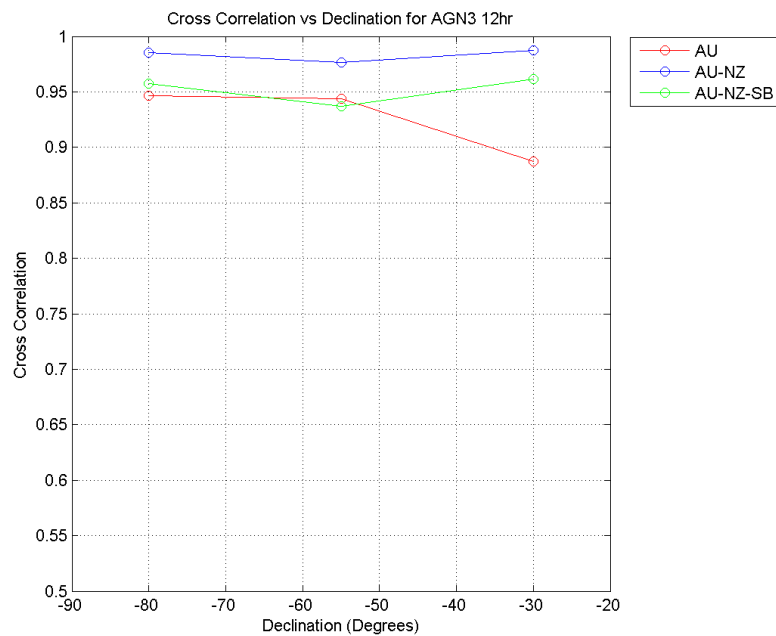


Figure 51: For AGN3 a plot of the normalized cross-correlation value vs. declination for each array with the 12hr observation

### 3.7.5. Figure of Merit Summary

All discussions and comparisons between the different methods presented in this section “3.7 Figure of Merit” except “Full Width to Half Maximum Intensity” have used data derived from 12hr observations of model sources AGN1, AGN2 and AGN3 with arrays AU, AU-NZ and AU-NZ-SB; thus allowing comparison.

From the previous sections various methods have been investigated to try and provide a quantifiable measure to compare the final CLEAN image in a consistent manner. It has been demonstrated that the different methods of “Mean Square Error” and “2-D Cross-Correlation” are not consistent with a visual inspection of the CLEAN images and further that due to their un-normalized nature it is impossible to use the values in comparing different arrays.

The “Normalized 2-D Cross-Correlation” values compare well with a visual inspection of image quality for the final CLEAN images. This measure also has the desirable feature of being normalized (the resulting value will be between -1.0 and 1.0) so can more readily be used to compare the different observations modelled. Thus we propose that the Normalized 2-D Cross-Correlation value can be used as a quantitative measure to compare different model sources and arrays. This value can be used with some confidence in comparing arrays and model source to CLEAN image, provided that common sense still prevails about comparing sources for arrays that would be unable to resolve the model source.

### **3.8.Noise and Errors Modelled**

For two or more antennae very far apart as in VLBI, each will experience very different atmospherics and during the course of an observation phases can move slightly. To attempt to reproduce this in MIRIAD it is possible to include other errors through such factors as antenna gain noise, antenna based phase noise and total power variations. If time had allowed, it would have been interesting to investigate the reduced dynamic range of the final CLEAN images due to the effect of noise and errors. For a more detailed discussion on this subject we refer the reader to (Perley 1999).

The only noise and error parameters used in the modelling of this work were the system sensitivity and antenna system temperature, the system sensitivity being included by default in MIRIAD. The system sensitivity was not set for the MIRIAD UVGEN task the default value used is  $12.7 \text{ Jy K}^{-1}$ , which is a typical value for the Hat Creek 6.1m antennas that represents a conservative value. For the antenna system temperature looking through the MIRIAD antenna file a value of 300 K was selected as a very conservative value based on data from Hat Creek and Hobart. For modern antennae with cryogenically cooled receivers system temperatures should be down in the 30-50 K range or lower.

These values were then used in MIRIAD to introduce some element of noise and error as would be experienced in real observations.

## **4. Simulation Model Results and Discussion**

This Chapter reports on the results of the simulation process described in Chapter 3, with the antenna array configurations defined in Section 3.2.1 and the model sources in Section 3.4.1.

The first three parts present the results for modelling the VLBI arrays Australian sub-array, Australian sub-array – New Zealand and finally Australian sub-array – New Zealand – Scott Base. Following the results are tables presenting the Normalized 2-D Correlation Figure of Merit for each array, observation time and source. At the end of each of these sections is a discussion and review of the results obtained.

These first three sub-sections are followed by a short section comparing the results for the above modelled scenarios.

The final part of this Chapter deals with the results for the SKA phased building model. This section deals with a comparison between two different scenarios for building the SKA, and the results for each scenario are presented. This section concludes with a summary and comparison of these two scenarios.

#### 4.1. Australian sub-array Only Array

For the Australian sub-array (as defined in Section 3.2.1) a plot of the source sky visibility vs. declination was generated and is presented in Figure 52. This shows the range of declinations a source will be visible to the whole array. This was calculated using a source RA of 0.0 hrs and date 2000-1-1; it has also been assumed that the antennae can track from horizon to horizon.

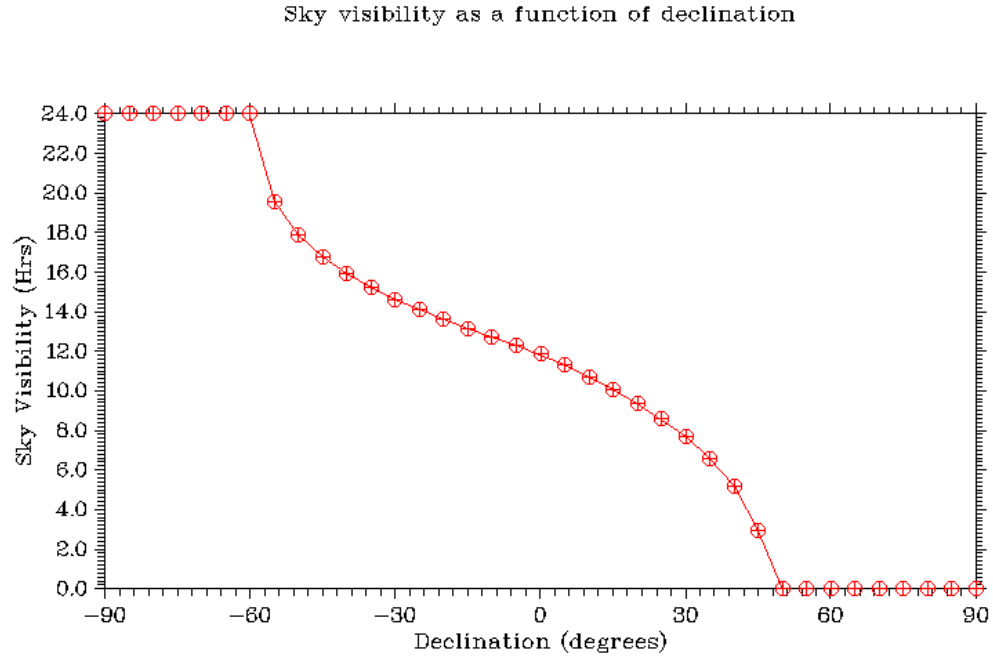


Figure 52: Sky Visibility vs. Declination for Australian sub-array antennas. The array is defined in 3.2.1. Note that it does not include Ceduna.

From the Sky Visibility plot in Figure 52 it can be seen that the antennae in this array have greater than 4 hrs visibility of the source between  $-90^{\circ}$  to  $40^{\circ}$  declination at RA of 0.0 hrs. From this plot we can determine a set of declinations to work with for this array, and by comparing the same plot for the other arrays a common set of declinations across all arrays to be modelled can be selected for a true comparison.



From the Sky Visibility plot in Figure 52 and the comparable plots for the other arrays in Figure 60 and Figure 68 the following Declinations were selected  $-80^\circ$ ,  $-55^\circ$  and  $-30^\circ$  as these will have 12hrs visibility of a source at Dec  $-80$ , RA 0hrs and are evenly spaced. Also a set of declinations where selected at  $10^\circ$ ,  $-20^\circ$ ,  $-50^\circ$  and  $-80^\circ$  for the minimum of 4hr visibility (this being the minimum defined in the SKA requirements).

#### **4.1.1. Simulation Results**

On each of the following pages is a set of plots and images for a defined observation period 12hrs or 4 hrs and declination. At the top of each page are two plots of the  $u,v$  coverage of the array. The left hand  $u,v$  plot is to the baseline scale of the array, the right hand  $u,v$  plot is to the baseline scale of the largest array of antennae modelled for comparison. Below these on the left are the model source images for comparison and on the right are the final CLEAN images from DIFMAP, top to bottom for sources AGN1, AGN2 and AGN3. These CLEAN images should be compared with the images for these model sources in Figure 25 (but which have been included on each page in the left hand column for convenience).

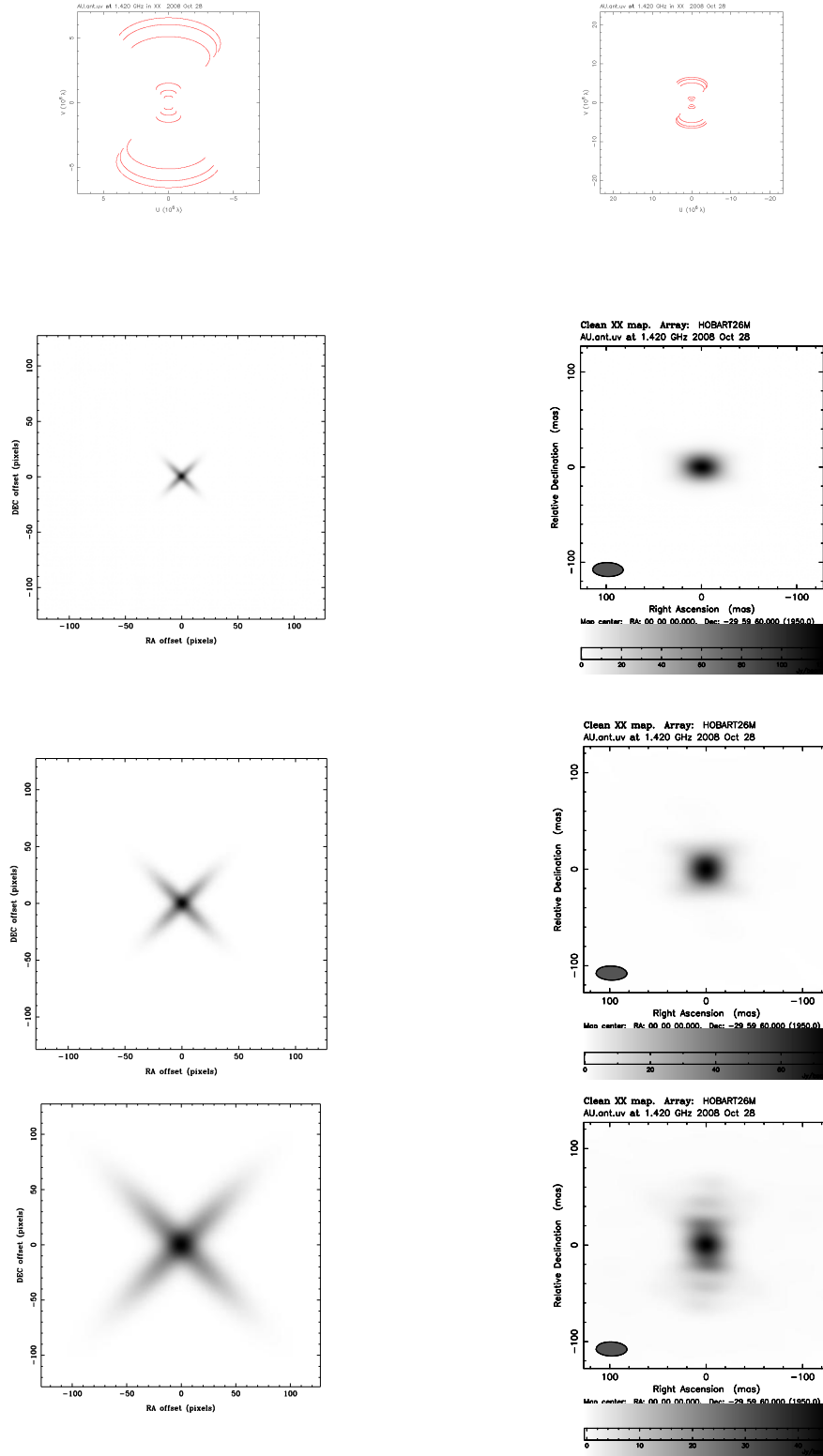


Figure 53: Australian sub-array -12 hr Integration,  $-30^\circ$  Declination

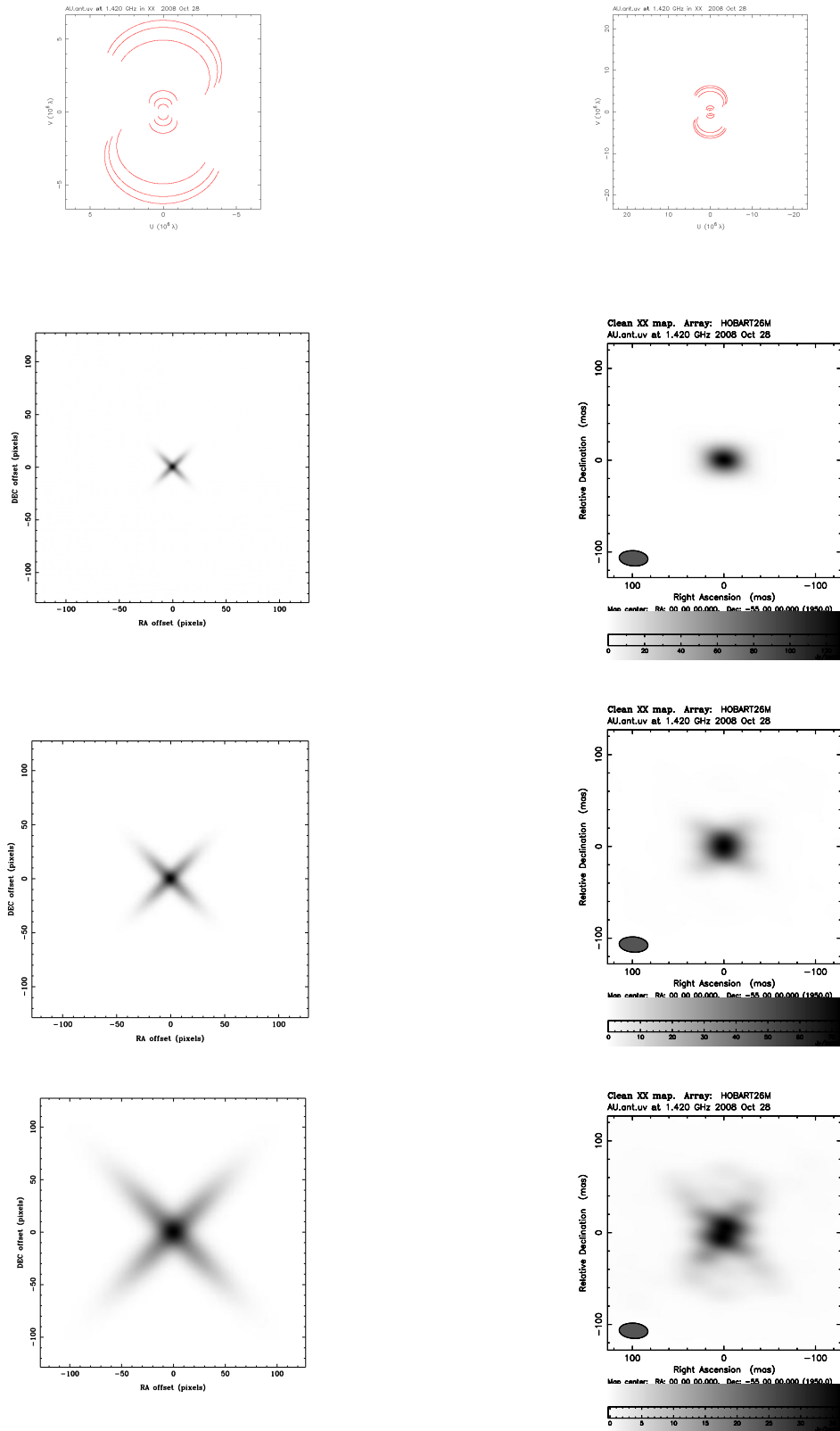


Figure 54: Australian sub-array - 12hr Integration,  $-55^\circ$  Declination

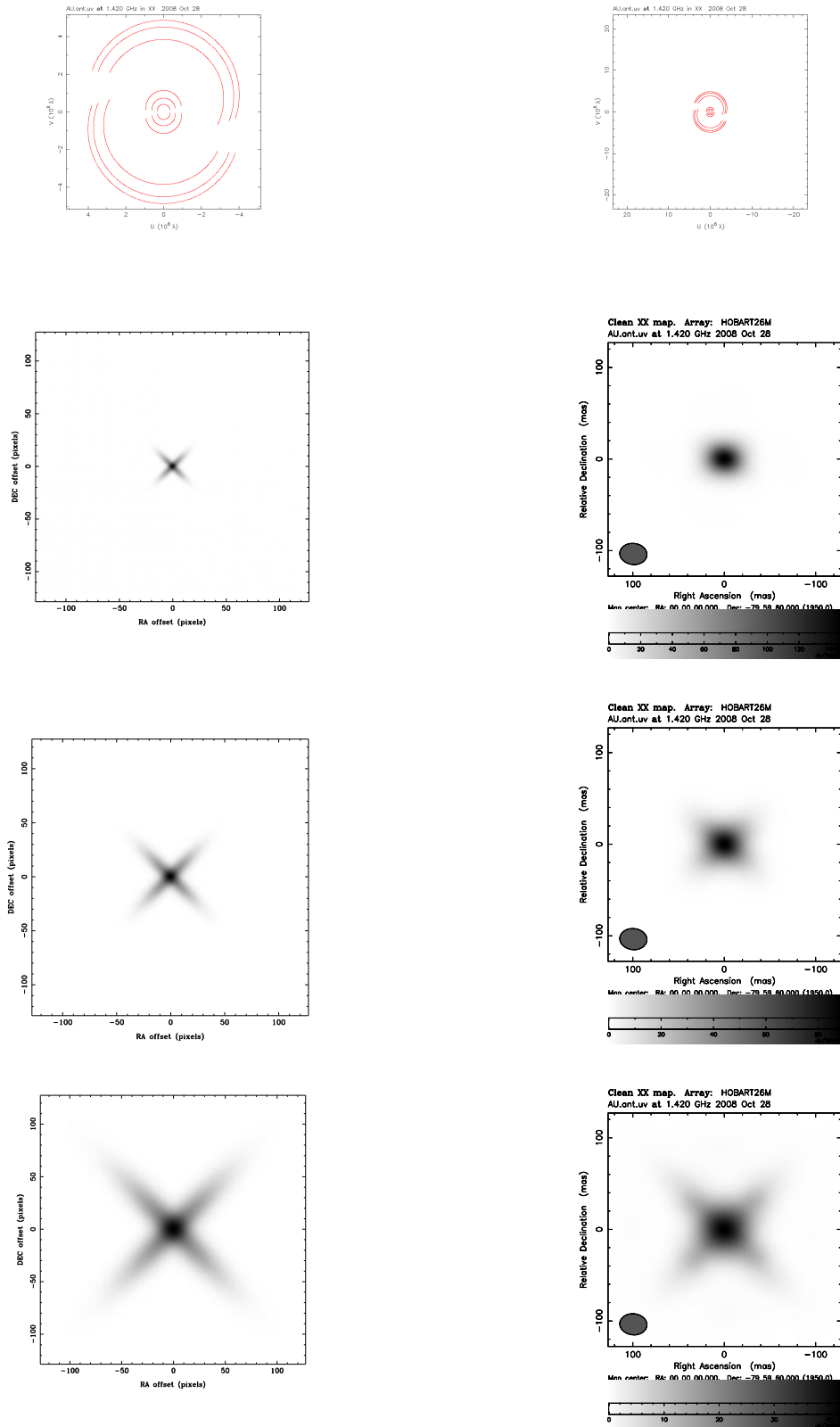


Figure 55: Australian sub-array -12hr Integration,  $-80^\circ$  Declination

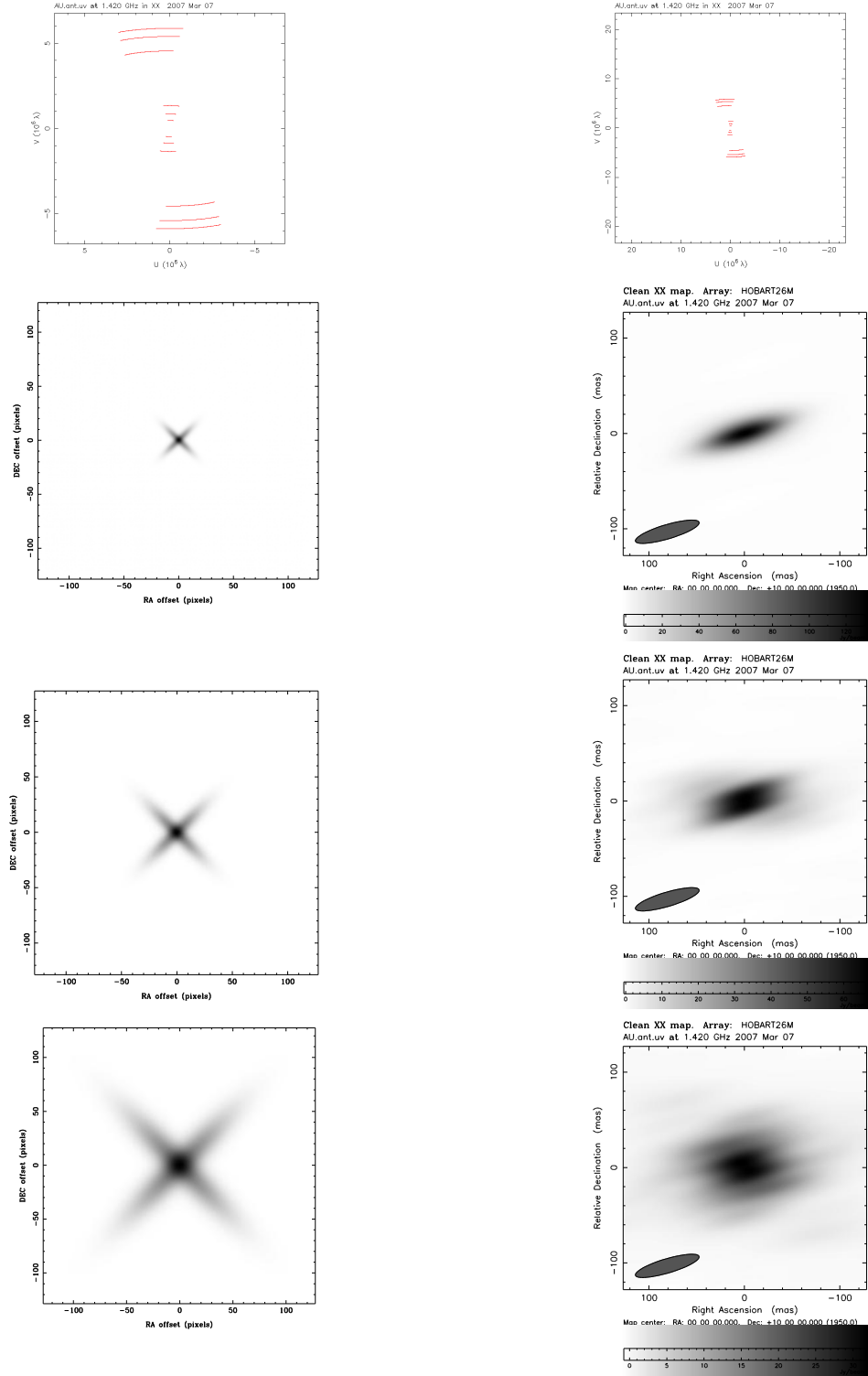


Figure 56: Australian sub-array - 4hr Integration,  $10^\circ$  Declination

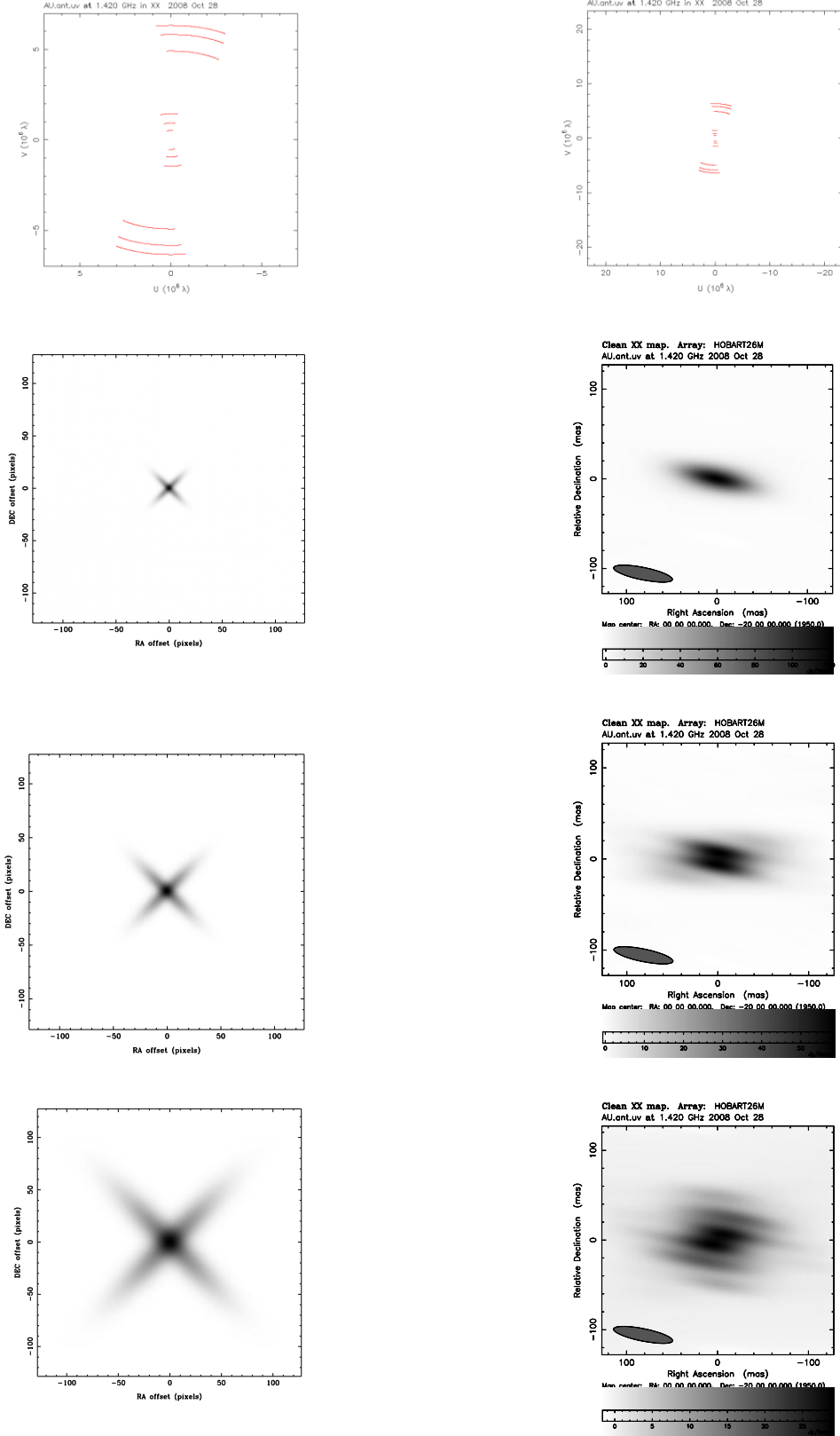


Figure 57: Australian sub-array - 4hr Integration, -20° Declination

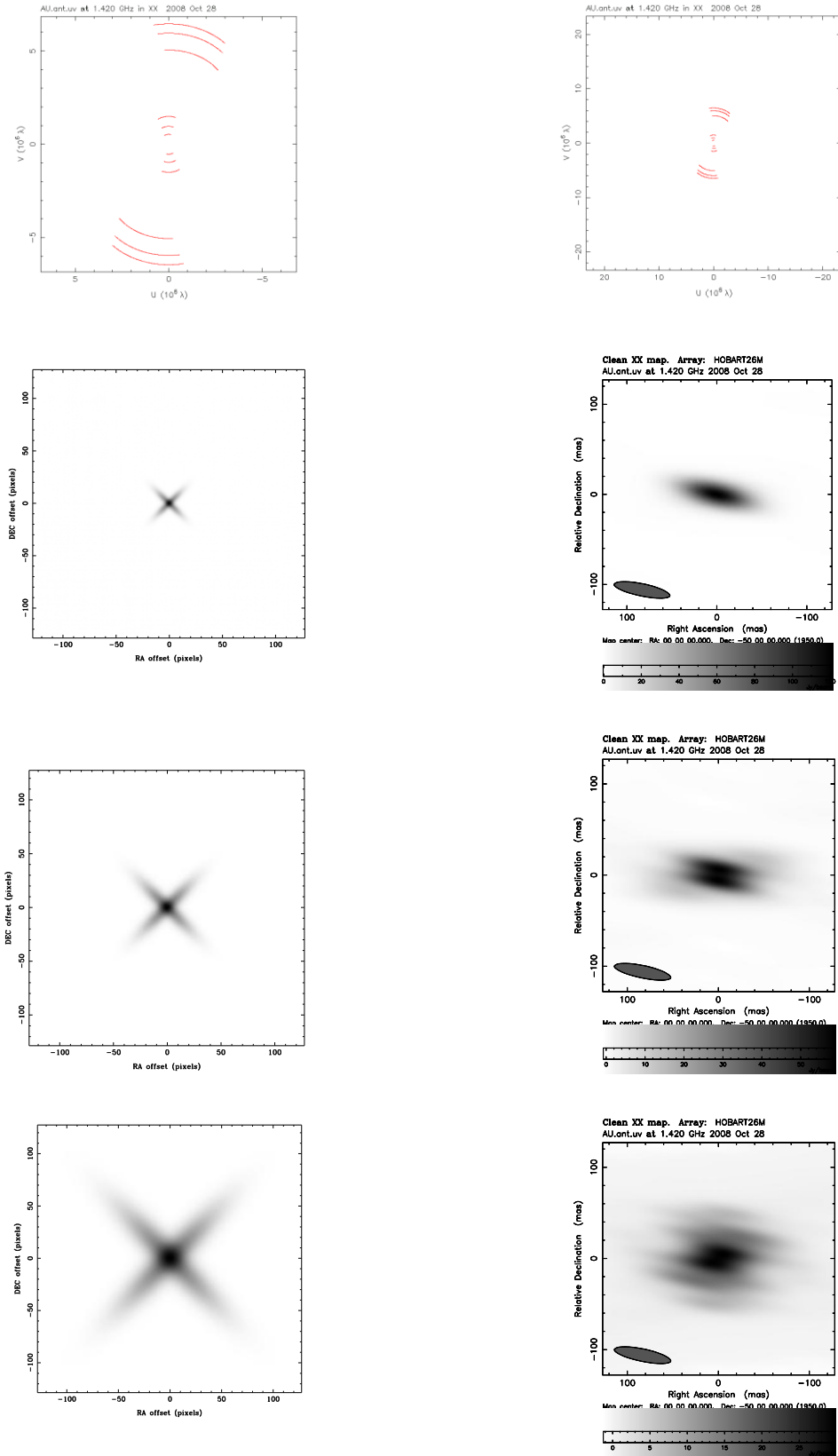


Figure 58: Australian sub-array - 4hr Integration,  $-50^\circ$  Declination



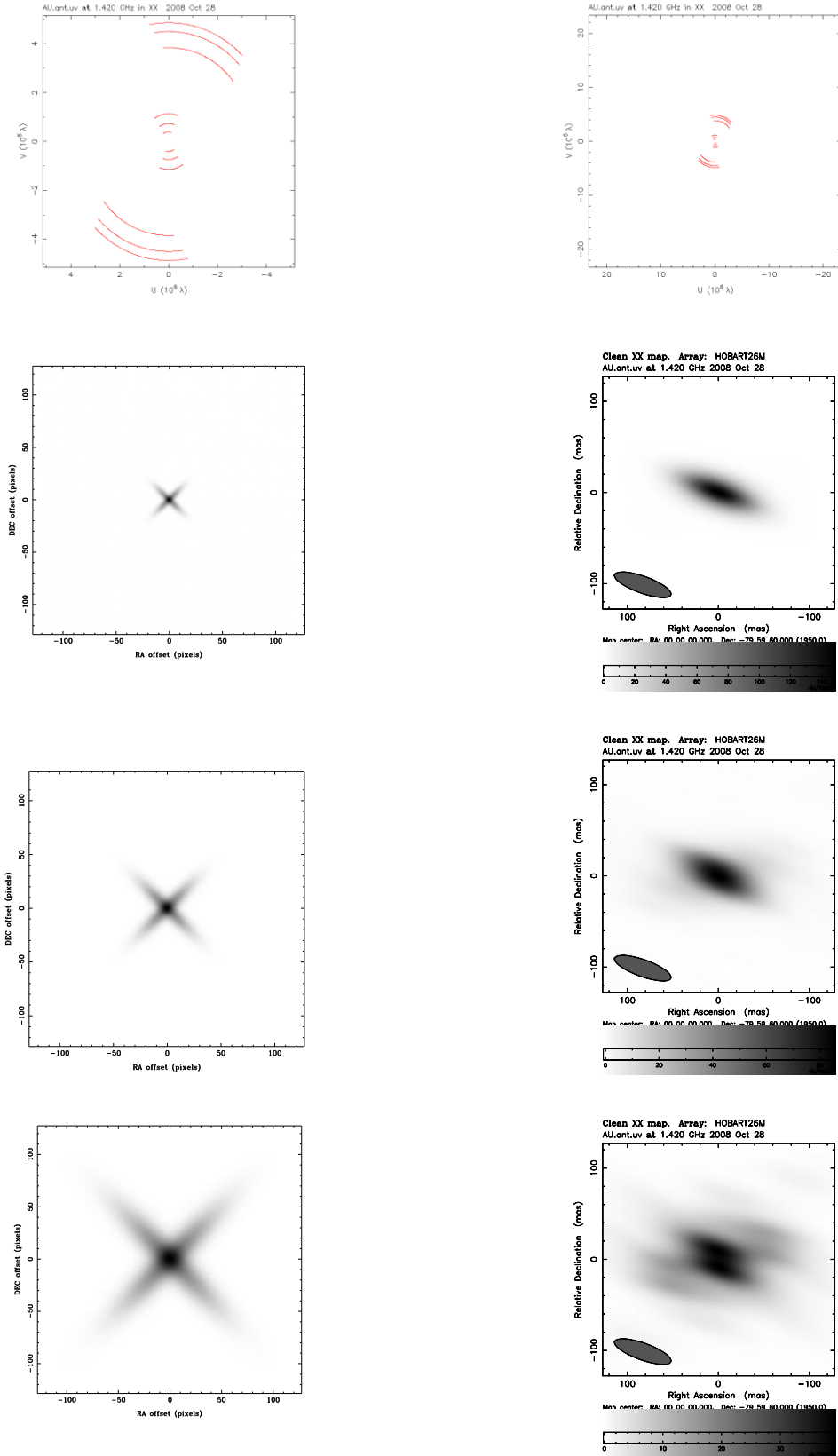


Figure 59: Australian sub-array - 4 hr Integration,  $-80^\circ$  Declination

#### **4.1.2. Analysis of Results**

For the array in Table 2 the theoretical resolution should be approximately 31 mas at 1.4 GHz. Comparing the sizes of the model sources, with this resolution we would expect that AGN2 should be partially resolved and AGN3 fully resolved. The smallest source AGN1 should not be resolved and its size and shape should be dictated by the beam shape.

#### **Simulation of a 12hr Observation**

From Figure 53 for a 12hr observation of a source at a declination of  $-30^\circ$ , it can be seen that for the smallest model source AGN1 the final clean image gives an elliptical Gaussian point source; thus the source has not been resolved. Progressing to the CLEAN image for AGN2 there is still quite a bright elliptical gaussian point source but with some fainter extended structure. Finally for AGN3 it can be seen that there is a very pronounced extended structure extending out from a bright core also other effects are apparent. Thus for AGN3 at this declination the array is able to resolve the source but due to the beam shape the true structure has not been correctly identified.

In Figure 54 for a source at a declination of  $-55^\circ$  it can be seen that the beam has become quite a pronounced ellipsoid at an angle of approximately  $315^\circ$  from the perpendicular, and the central bright point source component is quite clearly an ellipsoid for AGN1, AGN2 and AGN3. In the CLEAN image of AGN2 there is some extended X like shaped structure, but for AGN3 there is clear shape to the extended structure which has a much more pronounced X like shape.

Finally the 12hr observations in Figure 55 are for a source at a declination of  $-80^\circ$ . From the  $u, v$  plots it can be seen that the coverage of the  $u, v$  plane is more uniform than the previous two observations. The CLEAN images for AGN1 and AGN2 are very similar to Figure 54, but for AGN3 the extended structure has become a lot clearer and is approaching the input model image for AGN3.

### **Simulation of a 4hr Observation**

In Figure 56 is shown the CLEAN images for a 4hr observation of the sources at a declination of  $10^\circ$ . The  $u, v$  plots quite clearly show the difference in coverage of the  $u, v$  plane compared to the 12hr observations. This has a quite pronounced impact on the beam shape and hence the final CLEAN images. It can be seen that for AGN1 the source is quite clearly dominated by the beam shape and no extended structure can be distinguished. For AGN2 and AGN3 there is extended structure, but it bears no resemblance to the input model images.

The same holds true for the observation with the sources at a declination of  $-20^\circ$  as shown in Figure 57, also for the declination of  $-50^\circ$  observation in Figure 58. The resultant CLEAN images have no resemblance to the model images and would be of no use.

In Figure 59 for an observation with the sources at  $-80^\circ$  declination, the beam is still an ellipse but for AGN3 the extended structure has some meaningful shape compared to the model image but is quite diffuse and skewed.

### **Summary of the simulated observation**

In comparing the CLEAN images produced with the opening expectations in this section for the Australian sub-array only array, it is clear that although AGN3 was resolved the final CLEAN image is still some what diffuse. It was only for the 12hr observation at a declination of  $-80$  degrees where the  $u, v$  coverage was the most uniform that the extended structure agreed with the model source. The expectation for AGN2 with the theoretical resolution the results did not meet this expectation, although as expected no resolution of AGN1 was possible at any declination or observational period and it was in effect a point elliptical gaussian source.

Taking the CLEAN images for the 12hr observations and the model source images, then evaluating the Normalized 2-D Cross Correlation for each pair of images at the indicated declinations produces Table 20. For the 4 hr observations the Normalized 2-D Cross Correlation values are shown in Table 21.

Declination	-30°	-55°	-80°
Source			
agn1	0.69	0.69	0.67
agn2	0.86	0.85	0.84
agn3	0.88	0.94	0.94

Table 20: Normalized Cross-Correlation for Australian sub-array array with 12hr observation

Declination	10°	-20°	-50°	-80°
Source				
agn1	0.52	0.53	0.54	0.52
agn2	0.68	0.67	0.68	0.71
agn3	0.78	0.77	0.80	0.80

Table 21: Normalized Cross-Correlation for Australian sub-array array with 4hr observation

## 4.2. Australian sub-array – New Zealand Array

For the Australian sub-array – New Zealand Array (as defined in Section 3.2.1) a plot of the source sky visibility vs declination was generated and is presented in Figure 60. This shows the range of declinations a source will be visible to the whole array. This was calculated using a source RA of 0.0 hrs and date 2000-1-1. It has also been assumed that the antennae can track from horizon to horizon.

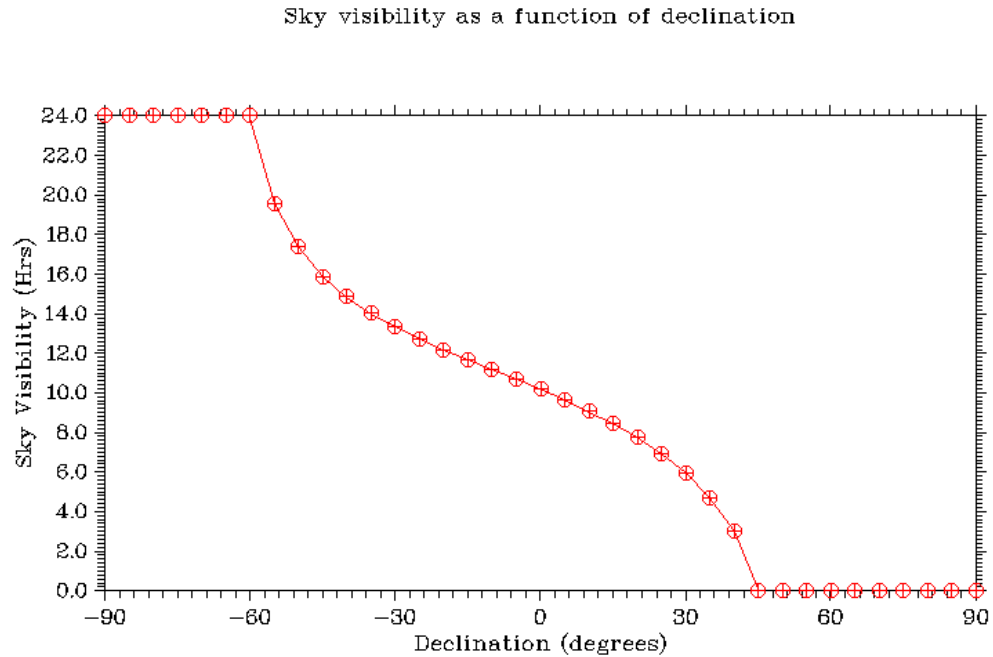


Figure 60: Sky Visibility vs. Declination for Australian sub-array & New Zealand Antennae

From the Sky Visibility plot in Figure 60 it can be seen that the antennae in this array have greater than 4 hrs visibility of the source from  $-90^{\circ}$  to  $37^{\circ}$  declination at an RA of 0.0 hrs. Using this plot as discussed at the beginning of Section 4.1 and comparing with the same plot for the other arrays a common set of declinations was selected to be used in the modelling process.

#### 4.2.1. Simulation Results

Following the order established in the previous section on each of the following pages is a set of plots and images for a defined observation period 12hrs or 4 hrs and declination. At the top of each page are two plots of the  $u,v$  coverage of the array. The left hand  $u,v$  plot is to the baseline scale of the array, the right hand  $u,v$  plot is to the baseline scale of the largest array of antennae modelled for comparison. Below these on the left are the model source images for comparison and on the right are the final CLEAN images from DIFMAP, top to bottom for sources AGN1, AGN2 and AGN3. These CLEAN images should be compared with the images for these model sources in Figure 25 which have been included on each page in the left hand column for convenience.

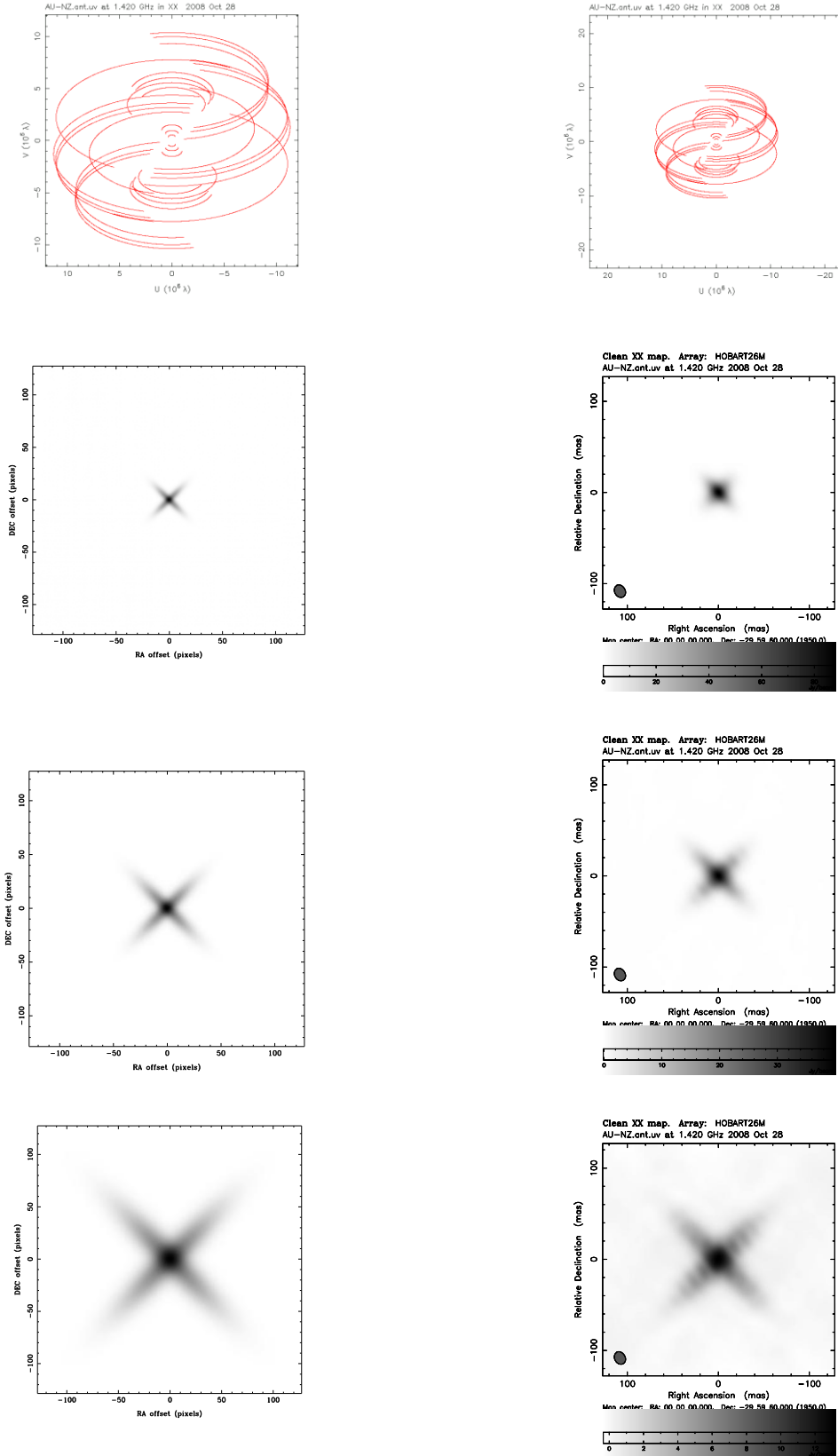


Figure 61: Australian sub-array & New Zealand – 12 hr Integration, -30° Declination

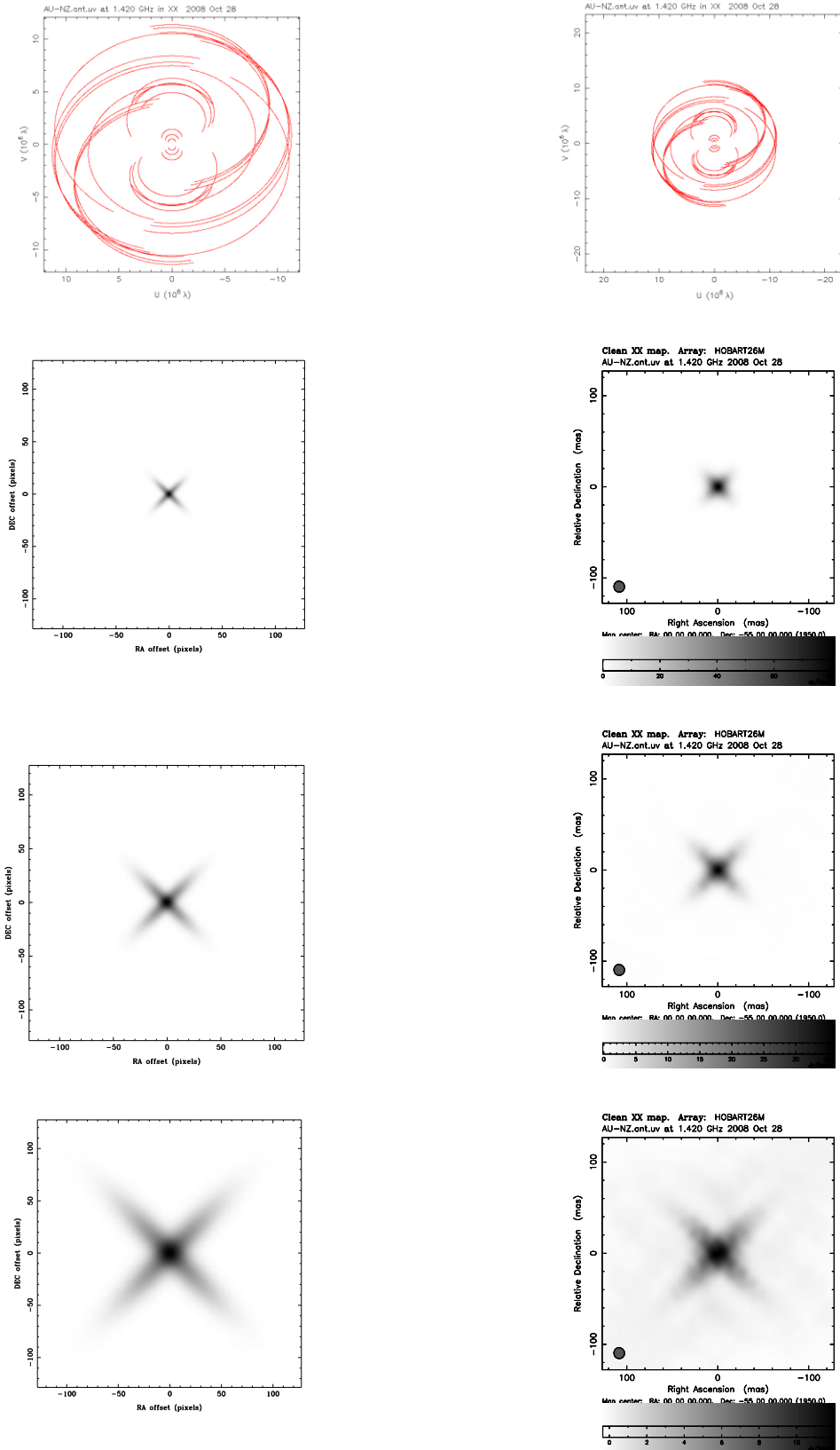


Figure 62: Australian sub-array & New Zealand – 12 hr Integration,  $-55^\circ$  Declination



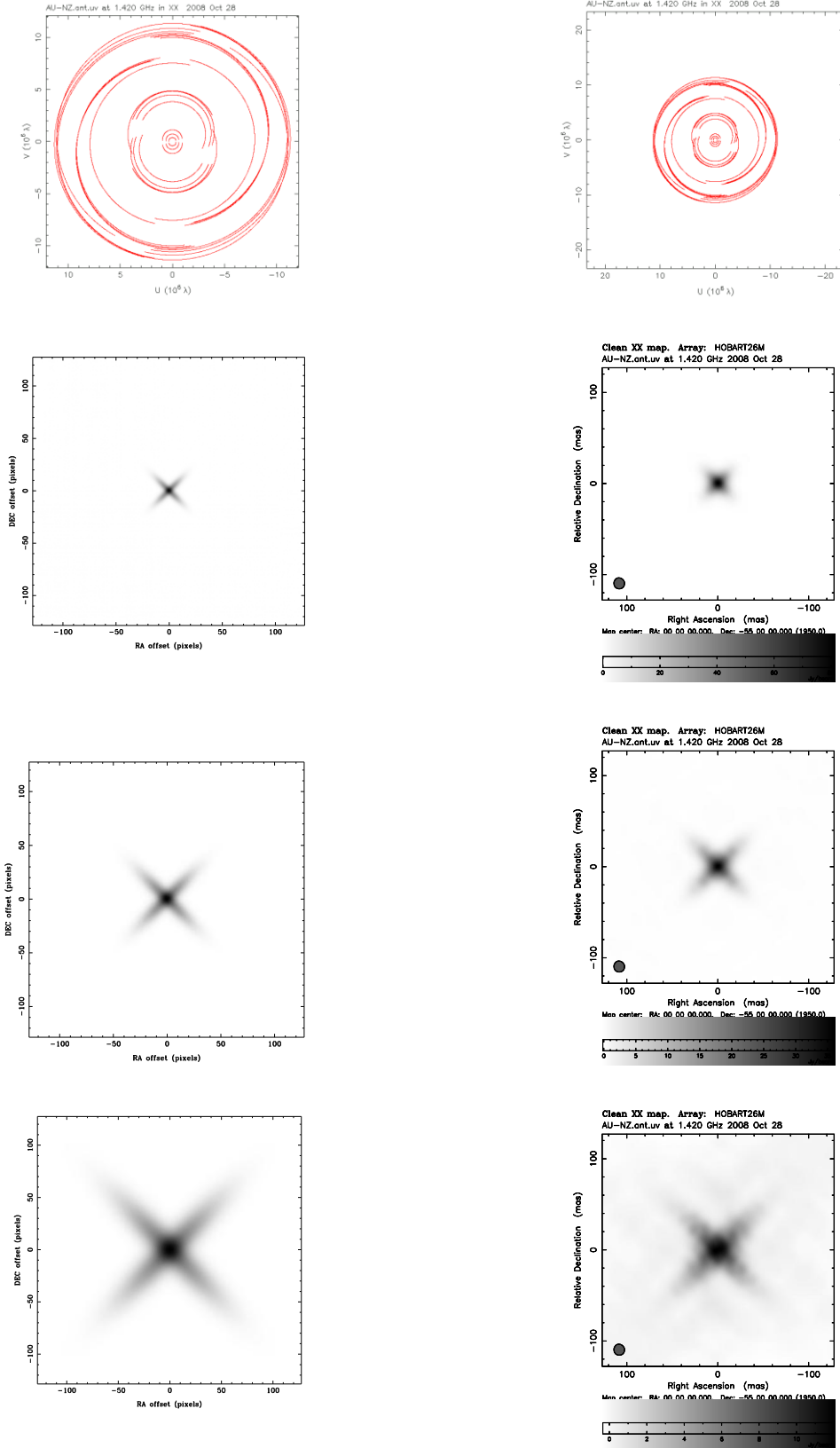


Figure 63: Australian sub-array & New Zealand – 12 hr Integration,  $-80^\circ$  Declination

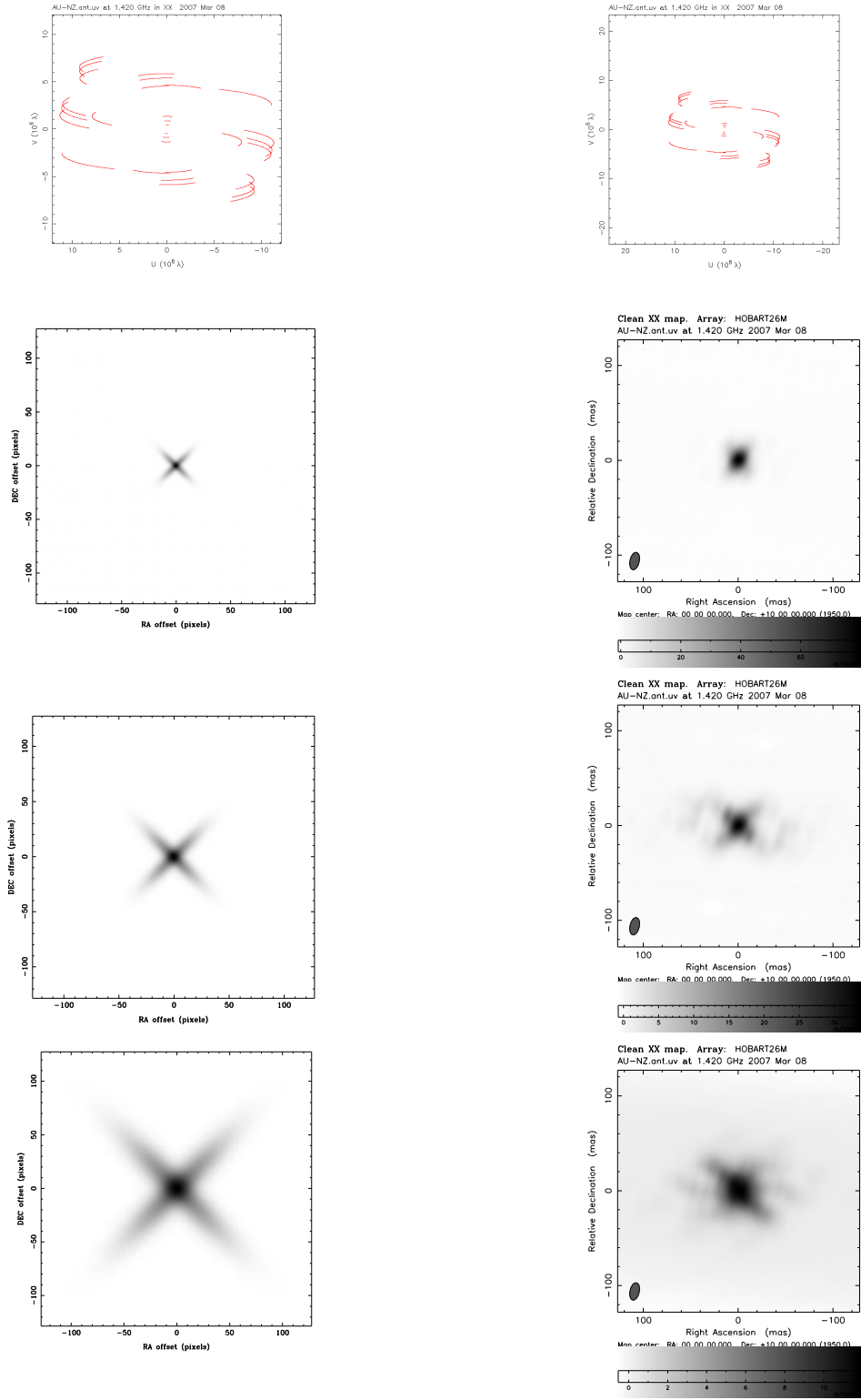


Figure 64: Australian sub-array & New Zealand – 4 hr Integration,  $10^\circ$  Declination

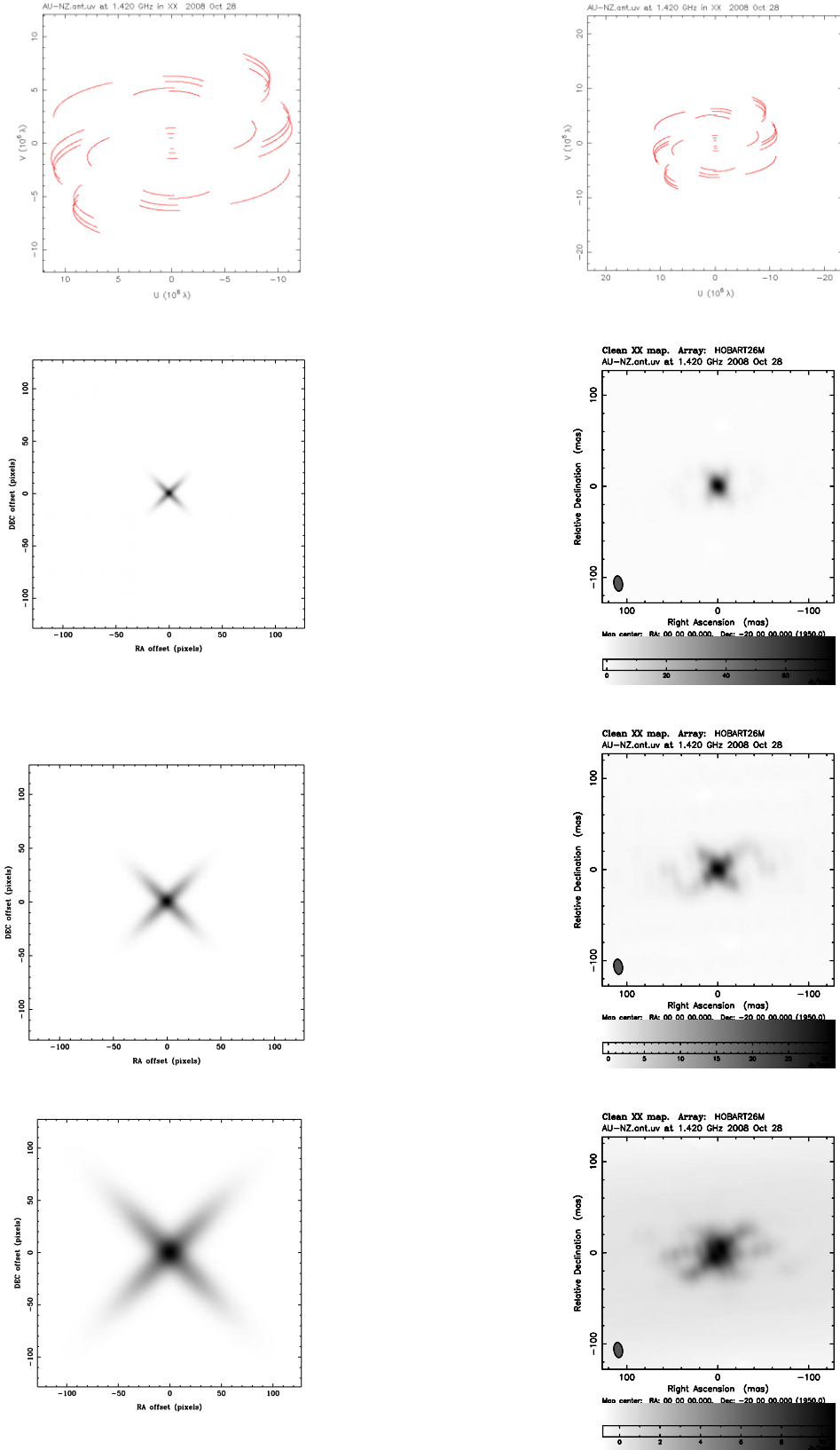


Figure 65: Australian sub-array & New Zealand – 4 hr Integration,  $-20^\circ$  Declination

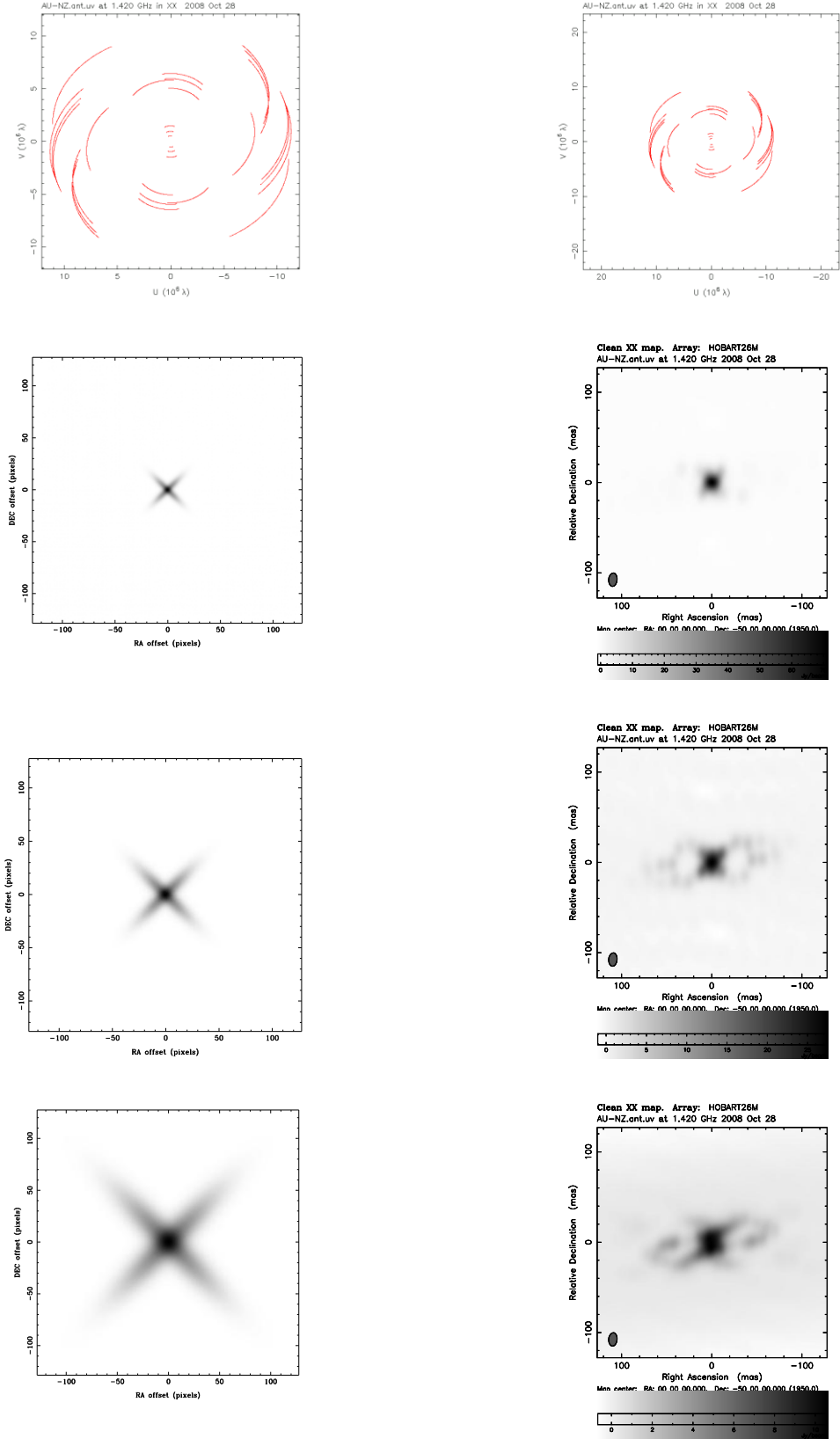


Figure 66: Australian sub-array & New Zealand – 4 hr Integration,  $-50^\circ$  Declination

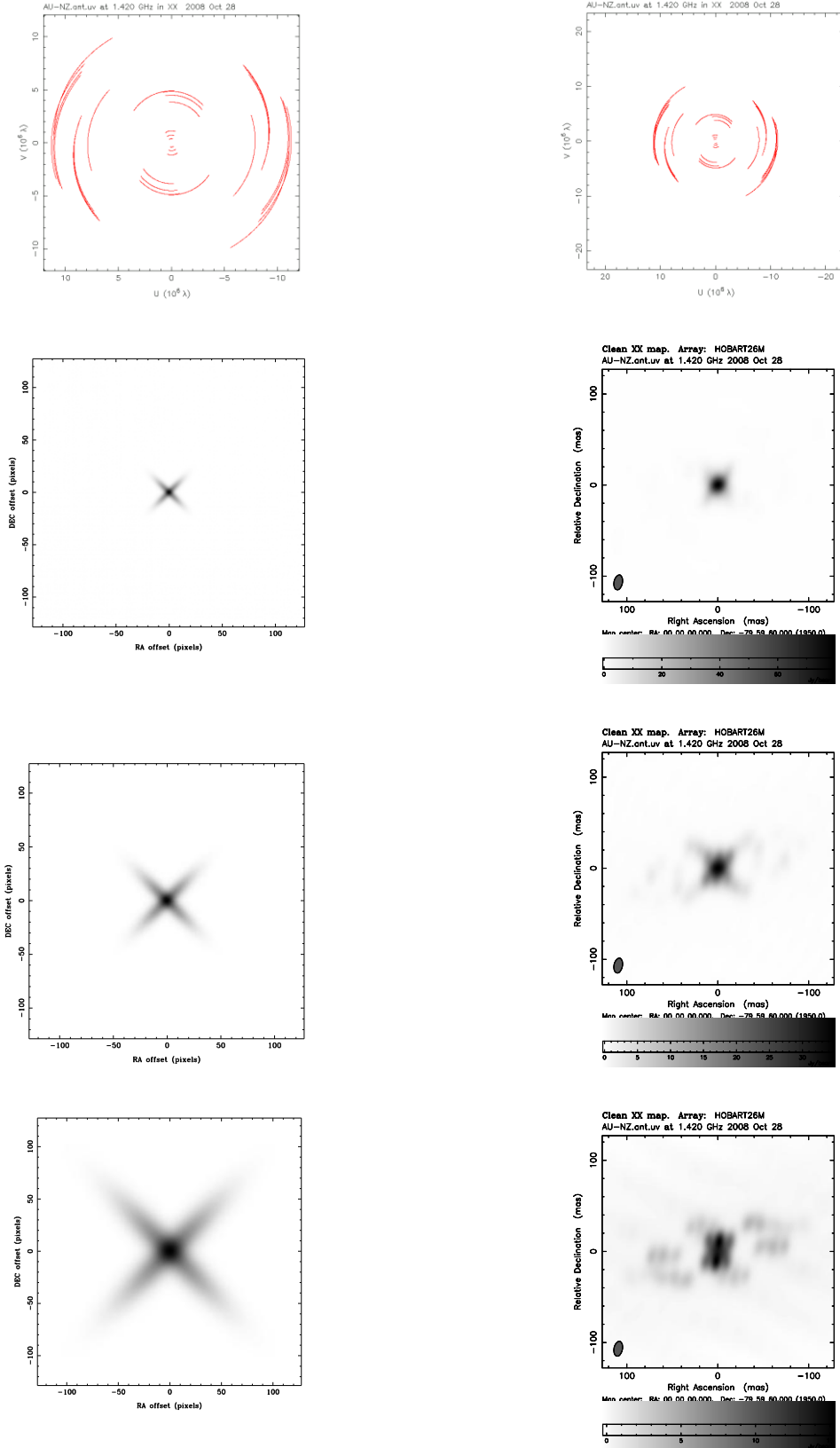


Figure 67: Australian sub-array & New Zealand – 4 hr Integration,  $-80^\circ$  Declination

#### **4.2.2. Analysis of Results**

For this array from Table 2 the theoretical resolution should be approximately 18 mas at 1.4 GHz. Comparing the sizes of the model sources, AGN3 should be fully resolved. For source AGN2 there should be partial resolution for the smaller components and the larger components will be fully resolved. For the smallest source AGN1 there should be some partial resolution of the large components in AGN1 but not of the smaller components.

#### **Simulation of a 12hr Observation**

We see results in Figure 61 for an observation with this array with the sources at a declination of  $-30^\circ$ . Immediately it can be seen that the  $u, v$  coverage is more complete than for the Australian sub-array only. The CLEAN image for AGN3 quite clearly shows an X, this is also true for AGN2 and AGN1 which show some X shaped extended structure. The beam shape is slightly oval but small and compact compared to the model sources. All three sources have clearly been resolved and the structure is quite clearly discernable. Between the different source declinations presented in Figure 61 to Figure 63 there is little difference for AGN1 and AGN2. For AGN3 a visual comparison shows the CLEAN image at a declination of  $-80^\circ$  to be the best image, with the poorest being at  $-55^\circ$ .

#### **Simulation of a 4hr Observation**

For this set of observations we have a very noticeable degradation in the final CLEAN image quality.

First looking at Figure 64 for the sources at a declination of  $10^\circ$  it can be seen for AGN1 that extended structure has become blurred and the shape lost compared to the previous set of 12hr observations. For the sources AGN2 and AGN3 the shape of the extended structure has been completely lost compared to the model image. For a declination of  $-20^\circ$ , the extended structure for AGN2 and AGN3 becomes discernable.

At declination  $-50^\circ$  Figure 66 the CLEAN image for AGN3 has an extended structure and appears to be a bared spiral. For AGN2 and AGN1 there is some extended structure with a X like shape, for AGN2 we see other artifacts appearing.

For a declination of  $-80^\circ$  Figure 67 there is structure to AGN3 but it does not match the model image, also other artifacts are appearing. For AGN2 and AGN1 there is some extended structure with a X like shape that compares with the model image in shape and size.

### **Summary of the simulated observation**

The CLEAN image quality and resolution for AGN1 with the 12 hr observation was better than expected. For all three sources the best images were obtained for the 12hr observation at declination  $-80^\circ$  as has now come to be expected due to the even  $u, v$  coverage. Again we see that the difference in image quality and resolution is very significant between 12hr and 4hr observations.

Taking the CLEAN images for the 12hr observations and the model images and calculating the Normalized 2-D Cross Correlation for each pair of images at the declinations produces Table 22. For the 4 hr observations the Normalized 2-D Cross Correlation values are shown in Table 23.

Declination	-30°	-55°	-80°
Source			
agn1	0.85	0.87	0.88
agn2	0.95	0.96	0.96
agn3	0.98	0.97	0.98

---

Table 22: Normalized Cross-Correlation values for the Australian sub-array - New Zealand array with a 12hr observation

Declination	10°	-20°	-50°	-80°
Source				
agn1	0.82	0.84	0.85	0.84
agn2	0.92	0.93	0.91	0.93
agn3	0.92	0.89	0.86	0.84

---

Table 23: Normalized Cross-Correlation values for the Australian sub-array - New Zealand array with a 4hr observation



### 4.3. Australian sub-array – New Zealand – Scott Base

For the Australian sub-array – New Zealand – Scott Base Array (as defined in Section 3.2.1) a plot of the source sky visibility vs. declination was generated and is presented in Figure 68. This shows the range of declinations a source will be visible for the whole array. This was calculated using a source RA of 0.0 hrs and date 2000-1-1. It has been assumed that the antennae can track from horizon to horizon.

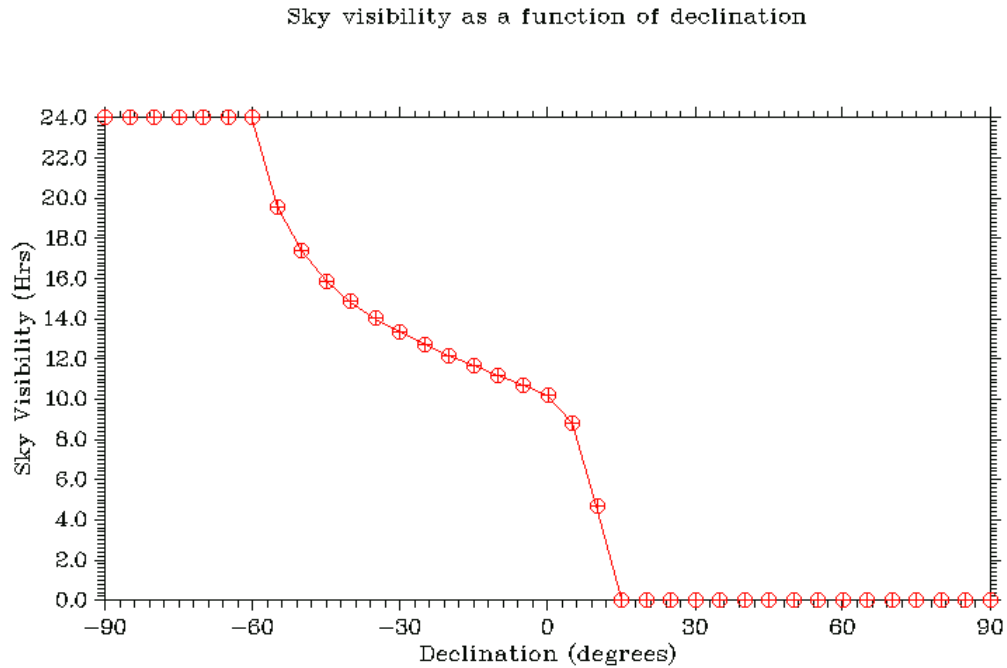


Figure 68: Sky Visibility vs. Declination for Australian sub-array, New Zealand & Scott Base Antennae

From the Sky Visibility plot in Figure 68 it can be seen that the antennae in this array have greater than 4 hrs visibility of the source between  $-90^{\circ}$  to  $10^{\circ}$  declination at RA of 0.0 hrs. Using this plot as discussed at the beginning of Section 4.1 and comparing with the same plot for the other arrays a common set of declinations was selected to be used in the modelling process.

#### 4.3.1. Simulation Results

On each of the following pages is a set of plots and images for a defined observation period 12hrs or 4 hrs and declination. At the top of each page are two plots of the  $u,v$  coverage of the array. The left hand  $u,v$  plot is to the baseline scale of the array, the right hand  $u,v$  plot is to the baseline scale of the largest array of antennae modelled for comparison. Below these on the left are the model source images for comparison and on the right are the final CLEAN images from DIFMAP, top to bottom for sources AGN1, AGN2 and AGN3. These CLEAN images should be compared with the images for these model sources in Figure 25 which have been included on each page in the left hand column for convenience. On these following figures the term Australia in the caption indicates the Australian sub-array as defined in Section 3.2.1.

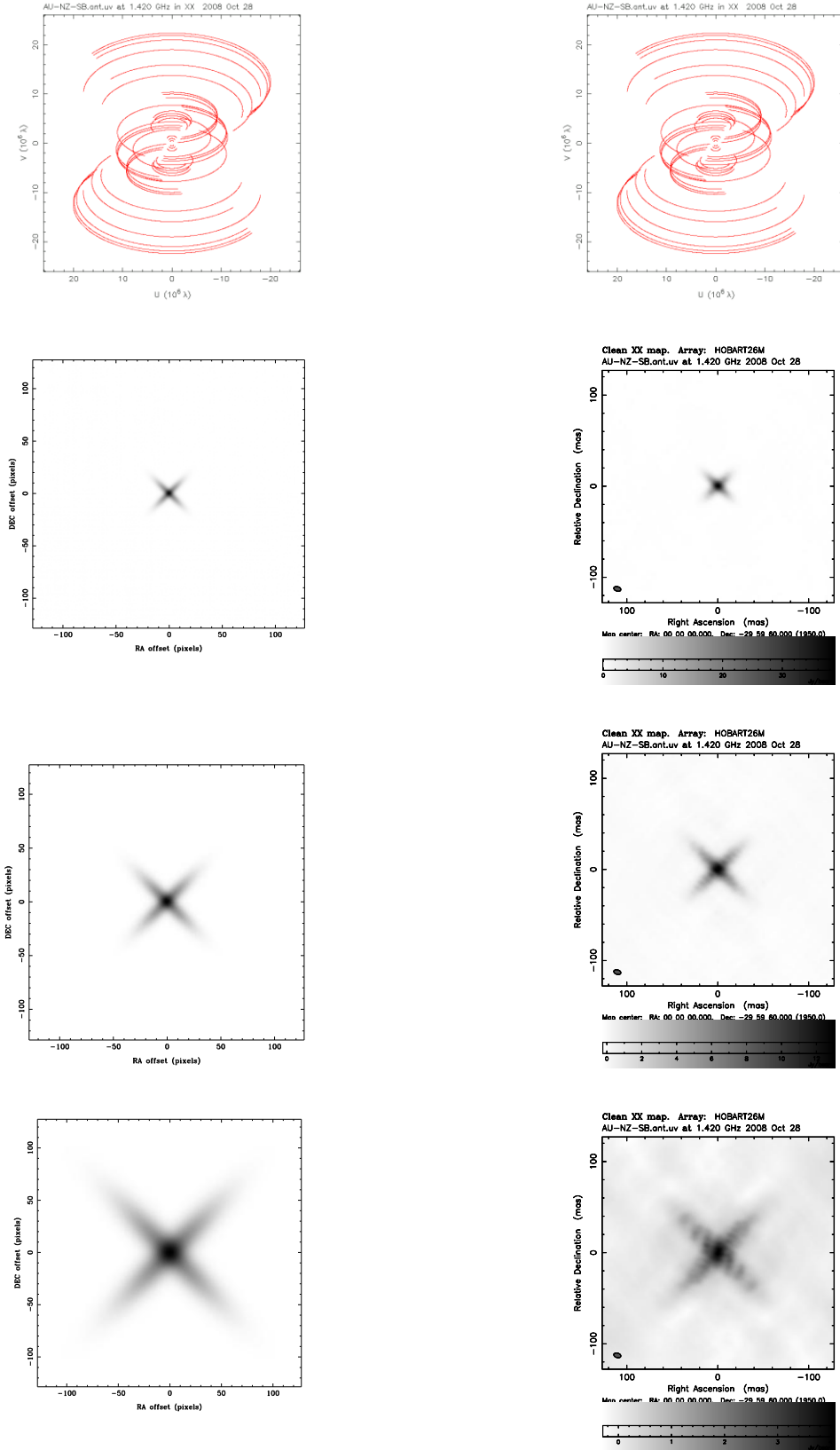


Figure 69: Australia, New Zealand & Scott Base – 12 hr Integration,  $-30^\circ$  Declination

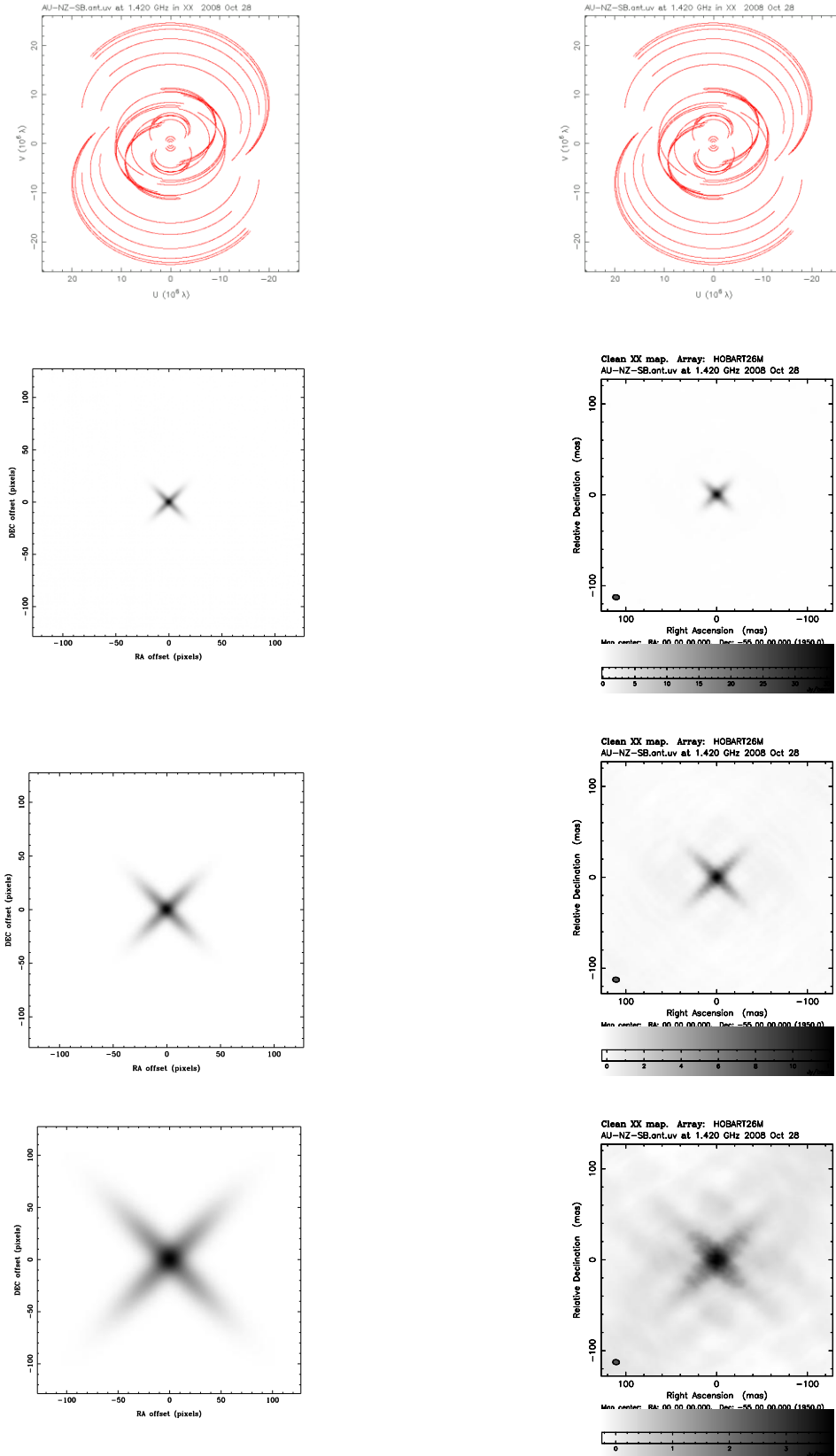


Figure 70: Australia, New Zealand & Scott Base – 12 hr Integration,  $-55^\circ$  Declination

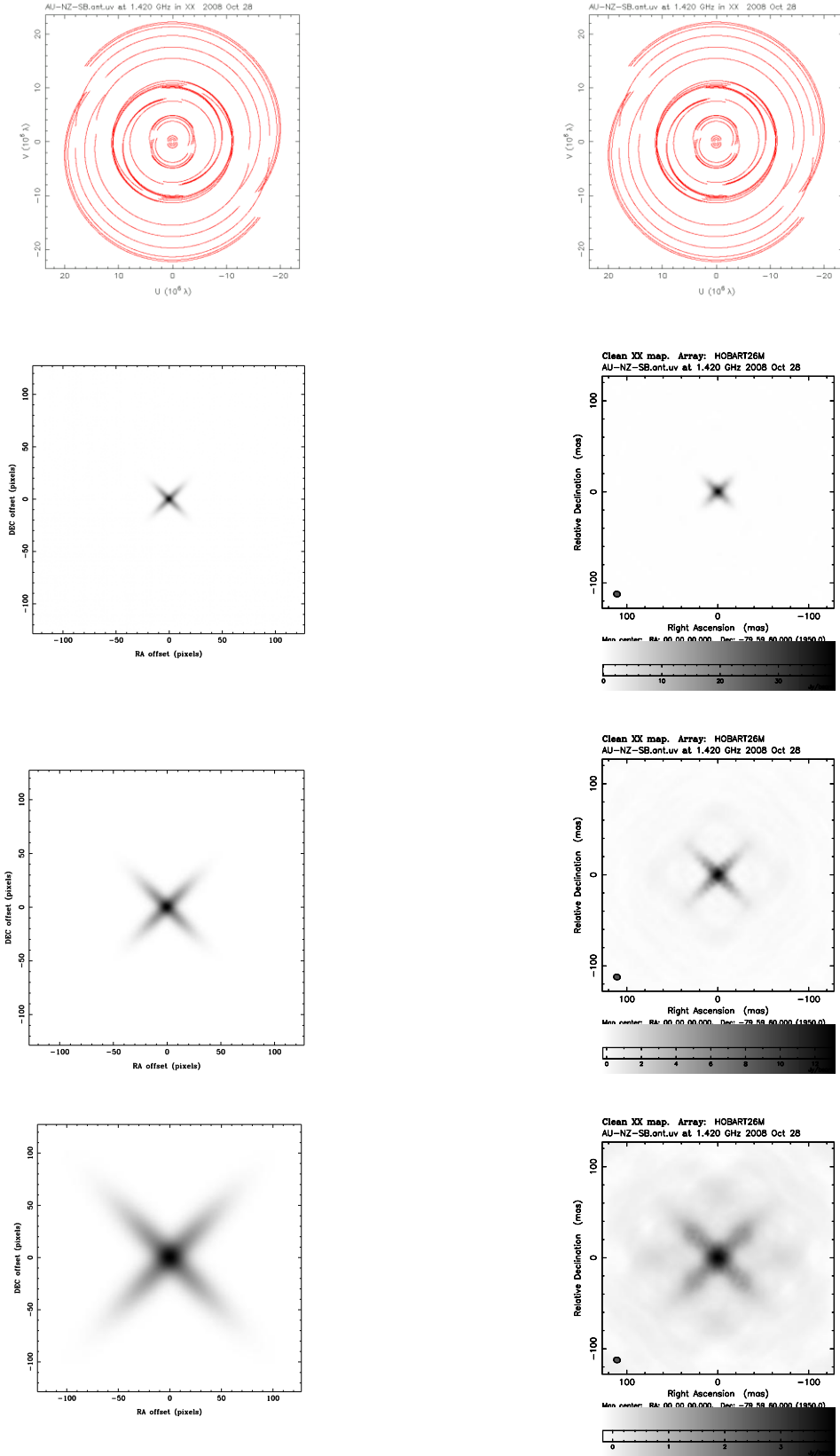


Figure 71: Australia, New Zealand & Scott Base – 12 hr Integration,  $-80^\circ$  Declination

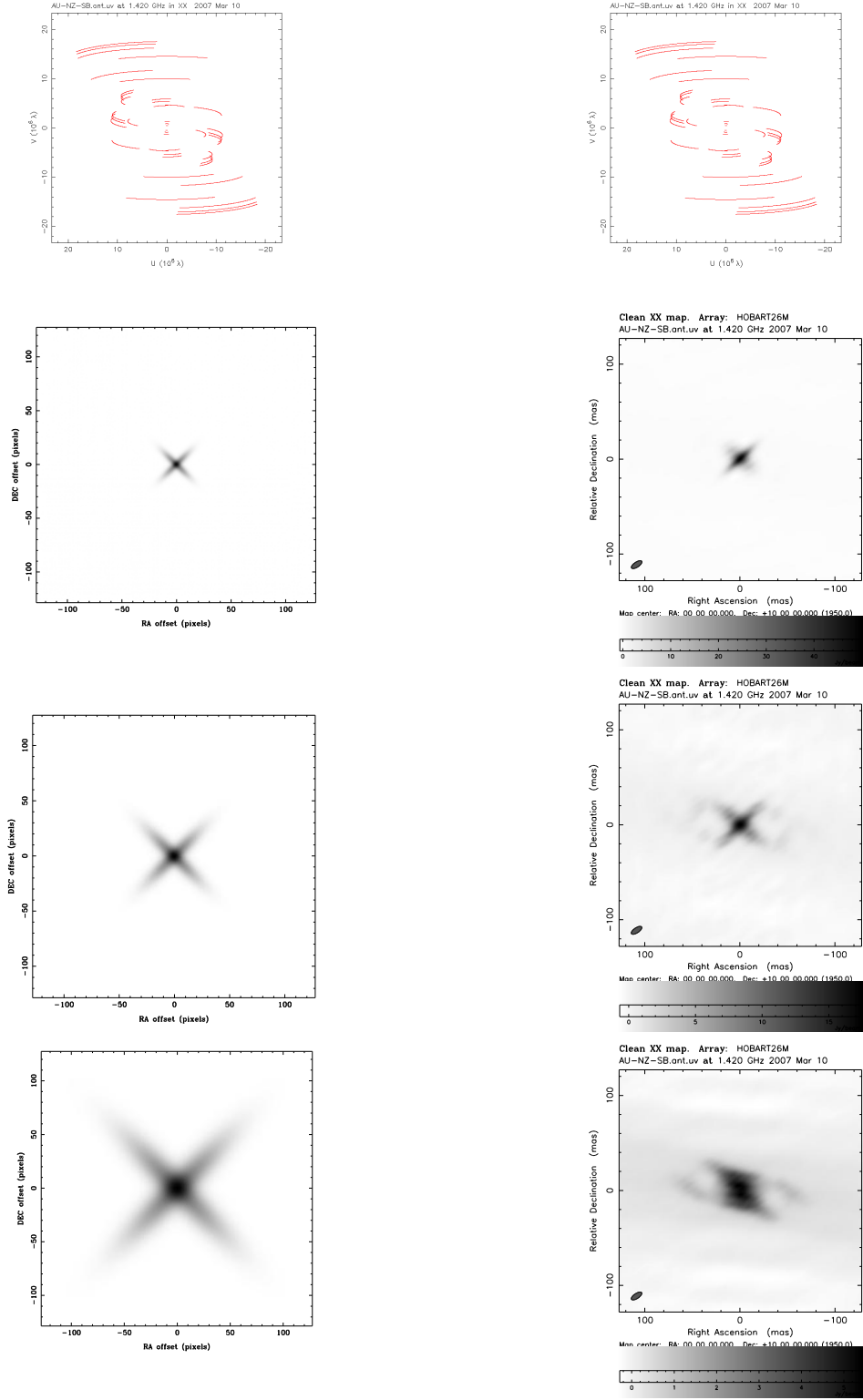


Figure 72: Australia, New Zealand & Scott Base – 4 hr Integration,  $10^\circ$  Declination

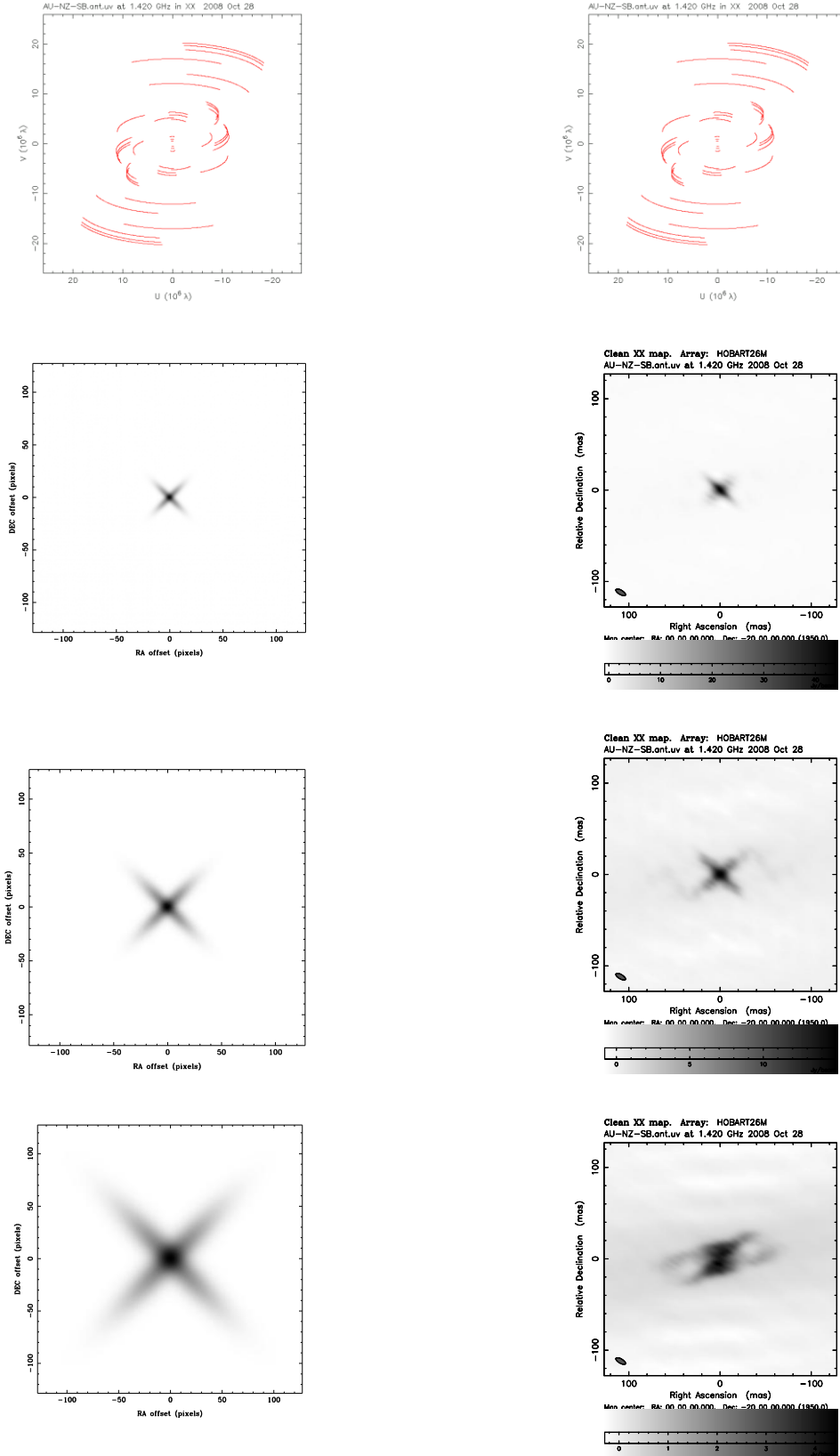


Figure 73: Australia, New Zealand & Scott Base – 4 hr Integration,  $-20^\circ$  Declination

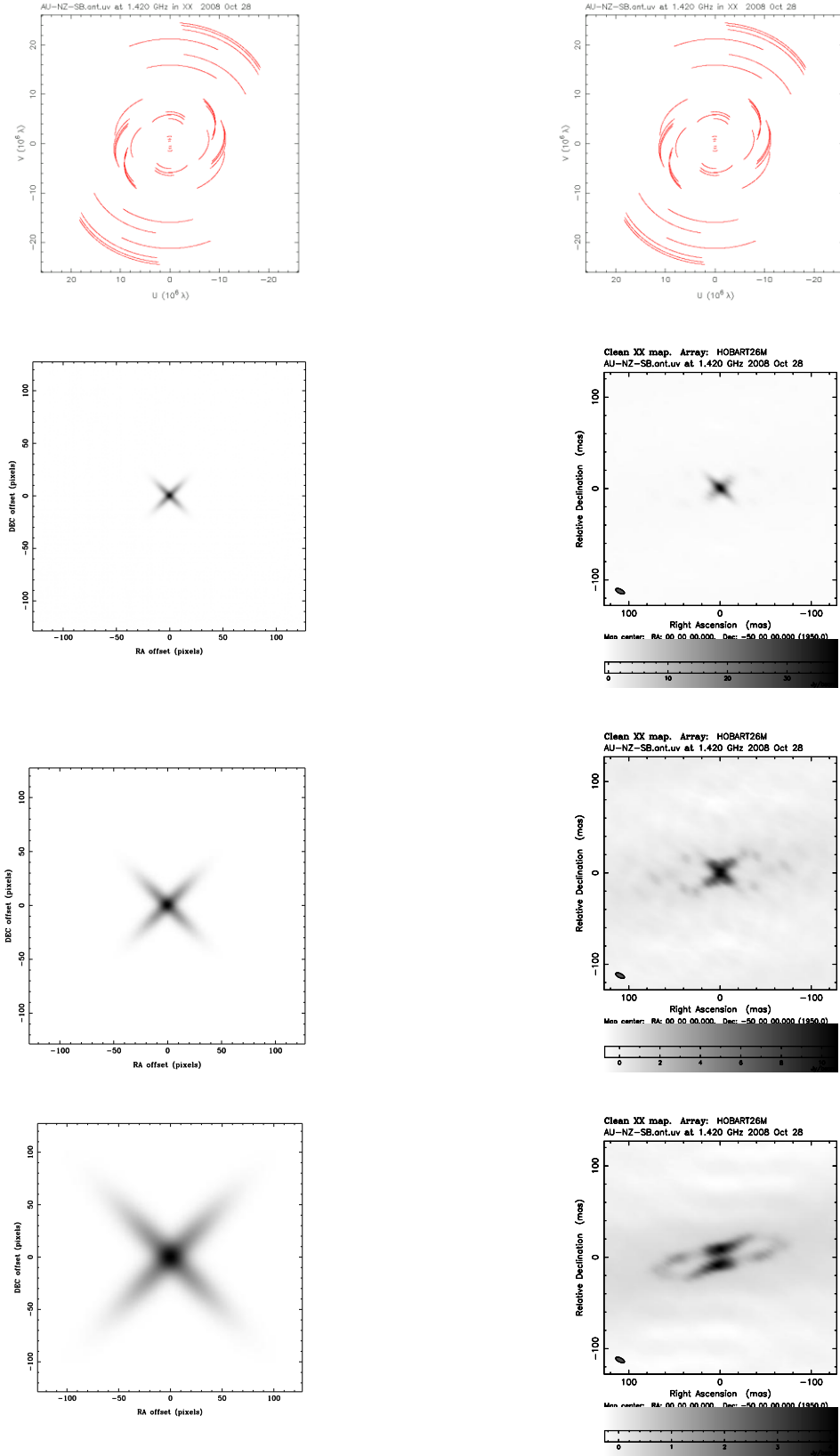


Figure 74: Australia, New Zealand & Scott Base – 4 hr Integration,  $-50^\circ$  Declination



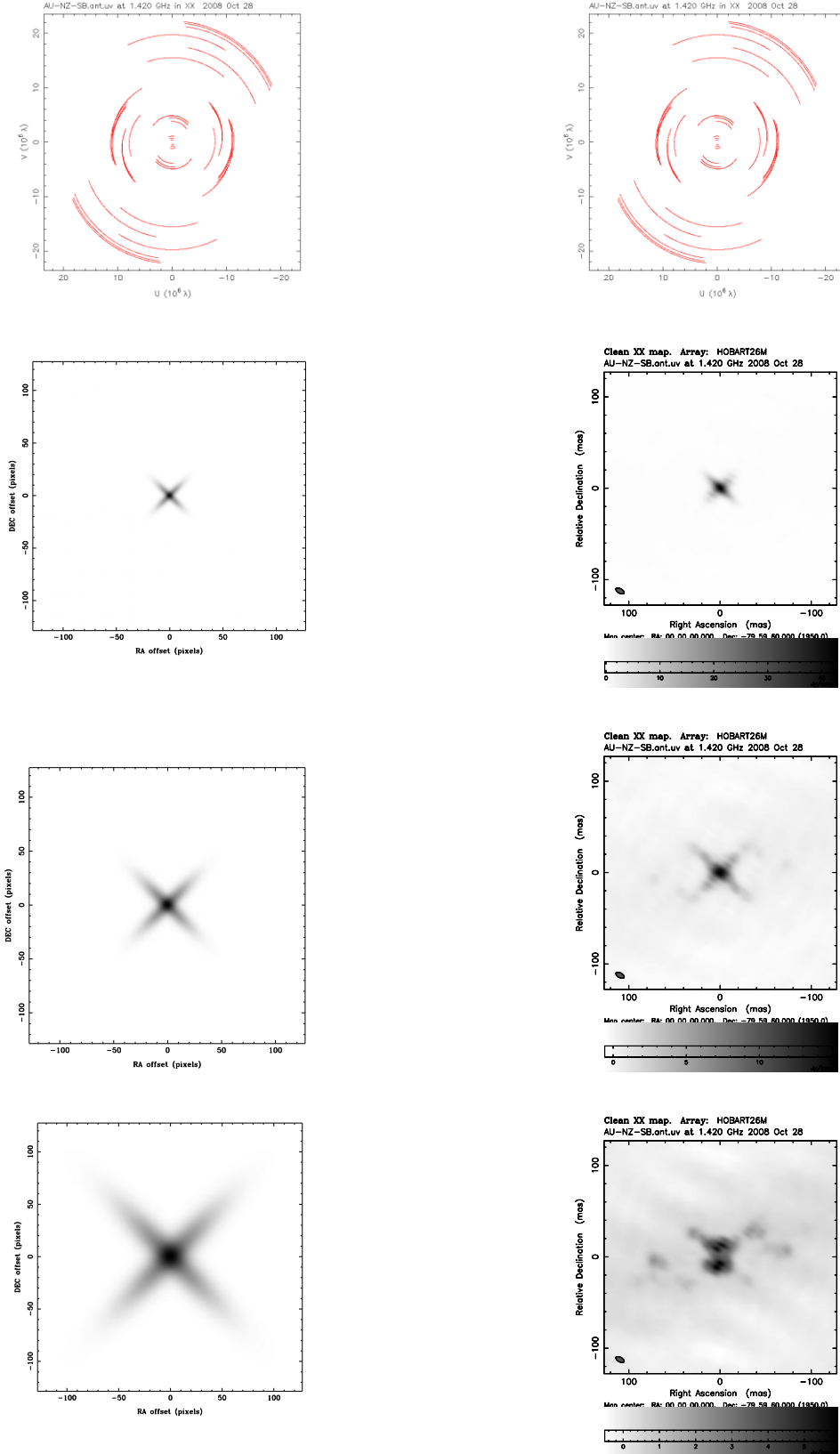


Figure 75: Australia, New Zealand & Scott Base – 4 hr Integration,  $-80^\circ$  Declination

### 4.3.2. Analysis of Results

For this array there are some very long baselines which from Table 2 result in a theoretical resolution of approximately 8 mas at 1.4 GHz. The smallest model source AGN1 has two elliptical gaussian sources with a major axis of 25 mas and a minor axis of 5 mas. Thus we would expect this source to be resolved with detail of the structure observed.

#### Simulation of a 12hr Observation

From Figure 69 through to Figure 71 for source declinations of  $-30^\circ$ ,  $-55^\circ$  and  $-80^\circ$ , AGN1 and AGN2 are clearly resolved and the extended structure matches the model well. The sharpest CLEAN images are for the source declination of  $-80^\circ$ , looking at the  $u,v$  plots we see at this declination the most uniform coverage of the  $u,v$  plane. For the largest model source AGN3 other effects are becoming apparent in the CLEAN image that produce background patterns to the CLEAN image. Note how small and compact the beam size and shape is on the CLEAN images.

#### Simulation of a 4hr Observation

Referring to Figure 72 through to Figure 75 a very similar out come in the CLEAN images is obtained as for the Australian sub-array - New Zealand array for the same declinations. For the large source AGN3 at any declination the extended structure fails to match the model image, at  $10^\circ$  we might say that it has 4 extensions and at  $-50^\circ$  we would call it a ring, other artifacts are very apparent and strong.

What is interesting is that a better image of AGN1 and AGN2 than is obtained for AGN3. In Figure 72 we see that due to the inclination ( $45^\circ$  from the perpendicular) of the beam whose shape is elliptical, it has resolved the corresponding model source elliptical component of the X at the same relative inclination slightly better than the other arm of the X ( $315^\circ$  from the perpendicular). The opposite is observed when the beam ellipsoide is angled at  $315^\circ$ .

### **Summary of the simulated observation**

All three sources were quite clearly resolved, with the best CLEAN images being obtained for the 12hr observation at a declination of  $-80^\circ$ . For the larger source we see the development of quite noticeable background components to the image. We again see that the difference in image quality and resolution is clearly demonstrated between the 12hr and 4hr observations.

Taking the CLEAN images for the 12hr observations and the model images and calculation the Normalized 2-D Cross Correlation for each pair of images at the declinations produces Table 24. For the 4 hr observations the Normalized 2-D Cross Correlation values are shown in Table 25.

Declination	-30°	-55°	-80°
Source			
agn1	0.95	0.96	0.95
agn2	0.98	0.98	0.98
agn3	0.96	0.93	0.95

---

Table 24: Normalized Cross-Correlation values for the Australian sub-array - New Zealand - Scott Base array with a 12hr observation

Declination	10°	-20°	-50°	-80°
Source				
agn1	0.91	0.92	0.93	0.93
agn2	0.94	0.93	0.89	0.94
agn3	0.86	0.82	0.76	0.81

---

Table 25: Normalized Cross-Correlation values for the Australian sub-array - New Zealand - Scott Base array with a 4hr observation

#### 4.4.Array Comparison

The Normalized 2-D Cross Correlation figure of merit values presented in the results for each array modelled in the preceding sections are discussed and compared.

To compare each array the figure of merit for each group of observations 12hr or 4hr, are plotted for each source and observation period. Each plot shows the figure of merit for each array as a function of declination.

The plots for the 4 hrs observations are as follows, for the source AGN1 this is Figure 76, source AGN2 is Figure 78 and for source AGN3 Figure 80. For AGN1 we see that the correlation value for each array at each declination is progressively higher as we move from AU ( with values in the range 0.52 to 0.54 ) to AU-NZ ( with values in the range 0.82 to 0.85 ) and finally AU-NZ-SB ( with values in the range 0.91 to 0.93 ). With AGN2 we see AU has the lowest range of values ( 0.67 to 0.71 ), but for the arrays AU-NZ and AU-NZ-SB there correlation values lie within the same range ( 0.89 to 0.94 ). For the AU-NZ-SB array with better resolution due to its longer baselines and improved  $u,v$  coverage we would expect the CLEAN images to be superior. Finally with AGN3 we see that the AU-NZ array has higher correlation values ( 0.84 to 0.92 ) than the AU array ( 0.77 to 0.80 ), but AU-NZ-SB correlation values lie within a similar range of values ( 0.76 to 0.86 ) to the AU array which is unexpected. For this larger source it would appear that the larger baselines with the AU-NZ-SB array has had a detrimental affect to the final CLEAN images.

The 12 hr observation plot for source AGN1 is Figure 77, source AGN2 is Figure 79 and for source AGN3 Figure 81. For AGN1 we can see that the correlation value for each array at each declination is progressively higher as we move from AU ( with values in the range 0.67 to 0.69 ) to AU-NZ ( with values in the range 0.85 to 0.85 ) and finally AU-NZ-SB ( with values in the range 0.95 to 0.96 ). We see a similar relationship for AGN2 where for each array at each declination the range of correlation values are progressively higher as we move from AU ( 0.84 to 0.86 ) to AU-NZ ( 0.95 to 0.96 ) and finally AU-NZ-SB ( 0.98 ). Finally for AGN3 we have a situation similar to the 4hr observation where there are progressively higher correlation values from AU ( 0.88 to 0.94 ) to AU-NZ ( 0.97 to 0.98 ) but AU-NZ-SB (0.93 to 0.96) lies within the same range as AU.

For all three sources comparing the Normalized 2-D Cross Correlation values between the 4hr and 12hr observations; it is very apparent that the 12hr values for all arrays lie within a higher and narrower band of values, 12hr AGN1 the values are between 0.67 to 0.96 but the 4hr AGN1 values lie between 0.52 to 0.93. This trend is continued for the other observations between 12hr and 4hr.

Thus it is felt that the Normalized 2-D Cross Correlation values as a figure of merit provide a guide in comparing the final CLEAN image with the original input model source between observations and arrays, but it is still not a truly quantitative measure that can be applied without the need for visual inspection and comparison and application of common sense.

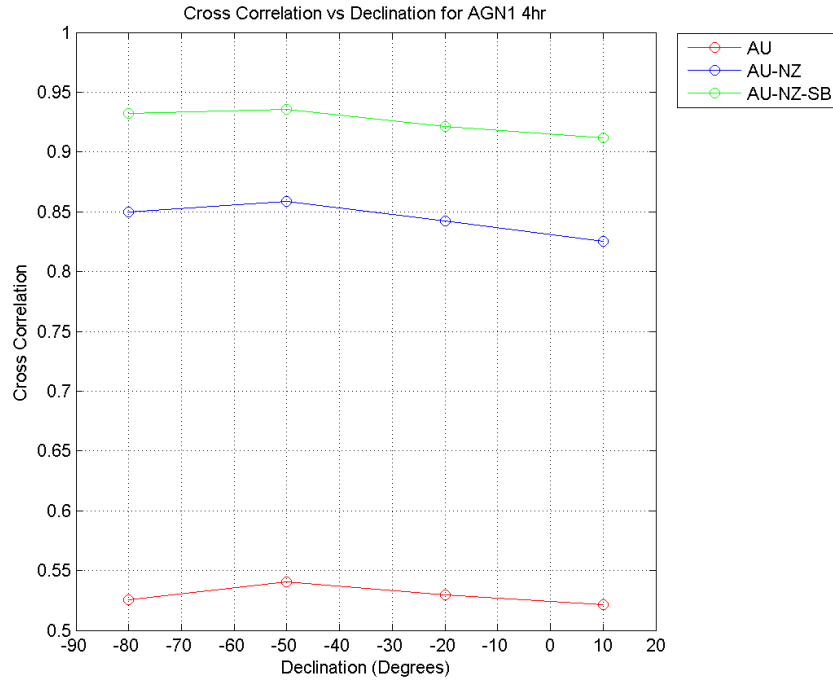


Figure 76: For AGN1 a plot of the Normalized 2-D Cross Correlation value vs. declination for each array with the 4hr observation

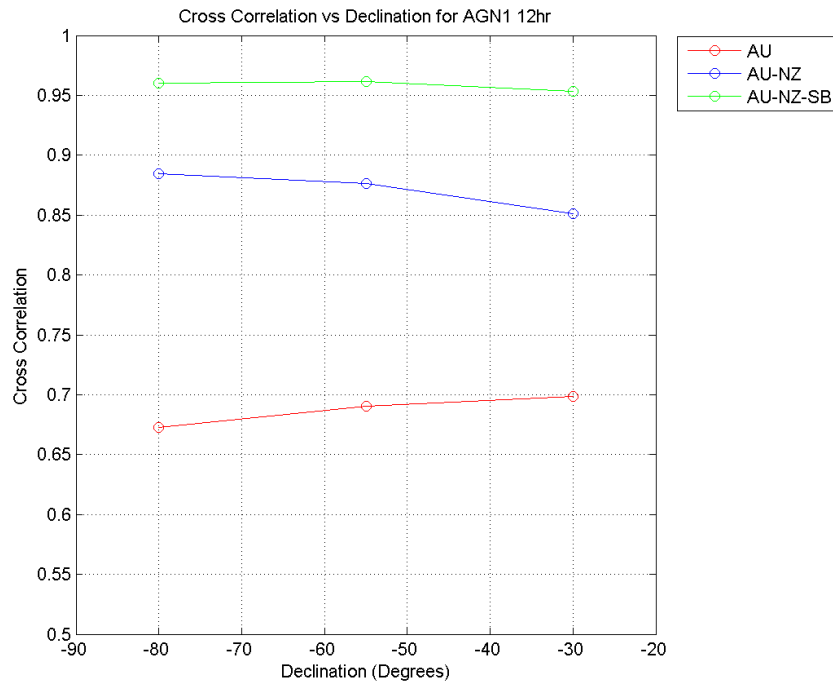


Figure 77: For AGN1 a plot of the Normalized 2-D Cross Correlation value vs. declination for each array with the 12hr observation

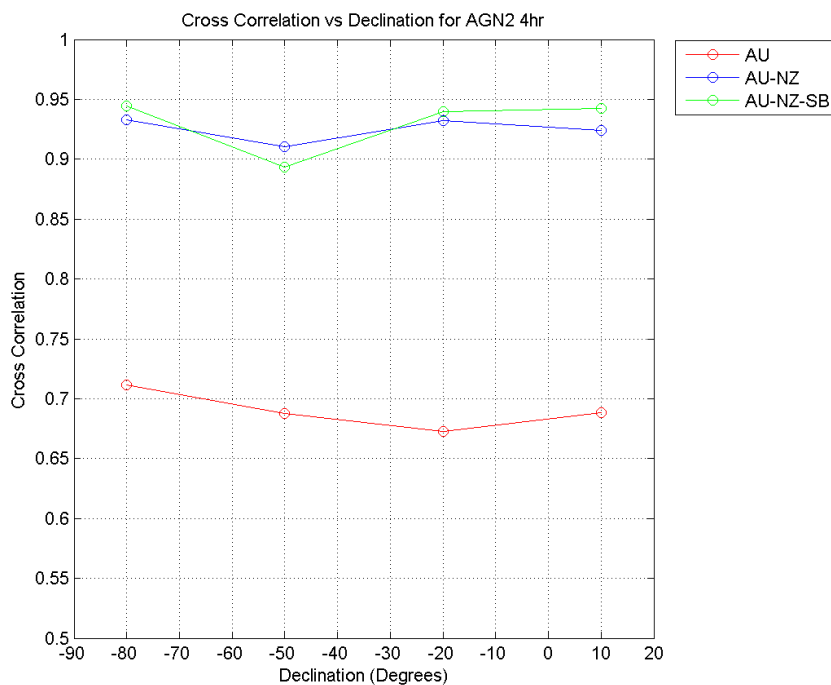


Figure 78: For AGN2 a plot of the Normalized 2-D Cross Correlation value vs. declination for each array with the 4hr observation

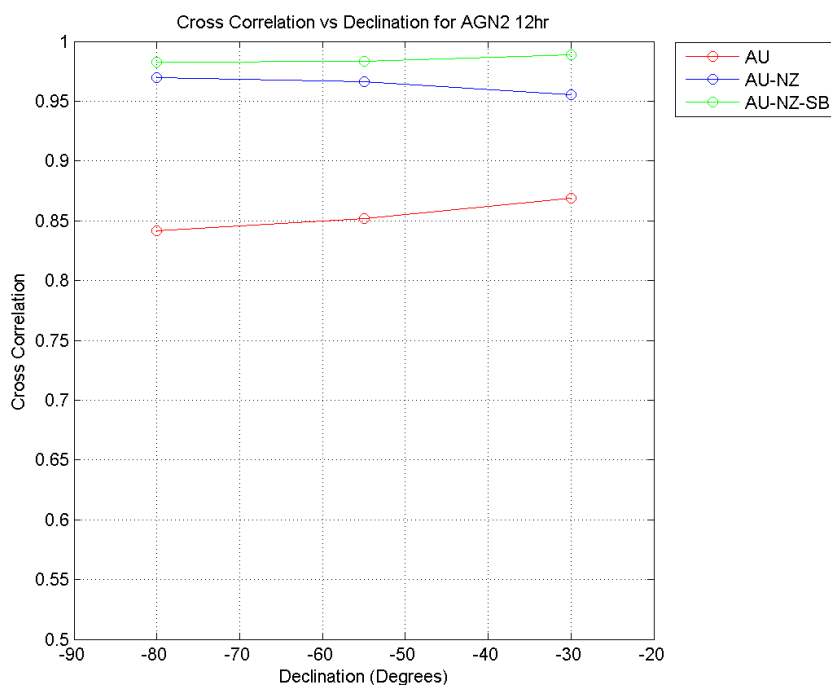


Figure 79: For AGN2 a plot of the Normalized 2-D Cross Correlation value vs. declination for each array with the 12hr observation



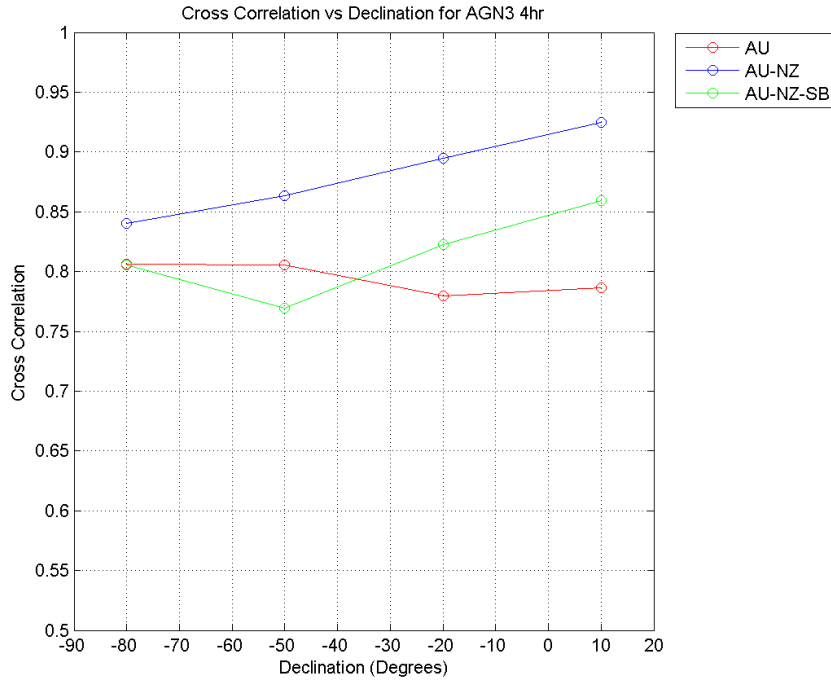


Figure 80: For AGN3 a plot of the Normalized 2-D Cross Correlation value vs. declination for each array with the 4hr observation

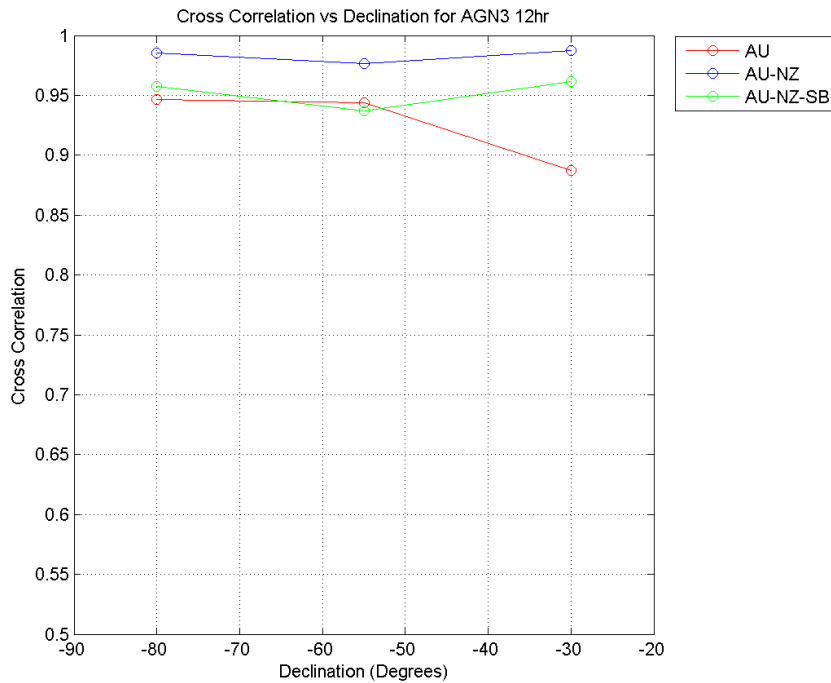


Figure 81: For AGN3 a plot of the Normalized 2-D Cross Correlation value vs. declination for each array with the 12hr observation

#### **4.5. SKA Phased Building Simulation**

The Australian SKA proposal consists of a central core in Western Australia with a large number of antennae. This is then supplemented by a number of out station antenna groups radiating out mainly to the east across Australia with some in New Zealand providing the longest baselines (SKA Memo 69, 2006).

As the SKA will require a significant construction period for such a large number of antennae at many remote sites with associated infrastructure having to be built from scratch, it is planned over a 10 year period. But as with any project of this magnitude and complexity this should be considered as a very optimistic time line.

Thus two scenarios were considered for the building of the Australian SKA proposal:

Scenario 1 investigates that first effort is concentrated on building the core and gaining high sensitivity and collecting area but not resolution. Then construction moves out and starts on the remote stations. We have assumed that this will progress outward from the core.

Scenario 2 part of the core is completed providing the basic infrastructure which can be built on easily. But after say 2 years construction moves to some of the outstations closest to existing infrastructure such as Hobart, Narrabri and Parkes. There is no loss in collecting area constructed vs. construction time, thus sensitivity is not sacrificed as shown in Figure 82. The immediate benefit is that the SKA gains long baselines very early in its construction and thus very high resolution.

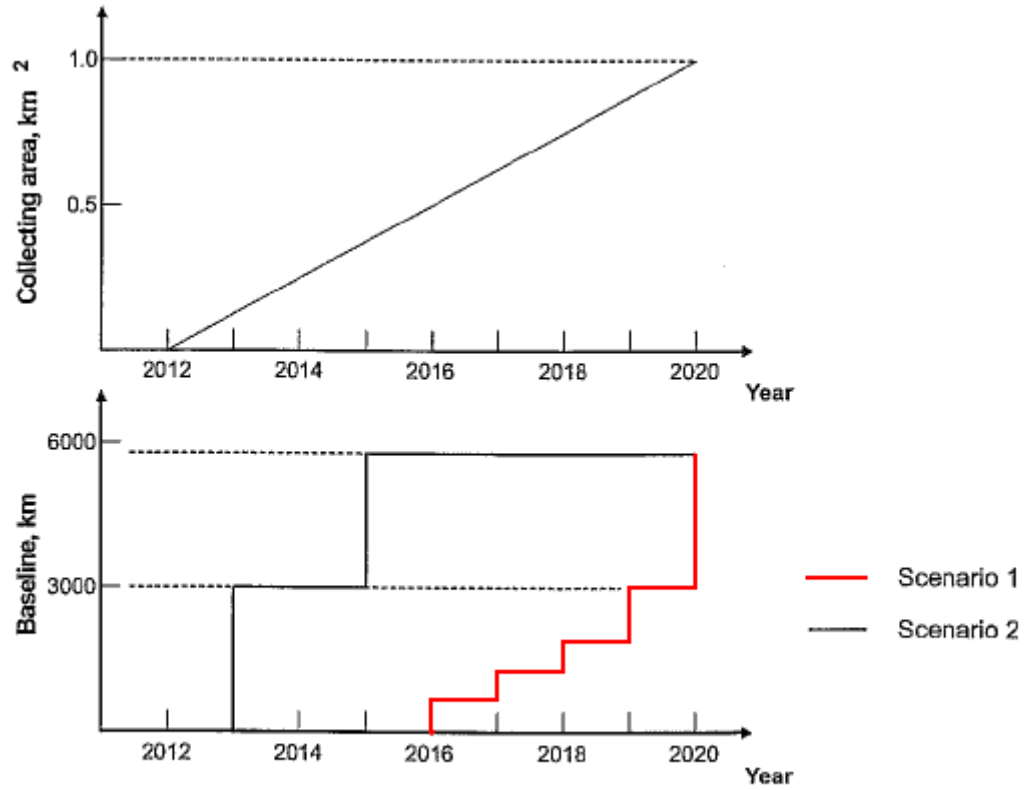


Figure 82: Collecting Area and Baseline during construction (Gulyaev and Weston 2007)

The process we developed in the previous sections was used to investigate a phased approach to the building of the SKA.

For the simulation a model source was used as described in Section 3.4.2. This contains a group of three active radio sources separated by a distance of 20 mas in a triangular formation, each source is an elliptical Gaussian source where the major axis is 6 mas and the minor 3 mas as defined in Table 26.

Flux (Jy)	RA (arcsec)	Dec (arcsec)	Bmaj (arcsec)	Bmin (arcsec)	Position Angle
25.0	0.01	0.005	0.006	0.003	45.0
25.0	-0.01	0.005	0.006	0.003	135.0
25.0	0.0	-0.01	0.006	0.003	90.0

Table 26: MIRIAD IMGEN definition for the SKA source

A small scale reproduction of the image for this model source is shown in Figure 83. The image is 512 x 512 pixels, where each pixel is 0.25 mas a larger scale image can be seen in

Figure 28.

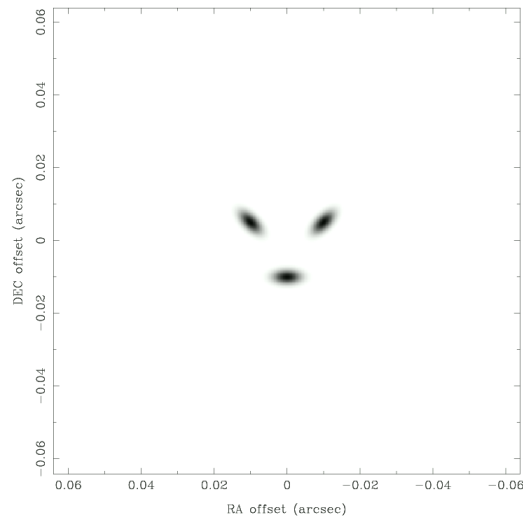


Figure 83: SKA Model Source

For scenario 1 the Sky Visibility plots for the four different phases in construction are presented in Figure 84 for the antenna groups introduced in Section 3.2.2, top is the CORE antennas only, then CORE+INT, followed by CORE+INT+MAX and finally CORE+INT+MAX+NZ (note that no elevation limit has been defined).

In Figure 85 are the Sky Visibility plots for scenario 2, top is CORE+MAX, then CORE+MAX+NZ and finally CORE+INT+MAX+NZ.

The criteria was to find a long observation time of far greater than 4hrs which is the stated SKA minimum common to all antenna arrays for both scenarios in each phase of construction to allow comparison. From a review of these visibilitys in Figure 84 and Figure 85 I chose a source of declination -80 degrees and a observation period of 12 hrs for these SKA simulations, longer periods are possible for a source near the south celestial pole but elevation limits for antenna would be a factor and make this impracticable.

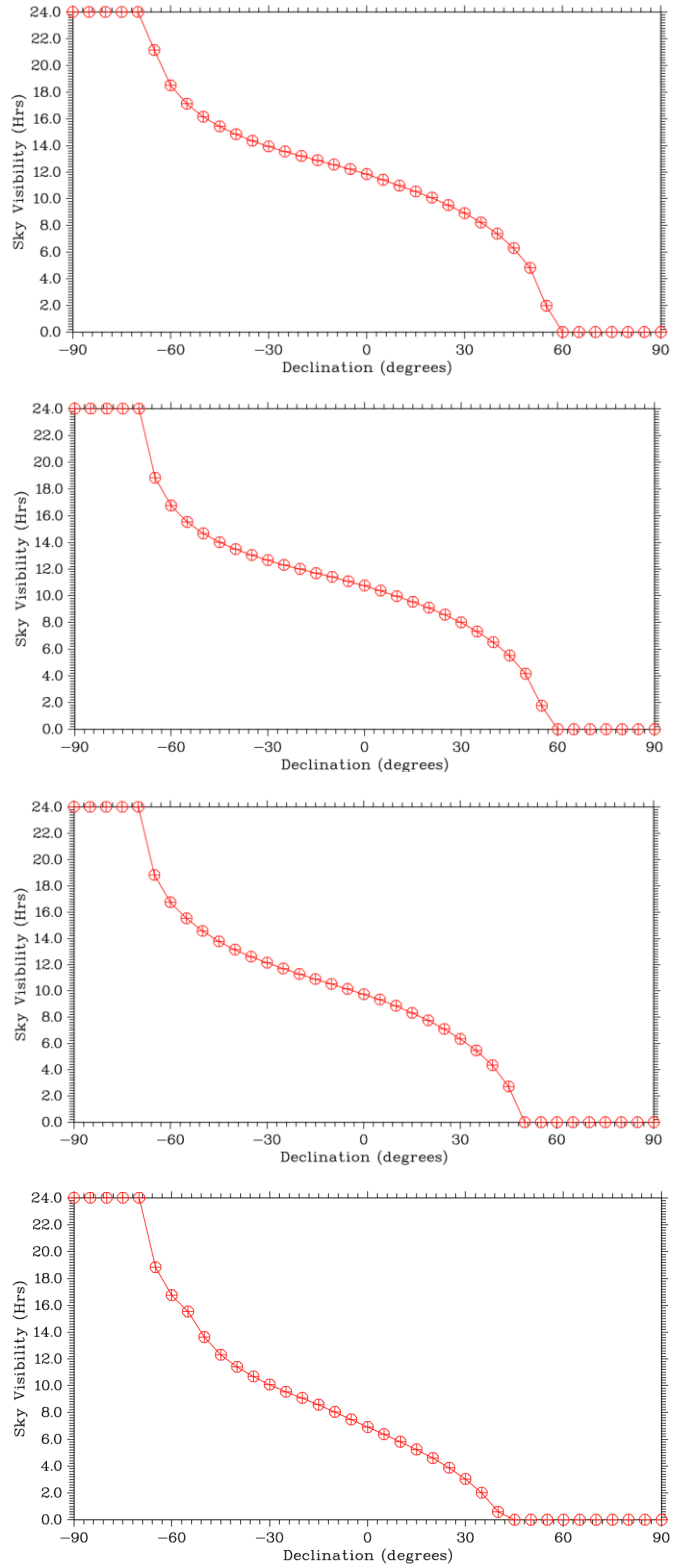


Figure 84: SKA Scenario 1 Visibility, Top CORE, CORE+INT, CORE+INT+MAX and Bottom CORE+INT+MAX+NZ

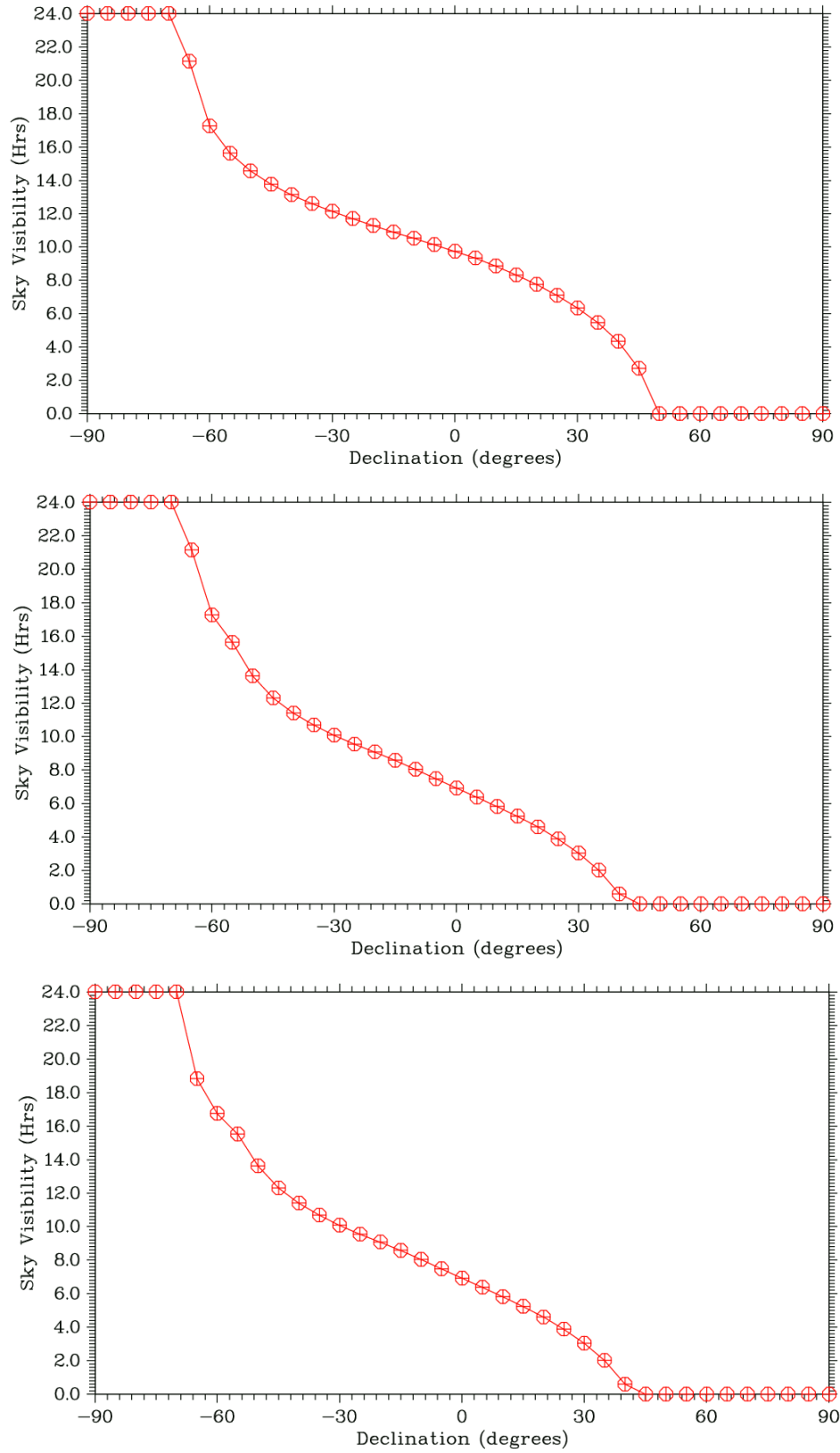


Figure 85: SKA Scenario 2 Visibility, Top CORE+MAX, Middle CORE+MAX+NZ and Bottom CORE+INT+MAX+NZ

The  $u,v$  FITS file is then processed using DIFMAP (Lovell 2001). Due to the nature of this array containing many long and short baselines use is made of weighting in applying the CLEAN algorithm as discussed in Section 3.6.1. First the dirty image is processed by CLEAN for a set number of iterations with uniform weighting (uvweight 2,-1) to emphasize short baselines in the image. Then the image is further processed again with the same number of iterations and a natural weighting (uvweight 0,-1) for long baselines. The final image is thus a combination of short and long baseline emphasis. The commands used in DIFMAP to achieve this are shown in Figure 86.

```
mapsize 512,0.5
uvweight 2,-1
do i=1,40
clean;selfcal
end do
uvweight 0,-1
do i=1,40
clean;selfcal
end do
```

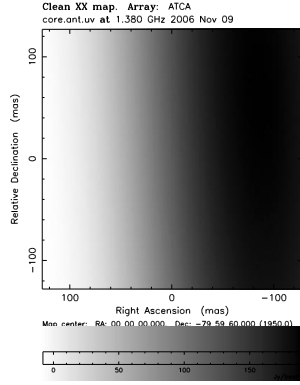
Figure 86: Example DIFMAP commands in applying  $u,v$  Weighting



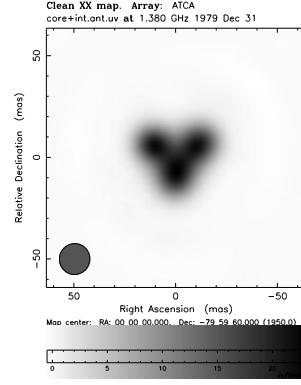
#### **4.5.1. SKA Building Scenario Results**

For Scenario 1 of the building of the SKA see Figure 87. The first row shows the CLEAN images obtained for each phase of this scenario, and the second row of plots are the corresponding  $u, v$  plots all to the same scale. Each column corresponds to a year in which a particular phase of building should be completed ascending in year from left to right. Scenario 2 is shown in Figure 88 and is similar to Figure 87 for layout. The CLEAN images should be compared with Figure 83 which is the input model image.

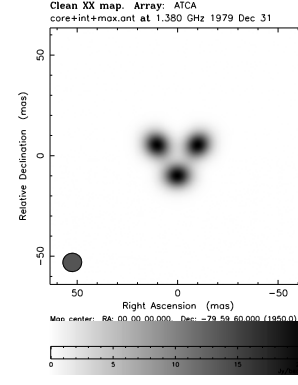
2014



2016



2018



2020

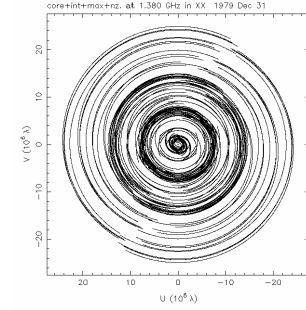
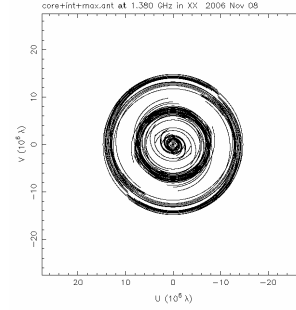
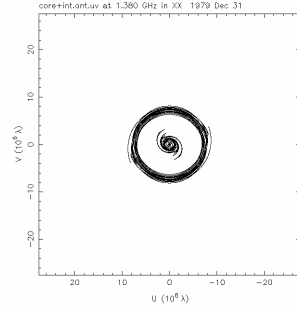
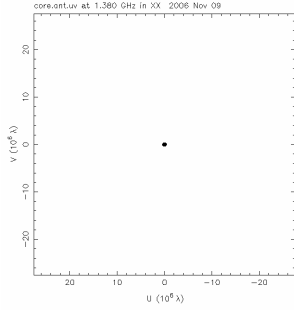
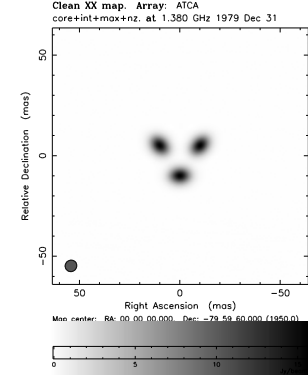


Figure 87: SKA Phased Building Simulation, Scenario 1

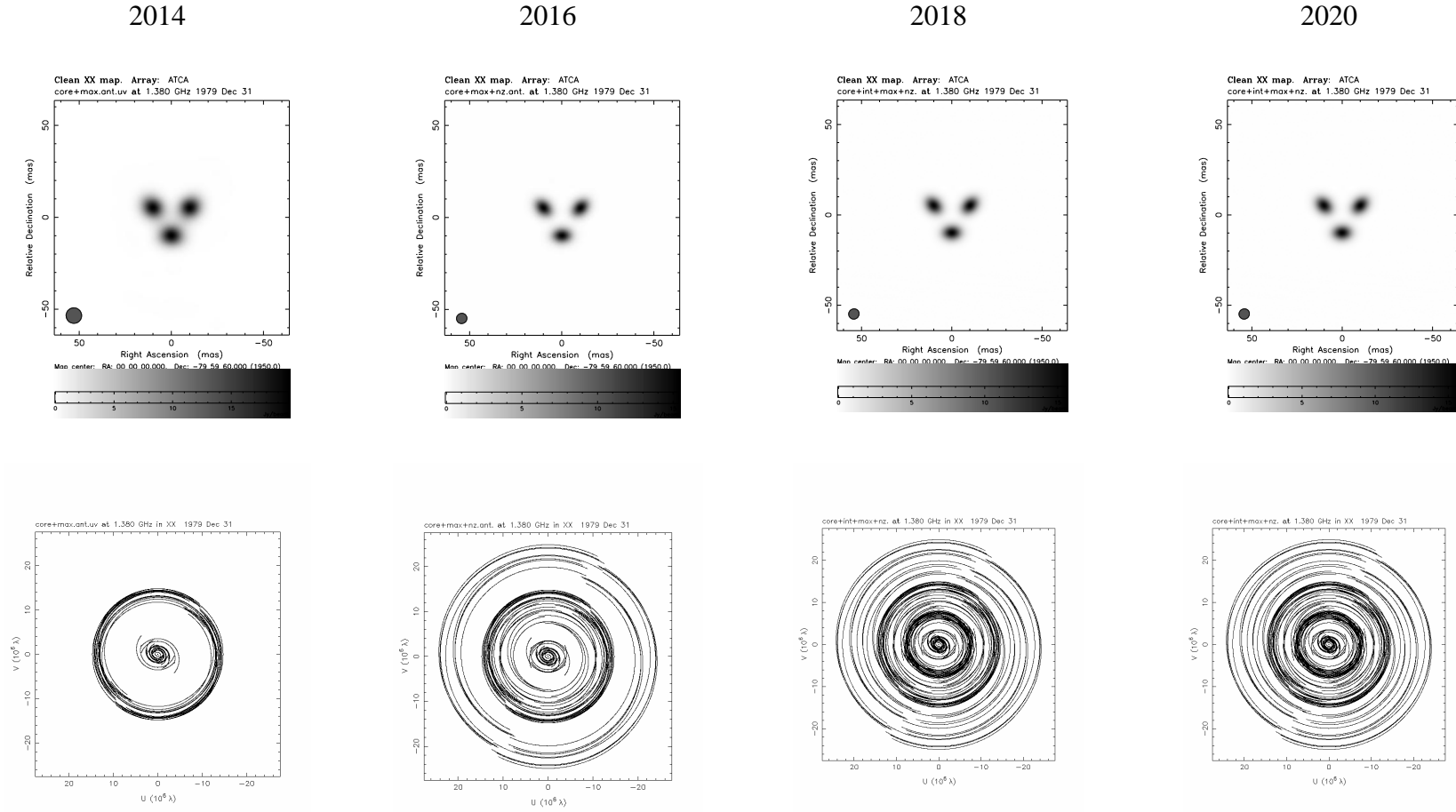


Figure 88: SKA Phased Building Simulation, Scenario 2

Taking the CLEAN images for the different phases of construction in Scenario 1 and the input model image to calculate the Normalized 2-D Cross Correlation the resultant values are presented in Table 27; also for Scenario 2 the Normalized 2-D Cross Correlation values are presented in Table 28.

2014	2016	2018	2020
-	0.38	0.57	0.70

Table 27: Normalized Cross-Correlation values per year for the SKA Scenario 1

2014	2016	2018	2020
0.63	0.74	0.70	0.70

Table 28: Normalized Cross-Correlation values per year for the SKA Scenario 2

### 4.5.2. Analysis of Results

We will now compare and discuss the results obtained from modelling these two scenarios.

#### Scenario 1

In Figure 87 are the results for the first scenario. Here the construction effort is concentrated on the core until 2016 and then at intervals construction moves out in steps to start building the remote stations. It is envisaged that construction will move out progressively in distance from the core, building infrastructure as required such as the high speed data network.

We can see from the start of construction in 2014 where effort is concentrated on the building of the core that the resolution of these antennae is unable to image the model source.

In 2016 the construction teams move out to the intermediate antennae giving baselines of approximately  $6 - 8 \times 10^6 \lambda$ . With these baselines the SKA is now able to image the model source and we are able to see that it has structure and possibly say that it is three discrete sources.

In 2018 the construction teams have progressed to constructing the antennae along the east coast of Australia extending the baselines to approximately  $14 \times 10^6 \lambda$ . The image now quite clearly shows the three distinct sources, but the resolution is still insufficient to resolve these individual sources. They appear as point Gaussian components with no identifiable orientation.

The final phase in 2020 sees the completion of antennae in New Zealand giving the maximum baselines of approximately  $24 \times 10^6 \lambda$ , this is nearly a doubling of the baselines available across Australia. It is now possible to see that the three components are elliptical gaussian with orientation.

## Scenario 2

For this scenario construction has commenced in 2010 at the core but in about 2012 work has also in parallel started on the outstations closest to existing infrastructure. Thus in Figure 88 we see in the image of the model source for antennae CORE+MAX<sup>7</sup> in 2014 that the components can be resolved as separate items. This should be compared to scenario one where this is not achieved until about 2018.

In 2016 where we now have CORE+MAX+NZ<sup>7</sup>, the longest baselines possible are approximately  $24 \times 10^6 \lambda$  and have been obtained 4 years earlier than Scenario 1. In the image it is now possible to see that the three components are elliptical gaussian with orientation.

For the proceeding years no improvement in resolution is achieved, but sensitivity increases with each additional antenna and thus collecting area is added; also  $u,v$  coverage will improve as these additional groups of antennae are built and brought on-line.

---

<sup>7</sup> Please refer to the section “SKA Antenna Data” and Figure 20 for an explanation of CORE, INT, MAX and NZ

### 4.5.3. Summary of the simulated SKA phased building

If we compare the model to CLEAN image with the Normalized 2-D Cross Correlation values as plotted in Figure 89 (using the values from Table 27 and Table 28), we can clearly see for Scenario 1 a steady improvement in CLEAN image quality as the SKA baselines are extended progressively during construction.

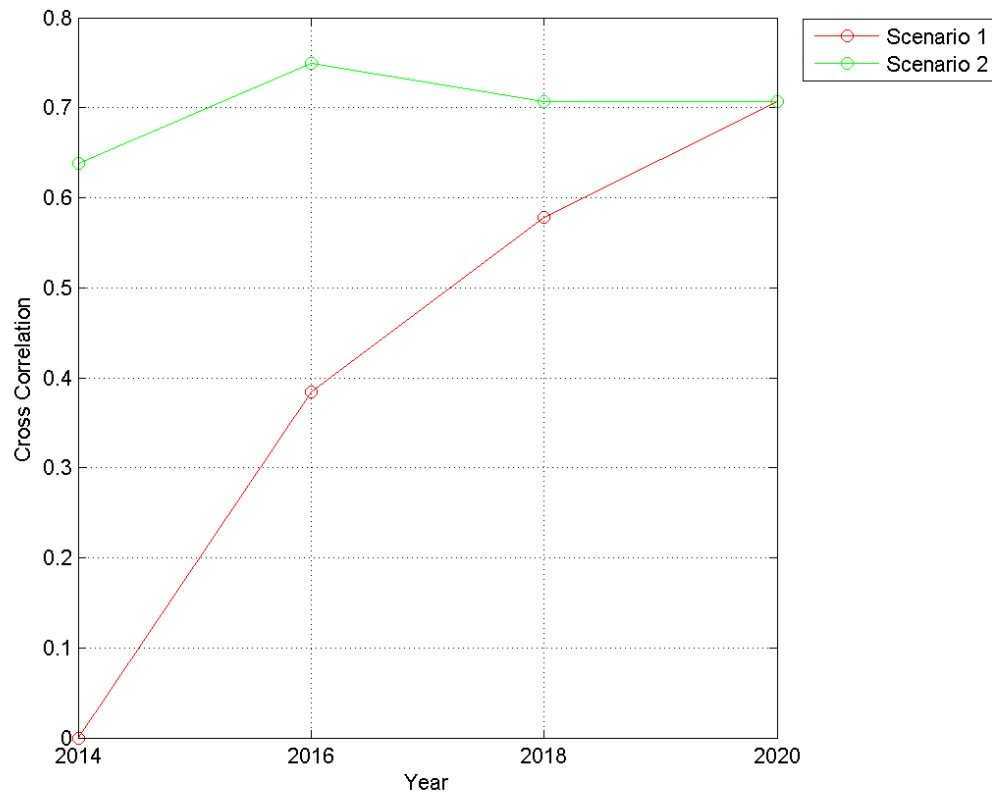


Figure 89: Plot of Normalized 2-D Cross Correlation value vs. year for each SKA construction scenario

Again from Figure 89 as discussed for Scenario 2 with the addition of long baselines using existing infrastructure along the Australian eastern seaboard; by 2014 far higher resolution will be obtained early with no loss in sensitivity and image quality is superior to Scenario 1 until the last phase of construction.

## Dynamic Range

The dynamic range for the CLEAN images as a further judgment of image quality was also investigated as a high value  $>10^6$  is an important requirement for the SKA (Carilli and Rawlings 2004), as with a wide field of view the ability to detect a weak source in the presence of strong sources is essential. Dynamic range is usually defined as the ratio between the peak brightness in an image and the r.m.s noise for a region in the image devoid of emission or components.

The dynamic range figures obtained for the two scenarios as determined from the CLEAN images in Figure 87 and Figure 88 are presented in Table 29 and Table 30.

Year	max	rms	DR
2014	-	-	-
2016	23	0.0017	13529.41
2018	21	0.00035	60000.00
2020	16	0.000563	28419.18

Table 29: Dynamic range values by date for SKA Scenario 1

Year	max	rms	DR
2014	20	0.0004	50000.00
2016	15.8	0.0006	26333.33
2018	16	0.000563	28419.18
2020	16	0.000563	28419.18

Table 30: Dynamic range values by date for SKA Scenario 2



A comparison of the CLEAN Image Dynamic Range between scenarios from Table 29 and Table 30 is presented in Figure 90. It can be seen that we are two orders of magnitude below the desired dynamic range for the SKA. Also the calculated dynamic range does not vary dramatically (the range is  $1.3 \times 10^4$  to  $6 \times 10^4$ ) between scenarios and construction dates.

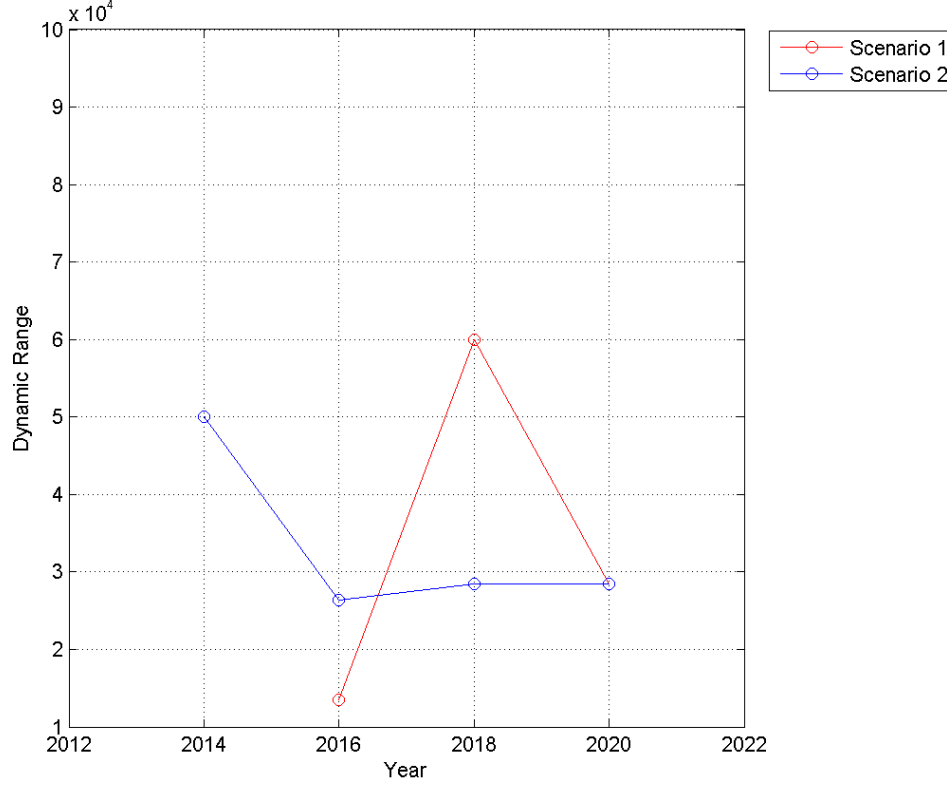


Figure 90: Dynamic range as a function of time (SKA construction phases) for the two scenarios

These values are somewhat lower than the required  $10^6$  for the SKA. The study by (Voronkov and Wieringa 2005) showed that the problem of dynamic range is mostly a software issue. When the  $w$  term in the relation between the sky brightness and visibilities (see Figure 12 for  $w$ ) is taken in to consideration a value of  $10^8$  or higher is achievable with the Cotton-Schwab CLEAN algorithm. The  $w$  term was not taken into account in this thesis, which resulted in a lower figure for dynamic range.

## **Summary**

A construction scenario that should be considered is one that allows simultaneous effort in building the core and remote stations. If the first remote stations tackled were close to existing infrastructure such as Hobart, Parkes, Narrabri and New Zealand then very quickly long baselines are established and linked to the progressing core. Thus high angular resolution is achieved very early in the construction, and as more antennae are added collecting area is increased steadily improving sensitivity.

There are other possibilities for the order of building the antennae. We believe the building of the antennae to obtain long baselines early in the construction is worth merit and due consideration.

A detailed discussion and presentation of this proposal is to be found in (Gulyaev and Weston 2007).

## 5. Conclusion

The aim of becoming familiar with some of the common astronomical software used in Radio Astronomy has been achieved, sufficient that we were able to make changes that were accepted by ATNF for MIRIAD. Existing work on a Sky Visibility utility for the SKA has been rewritten and enhanced for general usage.

A process linking existing radio astronomical software together has been produced and used to provide the core of the research for this thesis; it has also been used for other projects and ideas within the AUT IRSR group. Also demonstrated was friendlier graphical use interface /web interface using PERL/HTML and CGI that can be built around existing astronomical software. It has been found that software developed by the astronomical community lacks easy to use and intuitive user interfaces. Our HTML approach allows the software and user interface to be easily shared in a community through an Internet Browser on what ever platform the user chooses.

From the experiments of different array configurations we have demonstrated the improvement and benefits of combining antennae in New Zealand with Australia to produce a VLBI Array of higher resolution than the most commonly used sub-array of Australian antennas located on the East Coast and in Tasmania can achieve on their own (It should be noted that the Australian antennas available is evolving all the time such as Ceduna becoming available for L-Band observations in 2007, new antennas being planned and built such as the SKA Pathfinder in Western Australia). Also investigated was a possible antenna in Antarctic as part of a Australia – New Zealand array, as it is becoming a highly likely site for future optical instruments for Astronomical Research due to its elevation, good seeing and lack of light pollution; and for radio astronomy it should be relatively free from man made radio frequency interference.

There is also the possibility to link New Zealand with other countries in the Pacific Rim to achieve an even greater resolution due to some very large baselines coupled with excellent coverage of southern hemisphere objects of interest to research groups. This process can be now used to model these possible co operations.

The process developed has successfully modelled and demonstrated a possible phased approach to building the SKA that we believe is of merit and due consideration by the wider community.

Demonstrated is the effect of source declination,  $u, v$  coverage on beam shape and final CLEAN image. Observation time is also important to final quality of CLEAN image. A way of measuring  $u, v$  coverage uniformity to give an observer some indication to the final CLEAN image quality and validity of the observed structure could be for a future research.

The difference in synthesised image quality and resolution is very significant between the 12hr and 4hr observations, thus integration time is a very important factor in the final CLEAN image quality. Of some benefit would be to explore the relationship of image quality vs. integration time and identify the point of diminishing returns for ever longer periods.

A formal approach to characterization of synthesised image quality in terms of a single “Figure of Merit” was explored. Four different methods were proposed, examined and considered. It was shown that the method of normalized cross-correlation is promising for algorithm quality and array configuration assessment.

The background components and artefacts introduced on some images were investigated. For further study and research are the artefacts generated in the AU-NZ-SB AGN3 4hr images. The use of other imaging techniques and algorithms such as MEM, NNLS require further investigation. In addition further experimentation with noise and amplitude errors in the MIRIAD UVGEN module.

The principle aims of this research have been achieved but other avenues for further expansion and research have been identified.

## 6. References:

- International SKA Project Office, Ables, J. G. (1974). "Maximum Entropy Spectral Analysis." *Astron. Astrophys. Suppl.* 15: 383-393.
- ATNF. (2007). "MIRIAD." from <http://www.atnf.csiro.au/computing/software/miriad/>.
- Boyle, P. B. (2005). Proposal for Sitting the SKA in Australia. Submitted on behalf of Australasian SKA consortium, ATNF.
- Briggs, D. (1995). High Fidelity Deconvolution of Moderately Resolved Sources. Socorro, New Mexico, The New Mexico Institute of Mining and Technology  
Doctor of Philosophy in Physics.
- Briggs, D. S., F. R. Schwab, et al. (1999). "Imaging." ASP Conference Series 180.
- Burke, B. F. and F. Graham-Smith (2002). *An Introduction to Radio Astronomy*, Cambridge University Press.
- Carilli, C. L. and S. Rawlings (2004). "Science with the Square Kilometre Array." *New Astronomy Reviews* 48.
- Cheung, C. C. (2007). "First 'Winged' and 'X'-Shaped Radio Source Candidates." *Astronomical Journal* 133: 2097-2121.
- Clark, B. G. (1980). "An Efficient Implementation of the Algorithm "CLEAN"." *Astron. Astrophys.* 89: 377-378.
- Clark, B. G. (1995). *Interferometers and Coherence Theory. Very Long Baseline Interferometry and the VLBA*, Astronomical Society of the Pacific.
- Cohen, A. (2004). *Imaging Capability of the LWA Phase II*, Naval Research Laboratory, Code 7213, Washington, DC 20375, USA.
- Cornwell, T., R. Braun, et al. (1999). *Deconvolution. Synthesis Imaging in Radio Astronomy*, ASP.
- DGF. (1999). "Geodetic Reference System 1980 (GRS80)." from <http://www.dgfi.badw.de/geodis/REFS/grs80.html>.
- Diamond, P. J., S. T. Garrington, et al. (2003). *MERLIN User Guide*.
- Djorgovski, S. G., F. Courbin, et al. (2007). Discovery of a Probable Physical Triple Quasar, arXiv:astro-ph/0701155v1.

- Dolinar, S., K.-M. Cheung, et al. (1991). Compressed/reconstructed test images for CRAF/Cassini, Jet Propulsion Lab., California Inst. of Tech., Pasadena.: 88-97.
- Fouque, P., E. Gourgoulhon, et al. (1992). "Groups of galaxies within 80 Mpc. II - The catalogue of groups and group members." *Astronomy and Astrophysics Supplement* 93(2): 211-233.
- Frakes, S. (2003). "NGS Toolkit, Part 4: General Geodetic Computations." *Professional Surveyor* 23(9).
- FUKUZAKI, Y., K. SHIBUYA, et al. (2005). "Results of VLBI experimants conducted with Syowa Station, Antarctica." *Journal of geodesy* 79: 379-388.
- Gonzalez, R. C. and R. E. Woods (2002). *Digital Image Processing*, Prentice Hall.
- Gulyaev, S. (2005). "New Zealand Submission for Siting the SKA." SKANZ.
- Gulyaev, S. and S. Weston (2007). "SKA Simulation Modelling: Phased Approach to SKA Construction." *Southern Stars* 46(2): 5-19.
- Heddl, S. and A. Webster (2000). *Automation of Imaging Simulations for Array Configurations using Classic AIPS*. ALMA Memo, UK Astronomy Technology Centre, Institute for Astronomy Royal Observatory Edinburgh.
- Högbom, J. A. (1974). "Aperture Synthesis with a Non-Regular Distribution of Interferometer Baselines." *Astron. Astrophys. Suppl.* 15: 417-426.
- Johnson, K. E. (2004). "Star formation, massive stars, and super star clusters in nearby galaxies." *New Astronomy Reviews* 48(11-12): 1337-1347.
- Johnston, S., M. Bailes, et al. (2007). "Science with the Australian Square Kilometre Array Pathfinder." *Publications of the Astronomical Society of Australia* 24(4): 174-188.
- Lewis, J. P. (1995) Fast Normalized Cross-Correlation. from <http://www.idiom.com/~zilla/Papers/nvisionInterface/nip.html>
- Lovell, J. (2001). "Difmap Synthesis Imaging Software." from <http://www.atnf.csiro.au/people/jlovell/difmap/>.
- McKay, N., D. McKay, et al. (1997). "The Virtual Radio Interferometer (VRI)." from <http://www.jb.man.ac.uk/vri/>.
- Meeus, J. (1998). *Astronomical Algorithms*, Willmann-Bell Inc.
- NASA (2008). *International VLBI Service for Geodesy and Astrometry 2007 Annual Report*. D. Behrend and K. D. Baver, National Aeronautics and Space Administration.

- NASA/GSFC. (2006). "FITS The Astronomical Image and Table Format." from <http://fits.gsfc.nasa.gov/>.
- NGS. (2005). "XYZWIN." 2.0. from [http://www.ngs.noaa.gov/PC\\_PROD/XYZWIN/](http://www.ngs.noaa.gov/PC_PROD/XYZWIN/).
- NRAO. (2008). "Astronomical Image Processing System." from <http://www.aips.nrao.edu/>.
- Pedlar, A., H. S. Ghataure, et al. (1990). "The Radio Structure of NGC1275." R.A.S. Monthly Notices 246: 477.
- Perley, R. A. (1999). High Dynamic Range Imaging. Synthesis Imaging in Radio Astronomy II, Astronomical Society of the Pacific.
- Phillips, C. J. D., A.; Amy, S. W.; Tingay, S. J.; Tzioumis, A. K.; Reynolds, J. E.; Jauncey, D. L.; Stevens, J.; Ellingsen, S. P.; Dickey, J.; Fender, R. P.; Tudose, V.; Nicolson, G. D. (2007). "Detection of compact radio emission from Circinus X-1 with the first Southern hemisphere e-VLBI experiment." Monthly Notices of the Royal Astronomical Society: Letters 380(1): L11-L14.
- Ponsonby, J. E. B. (1974). "An entropy measure for partially polarized radiation and its application to estimating radio sky polarization distributions from incomplete aperture synthesis' data by the maximum entropy method." Monthly Notices of the Royal Astronomical Society 163: 369.
- Rohlfs, K. and T. Wilson (2004). Tools of Radio Astronomy, Berlin: Springer.
- Ryle, M. and A. Hewish (1960). "The synthesis of large radio telescopes." Monthly Notices of the Royal Astronomical Society 120: 220.
- Ryle, P. M. (1962). "The New Cambridge Radio Telescope." Nature 194: 517-518.
- Schwab, F. R. (1984). "Relaxing the isoplanatism assumption in self-calibration; applications to low-frequency radio interferometry." Astronomical Journal 89: 1076-1081.
- Shepherd, M. C. (1997). Difmap: An Interactive Program for Synthesis Imaging. Astronomical Data Analysis Software and Systems VI, ASP.
- Shepherd, M. C., T. J. Pearson, et al. (1995). Software Report: DIFMAP, Owens Valley Observatory. Bulletin of the American Astronomical Society.
- Sugiyama, M., D. Imaizumi, et al. (2001). "Subspace information criterion for image restoration --- Optimizing parameters in linear filters." IEICE Transactions on Information and Systems E84-D: 1249-1256.
- Taylor, G. (1997). The Difmap Cookbook, Department of Radio Astronomy, California Institute of Technology.

- Thompson, A. R. (1999). Fundamentals of Radio Astronomy. ASP Conference Series.
- Thompson, A. R., J. M. Moran, G.W. Swenson  
. (2004). Interferometry and Synthesis in Radio Astronomy, WILEY-VCH.
- Tingay, P. S. (2005). calculates sky visibility for SKA arrays. SKA array configuration studies - a guide for SKA site proposers.
- Voronkov, M. and M. Wieringa (2005). Dynamic Range of the SKA images, CSIRO ATNF.
- Walker, R. C. (2006). "The SCHED User Manual."
- Weston, S. (2006). DIFMAP User Guide, Centre for RadioPhysics and Space Research, Auckland University of Technology.
- Willis, A. G. (2000). Imaging and Dynamic Range Simulations for an SKA with Large Aperture Antennas, National Research Council of Canada.



## **Appendix A. Electronic Supplement**

It is not practical to present all code and images. So this material has been collated and attached as a CD-ROM, this has a directory structure following the same section structure of this thesis.

Some images within the thesis have been reduced in size and resolution for the purposes of printing. The original image files are included on the CD-ROM for more detailed study and comparison.

The CD-ROM has a file structure that matches the heading structure used in the thesis. For example the images used for Figure 13 which is in Section 2.4, upon the CD-ROM they will be found within the following directory tree:

Drive:\2.0 Discussion of VLBI and Aperture Synthesis Theory\2.4 Deconvolution  
and CLEAN

It is hoped that this will aid the reader.

## Appendix B. DIFMAP CLEAN Map explanation

In Figure 91 is shown a typical final CLEAN map produced by DIFMAP of a astronomical source image. The purpose of this appendix is to explain the items that are contained within this plot to aide the reader with the extensive use of this plot within the thesis.

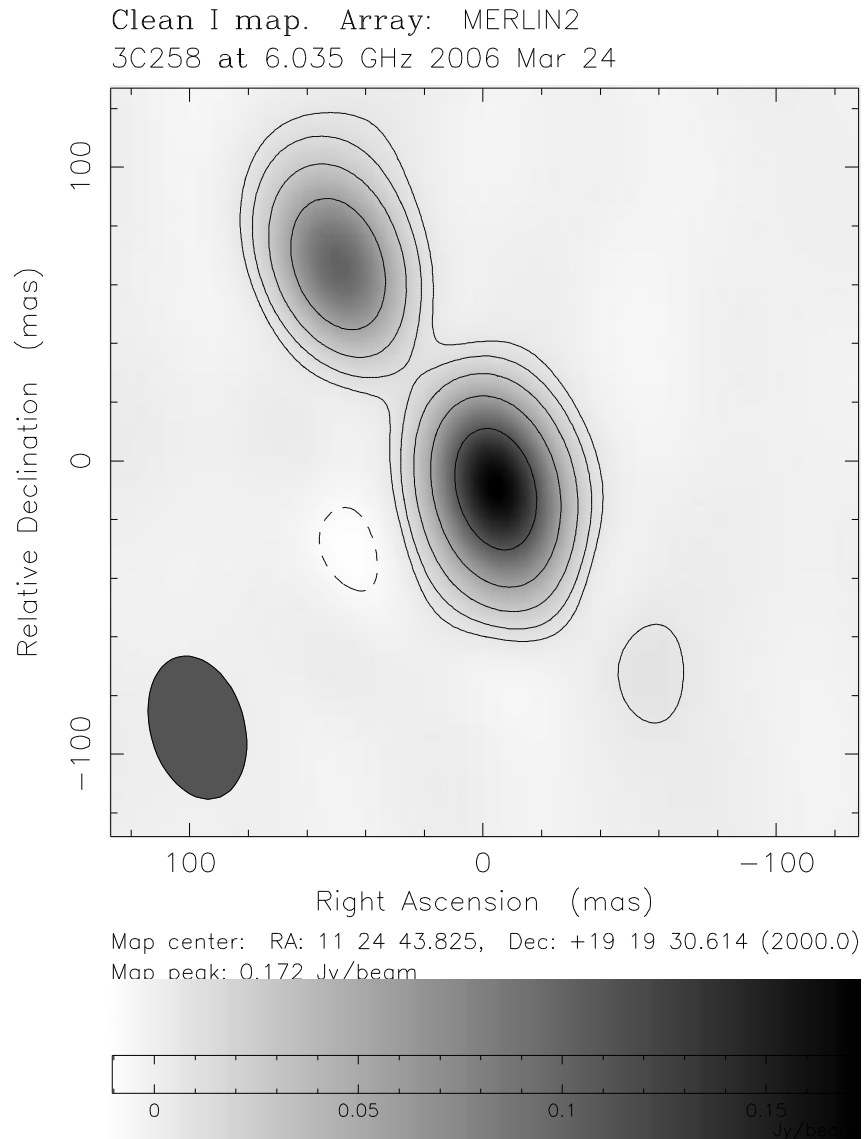


Figure 91: DIFMAP CLEAN Map

First at the top of the plot we have the title “Clean Map. Array: MERLIN2”. The text after “Array” is obtained from the input uv fits file header, and identifies which antenna array was used for the observation.

The second line of the title contains information about the observation, what source was observed in this case 3C258. The frequency of the observation, in this case 6.035 GHz and finally the date of the observation “2006 Mar 24”.

All of this information to date is recorded within the original  $u,v$  data fits file provided by the observatory.

The main body is a pixel image using a shading system based on pixel value. The images within this thesis use a grey scale where a dark colour indicates a high pixel value, and lighter shades indicate lower values. Right at the bottom of the plot is provided a greyscale showing the pixel value in Janskys to pixel colour. Also in this particular plot are contours which are lines joining pixels of equal value, this allows the structure of the source within the image to be represented. Near the bottom of the plot the values used for the contours are indicated, in this plot “%: -4 4 8 16 32 64”. So these are a % of the map peak pixel value.

This main body is plotted where the pixels are at a relative declination and ascension, the actual map center is given below as “RA: 11 24 43.825, Dec: +19 19 30.614 (2000.0)”.

Also within this main body of the plot in the bottom left hand corner is a grey ellipse, this shows the CLEAN beam (restoring beam) shape and size. At the bottom of the plot just above the grey scale is a line “Beam FWHM: 49.8 x 32.1 (mas) at 15.7°” which gives further information about the beam. The CLEAN beam is discussed by (Cornwell, Braun et al. 1999) in some detail.

Please note that DIFMAP can also produce plots using colour apart from the greyscale used here.

## **Appendix C. User Interface**

It has been our experience that User Interfaces to astronomical software for the first time user are very cumbersome and non intuitive. A case in point is AIPS; the learning curve for the interface alone is difficult without the additional task of understanding what the various modules do and how to use them.

Many of these packages have a long history and were originally developed on command line driven systems. Due to the large amount of intellectual property and knowledge now programmed into these systems there has been no serious attempt to port many of these applications to different languages and platforms with the exception of AIPS. AIPS++ is not so much a port but a complete re-write and has been ongoing for many years now. It was wondered if an attempt could be made to provide a more user friendly interface by bolting on a new interface, using Web Technology, to some of these existing packages.

Here we demonstrate the web interface written for the process used in this research. Using the provided URL the user is presented with the initial form shown in Figure 92. As can be seen this is a top level form allowing access to other modules and is laid out from top to bottom mirroring the developed process flow as shown in Figure 16.

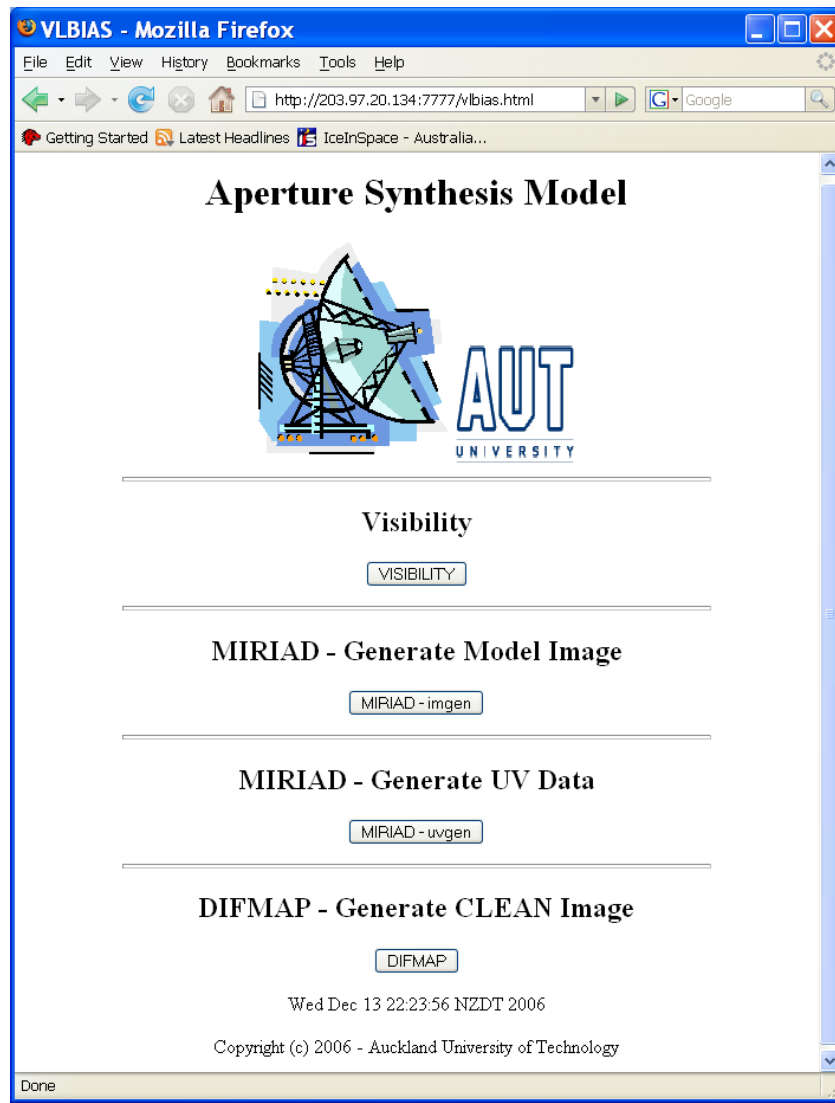


Figure 92: Aperture Synthesis Model Web Page

All of the buttons “VISIBILITY”, “MIRIAD- imgen”, “MIRIAD – uvgen” and “DIFMAP” lead to further forms on web pages that allow data/parameter input and displaying of results. This is I feel an improved interface certainly for the first time user rather than the existing cumbersome command line interfaces.

For this example the “VISIBILITY” button is pressed on the form taking the user to the top level form of the sky visibility program as shown in Figure 93.

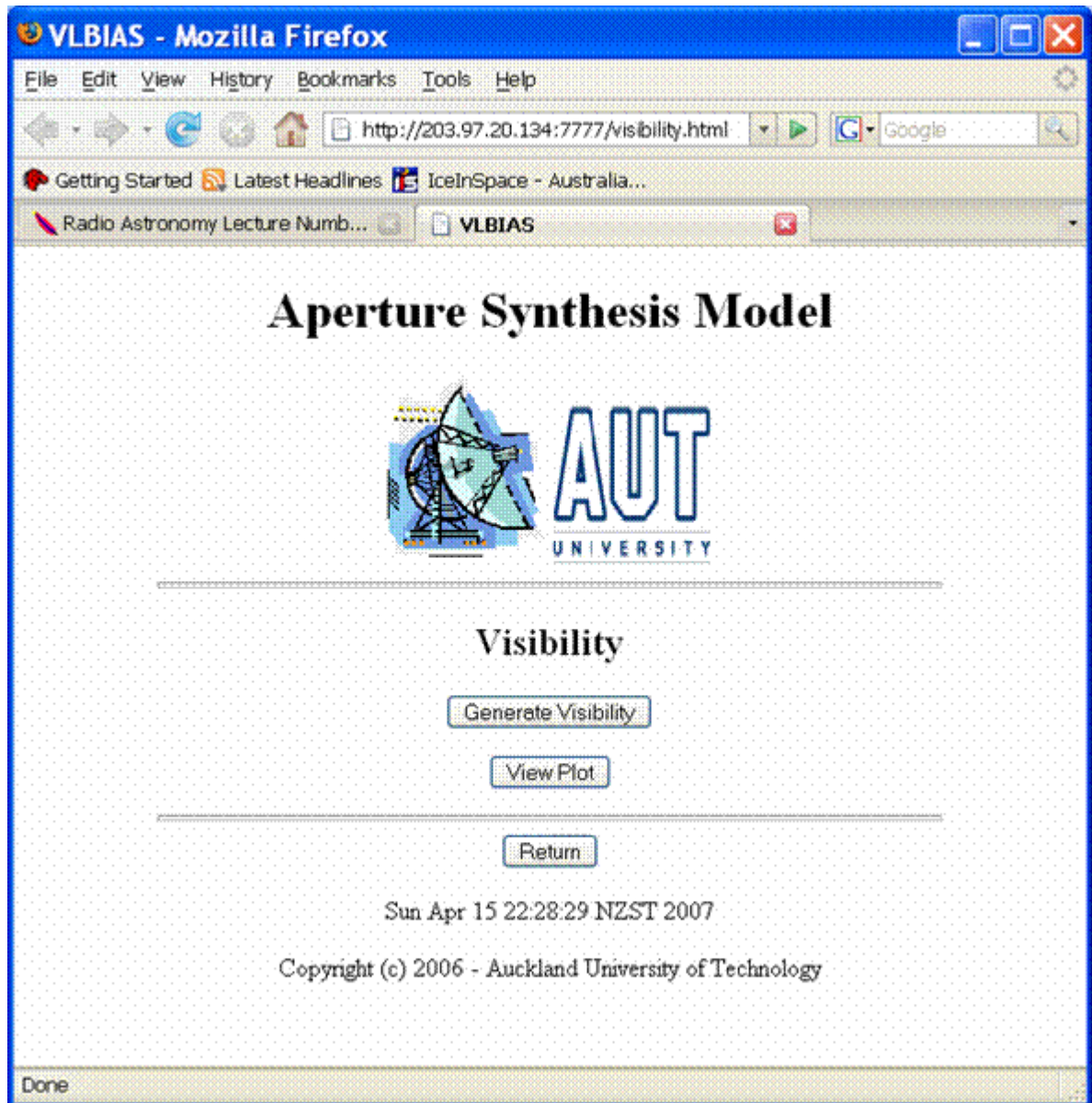
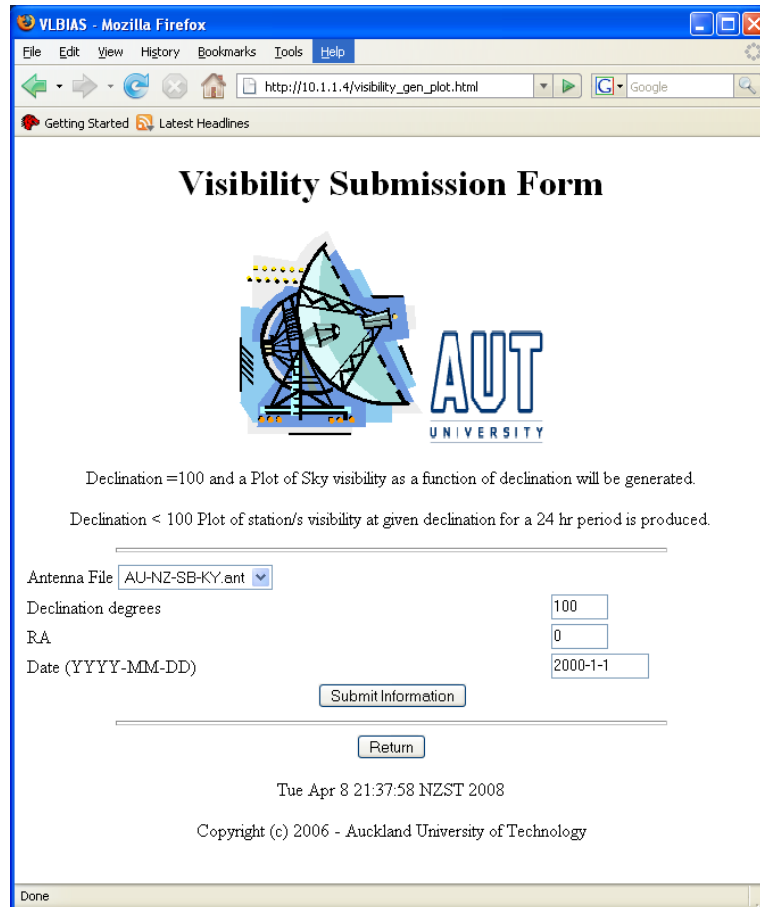


Figure 93: Web Page for the top level Visibility Program

On this form there are three buttons. The first “Generate Visibility” will take the user into a form allowing the input of antenna array parameters for a task in this case the Sky Visibility program as shown in Figure 94. The second button, “View Plot” will allow the user to view a plot produced by “Generate Visibility”. The final, third button, “Return” will return the user to the previous web page in the hierarchy.

Having clicked on the button “Generate Visibility”, the user is presented with the form in Figure 94. The fields in the form have preset defaults as shown, but the user can overwrite and submit their particular requirements if necessary.



The screenshot shows a web browser window titled "VLBIAS - Mozilla Firefox". The address bar displays "http://10.1.1.4/visibility\_gen\_plot.html". The page content includes the title "Visibility Submission Form" and the AUT University logo. Below the logo, there is explanatory text: "Declination = 100 and a Plot of Sky visibility as a function of declination will be generated." and "Declination < 100 Plot of station/s visibility at given declination for a 24 hr period is produced." The form contains a dropdown menu for "Antenna File" set to "AU-NZ-SB-KY.ant", and input fields for "Declination degrees" (100), "RA" (0), and "Date (YYYY-MM-DD)" (2000-1-1). There are "Submit Information" and "Return" buttons. The footer shows the date "Tue Apr 8 21:37:58 NZST 2008" and the copyright notice "Copyright (c) 2006 - Auckland University of Technology".

Figure 94: Web Page for the Visibility Submission Form

Upon clicking the button on the form “Submit Information”, the program is initiated on the host computer. As the program runs, output can be passed to the user in the form of feedback as shown in Figure 95.





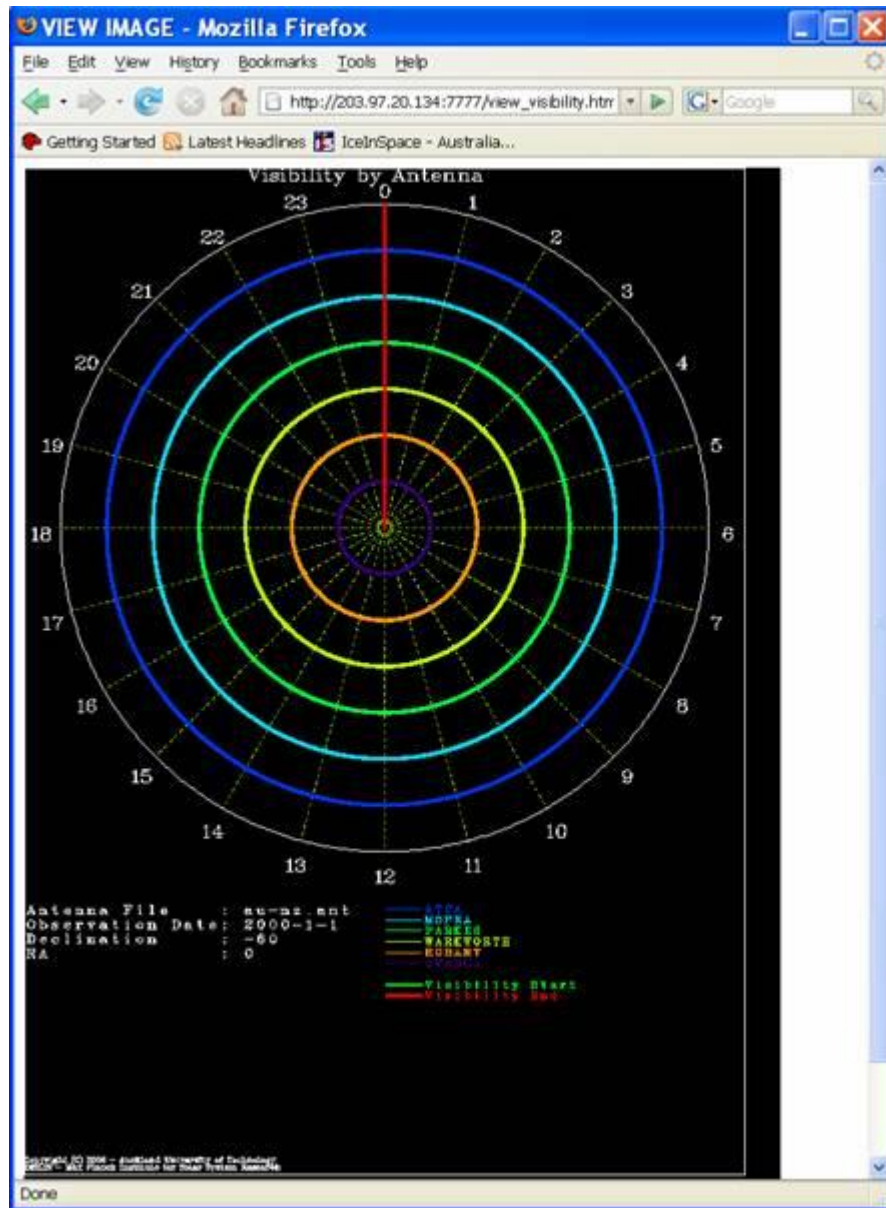


Figure 96: Web Page with Final Visibility Plot

Although this was a rough proto-type created as a proof of concept for this research, it is felt that the ability to bolt a web based interface onto existing applications has been demonstrated.

This interface for the Visibility program was shared with our colleagues in Australia (Prof S. Tingay) served from an Intel Linux server at AUT, by serving this program via web pages over the internet they were able to run the program and provide feedback. The interface can be taken further and does need further work to make it more polished.

## Appendix D. Visibility Perl Program

```
#!/usr/bin/perl
#=====
# vis - Generate visibility of a source for a group of antennae
#=====
#
# This perl cript required the dislin graphics library available from:
# http://www.mps.mpg.de/dislin
#
#=====
# Date:      August 2006
# Author:    Stuart Weston
# Email:     stuartweston@astronomy.org.nz
# Copyright (C) 2006 - Auckland University of Technology
#
# This program is free software; you can redistribute it and/or modify
# it under the terms of the GNU General Public License as published by
# the Free Software Foundation; either version 2 of the License, or
# (at your option) any later version.
#
# This program is distributed in the hope that it will be useful,
# but WITHOUT ANY WARRANTY; without even the implied warranty of
# MERCHANTABILITY or FITNESS FOR A PARTICULAR PURPOSE. See the
# GNU General Public License for more details.
#
# You should have received a copy of the GNU General Public License
# along with this program; if not, write to the Free Software Foundation,
# Inc., 59 Temple Place - Suite 330, Boston, MA 02111-1307, USA.
#=====
# This perl script was generated from a script written by Prof Steven Tingay
# called uptime to calculate sky visibility for SKA configurations.
# December 2004
#
# I am most gratefull to Prof Steven Tingay for providing the source
# of his UPTIME script used for the SKA proposal and the subsequent
# discussions to delevop this new version to be used for my M.Phil research.
#
# References:
# Astronomical Algorithms, 2nd Edition, Jean Meeus, 1998
#
# For Sidereal Time at Greenwich
# United States Naval Observatory Circular 163
# The IAU Resolutions on Astronomical Constants, Time Scales
# and the Fundamental Reference Frame
#=====

use Dislin;
use Math::Trig;

$pi = 3.1415926;
$f = $pi / 180.;
$vis_num=0;
$incdec=5;      # Declination increment (degrees)

# Write GNU Intro
write_gnu_intro();

# Read the input paramaters
read_param();

#Initialize the graphics environment
dislin_init();

# Read the input coords file
read_coords();

# Depending on Declination, plot appropriate graph
```

```

if ($dec < 100) {
    plot_clock_face();
} else {
    plot_vis_dec();
}

#Calculate the Sky visibility
if ($dec < 100) {
    $ddec=$dec;
    calc_sky_vis();
} else {
    for ($ddec=-90;$ddec<95;$ddec=$ddec+$incdec) {
        calc_sky_vis();
    }
    $nv=@a_dec;
    Dislin::curve(\@a_dec,\@a_diff,$nv);
}

#Finish with graphics
dislin_end();

exit;

#=====0=====1=====2=====3=====4=====5=====6

sub write_gnu_intro {

print "\n";
print "          Visibility Version 0.1\n";
print "          -----\n";
print " Visibility comes with ABSOLUTELY NO WARRANTY; \n";
print " for details type: perl vis.pl -gnu\n";
print " This is free software, and you are welcome to\n";
print " redistribute it under certain conditions.\n";
print "\n";

}

#ENDSUB=====

sub gnu_license {
    print "\n";
    print "Copyright (C) 2006 Stuart Weston\n";
    print "\n";
    print "This program is free software; you can redistribute it and/or\n";
    print "modify it under the terms of the GNU General Public License as\n";
    print "published by the Free Software Foundation; either version 2 of\n";
    print "the License, or (at your option) any later version.\n";
    print "\n";
    print "This program is distributed in the hope that it will be useful,\n";
    print "but WITHOUT ANY WARRANTY; without even the implied warranty of\n";
    print "MERCHANTABILITY or FITNESS FOR A PARTICULAR PURPOSE. See the\n";
    print "GNU General Public License for more details.\n";
    print "\n";
    print "You should have received a copy of the GNU General Public\n";
    print "License along with this program; if not, write to the Free\n";
    print "Software Foundation, Inc., 675 Massachusetts Ave, Cambridge,\n";
    print "\n";
    exit;
}

#ENDSUB=====

sub read_param {

# Read the input paramaters
# Valid paramaters are:
# -in=filename          - filename containing antenna data
# -dec=declination      - declination of the source
# -ra=right_assention   - right assention of the source
# -date=date            - date for observation

```

```

# -out=output          - output file name/type ie /xwin or /ps

# Date 2000 Jan 1.0
$date='2000-1-1';
# RA 00:00:00
$ra=0;
# Dec -37:00:00 (why -37, because the author is in Auckland,NZ)
$dec=-37.0;
$out_file=' ';
$num_args=@ARGV;
$amax=48;
$amin=0;

# Any parameters, no then provide usage
if ($num_args < 1 ) {
    usage ();
}

# Has the user entered -gnu to see the gnu license
for ($i=0; $i<$num_args; $i++) {
    if ($ARGV[$i]=~/-gnu/) {
        gnu_license();
    }
    if ($ARGV[$i]=~/-in/) {
        @words=split(/=/,$ARGV[$i]);
        $coord_file=$words[1];
    }
    if ($ARGV[$i]=~/-dec/) {
        @words=split(/=/,$ARGV[$i]);
        $dec=$words[1];
# If DEC is outside a valid range of -90 to 90 then assume
# Visibility (hrs) vs dec plot.
        if($dec > 90 || $dec < -90) {
            $dec=100;
        }
    }
    if ($ARGV[$i]=~/-ra/) {
        @words=split(/=/,$ARGV[$i]);
        $ra=$words[1];
    }
    if ($ARGV[$i]=~/-date/) {
        @words=split(/=/,$ARGV[$i]);
        $date=$words[1];
    }
    if ($ARGV[$i]=~/-out/) {
        @words=split(/=/,$ARGV[$i]);
        $out_file=$words[1];
    }
}

@dates=split(/-/, $date);
$year=@dates[0];
$month=@dates[1];
$day=@dates[2];
$stg=stg();

print "coords file          = $coord_file\n";
print "Declination          = $dec\n";
print "RA                      = $ra\n";
print "Date                    = $date\n";
print "Julian Date             = $jd\n";
print "Sidereal Time Greenwich = $stg\n";
print "output file            = $out_file\n";
}

#ENDSUB=====

sub usage {
    print "Usage: vis.pl -in=<antenna file> -dec=<source declination>\n";
    print "          -ra=<source ra> -date=<date for observation>\n";
}

```

```

print "                -out=<output file or format>\n\n";
print "<antenna file> \n";
print "<source declination> (Default -37)\n";
print "<source ra> Decimal hrs ie 5.4 (Default 0.0)\n";
print "<date for observation> YYYY-M-D (Default 2000-1-1)\n";
print "<output file name / format gif> (Default to screen) \n";
print "\n\n";
exit;
}

#ENDSUB=====

sub dislin_init {

if ($dec < 100) {
    Dislin::page (2000,2800);
}

# if out file not set then plot to screen
if ($out_file=~/^ /) {
    Dislin::metafl('cons');
} else {
    Dislin::metafl('gif');
    Dislin::setfil($out_file);
}
Dislin::disini ();
Dislin::complx ();
Dislin::pagera ();
}

#ENDSUB=====

sub plot_clock_face {

Dislin::messag ('Visibility by Antenna',622,1);
Dislin::height(15);
Dislin::messag ('Copyright (C) 2006 - Auckland University of Technology',1,2750);
Dislin::messag ('DISLIN - Max Planck Institute for Solar System Research',1,2770);
Dislin::height(36);

$oxy=1000;
$radius=900;
Dislin::circle ($oxy,$oxy,$radius);
Dislin::txtjus('CENT');
for ($i=0; $i>=360;) {
    $theta=$i * $f;
    $ny1=$radius*cos($theta)+$oxy;
    $nx1=$radius*sin($theta)+$oxy;
    $ny2=$oxy-$radius*cos($theta);
    $nx2=$oxy-$radius*sin($theta);
    Dislin::setrgb(0.65,0.65,0.65);
    Dislin::dotl;
    Dislin::line ($nx1,$ny1,$nx2,$ny2);
    Dislin::setclr(255);
    Dislin::solid;
    $ty2=$oxy-($radius+54)*cos($theta);
    $tx2=$oxy-($radius+54)*sin($theta);
    Dislin::number (-$i/15,-1,$tx2,$ty2);
    $i=$i+15;
}

Dislin::txtjus('LEFT');

# Write the input data part of the legend

$cdater = 'Observation Date: ' . $date;
$cinfile = 'Antenna File      : ' . $coord_file;
$cddec  = 'Declination      : ' . $dec;
$cra    = 'RA                : ' . $ra;
$my=2050;

```

```

Dislin::height(25);
Dislin::fixspc(1);
Dislin::messag($cinfile,1,$my);
$my=$my+40;
Dislin::messag($cdate,1,$my);
$my=$my+40;
Dislin::messag($cdec,1,$my);
$my=$my+40;
Dislin::messag($cra,1,$my);

}

#ENDSUB=====

sub plot_vis_dec {

$xo=450;
$yo=1800;
$xl=2200;
$yl=1200;

Dislin::axspos ($xo,$yo);
Dislin::axslen ($xl,$yl);

Dislin::name ('Declination (degrees)', 'X');
Dislin::name ('Sky Visibility (Hrs)', 'Y');

Dislin::labdig (-1, 'X');
Dislin::ticks (10, 'XY');

Dislin::titlin ('Sky visibility as a function of declination', 1);

Dislin::graf (-90,90.,-90,30.,0.,24.,0.,2.);

# Set dx and dy
$xo=$xo+$xl/2;
$dx=$xl/180;
$dy=$yl/24;

Dislin::title ();

Dislin::color ('foreground');

Dislin::height(15);
Dislin::messag ('Copyright (C) 2006 - Auckland University of Technology',1,1980);
Dislin::messag ('DISLIN - Max Planck Institute for Solar System Research',1,2000);
Dislin::height(36);

}

#ENDSUB=====

sub read_coords () {
$nr=0;
open(INFILE,$coord_file) || die "Can't open $coord_file\n";
while ($line=<INFILE>) {
chop $line;
if ($line!~/^\#/){
@array=split(/,/,$line);
push @ant_coords,@array;
$nr=$nr+1
}
}
close(INFILE);

# Lets sort the antenna by latitude
sort_antennae();

# Print out the antenna information

for ($i=0;$i<$nr;$i++) {

```

```

        $lat=$ant_coords[$i][0];
        $long=$ant_coords[$i][1];
        $alt=$ant_coords[$i][2];
        $elev_lim=$ant_coords[$i][3];
        $ant_name=$ant_coords[$i][4];
        printf "%-20s : Lat = %7.2f, Long = %7.2f, Alt = %7.2f, Elev =
%5.2f\n", $ant_name, $lat, $long, $alt, $elev_lim;
    }

}

#ENDSUB=====
#
# Sort the antennae by latitude descending

sub sort_antennae () {
    for ($i=0; $i<$nr-1; $i++) {
        for ($j=$i+1; $j<$nr; $j++) {
            if ($ant_coords[$j][0] <= $ant_coords[$i][0]) {
            } else {
                $lat=$ant_coords[$i][0];
                $long=$ant_coords[$i][1];
                $alt=$ant_coords[$i][2];
                $elev_lim=$ant_coords[$i][3];
                $ant_name=$ant_coords[$i][4];

                $ant_coords[$i][0]=$ant_coords[$j][0];
                $ant_coords[$i][1]=$ant_coords[$j][1];
                $ant_coords[$i][2]=$ant_coords[$j][2];
                $ant_coords[$i][3]=$ant_coords[$j][3];
                $ant_coords[$i][4]=$ant_coords[$j][4];

                $ant_coords[$j][0]=$lat;
                $ant_coords[$j][1]=$long;
                $ant_coords[$j][2]=$alt;
                $ant_coords[$j][3]=$elev_lim;
                $ant_coords[$j][4]=$ant_name;
            }
        }
    }
}

#ENDSUB=====
#
# For Sidereal Time at Greenwich
# Ref: United States Naval Observatory Circular 163
#       The IAU Resolutions on Astronomical Constants, Time Scales
#       and the Fundamental Reference Frame

# The bulk of the work is done here

sub calc_sky_vis () {
    Dislin::hsymbol(8);

    # Delta Radius, used for plotting the points on an arc

    $dr=$radius/($nr+1);
    $r=$radius;

    # Colour Increment, colour table 256
    $inc_colour=256/$nr+1;
    # Starting colour
    $colour=$inc_colour;

    # x,y point for legend
    $ly=2050;
    $lx=1000;

```



```

# Sidereal Time Greenwich
# $stg=100.46061837;

for ($i=0;$i<$nr;$i++) {

    @minmax=();

#    Decrement the radius for the arc being pollted
    $r=$r-$dr;

#    Convert lat & long to radians
    $lat=$pi*$ant_coords[$i][0]/180;
    $long=$pi*$ant_coords[$i][1]/180;

#    Convert Dec to radians
    $rdec=$pi*$ddec/180;

    $alt=$ant_coords[$i][2];
    $elev_lim=$ant_coords[$i][3];
    $ant_name=$ant_coords[$i][4];

# Loop through UT times 0 - 24
    for ($ut=0;$ut<24;$ut=$ut+0.01) {

#        This needs to be modified for date before/after J2000
        $lst=$pi*($stg+$ut*15)/180+$long;

#        Have to convert RA in hr angle to radians
        $ha=$lst-2*$pi*$ra/24;
        $h=180*asin(sin($lat)*sin($rdec)+cos($lat)*cos($rdec)*cos($ha))/pi;
#        Not used here for completeness
#        $az=180*atan(sin($ha)/cos($ha)*sin($lat)-tan($ddec)*cos($lat))/pi;

# if source elevation below station elevation limit - discard
        if ($h > $elev_lim) {
            push(@minmax,$ut);
# Plot a point for this visibility, if delta UT small enough
# we will get a line.
            plot_point($l,$ut);
        }

        vis_min_max();

        if($dec < 100 ) {
# write out the legend for antenna visibilities
            Dislin::setclr($colour);
            Dislin::height(20);
            Dislin::line($lx+5,$ly+10,$lx+100,$ly+10);
            Dislin::messag($ant_name,$lx+110,$ly);
            $ly=$ly+30;
        }

#        Change the colour index so each series of arcs
#        plotted are in a different colour.
        $colour=$colour+$inc_colour;

    }

# Print visibility and plot start & end for possible observation
    if($dec < 100) {
        plot_start_end();
    } else {
        $diff=int(100*($amax-$amin))/100;
        if($diff<0){ $diff=0;};
        if($diff>24){ $diff=24;};
        push(@a_dec,$ddec);
        push(@a_diff,$diff);
        Dislin::color('RED');
        Dislin::hsymb1(40);
        Dislin::symbol(10,$xo+$ddec*$dx,$yo-$diff*$dy);
    }
}

```

```

    }
}

#ENDSUB=====
#
# Thought about it and to work out the arcs to be plotted for the
# visibility's got too hard. So plot a series of points with delta
# UT small enough and at the screen resolution we will get an arc.
#
# nant - number of the antenna we are plotting visibilities for
# ha   - Time point which = hour angle on the clock face

sub plot_point() {
    my ($nant,$ha);
    $nant=$_[0];
    $ha=$_[1];

# The hour angle on the clock face = $UT
# Need to convert to radians
    $ha=$ha*$pi/12;

    $nx=$oxy+$r*sin($ha);
    $ny=$oxy-$r*cos($ha);

    Dislin::setclr($colour);
    Dislin::symbol (21,$nx,$ny);
}

#ENDSUB=====

sub dislin_end {
    Dislin::disfin ();
}

#ENDSUB=====

# Filter visibility and define min & max UT
# This sub is built from code provided by Prof Steven Tingay with
# comments from Marcelo Arnal. I have pulled it into a function.

sub vis_min_max {

    my($i);

    $n=@minmax;
    $day_zero=0;
    $day_one=0;
    $step=0;
    for ($i=0;$i<$n;$i++) {
        $day_zero=1 if (int($minmax[$i]*100)/100==23.99);
        $day_one=1 if (int($minmax[$i]*100)/100==0.01);
    }
    if ($day_zero==1 && $day_one==1 && $n<2400) {
        $k=0;
        $step=1 if (int($minmax[$k+1]*100)/100-int($minmax[$k]*100)/100>0.02);
        while ($step==0) {
            $minmax[$k]=$minmax[$k]+24;
            $k++;
            $step=1 if (int($minmax[$k+1]*100)/100-int($minmax[$k]*100)/100>0.02);
        }
        $minmax[$k]=$minmax[$k]+24;
    } elsif ($n<2400) {
        for ($i=0;$i<$n;$i++) {
            $minmax[$i]=$minmax[$i]+24;
        }
    }
    @sort= sort
    @minmax;
    if ($n==2400) {
        $min=0;

```

```

        $max=48;
    } else {
        $min=$sort[0];
        $max=$sort[$n-1];
    }
    $vis=$max-$min;

    if ($vis < 4 ) {
        printf "Visibility for Antenna %20s is less than 4 hr\n", $ant_name;
    }

    if ($max<$amax) {
        $amax=$max;
    }
    if ($min>$amin) {
        $amin=$min;
    }
}

#ENDSUB=====
#
# Function to plot the start and end hands for observation
# window.

sub plot_start_end {

    print "Min: $amin\nMax: $amax\n";

    $diff=int(100*($amax-$amin))/100;

    # if diff < 0 then we do not have visibility for all antennae
    # at this declination
    if ($diff < 0) {
        return;
    }

    print "Simultaneous visibility for dec=$ddec is $diff hr\n";

    # The hour angle on the clock face = $UT
    # Need to convert to radians

    Dislin::linwid(6);

    # Plot Observation Window Start Hand
    $angle=$amin*$pi/12;
    $nx=$oxy+$radius*sin($angle);
    $ny=$oxy-$radius*cos($angle);
    Dislin::color('GREEN');
    Dislin::line($oxy,$oxy,$nx,$ny);

    # Plot Observation Window End Hand
    $angle=$amax*$pi/12;
    $nx=$oxy+$radius*sin($angle);
    $ny=$oxy-$radius*cos($angle);
    Dislin::color('RED');
    Dislin::line($oxy,$oxy,$nx,$ny);

    # Add an item to the legend for these hour hands.

    $ly=$ly+30;
    Dislin::height(20);
    Dislin::color('GREEN');
    Dislin::line($lx+5,$ly+10,$lx+100,$ly+10);
    Dislin::linwid(1);
    Dislin::messag('Visibility Start',$lx+110,$ly);
    Dislin::linwid(6);
    $ly=$ly+30;
    Dislin::color('RED');
    Dislin::line($lx+5,$ly+10,$lx+100,$ly+10);
    Dislin::linwid(1);
    Dislin::messag('Visibility End',$lx+110,$ly);

```

```

}

#ENDSUB=====

# Julian Day
# Ref: Astronomical Algorithms, Jean Meeus
sub julian_day {

    my($a,$b,$yr,$mn,$exp1,$exp2,$exp3);

    if($month < 3) {
        $yr=$year-1;
        $mn=$month+12;
    } else {
        $yr=$year;
        $mn=$month;
    }

    $a=int($yr/100);
    $b=2-$a+int($a/4);

    $exp1=int(365.25*($yr+4716));
    $exp2=int(30.6001*($mn+1));
    $exp3=$day+$b-1524.5;

    $jd=$exp1+$exp2+$exp3;
    return $jd;
}

#ENDSUB=====

# Sidereal Time at Greenwich
# I have not included nutation as it is in the order of Seconds Arc
# to small for our resolution in this program.
# Ref: Astronomical Algorithms, Jean Meeus

sub stg {

    my($t,$jd,$stg,$exp1,$exp2,$exp3,$exp4);

    $jd=julian_day();

    $t=($jd-2451545.0)/36525;

    $exp1=100.46061837;
    $exp2=36000.770053608*$t;
    $exp3=0.00387933*$t**2;
    $exp4=$t**3/38710000;

    $stg=$exp1+$exp2+$exp3-$exp4;

    # Reduce result to 0-360 by adding or subtracting multiples of 360 untill $stg < 360
    while ($stg > 360) {
        $stg=$stg-360;
    }

    return $stg
}

```

## Appendix E. MIRIAD Observatories.dat

```
#-----
# observatories.dat
#-----
#
# NOTE: The list must be ordered alphabetically by observatory AND
#       parameter.
#
# Name      Name of the observatory
#
# Parameter Recognized observatory parameters are:
#           antdiam      Antenna diameter (m).
#           ellimit      Elevation limit (deg).
#           evector      Offset angle of the feed from the local
#                       vertical (deg).
#           ew           Positive if the telescope is an E-W array.
#           height       Height above sea level (m).
#           jyperk       Typical system gain (Jy/K).
#           latitude     Observatory latitude:
#                       sgn - sign, +1 or -1
#                       deg - degree (must be positive)
#                       min - arcmin
#                       sec - arcsec
#           longitude    Observatory longitude:
#                       sgn - sign, +1 or -1
#                       deg - degree (must be positive)
#                       min - arcmin
#                       sec - arcsec
#           mount        Telescope mount:
#                       0: ALTAZ
#                       1: EQUATORIAL
#                       3: XYEW
#                       4: NASMYTH
#           nants        Number of antennae normally in the array.
#           systemp      Typical system temperature (K).
#           subdiam      Subreflector diameter (m).
#
# Value      Value of the parameter.
#
# Note: there is a limit to how many entries can be stored in miriad as
#       defined by MAXPARAMS in obspar.h.
#
#       Extracted from obspar.for by Stuart Weston - Auckland University of
#       Technology, July 2006
#
# $Id: observatories.dat,v 1.2 2006/08/09 02:54:56 call103 Exp $
#-----
#
# Atacama Large Millimeter Array - provisional.
#
# From Simon Radford:
# At the Grenoble meeting Chajnantor South was chosen as the nominal
# array center. In 1999 November we measured this with a differential GPS:
#
#           N           E           alt
# Chajnantor South  7453228.830  627807.166  5016.792
#
# where the coordinates are UTM (m) on the Prov. S. Am. 1956 datum which
# we use for mapping and civil construction. This position is 544m south
# and 35m east of the NRAO container. By long integration with a navigation
# GPS I measured the position of the NRAO container (Memos 261 312):
#
# NRAO container  7453772  627772  5060
#
# on the same datum. Again using this datum the latitude and longitude of
# the NRAO container are:
#
# 23deg 1' 9.42'' South 67deg 45' 11.44'' West
```

```

#
# Note these coordinates are based on the PSAm56 datum and are not the
# "astronomical" latitude and longitude. The native datum for GPS the
# WGS84 datum is very close to the astronomical coordinate system
# determined from VLBI. In this datum the NRAO container is at:
#
# 23deg 1' 22.42'' South 67deg 45' 17.74'' West
#
alma          antdiam          12.0
alma          ellimit          12.0
alma          evector          45.0
alma          height           5017.0
alma          jyperk           40.7
alma          latitude         -1 23 01 22.42
alma          longitude        +1 067 45 17.74
alma          mount            ALTAZ
alma          nants            64.0
alma          systemp          40.0

# Australia Telescope Compact Array (ATNF).
# Geodetic coordinates on WGS84 from John Reynolds refer to station 35.
atca          antdiam          22.0
atca          ellimit          12.0
atca          evector          45.0
atca          ew               1.0
atca          height           236.87
atca          jyperk           13.0
atca          latitude         -1 30 18 46.3849
atca          longitude        +1 149 33 00.4997
atca          mount            ALTAZ
atca          nants            6.0
atca          subdiam          2.8
atca          systemp          50.0

# CARMA (Combined California Array - geometric mean of 10.4 and 6.1m).
carma         antdiam          8.0
carma         ellimit          5.0
carma         evector          90.0
carma         height           2200.0
carma         jyperk           80.0
carma         latitude         +1 37 16 43.00
carma         longitude        -1 118 08 32.00
carma         mount            ALTAZ
carma         nants            15.0
carma         systemp          200.0

# Ceduna 30m dish.
# Ref: Richard Dodson 2001/05/22.
ceduna30m     antdiam          30.0
ceduna30m     height           161.0
ceduna30m     latitude         -1 31 52 05.04
ceduna30m     longitude        +1 133 48 36.565
ceduna30m     mount            ALTAZ
ceduna30m     nants            1.0

# CSO (from Oliver Lay -> MCHW 20may1997 - some values need confirmation).
cso           antdiam          10.4
cso           ellimit          5.0
cso           evector          90.0
cso           height           4080.0
cso           jyperk           60.0
cso           latitude         +1 19 49 33.8
cso           longitude        -1 155 28 46.4
cso           mount            ALTAZ
cso           nants            2.0
cso           systemp          500.0

# GMRT.
gmrt          antdiam          45.0
gmrt          height           650.0
gmrt          latitude         +1 19 06 00.0

```

```

gmrt          longitude      -1 074 03 00.0

# Hatcreek mm array (BIMA).
# Jyperk and systemp given by Wright from 3mm vlbi.
hatcreek      antdiam        6.1
hatcreek      evector        0.0
hatcreek      height         1043.0
hatcreek      jyperk         120.0
hatcreek      latitude       +1 40 49 02.50
hatcreek      longitude      -1 121 28 18.49
hatcreek      mount          ALTAZ
hatcreek      nants          10.0
hatcreek      subdiam        0.61
hatcreek      systemp        300.0

# Hobart 26m dish.
# Ref: misc NGS skd file from Hobart.
hobart26m     antdiam        26.0
hobart26m     height         66.12
hobart26m     latitude       -1 42 48 12.9
hobart26m     longitude      +1 147 26 25.9
hobart26m     mount          XYEW
hobart26m     nants          1.0

# The IRAM mm array at Plateau de Bure.
# Ref: S.Guillaoteau etal. 1992 A&A 262 624.
iram15m       antdiam        15.0
iram15m       height         2650.0
iram15m       jyperk         24.0
iram15m       latitude       +1 44 38 02.00
iram15m       longitude      +1 005 54 28.40
iram15m       mount          ALTAZ
iram15m       nants          6.0
iram15m       systemp        300.0

# JCMT (from Oliver Lay -> MCHW 20may1997).
jcmt          antdiam        15.0
jcmt          ellimit        5.0
jcmt          evector        90.0
jcmt          height         4092.0
jcmt          jyperk         40.0
jcmt          latitude       +1 19 49 33.8
jcmt          longitude      -1 155 28 46.4
jcmt          mount          ALTAZ
jcmt          nants          2.0
jcmt          subdiam        0.75
jcmt          systemp        500.0

# Kitt Peak mm single dish (NRAO).
# Jyperk and systemp given by Wright from 3mm vlbi.
kittpeak      antdiam        12.0
kittpeak      height         1938.0
kittpeak      jyperk         55.0
kittpeak      latitude       +1 31 57 12.10
kittpeak      longitude      -1 111 36 51.12
kittpeak      mount          ALTAZ
kittpeak      nants          1.0
kittpeak      systemp        200.0

# Mopra 22m dish.
mopra         antdiam        22.0
mopra         height         866.44
mopra         latitude       -1 31 16 04.127
mopra         longitude      +1 149 05 58.706
mopra         mount          ALTAZ
mopra         nants          1.0

# Nobeyama 45m single dish.
# Jyperk and systemp given by Wright from 3mm vlbi.
nobeyama45    antdiam        45.0
nobeyama45    jyperk         6.0

```

```

nobeyama45      nants          1.0
nobeyama45      systemp        500.0

# Nobeyama mm array.
# Jyperk and systemp given by Wright from 3mm vlbi.
nro10m          antdiam        10.0
nro10m          height         1350.0
nro10m          jyperk         74.0
nro10m          latitude       +1 35 56 00.0
nro10m          longitude      +1 138 29 00.0
nro10m          nants          6.0
nro10m          systemp        300.0

# Onsala Dish.
# Jyperk and systemp given by Wright from 3mm vlbi.
onsala          antdiam        20.0
onsala          height         10.0
onsala          jyperk         28.0
onsala          latitude       +1 57 23 46.60
onsala          longitude      +1 011 55 45.40
onsala          nants          1.0
onsala          systemp        250.0

# Owens Valley Radio Observatory (mm array).
# Jyperk and systemp given by Wright from 3mm vlbi.
ovro            antdiam        10.4
ovro            height         1222.0
ovro            jyperk         74.0
ovro            latitude       +1 37 14 00.00
ovro            longitude      -1 118 17 00.00
ovro            mount          ALTAZ
ovro            nants          6.0
ovro            systemp        300.0

# Parkes.
parkes          antdiam        64.0
parkes          ellimit        30.5
parkes          height         414.80
parkes          latitude       -1 32 59 54.263
parkes          longitude      +1 148 15 48.636
parkes          mount          ALTAZ
parkes          nants          1.0
parkes          subdiam        3.0

# Some Penticton parameters.
penticton       antdiam        9.0
penticton       height         156.0
penticton       latitude       +1 49 19 24.0
penticton       longitude      -1 119 37 12.0

# Jyperk and systemp given by Wright from 3mm vlbi.
quabbin         antdiam        15.0
quabbin         jyperk         45.0
quabbin         systemp        240.0

# RPA - seti array near Leuchner.
rpa             antdiam        3.6
rpa             ellimit        8.0
rpa             height         238.0
rpa             jyperk         418.0
rpa             latitude       +1 37 55 03.6
rpa             longitude      -1 122 09 21.0
rpa             mount          ALTAZ
rpa             nants          6.0
rpa             systemp        60.0

# SEST.
sest            antdiam        15.0
sest            height         2400.0
sest            latitude       -1 29 15 34.0
sest            longitude      +1 070 44 04.0

```



```

# Submillimeter Array (SMA).
# Supplied by Ramprasad Rao.
sma          antdiam          6.0
sma          height          4080.0
sma          jyperk          130.0
sma          latitude         +1 19 49 33.8
sma          longitude        -1 155 28 46.4
sma          mount            NASMYTH
sma          nants            8.0

# SZA - Sunyaev-Zeldovich Array of eight 3.5m antennae - part of CARMA.
sza          antdiam          3.5
sza          ellimit          5.0
sza          evector          90.0
sza          height          2400.0
sza          jyperk          383.0
sza          latitude         +1 37 14 00.00
sza          longitude        -1 118 17 00.00
sza          mount            ALTAZ
sza          nants            8.0
sza          systemp          200.0

# SZA10 - SZA cross correlalations of 3.5m and 10.4m antennae - part of CARMA.
sza10        antdiam          6.0
sza10        ellimit          5.0
sza10        evector          90.0
sza10        height          2400.0
sza10        jyperk          128.0
sza10        latitude         +1 37 14 00.00
sza10        longitude        -1 118 17 00.00
sza10        mount            ALTAZ
sza10        nants            8.0
sza10        systemp          200.0

# SZA6 - SZA cross correlalations of 3.5m and 6.1m antennae - part of CARMA.
sza6         antdiam          4.6
sza6         ellimit          5.0
sza6         evector          90.0
sza6         height          2400.0
sza6         jyperk          220.0
sza6         latitude         +1 37 14 00.00
sza6         longitude        -1 118 17 00.00
sza6         mount            ALTAZ
sza6         nants            8.0
sza6         systemp          200.0

# Very Large Array (NRAO).
# Values taken from the Green Book (pages 1-10 1-16 6-17).
vla          antdiam          25.0
vla          ellimit          8.0
vla          height          2124.0
vla          jyperk          8.0
vla          latitude         +1 34 04 43.497
vla          longitude        -1 107 37 03.819
vla          mount            ALTAZ
vla          nants            27.0
vla          systemp          60.0

# Westerbork Synthesis Radio Telescope (NFRA).
# Longitude and latitude given by Noordam which differ from the
# the values in the ephemeris (+006:35:15.00, +52:55:00.90).
wsrt         antdiam          25.0
wsrt         evector          -90.0
wsrt         ew              1.0
wsrt         height          5.0
wsrt         jyperk          8.0
wsrt         latitude         +1 52 43 53.84
wsrt         longitude        +1 006 36 15.01
wsrt         mount            EQUATORIAL
wsrt         nants            14.0

```

wsrt

systemp

30.0

## Appendix F. MATLAB Scripts for FITS Image Correlation

### 2-D Cross Correlation

```
%=====
%MATLAB
%
% fom.m
%
% Produce a figure of merit between a model image and the final
% CLEAN image. Using xcorr2
%
% Stuart Weston
% Auckland University of Technology 2007
%
% This program is free software; you can redistribute it and/or modify
% it under the terms of the GNU General Public License as published by
% the Free Software Foundation; either version 2 of the License, or
% (at your option) any later version.
%
% This program is distributed in the hope that it will be useful,
% but WITHOUT ANY WARRANTY; without even the implied warranty of
% MERCHANTABILITY or FITNESS FOR A PARTICULAR PURPOSE. See the
% GNU General Public License for more details.
%
% You should have received a copy of the GNU General Public License
% along with this program; if not, write to the Free Software
% Foundation, Inc., 59 Temple Place, Suite 330, Boston, MA 02111-1307 USA
%
%=====

% read in the model image

image1=fitsread('D:\WORKING\Stuart Weston\AUT\MPhil-Thesis\3.0 Simulation Model
Method\2.4 Model Source\ska4.source.fits');

[m,n]=size(image1);
amax=max(max(image1));
amin=min(min(image1));
amax
amin

% read in the CLEAN image

image2=fitsread('D:\WORKING\Stuart Weston\AUT\MPhil-Thesis\4.0 Simulation Model
Results\3.4 SKA Phased\core+int\clean_ska4.fits');
bmax=max(max(image2));
bmin=min(min(image2));
bmin
bmax

% calculate normalization function

norm=(amax/(bmax-bmin));
norm

% generate a normalized image2 (CLEAN)

for i=1:m
    for j=1:n
        nimage2(i,j)=(image2(i,j)-bmin)*norm;
    end
end

% 2-D Cross Correlation

ccimage=xcorr2(image1,nimage2);
```

```
ccimage=conv2(image1,nimage2);  
maxcor=max(max(ccimage));  
sprintf('Maximum Correlation Value = %d',maxcor)  
maxcor=sum(sum(ccimage));  
sprintf('Sum Correlation Value = %d',maxcor)
```

## Normalized 2-D cross-correlation

```
%=====
%MATLAB
%
% fom.m
%
% Produce a figure of merit between a model image and the final
% CLEAN image. Using xcorr2
%
% Stuart Weston
% Auckland University of Technology 2007
%
% This program is free software; you can redistribute it and/or modify
% it under the terms of the GNU General Public License as published by
% the Free Software Foundation; either version 2 of the License, or
% (at your option) any later version.
%
% This program is distributed in the hope that it will be useful,
% but WITHOUT ANY WARRANTY; without even the implied warranty of
% MERCHANTABILITY or FITNESS FOR A PARTICULAR PURPOSE. See the
% GNU General Public License for more details.
%
% You should have received a copy of the GNU General Public License
% along with this program; if not, write to the Free Software
% Foundation, Inc., 59 Temple Place, Suite 330, Boston, MA 02111-1307 USA
%
%=====

% read in the model image

image1=fitsread('D:\WORKING\Stuart Weston\AUT\MPhil-Thesis\2.0 Method\2.4 Model
Source\agn3.source.fits');

[m,n]=size(image1);
m
n
amax=max(max(image1));
amin=min(min(image1));
amax
amin

% read in the CLEAN image

image2=fitsread('D:\WORKING\Stuart Weston\AUT\MPhil-Thesis\3.0 Results\3.3 AU-NZ-SB\AU-
NZ-SB.12hr.-80Dec\clean_agn3.au-nz-sb.fits');
[m,n]=size(image2);
m
n
bmax=max(max(image2));
bmin=min(min(image2));
bmin
bmax

% generate

nimage=zeros(0,1024)

for i=1:m
    for j=1:n
        nimage(i+256,j+256)=image2(i,j);
    end
end

% 2-D Normalized Cross Correlation

%ccimage=xcorr2(image1,nimage2);
ccimage=normxcorr2(image1,nimage2);
%figure, surf(ccimage), shading flat
```

```
cor=max(ccimage(:));  
sprintf('Correlation Value = %d',cor)
```